THE UNIVERSITY *of* EDINBURGH

The Effect of Matrix Stiffness on the Behaviour of Liver Resident Cell Populations in Chronic Liver Disease and Hepatocarcinogenesis

Timothy Thomas Gordon-Walker

BSc MBChB MRCP

Submitted for the degree of Doctor of Philosophy

University of Edinburgh

2013

Declaration of Authorship

I declare that the thesis presented here has been produced in accordance with the regulations put forward by the University of Edinburgh as stated below:

(a) The thesis has been composed by the student
(b) Either that the work is the student's own, or, if the student has been a member of a research group, that the student has made a substantial contribution to the work, such contribution being clearly indicated, and
(c) That the work has not been submitted for any other degree or professional qualification except as specified.

Signed: ……..

Date: ……...

Abstract

The Effect of Matrix Stiffness on the Behaviour of Liver Resident Cell Populations in Chronic Liver Disease and Hepatocarcinogenesis

Dr Timothy Thomas Gordon-Walker

Introduction: The development of liver fibrosis is characterised by dramatic changes in the biomechanical composition and mechanical properties of the extracellular matrix (ECM). Increases in matrix stiffness associated with inflammation and fibrosis are implicated in promoting cancer development. Clinical studies have demonstrated a close association between increases in liver stiffness and the incidence of hepatocellular carcinoma (HCC). The effect of changes in matrix stiffness on tissue-resident hepatic progenitor cells (HPC) is unknown. Aberrant HPC proliferation has been implicated in the pathogenesis of HCC.

It was hypothesised that changes in the stiffness of the cellular microenvironment are important in regulating the behaviour of liver-resident cell populations and may promote the development of HCC.

Aims: i) to determine how changes in the stiffness of the cancer cell niche might regulate proliferation, differentiation and chemotherapeutic resistance in HCC; ii) to determine the relationship between changes in liver stiffness and hepatic progenitor cell (HPC) response in rodent models of chronic liver disease; and iii) to determine whether changes in the stiffness of the HPC niche regulate proliferation and differentiation in these cells. A secondary aim of the thesis was to characterise the pattern of histological changes observed in rodent models of chronic hepatic congestion and whether this might provide insight into the effect of oedema and congestion on the development of liver fibrosis.

Methods: Cell culture experiments in HCC (Huh7/ HepG2) and HPC cell lines were performed using a system of ligand-coated polyacrylamide (PA) gel supports of variable stiffness. The stiffness of the PA supports (expressed as shear modulus) was altered across a physiological change (1-12kPa) corresponding to values encountered in normal and fibrotic livers. Thiacetamide and carbon tetrachloride (CCl_4) models of liver fibrosis were used to investigate the relationship between increasing liver fibrosis, changes in matrix stiffness and HPC response. The pattern of histological changes in the liver in response to hepatic congestion was assessed in two unrelated murine models of dilated cardiomyopathy; the python and CREB S133A mice.

Results: Increases in matrix stiffness, as would be encountered in liver fibrosis, promote HCC cell proliferation. Increasing matrix stiffness is associated with enhanced basal and hepatocyte growth factor-mediated signalling though ERK, PKB/ Akt and STAT3. Stiffness-dependent HCC cell proliferation is modulated by β1-integrin and focal adhesion kinase. Increasing matrix stiffness is associated with a reduction in chemotherapy-induced apoptosis in HCC cells. However, following chemotherapy there was an increase in the frequency of clone-initiating cells for cells maintained in a low stiffness environment. Flow cytometry in HepG2 cells demonstrated that culture in a low stiffness environment was associated with an increase in the frequency of the stem cell markers CD44, CD133 and CXCR-4. This effect was further enhanced in the presence of chemotherapy.

There is a close association between HPC numbers and liver stiffness measurements in a rat CCl_4 model of chronic liver fibrosis. The major expansion in HPC numbers in this model coincides with a similarly large increase in fibrous tissue deposition. *In vitro* experiments using PA supports demonstrate that increasing matrix stiffness promotes the proliferation of both primary murine HPCs and an immortalised HPC line (BMOL). Changes in matrix stiffness regulate the expression of hepatocyte and biliary markers in BMOL cells.

Histological studies in both the Python and CREB S133A models reveal findings consistent with acute on chronic cardiac hepatopathy (ischaemic hepatitis). Features of chronic passive congestion and centrilobular necrosis are present concurrently and develop rapidly. Bridging fibrosis and cirrhosis are not present.

Conclusions: Physiologically-relevant changes in matrix stiffness regulate proliferation, differentiation, chemotherapeutic-resistance and stem cell marker expression in HCC cells. Similarly, increases in matrix stiffness are closely correlated to HPC response *in vivo* and regulate HPC proliferation and differentiation *in vitro*.

List of contents

Chapter 2: Materials and methods

Chapter 5: Studies to characterise the effect of chronic passive congestion on liver fibrogenesis

Chapter 6: General Discussion

List of figures

Chapter 1

Chapter 2

Chapter 3

Chapter 4

Chapter 5

List of tables

Publications and presentations arising from this thesis

Publications:

Schrader J*, **Gordon-Walker TT***, Aucott RL, Van Deemter M, Quaas A, Walsh S, Benton D, Forbes SJ, Wells RG and Iredale JP. Matrix stiffness modulates proliferation, chemotherapeutic response and dormancy in hepatocellular carcinoma cells. Hepatology. 2011: 53(4); 1192-1205 **(*Joint First Authors)**

Abstracts:

Gordon-Walker TT, Schrader J, Aucott RL, Van Deemter M, Benton D, Forbes SJ, Wells RG and Iredale JP. Matrix stiffness modulates proliferation, differentiation and chemotherapy resistance in hepatocellular carcinoma. Hepatology. 2010: 52(4); 936A

Gordon-Walker TT, Schrader J, Benton D, Van Deemter M, Forbes SJ, Wells RG and Iredale JP. Matrix stiffness regulates proliferation, differentiation and chemotherapeutic responsiveness in hepatocellular carcinoma. Gut. 2010: 59; A26-27

Fallowfield J, Hayden AL, Aucott RL, Schrader J, **Gordon-Walker TT**, Mole D, Collins JE and Iredale JP. Relaxin inhibits hepatic myofibroblast contractility and modulates portal hypertension *in vivo*. Hepatology. 2010: 52(4); 343A

Schrader J, **Gordon-Walker TT**, Aucott R and Iredale JP. Co-culture of hepatoma cells with hepatic stellate cells promotes tumour cell proliferation and survival. J Hepatology 2009; 50 Supplement 1: S200

Presentations:

Gordon-Walker TT, Aucott, RL, Hay DC, Wells RG and Iredale JP. Uniaxial Strain Facilitates Cytoskeletal Realignment and Promotes a Fibrogenic Phenotype in Hepatic Stellate Cells in vitro. 04/13. Poster Presentation. EASL. Amsterdam, Netherlands

Gordon-Walker TT, Schrader J, Boulter L, Robson AJ, Wells RG, Forbes SJ and Iredale JP. Physiological Changes in Matrix Stiffness Modulate Hepatic Progenitor Cell Morphology, Proliferation and Differentiation. 06/2012. Oral Presentation. Digestive Diseases Federation Meeting. Liverpool, UK

Gordon-Walker TT, Schrader J, Benten D, Van Deemter M, Forbes SJ, Wells RG and Iredale JP. Matrix Stiffness Modulates Proliferation, Differentiation and Chemotherapy Resistance in Hepatocellular Carcinoma. 11/2010. Poster Presentation. The Liver Meeting. AASLD. Boston. USA

Gordon-Walker TT, Schrader J, Benten D, Van Deemter M, Forbes SJ, Wells RG and Iredale JP. Matrix Stiffness Regulates Proliferation, Differentiation and Chemotherapeutic Responsiveness in Hepatocellular Carcinoma. 09/2010. Poster Presentation. BASL. London. UK

Gordon-Walker TT, Schrader J, Benten D, Van Deemter M, Forbes SJ, Wells RG and Iredale JP. Matrix Stiffness Determines the Malignant Phenotype of Hepatocellular Cancer. 11/2009. Oral Presentation. Scottish Society of Gastroenterologists. Dundee, UK

Gordon-Walker TT, Hough TA, Schrader J, Docherty L, Towlson C, Cheeseman M, Forbes SJ, Simpson KJ, Dear N and Iredale JP. Hepatic Fibrosis in Chronic Hepatic Congestion: The Characterisation of a Novel Murine Model of Cardiac Hepatopathy (Python Mouse). 09/2009. Poster Presentation. BASL. Edinburgh. UK

Acknowledgements

I would like to thank the many people who have contributed to the work presented in this thesis. Firstly I would like to thank my principal supervisor, John Iredale for his assistance in securing an MRC Clinical Research Training Fellowship and for his help, encouragement and mentorship throughout the course of my research. I would also like to thank Stuart Forbes and Ken Simpson for their contribution in directing my research. Special thanks are due to Joerg Schrader who taught me a number of important laboratory techniques and with whom I collaborated closely in respect to my work on hepatocellular carcinoma. I should also thank everyone in the Tissue Injury and Repair Group who assisted with this research, but particularly: Rebecca Aucott, for her tireless organisation of the laboratory and assistance with immunohistochemistry; Andrew Robson, for his assistance with the thioacetamide model of liver fibrosis; and Luke Boulter, for his assistance with hepatic progenitor cell work.

Special consideration and thanks are due to Rebecca Wells who provided the protocol for polyacrylamide gel fabrication that was fundamental to this research and kindly gifted both tissue and stiffness measurements from her rat CCl_4 model of liver fibrosis. I would like to thank Michael Cheeseman and Neil Dear who developed and bred the Python mouse. I am also indebted to Tertius Hough and Craig Lygate for their work in respect to measurement of liver function tests and haemodynamic parameters in the Python model. I am indebted to Dr Timothy Kendall for his assistance in evaluating the histological changes seen in both the Python and CREB S133A models of cardiac hepatopathy. I would also like to thank my US collaborators Gordon Huggins and Nicholas Birdsey who kindly provided me with liver tissue from the CREB S133A mouse.

I wish to extend my gratitude to the MRC for funding my research.

Finally, I would like to thank Anne, who managed to put up with me throughout the course of my research and my many irrational moments. I especially thank Eve and Harry who provided me with ample welcome distraction.

List of abbreviations

2D, two dimensional

3D, three dimensional

5FU, 5-flurouracil

APS, ammonium persulphate

AFM, atomic force microscopy

AFP, alpha-foeto-protein

ALT, alanine aminotransferase

3-APTMS, (3-aminopropyl)-diethoxy-methylsilane

ATP, adenosine triphosphate

AST, aspartate aminotransferase

αSMA, alpha smooth muscle actin

BAPN, 3-aminopropanenitrile

BCL-2, B-cell lymphoma-2

BD, bile duct

BMOL, bipotential murine oval cell line

BSA, bovine serum albumin

cAMP, cyclic adenosine monophosphate

CBP, CREB-binding protein

CD, cluster of differentiation

CREB, cAMP response element binding protein

CCF, congestive cardiac failure

CCL_3, trichloromethyl radical

CCL_4, carbon tetrachloride

CDE, choline-deficient ethionine supplemented

CDK, cyclin-dependent kinase

CK7, cytokeratin-7

CK19, cytokeratin-19

CLN, centrilobular necrosis

CM, cell monolayer

COL1A1, collagen 1A1

COL3A1, collagen 3A1

CPC, chronic passive congestion

Ct, cycle threshold

CVP, central venous pressure

CYP7A1, cytochrome P450 7A1

DAB, 3,3'-diaminobenzidine

DAPI, 4',6-diamidino-2-phenylindole

DCM, dilated cardiomyopathy

Dlk1, delta-like protein-1

Dlp1, dynamin-like protein-1

DMEM, Dulbecco's modified eagle medium

DMSO, dimethyl sulfoxide

DNA, deoxyribonucleic acid

DNAse, deoxyribonuclease

Dnm1l, dynamin-like gene

dNTP, deoxynucleotide triphosphate

DSC, drug-surviving cells

DTT, dithiothreitol

E, Young's modulus

E-cadherin, epithelial cadherin

ECM, extracellular matrix

EDB, extracellular domain B

EDTA, ethylene diamine tetra-acetic acid

EGTA, ethylene glycol tetra-acetic acid

EGFR, epithelial growth factor receptor

EMT, epithelial to mesenchymal transition

ENU, E-ethyl-N-nitosurea

Ep-CAM, epithelial cell adhesion molecule

ERK, extracellular regulated kinase

FAK, focal adhesion kinase

FHVP, free hepatic venous pressure

FCS, foetal calf serum

FRNK, FAK lacking kinase activity

G', shear modulus

G1, growth phase 1

GAPDH, glyceraldehyde phosphate dehydrogenase

γGT, gamma glutamyl transferase

GTPase, guanine triphosphatase

HBSS, Hank's buffered salt solution

HBV, hepatitis B virus

HCC, hepatocellular carcinoma

HCV, hepatitis C virus

HEPES, 4-(2-hydroxyethyl)-1-piperazineethanesulfonic acid

HGF, hepatocyte growth factor

HNF4α, hepatocyte nuclear factor-4α

HPC, hepatic progenitor cell

HRP, horseradish peroxidase

HSC, hepatic stellate cell

HV, hepatic vein

IL-6, interleukin-6

LOX, lysine oxidase

LSM, liver stiffness measurement

LVEDP, left ventricular end-diastolic pressure

N, Newton

NOD, non-obese diabetic

ns, not significant

MAP kinase, mitogen activated protein kinase

MCL-1, induced myeloid leukaemia cell differentiation protein-1

MCP-1, macrophage chemoattractant protein-1

MEC, murine epithelial cell

MEF, murine embryonic fibroblast

MET, mesenchymal to epithelial transition

MHC, myosin heavy chain

MIP-2 (CXCL2), macrophage inhibitory protein-2

MLC-P, phosphor-myosin light chain

MFB, myofibroblast

MMP, matrix metalloproteinase

MTT, (3-(4,5-dimethylthiazol-2-yl)-2,5-diphenyltetrazolium

NCAM, neural cell adhesion molecule

OCT4, octomer-4

p130Cas, p130 Crk-associated substrate

PA, polyacrylamide

Pa, Pascal

PAGE, polyacrylamide gel electrophoresis

PaO2, partial pressure of oxygen

PARP, poly-ADP ribose polymerase

PBS, phosphate buffered saline

PCR, polymerase chain reaction

PE, phycoerythrin

PF, portal fibroblast

PKB/ Akt, protein kinase B

PV, portal vein

Py, python

Rho, rhodamine

RIA, radioimmunoassay

RNA, ribonucleic acid

RNAse, ribonuclease

RPMI, Roswell Park Memorial Institute medium

ROCK, Rho mediated kinase

PSR, pico-sirius red

RAP, right atrial pressure

RT-PCR, reverse transcriptase polymerase chain reaction

SCID, severe combined immune deficiency

SD, Sprague-Dawley

SDS, sodium dodecyl sulphate

SEM, standard error of mean

siRNA, small inhibitory ribonucleic acid

Src, sarcoma proto-oncogene

SEC, sinusoidal endothelial cell

STAT3, signal transducer and activator of transcription-3

Sulpho-SANPAH, sulfosuccinimidyl 6 (4'-azido-2'-nitrophenylamido) hexanoate

TAA, thioacetamide

TAN, total adenine nucleotides

TBS, tris buffered saline

TBS-T, tris buffered saline with tween

TEMED, tetramethylethylenediamine

TGFβ, transforming growth factor beta

TIMP, tissue inhibitor of metalloproteinase

TISC, tumour initiating stem cell

TNFα, tumour necrosis factor alpha

TPER, tissue protein extraction reagent

Tris, tris (hydroxymethyl) aminomethane

ULN, upper limit of normal

UV, ultraviolet

VEGF, vascular endothelial growth factor

WHVP, wedged hepatic vein pressure

Chapter 1: Introduction

1.1. Chronic liver disease and hepatocellular carcinoma (HCC): a clinical perspective

Liver fibrosis develops as a generic wound-healing response to chronic or repeated liver damage, which may due to a diverse range of aetiological factors (1). These include; alcoholic liver disease, chronic viral hepatitis, autoimmune, metabolic and vascular disorders. Progressive liver damage, accompanied by the deposition of a fibrotic extracellular matrix (ECM) leads to the development of liver cirrhosis. Cirrhosis is defined histologically as the presence of advanced liver fibrosis in associated with regenerative nodules and prominent vascular abnormalities. The formation of mature fibrous vascularised septa linking central veins and portal tracts is a critical feature of liver cirrhosis. These structures are relatively resistant to proteolytic degradation and their formation creates a direct anastomosis between portal vessels and central veins leading to shunting of blood, liver cell dysfunction and portal hypertension. These histological changes result in a number of clinical complications, including; hepatic encephalopathy, abdominal ascites, variceal haemorrhage and hepatorenal syndrome, impacting heavily upon the morbidity and mortality of patients with chronic liver disease. In addition, factors associated with chronic liver disease promote the development of malignancy. Indeed, liver cirrhosis is the most important risk factor for the development of hepatocellular carcinoma (HCC), the fifth most common cancer worldwide. The majority (80%) of HCCs develop in the context of either advanced liver fibrosis or cirrhosis (2). Worldwide, chronic viral hepatitis due to persistent hepatitis B (HBV) and hepatitis C (HCV) infection is responsible for the majority (80%) of cases of HCC. However, cirrhosis of any aetiology may be complicated by HCC.

The overall prevalence of liver fibrosis is increasing. Within the UK, the incidence of liver disease has increased dramatically in the past 20 years (3). Between the periods 1987 to 1991, and 1997 to 2001, rates of cirrhosis in men in Scotland have more than doubled (104% increase), while they have increased by more than two-thirds (69%) in England and Wales. In the same period, mortality rates from cirrhosis in women have also increased (46% increase in Scotland/ 44% increase in England and Wales). These changes have been attributed to similarly dramatic increases in alcohol consumption. Similarly, epidemiological studies have suggested that the incidence of HCC is also increasing (4-7). In the United States, between the periods 1976 to 1980, and 1991 to 1995, the incidence of histologically-proven HCC increased from 1.4 per 100,000 to 2.8 per 100,000 of the

population (6). This is perhaps unsurprising since HCC is the main cause of liver-related death in patients with compensated cirrhosis (8). HCC continues to carry a poor prognosis, with a median survival from diagnosis of only 12 months (9-11). Only 10-20 percent of HCCs are suitable for surgical resection at the time of presentation (11). However, even in this selected cohort, the effectiveness of both hepatic resection and liver transplantation for HCC are limited by tumour recurrence, occurring months or years after surgical resection of a primary tumour (12-14). Furthermore, systemic chemotherapy has proven ineffective, both in the treatment of advanced HCC and in an adjuvant/ neoadjuvant setting for the eradication of disseminated (dormant) tumour cells, the progenitors of clinically relevant metastases. The precise mechanism underlying chemotherapeutic resistance in HCC are incompletely understood.

Overall, it is evident that chronic liver disease and the clinically important sequelae of liver cirrhosis and HCC represent a significant and increasing healthcare burden worldwide. There is therefore a clear imperative to develop a greater understanding of the fundamental mechanisms underpinning liver fibrosis and how these might promote carcinogenesis within the liver.

1.2. Changes in composition and structure of the extracellular matrix (ECM) in chronic liver disease

The histological structure of liver parenchyma is traditionally described in relation to the hepatic lobule (Figure 1.1) (15). When viewed in cross-section, the hepatic lobule is roughly hexagonal in shape, reflecting its polyhedral three-dimensional structure. Terminal branches of the portal vein and hepatic artery are located in portal tracts at the angles of the lobule. Blood from the portal tracts drains across the lobule in sinusoids, which converge upon a terminal hepatic venule, a terminal branch of the hepatic vein. Bile excreted by hepatocytes is transported across the lobule in canaliculi which drain into bile ducts located in the portal tracts. Surrounding the central veins and separated by the vascular sinusoids are plates of hepatocytes which extend out towards the portal tracts. Hepatocytes are separated from sinusoidal endothelial cells (SEC) by the space of Disse. This narrow space, less than 1μm in diameter, lacks the continuous basement membrane found in most epithelial tissues. In its place is a discontinuous layer composed of discrete deposits of collagen-III and collagen-IV, and more homogeneously arranged collagen-VI. Abundant fibronectin deposits surround the hepatocyte microvilli. Gradients exist in respect to the relative abundance of matrix

components across the sinusoids, and are believed to be important in determining the phenotype of both hepatocytes and SECs (16, 17). An array of finely arranged collagen-I fibres extend across the hepatic lobule, and so provide structural support. Inhabiting the space of Disse are hepatic stellate cells (HSCs). These retinoid-storing cells have fine processes that surround the vascular sinusoids and are believed to play a prominent role in regulating blood flow through these vascular channels. The term hepatic acinus is used in reference to the functional unit of the liver, consisting of a diamond shaped mass of liver parenchyma composed of a portal triad (hepatic artery branch/ portal vein branch/ bile duct), hepatic vein branch and intervening hepatocyte plates and bile canaliculi (Figure 1.1B).

Chronic liver disease is characterised by changes in both the biochemical and physical properties of the ECM. Damage to hepatocytes and cholangiocytes, resulting in necrosis and apoptosis, leads to the activation of resident inflammatory cells and the recruitment of further inflammatory cell populations (18). Prominent amongst these are cells of the monocyte/ macrophage lineage, with additional contributions from other immunocompetent cells in specific disease states, including lymphocytes, neutrophils and platelets (19). Inflammatory cytokines and other soluble mediators, both released in response to tissue damage or from recruited inflammatory cells, promote liver fibrosis and cellular regeneration. In acute liver injury there is a temporary and limited deposition of ECM prior to restoration of normal liver architecture. However, in chronic liver disease, sustained inflammation promotes significant expansion and alteration in the composition of the ECM (20-24). This is a product of both enhanced matrix deposition and impaired degradation (25). The discontinuous collagen-IV-rich basement membrane of the subendothelial space is replaced by a continuous interstitial matrix enriched in collagen-I, collagen-III, laminin, undulin, proteoglycans, hyaluronan and elastin (21). Fibrous ECM is deposited at sites of cellular necrosis and apoptosis, the purpose of which is to maintain tissue integrity and promote regeneration. This fundamental relationship between tissue injury and fibrogenesis is responsible for the differing patterns of fibrosis found in specific liver disorders (26, 27).

Under normal conditions, both hepatocytes and cholangiocytes retain the ability to proliferate following liver injury. However, in cirrhosis and other conditions in which the regenerative capacity of hepatocytes is overwhelmed, regeneration is achieved by proliferation and differentiation of hepatic progenitor cells (HPCs). HPCs are tissue resident bi-potential stem cells that have the potential to differentiate into either hepatocytes or cholangiocytes. HPCs are believed to reside in a stereotyped stem cell compartment or niche

(28). The anatomical location of this stem cell compartment is believed to be the canals of Hering, which are remnants of the foetal ductal plates (29, 30). Following severe or sustained liver injury, HPC proliferation is evident as streaming cords or ducts of small oval cells emanating from the portal tracts ("the ductular reaction").

Figure 1.1 Histological organisation of the liver

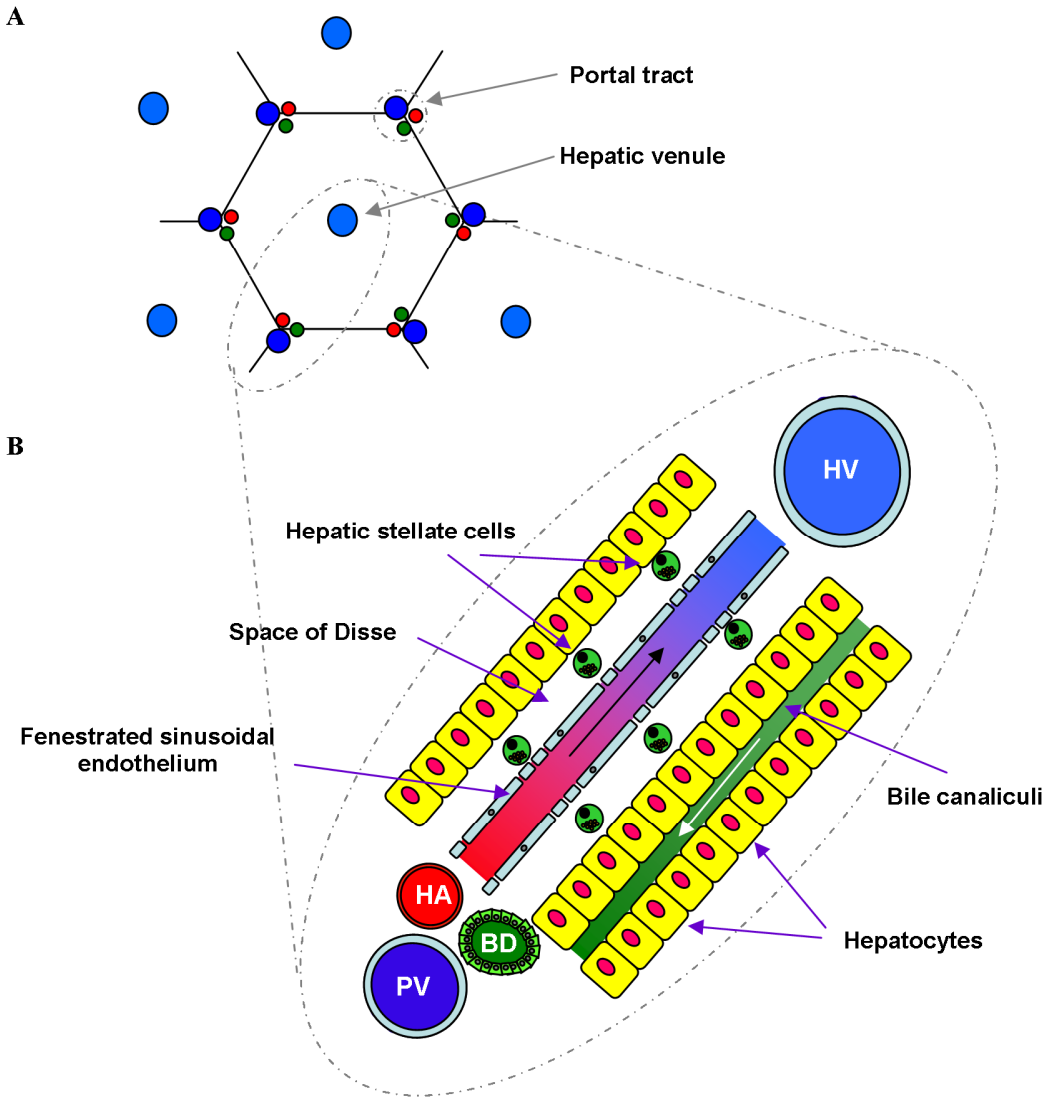

Figure 1.1 Schematic representation of the micro-architectural organisation of the (A) hepatic lobule and (B) hepatic acinus. Hepatic acinus is the term used for the functional unit of the liver, comprising a diamond shaped mass of liver parenchyma including a portal triad (hepatic artery branch/ portal vein branch/ bile duct), hepatic vein branch and intervening hepatocyte plates and bile canaliculi. Abbreviations: hepatic venule (HV); hepatic artery (HA); portal venule (PV) and bile duct (BD). Red colouring indicates oxygenated arterial blood. Blue colouring indicates deoxygenated venous blood. The black arrow indicates the normal direction of blood flow within the vascular sinusoid from the portal tracts into the central hepatic venule. The white arrow indicates the normal direction of bile flow in the hepatic canaliculi, which drain into bile ducts located in the portal tracts.

1.3 The role of the hepatic myofibroblast in liver fibrosis

The hepatic myofibroblast (MFB) is the principle cell responsible for the deposition of ECM in, and regulation of, liver fibrosis. Historically, HSCs were defined as the most prominent source of activated myofibroblasts within the liver. However, it is now apparent that hepatic MFBs are derived from a number of distinct cell populations, each with discreet localisation and immunological characterisation (31). These include activated HSCs, portal fibroblasts (PFs) and interface myofibroblasts. There is also evidence that bone marrow-derived cells, including myofibroblast precursors (32, 33) and fibrocytes (34) contribute functionally to ECM deposition in liver fibrosis. Nevertheless, there is evidence that HSCs account for the majority of ECM deposition in chronic liver disease (1). Following liver injury, HSCs are activated (transdifferentiate), becoming contractile and ECM-producing MFBs. Activation occurs in response to numerous factors, including; hypoxia, reactive oxygen species, ingestion of apoptotic debris, lipopolysaccharide and paracrine factors produced by hepatocytes, cholangiocytes, SECs and recruited inflammatory cells. Perpetuation of the MFB activation is facilitated by numerous cytokines and soluble factors. In addition, there is strong evidence that the biochemical and physical properties of the ECM in liver fibrosis may perpetuate MFB activation. Indeed, specific interactions between cell surface receptors (including integrins and discoidin domain receptors) and collagen-I have been shown to promote MFB activation and proliferation (35-37).

The accumulation of fibrotic scar is dependent upon both increased matrix deposition and a concurrent reduction in matrix degradation (38). MFB activation is accompanied by a marked upregulation of potent tissue inhibitors of metalloproteinases (TIMPs). The resulting inhibition of matrix-degrading metalloproteinases (MMPs) shifts the equilibrium towards matrix accumulation. Similarly, the resolution of liver fibrosis is accompanied by MFB apoptosis, simultaneously removing both an important source of ECM deposition and TIMP production (39). Liver fibrosis is a reversible process (1). In both animal models and human disease, the resolution of liver fibrosis has been demonstrated following treatment/ removal of the underlying cause of tissue injury (38, 40, 41). However, it is also clear that there are both reversible and irreversible components of liver fibrosis. The development of septal fibrosis is thought to define the extent to which fibrosis is reversible (26). Septa may develop between portal tracts and central veins, and may extend over variable distances, in either direction. Histological features have been identified that confer resistance to remodelling. These include portal-central bridging, prominent angiogenesis and the

presence of mature paucicellular scars enriched in crosslinked collagen (42) and elastin (43). Collagen crosslinking confers upon the matrix resistance to enzymatic degradation (42) and is associated with tissue stiffening in a range of fibrotic conditions, including liver fibrosis (44-47). Cirrhosis is defined as a state of advanced liver fibrosis in association with septal fibrosis (incorporating vascular shunts) and nodular parenchymal regeneration. As such cirrhosis has been viewed as an irreversible state of advanced liver fibrosis, although it is now apparent that in the absence of ongoing liver injury, significant remodelling can occur (26, 48).

1.4 The cellular origin of hepatocellular carcinoma (HCC)

In chronic liver injury there is a constant flux of cells transitioning from the stem cell compartment to terminally differentiated cells. It has been proposed that HCCs develop from a range of founder cells across this continuum, from HPCs through transient amplifying cells to fully differentiated hepatocytes (49, 50). The proliferation of cells at the time of carcinogen exposure is essential for the propagation of genomic alterations in cancer development. The clonality of HCC tumours has been clearly demonstrated through detailed genetic analysis of DNA alterations in tumour cells (49). A number of investigators have, through the analysis of HBV DNA viral integration sites in tumour cells, demonstrated that individual HCC tumours are monoclonal (51, 52). However, there was previously some uncertainty as to the identity of the cell involved in cancer initiation. Sell was the first to propose that cancer within the liver may be derived from at least four distinct lineages, including hepatocytes, mature cholangiocytes, HPCs and periductular cells (50, 53). This proposal was based upon detailed histological examination of different experimental models of hepatocarcinogenesis and this model has been confirmed in subsequent immunological and genetic studies. Using monoclonal antibodies generated against an oval cell line, Hixson *et al* demonstrated that HCC induced by choline-deficient ethionine-supplemented (CDE) diet express many of these HPC/ cholangiocyte markers, suggesting a transitional state between HPC and hepatocytes (54). Furthermore, it has also been shown that HPCs isolated from p53-deficient mice produce HCCs when transplanted into athymic nude mice (55). Subsequent to this, genetic profiling has been used to demonstrate that HCCs can been sub-divided within established differentiation stages based upon the genetic profile of cancer cells (56). HCCs with progenitor cell phenotype (e.g. $EpCAM^{+}$) demonstrate characteristics of tumour-initiating stem cells, including bi-potentiality, self-renewal and increased tumour-initiating capacity, in comparison to $EpCAM^{-}$ tumour cells (57). Similarly, CK-19

expression defines a sub-population of progenitor-derived HCC with features of tumour initiating stem cells (58). CK-19 expression in human HCC is associated with a poorer prognosis and increased risk of tumour recurrence.

1.5 Changes in composition and structure of the ECM in HCC

The development of liver fibrosis and cirrhosis is characterised by distinct changes in the histological structure and biochemical composition of the liver (2). The majority of HCCs develop in the setting of cirrhosis (80%) in which the ECM is significantly modified. In cirrhotic patients with HCC, the predominant underlying causes of chronic liver disease include: HCV infection (27-73%), HBV infection (12-55%) and alcoholic liver disease (4-38%) (59-63). In the minority of patients who develop HCC in a non-cirrhotic liver, underlying chronic liver disease is typically present: HCV infection (3-54%), HBV infection (4-29%) and alcoholic liver disease (0-28%). Thus, even in the absence of cirrhosis, HCC seldom occurs in a histologically normal liver. Therefore, irrespective of specific viral mediated mechanisms that may promote carcinogenesis within the liver, factors related to chronic inflammation appear to promote HCC development. These may include changes in the composition and properties of the ECM associated with chronic liver disease. In addition, the development and progression of HCC is associated with further modification of the ECM (64).

HCC development is characterised by disturbance of the lobular architecture of the liver. As discussed earlier, hepatocytes in the normal liver are arranged in single-cell thick plates separated by vascular sinusoids. In HCC the thickness of these plates is increased to a variable extent. This abnormal trabecular pattern is the most common architectural variant of HCC, although solid and tubular HCC growth patterns are also described. An absence of portal tracts within tumour tissue is a consistent feature of HCC that is helpful in aiding histological diagnosis. HCC growth is often associated with the formation of a fibrous capsule (65). Histological studies have shown that the capsule is composed of type-I- and type-III collagen (66). This is thought to be produced by mesenchymal α-smooth-muscle-positive cells located at the interface of the tumour nodule and surrounding liver tissue (65). While malignant cells from well-differentiated tumours retain morphological features of fully differentiated hepatocytes, cells from more poorly differentiated tumours lose these characteristics and there is an increased frequency of nuclear and cytological atypia. The

most poorly differentiated tumours are characterised by a solid growth pattern, with large tumour nodules separated by thick fibrous bands.

The ECM located in and around HCC is different to that found in the normal liver (64, 67, 68). As seen in cirrhosis, there is 'capillarisation' of the vascular sinusoids with development of a continuous thickened basement membrane (69). There is increased deposition of a number of ECM components, including laminin, tenascin, vitronectin and fibronectin. The expression of collagen-IV may be identical or increased in comparison to that seen in the cirrhotic liver, but is reduced in more poorly differentiated HCC (67). In HCC, laminin, which is not present along the sinusoids in normal liver, is present as linear deposits between the sinusoidal epithelium and hepatoma cells, and as more heterogeneous deposits surrounding malignant cells (70). The expression of laminin-5, which is absent from the normal liver, is increased in metastatic HCC and may play a role in promoting cancer cell migration and metastasis (71, 72). Fibronectin expression is increased in all HCCs, in comparison to cirrhosis, but the pattern of expression varies as a function of tumour differentiation (64). Fibrous bands stain positively for fibronectin in all grades of HCC. Sinusoidal staining is seen in well-differentiated trabecular HCCs and pericellular staining is seen in moderately differentiated, but not poorly differentiated HCC. Furthermore, the expression of EDB splice variants of fibronectin, and oncofetal forms of cellular fibronectin are seen exclusively in most HCCs but not in normal or cirrhotic liver. It is thought that the expression of these variants of fibronectin may be involved in modulating cell-matrix interactions in cancer development (73). Tenascin (an ECM glycoprotein) with multiple functions related to development, inflammation and tumorigenesis, is also upregulated in HCC in comparison to the cirrhotic liver (67, 74). Tenascin is expressed both in the fibrous capsule and lobular septum of HCC, but is more variably expressed in the sinusoidal walls of tumours (64, 74). Sinusoidal expression of tenascin appears to be reduced in poorly differentiated HCCs (64).

Interactions between cells and the ECM are largely mediated by integrins, a family of heterodimeric transmembrane molecules, made up of interchangeable α- and β-chains (75). In the normal liver, hepatocytes express a limited repertoire of integrin dimers, including; a collagen and laminin receptor α1β1, a fibronectin receptor α5β1 and a tenascin receptor α9β1. This is believed to represent an adaptation to the distinct ECM encountered by hepatocytes. HCC development is associated with particular changes in the expression of both ECM components and their cognate receptors. The development of HCC is

accompanied by changes in integrin expression, with up-regulation of α1β1, α2β1, α3β1, α6β1, αvβ1, αvβ3 and αvβ5 integrins (64, 76-78). There is now a growing understanding as to the functional relevance of specific alterations in integrin expression by malignant cells. For example, it has been shown that laminin-5 promotes HCC cell proliferation through a α6β4- and α3β1-dependent mechanism (79). Integrins are also implicated in modulation of cell adhesion and migration in HCC. Induction of α6β1 integrin is recognised as an early event in hepatocellular carcinogenesis (77). Inhibition of α6β1 integrin function is associated with reduced migration and cellular migration in HCC cell *in vitro* (77, 80). These effects are believed to mediated by disruption of α6β1 integrin-dependent activation of mitogen activated protein (MAP) kinase and focal adhesion kinase (FAK) (77). Similarly, increased expression of αv-integrins, in response to stimulation with tumour necrosis factor-α (TNFα) and transforming growth factor-β (TGFβ) promotes adhesion and migration in HCC cells (78). Finally, β1-integrin has been found to be effective in protecting hepatoma cells from chemotherapy-induced apoptosis *in vitro*, via a MAP kinase-dependent pathway (81).

1.6 The biomechanical properties of the ECM

The development of liver fibrosis and hepatocellular carcinoma is accompanied by changes in both the biochemical and physical properties of the ECM. In turn, cell behaviour is governed by both biochemical and physical determinants (82, 83). However, while there has been considerable research into how changes in the biochemical composition of the ECM regulate cellular behaviour, the role of physical factors in regulating cell behaviour is incompletely studied.

1.6.1 Basic principles of cellular mechanotransduction

It is evident that the mechanical properties of a cell and its surrounding environment, determine its phenotype (82). The process of mechanotransduction allows cells to respond directly to changes in their physical environment. This requires critical interpretation of complex mechanical loading conditions, including composite tensile, compressive and shear-forces. These loads may be applied externally, or generated internally within a contractile cytoskeleton. The terminology that should be used in describing the biomechanical properties of cells and tissues is summarised below (Table 1.1). Within tissues, most cells are embedded within an ECM, requiring adherance to a solid structure to promote cell

survival (anchorage-dependent growth). Normal adherent cells fail to divide when confined to a spherical shape, either by placing them in suspension or permitting them to attach but not to spread (84). The cytoskeleton is attached to the ECM through trans-cellular adhesions (focal complexes), centred on integrins, cadherins and other adhesion molecules. These multi-molecular complexes represent sites of convergence for both internally- and externally-applied forces. The cytoskeleton exists in a constant state of flux, enabling cells to attach to and pull on their surroundings. Contractile forces are generated within cells by the interaction between myosin-based contractile motors and actin filaments. These forces are transmitted to the ECM through transcellular adhesions and can be demonstrated experimentally in the deformation by adherent cells of soft rubber substrates (85). Importantly, this cellular contractility allows cells to probe the mechanical properties of their immediate surroundings. Stress may only be generated at a transcellular adhesion if an equal and opposite force is provided by the ECM. This, in turn, is dependent upon the substances resistance to deformation, or stiffness. Using atomic force microscopy, it can be shown that within a range of stiffness spanning that of soft tissue, cells tune their internal stiffness to match that of their substrate, a process termed stiffness-sensing (86).

The basic molecular mechanisms underlying the process of stiffness-sensing are poorly characterised. It is hypothesised that forces applied to individual proteins, either at the site of adhesion between cells and the ECM, or within the cytoskeleton itself, cause conformational changes in these proteins that alter their binding affinity for other intracellular molecules (87). The resulting incremental recruitment of focal adhesion components with distinct structural and signalling functions underlies the process of mechanotransduction. For example, mechanical force is required for the recruitment of vinculin to focal adhesions (88). It has been proposed that force-induced activation of vinculin-binding domains on the focal adhesion protein talin, may be responsible for force-induced vinculin recruitment (87, 89).

Forces applied to integrins at focal complexes produce stress-induced strengthening responses, accompanied by focal adhesion growth (maturation). This has been shown using a number of experimental techniques in which well-defined tensile forces have been applied directly to cells. For example, in an elegant series of experiments, it was shown that force is required for the maturation of integrin-based focal complexes that form at the sites of attachment between the cell surface and collagen-coated magnetic beads (90). When a magnetic field was applied to pull upon these attachment points, there was a progressive

increase in focal adhesion size, accompanied by activation of myosin-II and the recruitment of the adapter protein, filamin A. As the focal adhesions mature, and with the recruitment of additional myosin-II motors, the cell is able to resist the applied force and subsequently pull the bead back. Similarly, agents that increase actinomyosin contractility, such as lysophosphatidic acid or thrombin, promote focal adhesion growth in cells plated on rigid substrates (91, 92). Thus cellular responses to externally-applied and internally-derived forces are inextricably linked. Indeed, cellular responses to applied forces are lost when myosin-based contractility is inhibited (93, 94).

A similar process of focal adhesion maturation is observed in cellular responses to increasing substrate stiffness. In a landmark study, Pelham and Wang used a system of collagen-coated polyacrylamide gels of varying stiffness to investigate the effect of substrate stiffness on fibroblast behaviour (95). They showed that fibroblasts cultured on soft substrates displayed increased motility and reduced cellular spreading in comparison to cells cultured on stiff substrates. Focal adhesions of cells on soft substrates were highly dynamic, in contrast to the more stable adhesions seen in cells on stiffer substrates. Increasing substrate stiffness was accompanied by increased vinculin recruitment and tyrosine phosphorylation at adhesion sites. Cellular responses to changes in substrate stiffness were inhibited by myosin-II inhibition. ECM stiffness has subsequently been shown to be an important regulator of cellular homeostasis and affects numerous cellular processes, including cell migration, proliferation and differentiation (96-98). The stiffness of different organs and tissues spans many orders of magnitude (Figure 1.2) (83). The stiffness of most soft tissues, including liver, lung and kidney is in the range 0.2-4 kPa (99). In contrast, the stiffness of tendon and bone is expressed in Megapascals. Within these tissues, under normal conditions, differentiated cells operate within a narrow range of environmental stiffness (10-15%) (100). However, tissue stiffness may change dramatically throughout development and during pathological processes, such as inflammation, fibrosis and tumourigenesis. Understanding how cells respond to pathophysiological changes in tissue stiffness may provide important insight into the complex biomechanical regulation of these processes.

Figure 1.2 Schematic representation of the range of stiffness values (kPa) encountered in selected human tissues and synthetic materials

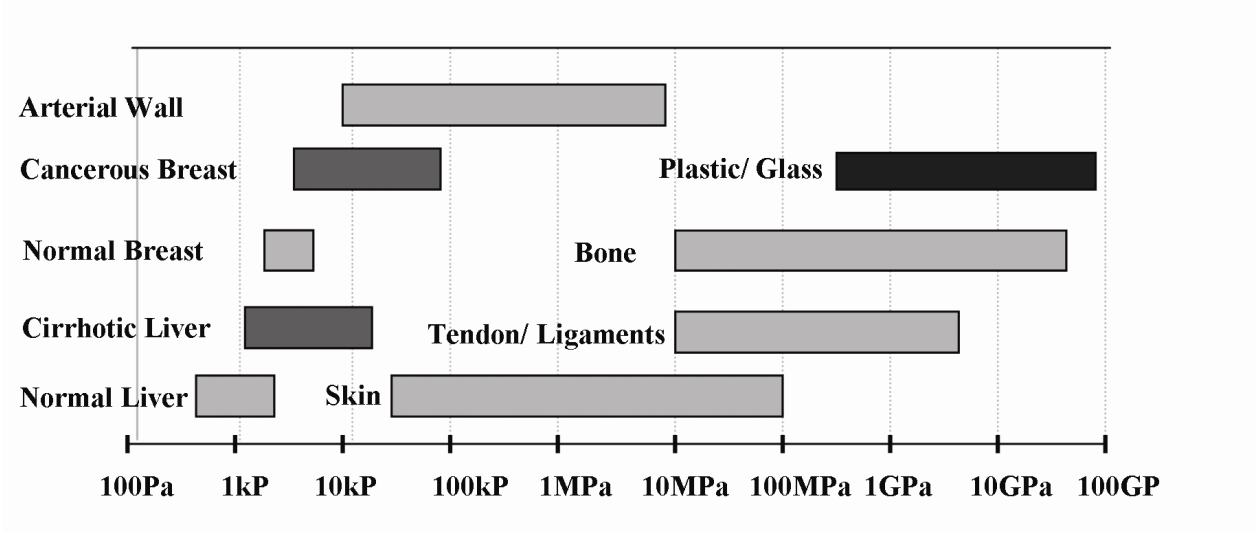

Adapted from: Nemir *et al*. Annals of Biomedical Engineering. 2010 (83)

Table 1.1 Terminology used in describing key biomechanical concepts

Mechanical Terminology	Definition
Mechanical Stress	**Stress** can be defined as the mean force per unit surface area exerted on a deformable body. The S.I. unit of stress is the Pascal (Pa) or N/m^2. Forces exerted perpendicular to a surface result in **extension** or **compressive** stress. Forces exerted parallel to a surface result in **shear** stress.
Mechanical Tension	**Tension** is defined as the magnitude of opposing/ balanced forces that would cause extension. The S.I. unit of tension is the Newton (N). Tension is only generated by the interaction of opposing active and reactive forces (in accordance with Newton's third law of motion).
Strain	**Strain** is a dimensionless number that refers to the geometrical deformation of an object in response to an applied force.
Stiffness	**Stiffness** is a measure of the resistance of a substance to deformation in response to an applied force. The term is often used interchangeably with elasticity.
Compliance	**Compliance** is the reciprocal of stiffness. It is a measure of a substances capacity to deform in response to an applied force.
Elasticity	**Elasticity** describes the property of a material to deform to a defined extent in response to an applied force and then return to its original state upon removal of this force.
Elastic Modulus	**Elastic modulus** is a constant that describes the resistance of a material to deformation, defined as the ratio of stress to strain. As strain is a dimensionless number, if stress is measured in Pascals then the unit of elasticity is also the Pascal (Pa).
Young's Modulus (E)	**Young's modulus (E)** is a constant used to quantify elastic resistance to elongation or compression.
Shear Modulus (G)	**Shear Modulus (G)** is a constant used to quantify elastic resistance to shear force.
Linear Elasticity	**Linear elasticity** describes the situation where there is a linear relationship between stress and strain, i.e. the elastic modulus of a material remains constant during deformation.
Non-linear Elasticity	**Non-linear elasticity** describes the situation where there is a non-linear relationship between stress and strain. Many complex biological materials exhibit non-linear elasticity, whereby elastic modulates changes as a function of increasing strain.

Adapted from: Janmey PA *et al*. Journal of Cell Science. 2011 (82)

1.6.2 Changes in matrix stiffness in chronic liver disease

Alterations in ECM stiffness in chronic liver disease have long been recognised, as demonstrated in the firm liver edge indicative of liver fibrosis and the hard liver nodules found in hepatocellular carcinoma. Histological examination of liver tissue obtained by percutaneous liver biopsy is still considered as the gold-standard in the assessment of liver fibrosis. However, this technique is associated with potentially life-threatening complications. Furthermore, the utility of liver biopsy is limited by problems with intra-/inter-observer variability and sampling error that may lead to either an over- or under-estimation of the degree of liver fibrosis (101, 102). More recently, ultrasound and magnetic resonance (transient) elastography have been developed as non-invasive methods of assessing liver fibrosis. In studies of patients with chronic HCV infection, it has been shown that liver stiffness values obtained by ultrasound elastography correlate strongly with the Metavir fibrosis stage (103, 104). Similarly, ultrasound elastography can be used to accurately assess the degree of liver fibrosis in patients with chronic HBV infection (105), alcoholic liver disease (106), cholestatic liver disease (107) and non-alcoholic steatohepatitis (108). In comparison to standard laboratory tests and non-invasive scores, ultrasound elastography has been shown to have superior diagnostic performance in the early diagnosis of cirrhosis (103). Transient elastography measurements have been shown to correlate closely with portal pressure measurements in patients with chronic HCV infection (109) and may be useful in predicting the presence of oesophageal varices (110). There has been significant debate as to how best to interpret liver stiffness values in clinical practice. Normal liver stiffness has been assessed in a study of 429 healthy subjects with no evidence of liver disease and normal liver enzymes (111). In this cohort, the mean liver stiffness value was 5.5 ± 1.6 kPa. In patients with chronic HCV infection, when liver stiffness values are between 2.5-7.5kPa, liver biopsies will typically show absent or mild liver fibrosis (112). In contrast, liver stiffness estimations exceeding 12.5 kPa are strongly predictive of underlying cirrhosis (Figure 1.3). It must be stressed that factors other than fibrosis may affect liver stiffness measurements. Liver stiffness values may be increased transiently in the absence of significant fibrosis by acute hepatitis (inflammation) (113, 114) or hepatic congestion (right-heart failure) (115).

Figure 1.3 Clinical significance of liver stiffness values in chronic liver disease

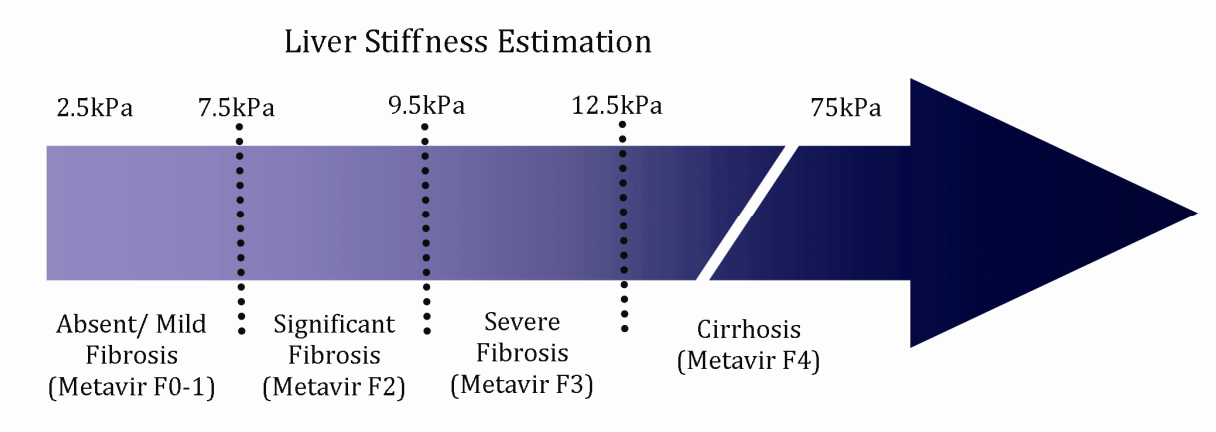

Adapted from: Castera *et al*. Journal of Hepatology. 2008 (116)

1.6.3 Changes in matrix stiffness in HCC

Liver cirrhosis represents the single most important risk factor for the development of HCC. Recent studies involving ultrasound elastography have demonstrated that, even after adjustment for other risk factors, increased liver stiffness measurement (LSM) was a strong predictor of HCC development (117, 118). In one prospective study of patients with chronic HCV infection it was shown that in comparison to patients with a baseline LSM of ≤ 10kPa, the hazards ratio for HCC development increased progressively from 16.7 (95% confidence interval 3.71-75.2 p<0.001), in patients with LSM 10.1-15kPa, to 45.5 (9.75-212.3, p<0.001) in patients with baseline LSM ≥25 kPa (118). Furthermore, using both transient elastography (119) and atomic force microscopy (120), it has also been shown that HCC development is associated with further increases in tissue stiffness to values markedly greater that of the surrounding parenchyma. In a small study of 40 patients, increased tissue stiffness (assessed by transient elastography) was found to be a feature not only of HCC, with median tumour stiffness (E) of 55kPa, but also of other liver tumours, including cholangiocarcinoma (E 75 kPa) and liver metastases (E 66.5 kPa) (119).

Liver stiffness is considered to be a surrogate marker for liver fibrosis. It is unclear whether increasing matrix stiffness, or indeed liver fibrosis, plays a mechanistic role in hepatocarcinogenesis. Liver fibrosis itself may be a surrogate marker for DNA damage/

genomic instability as a consequence of chronic inflammation and regeneration. However, it has been shown in animal studies that the induction of liver fibrosis is associated with accelerated tumour growth following orthotopic HCC implantation (121, 122). Furthermore, histological examination of human HCC specimens has demonstrated an association between the presence of hepatic fibrosis and enhanced tumour cell proliferation (123). This, in turn, may be related to matrix stiffness. It has been one of the aims of this thesis to determine whether alterations in stiffness directly affect the behaviour of HCC cells.

1.7 The effect of substrate stiffness on cellular proliferation

Matrix stiffness is an important regulator of cellular proliferation in non-transformed cells (97, 124). Fibroblasts cultured in tethered (mechanically stressed) matrices proliferate in response to growth factor stimulation, while cells in free-floating (relaxed) matrices are more refractory to mitogenic stimulation (125). Similarly, when cultured in sheets of different shape, endothelial cells show increased levels of proliferation in areas under the highest degree of tensional stress (126). Cell cycle progression is regulated by the expression of cell cycle regulators, including; cyclins, cyclin-dependent kinases (CDKs) and cyclin-dependent kinase inhibitors. Type-D cyclins are critical regulators of cell cycle progression and have been implicated in the stiffness-dependent regulation of cell proliferation (127). Cyclin D1 expression and its subsequent binding to CDK4/6 and CDK2 is a rate-limiting step in the regulation of G1 progression. Cyclin D1 represents a convergence point for multiple signalling pathways, relaying information both from the ECM and numerous soluble mediators. ECM proteins signal by binding to and activating integrins. Numerous studies have demonstrated that integrin-dependent signalling events support G1 phase progression through both induction of cyclin D1and downregulation of the cip/kip family of CDK inhibitors (128). A number of integrin-dependent signalling pathways have been identified that regulate the expression both of cyclin D1 and cip/kip family of CDK inhibitors. These include extracellular-regulated kinase (ERK), mitogen-activated protein (MAP) kinases, Rho-family GTPases and focal adhesion kinase (FAK).

Studies have been performed using collagen gels to investigate the effect of matrix stiffness on integrin signalling and cell cycle progression. It has been shown that human foreskin fibroblasts in compliant free-floating collagen gels do not express cyclin D1, have high levels of the CDK inhibitor $p27^{kip1}$ and do not phosphorylate ERK (129, 130). In contrast, cells in mechanically-loaded tethered collagen gels have higher levels of cyclin D1, down-

regulate expression of $p27^{kip1}$ and have higher basal levels of ERK phosphorylation. Similarly, in experiments using matrix protein-coated PA hydrogels, Klein *et al* demonstrated that matrix stiffness regulates proliferation in mouse embryonic fibroblasts, mammary epithelial cells, vascular smooth muscle cells and osteoblasts (97). Matrix stiffness, across a physiologically-relevant range (G' 2-24 kPa), was found both to regulate the expression of cyclin D1 and the ability of ectopically-expressed cyclin D1 to stimulate retinoblastoma protein (Rb) phosphorylation and S-phase entry. Interestingly, although mitogen-dependent induction of cyclin D1 mRNA was strongly affected across the range of matrix stiffness that affected mitogenesis, other mitogenic events, previously thought to be integrin-dependent, including CDK inhibitor expression ($p21^{cip1}$/ $p27^{kip1}$) and ERK activation, were relatively resistant to changes in matrix stiffness. Overall, it was their conclusion that physiological stiffness acted as an inhibitor of cell cycle progression. In contrast, it has been proposed that increases in matrix stiffness (≥12kPa) may promote aberrant cell cycle progression (46, 97, 124, 131).

1.8 The effect of substrate stiffness on cellular differentiation

The stiffness of the cellular environment is important in both determining and maintaining cellular differentiation. Matrix stiffness has been shown to direct differentiation of mesenchymal stem cells as evident in cellular morphology, marker proteins and transcript profiles (98). Soft matrices (E 0.1-1 kPa), mimicking the stiffness of brain tissue, were found to promote neuronal differentiation. Intermediate matrices (E 8-17 kPa), mimicking striated muscle stiffness promote myoblast differentiation. Stiff matrices (E 25-40 kPa) with stiffness characteristics similar to the cross-linked collagen of osteoid, yielded polygonal cells with morphological and transcript profiles indicative of osteoblast differentiation. It is also thought that the stiffness of a cell's environment might be important in maintaining its stem cell characteristics. Mouse muscle stem cells when freshly isolated from striated muscle and immediately injected into mouse tibialis muscle, differentiate into mature myocytes (132). It has been shown that the ability of these cells to differentiate into mature myocytes *in vivo* is lost if they are pre-cultured on standard tissue culture plastic ($E > 10^9$ Pa). However, if isolated muscle stem cells are cultured on hydrogels with stiffness characteristics similar to striated muscle (E 12kPa) prior to transplantation, then the stemness characteristics of these cells were maintained.

It is also apparent that the range of stiffness across which cells will respond, in respect to alteration in morphology, proliferation or differentiation, differs between individual cell types. Matrix stiffness has been shown to modulate the growth characteristics of both neurones and astrocytes in mixed culture *in vitro* (100). Cells derived from embryonic cortical dissociations were cultured on laminin-coated polyacrylamide gels and fibrin scaffolds of varying stiffness. Laminin-coated soft gels encouraged the attachment and growth of neurones while suppressing astrocytes growth. In contrast, the number of neurones on stiff gels was lower, and neurones plated on stiff gels adhered preferentially to astrocytes rather than forming direct contacts with the stiff substrate. Increasing substrate stiffness promoted astrocyte proliferation. Importantly, astrocytes on soft gels did not spread and had disorganised F-actin staining in comparison to cells grown on stiff matrices. In contrast, neurones developed stress fibres and neurite growth on both soft and stiff gels. This is important as the stiffness range across which F-actin organisation occurs is thought to represent the stiffness-sensing potential of a cell. Mechanisms that regulate a cells stiffness-sensing potential have yet to be determined.

1.8.1. The effect of liver stiffness on myofibroblast function

Liver stiffness measurements (provided by transient elastography) are now widely used in clinical practice as a non-invasive marker of liver fibrosis. However, it has more recently become apparent that changes in the stiffness of the liver may be mechanistically important in regulating the behaviour of a number of liver-resident cell populations. The relevance of changes in matrix stiffness to cellular function and differentiation are best illustrated in respect to hepatic MFBs. The response of hepatic MFBs to alterations in matrix stiffness has been investigated using collagen-I-coated polyacrylamide gels with stiffness characteristics (400Pa-12kPa) similar to those encountered in normal and fibrotic/ cirrhotic livers (133, 134). After 10-days in culture, both HSCs and PFs cultured on soft supports (400 Pa) retained characteristics similar to freshly isolated cells. With increasing support stiffness, these cells developed features of increasing myofibroblast phenotype. These included enhanced cell spreading, α-smooth-muscle actin (αSMA) expression and stress fibre organisation. Functional analysis revealed that these cells had a fibrogenic phenotype with enhanced expression of mRNA for type-1 and type-3 collagens. Thus, rather than simply accompanying the development of liver fibrosis, increased liver stiffness may promote hepatic scar formation. In support of this hypothesis, it has been shown that increases in liver stiffness (based on shear modulus measurements) precede the development of fibrosis

(collagen deposition) in an iterative carbon tetrachloride (CCl_4) model of rat liver fibrosis (135). The factors responsible for this early increase in liver stiffness are uncertain but may include matrix cross-linking or interstitial oedema (136). It is tempting to speculate that this early increase in liver stiffness may be mechanistically important in regulating cellular responses to tissue injury. Finally, it is important to note that although transient elastography can provide an accurate estimation of the stiffness characteristics of the whole liver, it does not provide information in respect to regional variation in stiffness (137). Individual cells sense stiffness over a limited distance. Therefore regional variations in stiffness across the hepatic acinus may be important in determining individual cell behaviour in liver disease.

1.8.2 The effect of substrate stiffness on hepatocyte differentiation

As previously discussed, within the normal liver, hepatocytes reside in a unique biomechanical niche. Hepatocytes are notoriously difficult to maintain in a differentiated state in tissue culture (138). There is a significant body of evidence that suggests that the mechanical properties or stiffness of this environment are important in maintaining hepatocyte differentiation (137). Primary hepatocytes cultured on stiff substrates coated with monomeric collagen proliferate and de-differentiate. However, hepatocytes cultured on soft collagen gels remain rounded and growth arrested (139, 140). A differentiated phenotype is also maintained when hepatocytes are cultured on soft substrates such as dilute collagen or matrigel (138, 140, 141). It is thought that this may be a function of the mechanical properties of these materials. The relationship between substrate stiffness and hepatocyte differentiation has been more directly addressed using a model system in which the stiffness of matrigel was manipulated by cross-linking with glutaraldehyde (142). Hepatocytes maintained on softer substrates demonstrated higher levels of albumin excretion and differential responses to growth factor stimulation, indicative of a more differentiated phenotype. Hepatocytes on stiffer substrates were more proliferative and demonstrated progressive de-differentiation. Substrate stiffness has also been found to regulate cellular responses to fibronectin (143). Hepatocytes grown on soft supports (G' 1.9 kPa) maintained spheroid morphology and were relatively insensitive to changes in fibronectin ligand density, in contrast to the highly spread cells seen on supports of intermediate matrix stiffness (G' 5.6 kPa). Mechanical factors have also been shown to influence hepatocyte morphology and differentiation in three-dimensional culture (144-146). In general, hepatocytes grown in conditions of low mechanical stiffness remain growth arrested and differentiated, whereas as at higher levels of substrate stiffness they are increasingly proliferative and de-differentiated.

The effect of changes in matrix stiffness on HPC proliferation and differentiation is poorly characterised.

1.9 A biomechanical model of cancer development

What effect might changes in the biomechanical properties of the ECM have in relation to cancer development within the liver? The process of cancer development has traditionally been viewed as a multi-step process, reflecting progressive acquisition of genetic mutations that drive the malignant transformation of cells. Through this process - analogous to Darwinian evolution - cells acquire a set of functional capabilities that have been defined as the 'Hallmarks of Cancer' (147). These include; evasion of apoptosis; self-sufficiency in growth signals; insensitivity to anti-growth signals; sustained angiogenesis; tissue invasion and metastasis; and limitless replicative potential. However, it is increasingly apparent that cell behaviour is dictated by networks of molecular interactions with extensive cross-talk both at a regulatory protein and genome-wide level. This is perhaps best exemplified by the manner in which fibroblasts can be induced to revert to pleuripotent embryonic stem cells by simultaneous co-expression of a limited number of transcription factors, which in turn effect the expression of multiple downstream genes (148-150). Thus, environmental factors with wide-ranging effects on cellular behaviour may be important in promoting cancer development (151). This principle is supported by the manner in which cell fate (differentiation, proliferation, apoptosis and motility) can be regulated by changes in ECM structure and cell shape (152-155).

It has previously been demonstrated that certain cancers can be induced to differentiate and normalise their growth in response to manipulation of their cellular microenvironment (156-160). For example, poorly differentiated (anaplastic) rat tumour tissue of renal origin can be induced to form tubules when cultured on filter rafts supported by nutrient agar (157). In addition, it has been shown that co-culture with normal mesenchymal elements is sufficient to enhance differentiation and attenuate tumour cell proliferation in pancreatic carcinoma cells (158, 159). Similar attenuation of the 'cancer phenotype' has been demonstrated when carcinoma cells of breast (161) and prostatic (160) origin are cultured with embryonic mesenchymal tissue. Conversely, the transplantation of malignant human epithelial cells into nude mice results in the formation of tumours composed of both engrafted epithelial cells and host stroma (162). Host mesenchymal cells derived from these tumours appear transformed and are tumourigenic in nude mice. On this basis, it has been proposed that

cancer development is in essence a disease of tissue development (151). Tumour development may occur in part due to alterations in ECM structure and epithelial-mesenchymal interactions. Indeed it has been shown that manipulation of the physical characteristics of the ECM may be sufficient to promote cancer development (46, 163). Further support for this model of cancer development comes from the observation that phenotypically normal mammary epithelial cells, which normally form epithelial glandular structures *in vivo*, can be induced to form invasive mesenchymal-like tumours in response to tetracycline-regulated MMP3/ stromolysin-1 expression (164). Once initiated, tumour growth becomes independent of ongoing MMP3/ stomolysin-1 expression. Furthermore, these cells, transformed as a result of manipulation of ECM structure, demonstrate genomic abnormalities (164, 165). This suggests that there may be mutual potentiation between genetic and structural determinants of cancer development.

Is it the structural or biochemical properties of the ECM that promote cancer development? There is a growing body of evidence to suggest that changes in the mechanical properties of tissues may contribute to tumour development. Landmark observations made by Bischoff *et al*, demonstrated that implantation of rigid pieces of plastic or metal could induce tumour formation in animals, while tumours did not form if the same material was introduced as a powder (166). It has been suggested, on this basis, that changes in the biomechanical properties of the cellular micro-environment may contribute to tumour development. It is now widely accepted that chronic inflammation, a process associated with wide-ranging alterations in the biochemical and physical properties of the cellular microenvironment, may promote cancer development (167, 168). However, the precise mechanisms through which this may occur remain incompletely characterised.

1.9.1 Matrix stiffness and cancer development

Cancer development is typically associated with alterations in the mechanical properties of tissues. Indeed, the diagnosis of cancer is frequently heralded by the palpation of an abnormally hard mass or lump. Alterations in the physical characteristics of cancerous tissues (based on tissue density) are utilised in cancer diagnosis by a range of imaging modalities, including; plain radiography, computed tomography and ultrasound. Furthermore, it has been shown that the presence of a “stiff” fibrotic focus in breast carcinomas is an independent risk factor for early metastasis and poor prognosis (169). The factors responsible for enhanced stiffness characteristics of cancerous tissue are

multifactoral, including; elevated interstitial tumour pressure and solid stress due to tumour expansion and aberrant tumour vasculature (170); increased elastic modulus of transformed cells mediated by changes in cytoskeletal organisation (171); and matrix stiffening linked to fibrosis (172). However, there is an increasing body of evidence that changes in the stiffness of the cellular microenvironment may actively promote malignant transformation (155).

In a detailed series of experiments, Paszek *et al*, investigated the relationship between tissue rigidity and cancer cell behaviour at a molecular level (155). Using tissue micro-indentation they demonstrated that cancer development in mouse mammary pads (analogous to breast cancer) was associated with a marked increase in the stiffness of both the stromal matrix adjacent to transformed cells and the tumour itself. Matrix-coated PA hydrogels were then used to recapitulate the range of stiffness values encountered by cells between normal mammary glands and malignant tumours. Mammary epithelial cells (MECs) grown on supports with stiffness characteristics matched to normal mammary glands (170 Pa), formed well-differentiated/ polarised glandular structures with a central lumen. However, even a small increase in support stiffness disrupted tissue organisation, enhancing cell growth, while inhibiting lumen and adherens junction formation.

It has previously been demonstrated that mammary epithelial cells differentiate into tubules when cultured in free-floating three-dimensional (3D) collagen gels, but not when cultured in an identical matrix that is tethered to the tissue culture dish (173). Tubulogenesis required the contraction of floating collagen gels through Rho and Rho-mediated kinase (ROCK)-mediated contractility. Rho, a small GTPase, has been implicated in the regulation of multiple steps in cancer development, including: proliferation, invasion, anti-apoptosis and metastasis (174). Rho can stimulate cellular contractility through its ability to activate Rho-associated kinase (ROCK), which, in turn inhibits myosin light chain (MLC) phosphatase and activates MLC kinase, favouring net MLC phosphorylation (promoting cellular contractility). Rho activity is frequently elevated in a range of tumours (175). ROCK activation is associated with enhanced tumour invasion, angiogenesis (176) and metastatic potential (172). ROCK-mediated contractility reduced Rho activity in floating 3D collagen gels, a process that was accompanied by loss of focal adhesion kinase (FAK) phosphorylation (Y397) at matrix adhesions. These results indicated the presence of a ROCK-dependent feedback loop, regulating Rho activity. Increased matrix density disrupted tubule formation, promoted FAK phosphorylation and resulted in sustained Rho activity.

FAK – the canonical mediator of integrin-related signalling – is a non-receptor tyrosine kinase that functions as a signalling-protein scaffold for the assembly and subsequent maturation of focal contacts (177). FAK is implicated in multiple aspects of cancer development (178). FAK may be activated by either ECM or growth factor signalling and FAK phosphorylation is an early event associated with the formation of focal contacts. Localisation to integrins is mediated by the focal adhesion targeting (FAT) domain on FAK. Engagement of integrins with the ECM and subsequent integrin-clustering promotes autophosphorylation of FAK at Tyr397. Tyr397 phosphorylation promotes interactions between FAK and various Src-homology-2 proteins. These interactions result in phosphorylation of other sites on FAK and other focal adhesion proteins including paxillin and p130Cas (177). FAK also possesses a proline-rich C-terminal domain that provides binding sites for SH3-domain containing proteins. These interactions, in turn allow FAK activation to be linked to multiple signalling pathways, including: extracellular signal-regulated kinase (ERK), mitogen-activated protein kinase and small GTPases including Rho and Rac. FAK also contributes indirectly to focal adhesion structure and function by phosphorylating and activating a range of focal adhesion proteins, including the F-actin cross-linking protein α-actinin (179). FAK Tyr397 phosphorylation is closely associated with focal adhesion growth and FAK plays an important role in regulating cytoskeletal tension (178). FAK knockout mice have an embryonic lethal phenotype. However, using cell derived from FAK knockout embryos, it has been shown that while wild-type fibroblasts increase their traction forces as substrate stiffness increases, cells derived from FAK knockout mice (FAK -/-) maintain lower traction forces (180). It is believed that FAK may itself function as a mechanosensor. Indeed, computer simulations suggest that the application of tractional force to the FAT domain of FAK may increase its binding affinity for vinculin (181). FAK is widely over-expressed in tumour cells and its expression is correlated with increasing tumour malignancy (177, 182). For this reason, FAK has become an important therapeutic target in cancer and the efficacy of small molecular inhibitors of FAK is currently being investigated in phase I clinical trials (178).

The experiments of Paszek *et al* more explicitly investigated the relationship between matrix stiffness and Rho-mediated cellular contractility in respect to cancer cell biology. They showed that MECs interacting on either a soft or stiff matrix could form integrin-based adhesions, indicated by the co-localisation of FAK and talin with β1-integrin (155). However, MECs could only phosphorylate FAK (Y397) and recruit vinculin to their integrin-based adhesions when interacting on a stiff matrix. Increased matrix stiffness

disrupted tissue architecture and enhanced tumour growth by inducing Rho-generated cytoskeletal tension, promoting focal adhesion assembly and growth factor-dependent ERK activation. Furthermore, it was shown that highly contractile epithelial growth factor receptor (EGFR)-transformed epithelium with high basal Rho and ERK-activity could be induced to revert to a well-differentiated acinus-forming phenotype if either Rho-generated cytoskeletal tension or ERK-activity was reduced. This observation forms the basis for a model of tensional homeostasis and force-dependent malignant transformation (Figure 1.4). It is proposed that a chronic increase in cytoskeletal tension, mediated either by increased matrix stiffness (chronic inflammation), or elevated ERK activation (as a result of oncogene activation), if of sufficient magnitude or duration, could drive the assembly/ maturation of focal adhesions to enhance growth and disrupt cellular differentiation, driving malignant transformation. Many cancer cells overcome tensional control of growth and are able to proliferate in conditions with limited ECM and cell-cell interactions (anchorage-independent growth). This occurs as a result of genomic instability and disruption to the normal regulatory processes that govern cellular proliferation. However, in other situations *in vivo*, tumours appear to modify their microenvironment in order to create a rigid environment ("desmoplastic reaction") in order to stimulate growth (183). Further support for the concept of force-dependent malignant transformation comes from detailed *in vivo* experiments, in which it has been shown that a reduction in tissue stiffness by inhibition of collagen-cross-link formation impedes malignant growth and tumour development in a murine model of breast cancer (46). Increasing matrix stiffness has also been shown to promote the *in vitro* migration and proliferation of transformed glioma cells (184). Furthermore, the manipulation of integrin-mediated attachment to the ECM has been shown to restore normal growth pattern and tissue organisation in transformed mammary epithelial cells *in vitro* and inhibit tumour formation *in vivo* (185). The characteristics of HCC make it an attractive model in which to explore the relationship between matrix stiffness and cancer cell phenotype. HCC is a tumour that develops in the context of an altered biomechanical environment characterised by increased environmental stiffness (118). It has also been established that tumour development is associated with a further increase in stromal stiffness (119, 120). It is the principle aim of this thesis to investigate whether changes in the stiffness of the tumour microenvironment perform a mechanistic role in modulating the malignant phenotype of HCC, in respect to tumour proliferation, differentiation and resistance to chemotherapy.

Figure 1.4 Model of tensional homeostasis and force-dependent malignant transformation

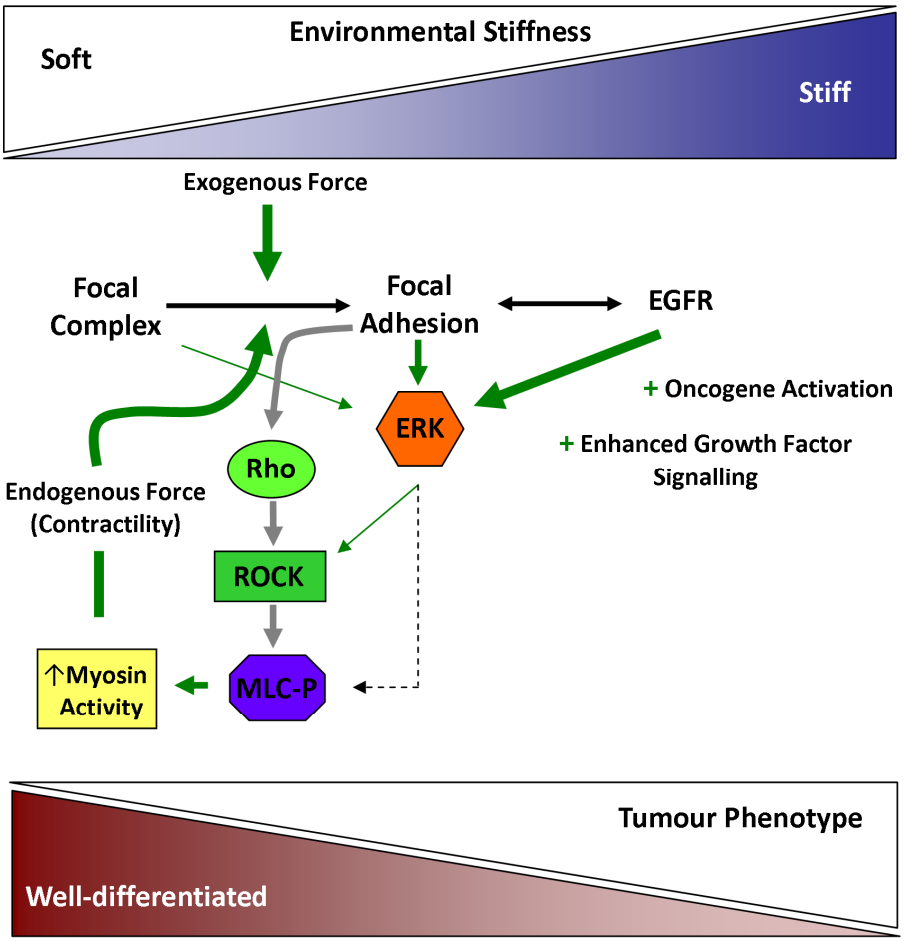

Schematic representation of proposed model for tensional homeostasis and force-dependent malignant transformation Abbreviations: extracellular regulated kinase (ERK); epidermal growth factor receptor (EGFR), Rho-associated protein kinase (ROCK); phospho-myosin light chain (MLC-P).

Adapted from: Paszek *et al*. Cancer Cell. 2005 (155)

1.10 Experimental methods for modelling physiological stiffness for *in vitro* cell culture

The response of cells to alterations in matrix stiffness has been studied in a number of model systems (83, 186). ECM gels composed of collagen and Matrigel provide culture conditions with mechanical properties approximating that found in normal tissues. Substrates including fibrin, collagen, or a mixture of collagen, laminin and other proteins (Matrigel), can be used to produce two- or three-dimensional substrates of controlled stiffness. Cross-linked polysaccharides, including alginate and agar, have also been employed for cell culture. The behaviour of cells on soft substrates has been widely used to identify important changes in cell phenotype, e.g. the growth of cells on soft agar has been widely employed as an assay to identify cancer cells (187). The elastic moduli of these substrates can be regulated by altering polymer mass. Proteins in solution can be induced to polymerise by alteration in electrolyte concentration, temperature or the addition of specific enzymes. The elastic modulus of a polymerized network is approximately proportional to the square of the protein concentration (188). In addition, a range of other techniques have been employed to modulate the stiffness characteristics of polymerised matrices. For example, the stiffness of Matrigel can be manipulated by chemical cross-linking with glutaraldehyde (142). The addition of fibronectin increases the tensile strength of collagen networks (189) and variation in calcium and zinc ion concentration can stiffen fibrin gels at physiological pH (190). Hydrogel-based systems allow independent control of biochemical and mechanical properties, but with the additional advantage that cells are fully encapsulated within the gel matrix, and so the influence of stiffness can be studied in three-dimensional culture. However, the major disadvantage of ECM gels is the difficulty that exists in separating biological effects related to changes in substrate stiffness, from those which might be mediated by changes in ligand density or cross-linker concentration. In addition, protein and polysaccharide gels interact directly with the cell surface and bind serum proteins in a manner that is difficult to control or quantify.

Anchorage can be used to manipulate the tensile properties of ECM gels without altering the biochemical composition of the polymer used. Cells can be embedded in collagen gels that are physically tethered to the container in which they have been fabricated (polymerised). The subsequent release of these gels from the sides of their container is associated with a reduction in the tension across the gel. Cells embedded in physically tethered gels show distinct morphological characteristics when compared to those in free-floating (released)

gels. For example, fibroblasts cultured in constrained gels develop prominent F-actin stress fibres and assemble fibronectin into fibrils, whereas cells on untethered gels do not (191). Similarly, mammary epithelial cells form tubules when cultured on relaxed free-floating collagen gels, while this architectural organisation is lost when cells are maintained in tethered gels (173). The rate of contraction of untethered ECM gels can be used as a measure of cell contractility and gel contraction assays been widely employed to investigate factors that may influence cell contractility (192). The disadvantage of this system is the inability to fine-tune the tensile properties of tethered and released gels.

Ligand-coated polyacrylamide (PA) supports have become established as a widely used and versatile system in which to investigate stiffness-dependence of cytoskeleton-regulated cell behaviour (193). This system allows cells to be cultured in conditions of defined and tailored stiffness, without altering the biochemical properties of the surface to which cells are exposed. The biochemical properties of polyacrylamide are ideally suited to allow separation of chemical and mechanical signalling. Polyacrylamide is almost completely inert as an adhesive surface. It is this property that underlies its utility as a medium for the separation of proteins and nucleic acids by electrophoresis. This also ensures that cell surface receptors and adhesive proteins cannot bind to the gel directly. Indeed, only molecules (ECM components) covalently cross-linked to the PA matrix can act as ligands for cell attachment. This provides added benefits over tissue culture substrates such as plastic, where there is considerable uncertainty in respect to the mechanism of cell attachment. The stiffness of polyacrylamide can be varied over many orders of magnitude (G' 100 Pa – 100kPa) by changing the concentration of dimeric *bis*-acrylamide cross-linker, while the polymer concretration is kept constant. This prevents concomitant changes in surface texture and ligand density. The pore size of these PA gels is in the order of 100nm, which is sufficiently small that cells (~15µm) and cellular processes (~5µm) are too large to enter the gel matrix (194). A potential disadvantage of this system is that covalent attachment of fragile proteins to polyacrylamide may be difficult. However, techniques have been developed to overcome these difficulties, including the use of poly-D lysine to promote ligand attachment to polyacrylamide (194).

For the purpose of this thesis, PA gels of variable stiffness were prepared on glass coverslips using a modification of the method initially described by Pelham and Wang (95). The use of PA supports for cell culture has previously undergone extensive validation at the University of Pennsylvania (194-196). PA matrix stiffness has been determined by two independent

methods. Atomic force microscopy (AFM) was used to measure nano-scale stiffness across the gels (195). Macroscopic or bulk elastic measurements were also made using AFM-probed samples by a simple tension method as described by Pelham *et al* (95, 195). It has been shown that PA gels demonstrate linear elasticity, and macroscopic tests show that this linearity extends over a broad range of strain measures. Both AFM and bulk measurements have been made for gels with a range of *bis*-cross-linker concentrations. It has been shown that the ECM coating does not affect the overall stiffness of the system (194, 195). Gel porosity, which varies as a function of *bis*-cross-linker concentration, could influence cell accessible ligand density by allowing these molecules to migrate into the gel itself. This may produce uncertainty in respect to surface ligand density. However, it has been demonstrated that micron-sized beads, much larger than the pores and bearing anti-collagen antibodies, bind almost identically to collagen-coated gels of very different porosity (96). Furthermore, it has been shown that *bis*-acrylamide cross-linker concentration does not affect the relative surface ligand density. Pelham *et al* used a modified radio-immunoassay (RIA) employing a monoclonal antibody against collagen-I and ^{125}I-labelled anti-mouse IgG to determine the relative amount of collagen bound to PA sheets (95). This demonstrated that the relative concentration of collagen differed by less than 3% between PA substrates of different stiffness. Finally, in order to exclude the possibility that observed changes in the behaviour of cells on different PA supports were due to differential loss of covalently bound ligands from the substrate, cells were cultured on either 0.25% or 0.03% bis-acrylamide gels, then lysed with 0.5% Triton-X-100 (95). RIA with anti-collagen-I antibodies indicated that the collagen-concentration did not decrease on either soft or stiff PA supports as a result of cell growth, when compared to control supports not used in cell culture. Thus, ligand-coated PA supports represent a robust and well-characterised system in which to investigate the stiffness-dependence of cytoskeleton-regulated biological processes.

1.11 The role of *in vivo* models to investigate the impact of physical factors on cell behaviour

Advances in our understanding of how mechanical factors regulate cell behaviour have come about predominantly as a result of experiments undertaken in an *in vitro* setting. This approach has enabled investigators to attempt to separate the effects of biochemical and physical signalling, while minimising the impact of potential confounding factors that may independently affect cell behaviour. However, these *in vitro* systems will never be able to recapitulate the complexity inherent to the *in vivo* environment. Important insight has been

gained into how mechanical factors might influence pathophysiological processes including chronic liver disease (135) and tumour development (155), with the use of detailed *in vivo* measurements of mechanical properties such as tissue stiffness. Interventions that attempt to modulate the physical properties of tissues *in vivo* will almost inevitably have secondary effects that may impact upon the observed outcome. For example, the increase in parenchymal stiffness associated with the induction of liver fibrosis in rodents is accompanied by dramatic changes in both the cellular composition of the liver and the prevailing cytokine milieu. Even more modest interventions to modulate the physical properties of the cellular microenvironment will have potentially confounding effects. For example, lysyl oxidase (LOX) is a copper dependent amine oxidase which initiates intra- and inter-molecular cross-linking of collagen. It has been shown that active LOX stiffens tissues and can compromise their function. Furthermore, reducing LOX activity with β-aminopropionitrile (BAPN) attenuates tissue stiffness and prevents liver fibrosis (135). In addition, it has been shown that BAPN treatment (LOX inhibition) is associated with a reduction in tissue stiffness, and attenuated tumour growth in a murine model of breast cancer (46). However the activities of LOX and other members of the LOX family are manifold and complex (197). LOX has been shown to regulate events including chromatin compaction, gene transcription and cell differentiation. Hydrogen peroxide released as a consequence of LOX-mediated catalysis triggers phosphorylation and activation of two key signal transcription pathway activators (FAK and Src) and as such may have pervasive effects on cell biology.

Clearly there are considerably limitations to the utility of *in vivo* models in advancing our understanding of how mechanical factors such as stiffness may modulate cell behaviour in pathological processes such as chronic inflammation or tumourigenesis. In complex pathological processes, such as liver fibrosis, it will prove extremely difficult to disentangle the complex web of solid-state and soluble regulators of cell behaviour. However, important insight may be gained by the characterisation of convergent models of liver fibrosis in which physical factors may play an important regulatory role. Tissue oedema, as occurs in both acute inflammation and passive congestion (right-heart failure), will result in a number of distinct biochemical and physical changes to the environment in which cells reside. Therefore, models of chronic hepatic congestion may provide us with the opportunity to define a common sequence of events through which cells respond to oedema.

1.12 Hypothesis and aims

1.12.1 Hypothesis

Changes in the stiffness of the cellular microenvironment are important in regulating the behaviour of liver-resident cell populations in chronic liver disease and hepatocarcinogenesis.

1.12.2 Principle Aims

- To determine whether changes in the stiffness of the cancer cell niche regulate proliferation, differentiation and chemotherapeutic resistance in HCC cells

- To determine the relationship between changes in liver stiffness and HPC response in rodent models of chronic liver disease

- To determine whether changes in the stiffness of the HPC niche regulate the proliferation and differentiation of HPCs.

1.12.3 Secondary Aim

- To characterise the pattern of histological changes observed in rodent models of chronic hepatic congestion and assess whether these might provide insight into the effects of oedema and congestion on the development of liver fibrosis

Chapter 2: General Materials and Methods

Appropriate home office licence and local ethical committee approval was obtained prior to animal experiments being undertaken.

2.1 Experimental models of liver fibrosis and congestive cardiac hepatopathy

Animals were maintained in high health status facilities, with access to food and water *ad libitum.* Experiments were conducted in accordance with UK Home Office licence regulations.

2.1.1 Thioacetamide (TAA) model of rat liver fibrosis

A thioacetamide (TAA) model of liver fibrosis in rats was used as previously described (198, 199). The intrahepatic metabolism of TAA results in the formation of reactive intermediates that both bind to hepatic macromolecules (including proteins and nucleic acids) and facilitate glutathione depletion (200). Oral administration of thioacetamide reliably induces hepatocyte damage and liver fibrosis/ cirrhosis in rats (199). Rat liver tissue from experiments with TAA was kindly donated by Dr Andrew Robson (University of Edinburgh). Cohorts of adult male Sprague-Dawley (SD) rats (weight 300-350g) were used in these experiments. Animals in the experimental group obtained TAA (Sigma, Poole, UK) in drinking water at a concentration of 300mg/l (0.03%) *ad libitum*. Animals in the control group were housed in identical conditions and supplied with standard drinking water *ad libitum*. Animals were then sacrificed and liver tissue analysed at 4, 8, 10, 14, 18, 20 and 26 weeks.

2.1.2 Carbon tetrachloride (CCl_4) model of rat liver fibrosis

Carbon tetrachloride (CCl_4) administration to mice and rats is a widely-accepted and well-characterised model of liver fibrosis (201, 202). CCl_4 is oxidised in the liver by cytochrome P450 to the highly reactive trichloromethyl (CCl_3) radical. This free radical can initiate lipid peroxidation and react with sulphydrol- groups in proteins. This, in turn, leads to the development of steatosis and centrilobular (zone 3) hepatocyte necrosis, accompanied by HSC-activation and subsequent liver fibrosis. The pattern of histological changes seen with CCl_4-induced liver injury mirrors in many respects that seen with toxic liver injury (e.g.

alcoholic liver disease) in humans. Repeated administration of CCl_4, either by intraperitonial injection or oral gavage, can be used to predictably induce bridging fibrosis (4 weeks of bi-weekly administration) or cirrhosis (8-12 weeks of bi-weekly administration).

Rat liver tissue from experiments involving CCl_4-induce liver injury was kindly donated by Prof Rebecca Wells (University of Pennsylvania). All animal studies were approved by the University of Pennsylvania Institutional Animal Care and Use Committee. Male SD rats (Charles River Laboratories, Wilmington, USA) received twice weekly intraperitonial injection with 0.2ml/100g of a 1:1 mixture of CCL_4 (Sigma-Aldrich, St Louis, USA) in olive oil, or olive oil alone. After 2 weeks the dose of this mixture was reduced to 0.1mg/ 100g. Animals were sacrificed after CO_2 inhalation at 7, 14, 28, 42, 56 and 70 days. Six uninjected animals were used as controls. At each time point, there were two vehicle-injected control rats and five or six CCl_4-injected rats. Following sacrifice the livers were removed and systematically divided for rheometry, formalin-fixation and snap freezing in liquid nitrogen.

Additional experiments were undertaken by Prof Rebecca Wells (University of Pennsylvania) to investigate the effect of β-aminopropionitrile (BAPN) on HPC responses following CCL_4-induced liver fibrosis. BAPN is an inhibitor of lysyl oxidase (LOX): a copper dependent amine oxidase that initiates intra- and inter-molecular cross-linking of collagen. In these experiments liver fibrosis was induced by twice-weekly injection of 0.2mg/100mg of a 1:1 mixture of CCL_4 in olive oil for between 6-14 days. In a second cohort, rats also received treatment with BAPN (2mg/ml) in drinking water *ad libitum* for the duration of CCL_4-induced injury. Both vehicle treated (olive oil alone), non-injected and non-injected/ BAPN treated animals were used as controls. At each time point animals (n=5-6) were sacrificed and harvested as described above. Formalin fixed tissue from these experiments was kindly donated for the purpose of investigating the effect of liver stiffness/ BAPN on HPC responses in the liver.

2.1.3 Python model of congestive cardiac hepatopathy

Python mice (Py/+) were a gift from Prof Neil Dear (University of Leeds) and were generated as part of the MRC rodent mutagenesis program based at the MRC Mary Lyon Centre, Harwell. The Py/+ mice were produced using N-ethyl-N-nitrosurea (ENU) mutagenesis, as previously described (203). All experiments undertaken in python mice and littermate controls, was approved by the Animal Ethical Review Committees of MRC

Harwell, University of Sheffield and University of Leeds, and the UK Home Office. These experiments were undertaken under the guidance of Prof Neil Dear (University of Leeds). Experiments were conducted using male python (Py/+) mice and littermate wild-type (+/+) controls on a C3H/ HeN. Male python (Py/+) spontaneously develop a dilated cardiomyopathy. Overt features of congestive cardiac failure (CCF) include; shallow-breathing, piloerection, weight gain, ascites and peripheral oedema. The median onset of features on overt CCF in male mice on a C3H/ HeN genetic background develop is 83 days. Experiments were undertaken to characterise the pattern of pathological changes in the liver in this spontaneous model of dilated cardiomyopathy. Groups of python (Py/+) mice and aged-matched wild-type (+/+) controls were culled at 5, 7, 9 and 11 weeks, and at the onset of overt features CCF.

2.1.4 CREB S133A of congestive cardiac hepatopathy

Liver specimens from CREB S133A mice were kindly donated by Dr Gordon Huggins (Tufts University School of Medicine, Boston) and Dr Nicolas Birdsey (University of Colorado, Denver). All experiments undertaken CREB S133A mice and littermate controls was approved by local Animal Care Committees of Tufts University and the University of Colorado. The CREB S133A is a transgenic murine model of dilated cardiomyopathy, the generation of which has previously been described (204). CREB S133A transgenic mice have been developed (ICR/CD1 background) that express this dominant-negative repressor of CREB-mediated signalling under the transcriptional control of the cardiac myocyte-specific alpha-myosin heavy chain (MHC) promoter (204). Expression of the CREB S133A transgene is restricted to the heart, as demonstrated by Northern blot analysis (204). It has been demonstrated that CREB S133A transgenic mice develop a form of dilated cardiomyopathy (DCM) that closely resembles idiopathic dilated cardiomyopathy in humans. Histological analysis of hearts from CREB S133A mice demonstrates progressive four chamber dilatation. Experiments were conducted in male CREB S133A mice in order to characterise the morphological changes occurring within the liver during the development of progressive cardiac failure. Cohorts (n=3-5) of male CREB S133A mice (ICR/CD1 background) and age-matched wild-type controls were culled at 4, 8 and 12 weeks, during which period male CREB S133A mice developed clinical features of progressive cardiac failure.

2.2 Tissue collection and processing

Following each experimental protocol, all mice were culled by a Schedule 1 method (UK Home Office Guidelines). Tissue was harvested in accordance with a defined experimental protocol. Tissue specimens (including the left lobe of the liver, spleen, heart and kidneys) were fixed in formalin solution (12 hours) and embedded in paraffin. The right lobe of each liver was snap frozen in liquid nitrogen and stored at -80^{o}C prior to protein and RNA analysis. Blood samples were obtained by direct cardiac puncture post-mortem. Serum samples were prepared by centrifugation (10 minutes/ 5000g) in 1.5ml tubes containing lithium heparin solution (Sigma, Poole, UK).

2.3 Histological analysis

Basic histological analysis was performed on 5µm formalin fixed sections stained with haematoxylin and eosin solutions.

2.3.1 Picosirius red (PSR) staining

PSR staining was performed on 5µm liver sections. Sections were de-paraffinised in xylene and rehydrated in ethanol (50-100%) and distilled water. Sections were then incubated for 2 hours in saturated picric acid solution containing 0.1% Sirius red and 0.1% Fast green. Sections were then rinsed in distilled water to remove excess dye and dehydrated in ethanol (50-100%) and xylene. Slides were mounted on glass cover slips with aqueous Permount^{TM} mounting media (Fischer Scientific, Loughborough, UK). Sirius red staining of liver specimens was quantified by digital image analysis (Photoshop, Adobe, San Francisco, USA) of 20-30 randomly selected and blinded high magnification (x200) photomicrographs. Detection thresholds were set for the red colour of PSR stained collagen from an area of intense staining and an arbitrary colour threshold range was applied.

2.3.2 Reticulin staining

Reticulin staining was performed on 5µM liver sections using a modification of the protocol described by Gordon and Sweet (205). Sections were deparaffinised in xylene and rehydrated in ethanol (50-100%) and distilled water. Sections were immersed in acidified potassium permanganate (0.5%) solution for 3 minutes and then rinsed in distilled water.

Sections were then treated with 2% oxalic acid for 1 minute, rinsed in distilled water and immersed in 4% alum solution for 10 minutes. After a further rinse in distilled water, the sections were impregnated with ammoniacal silver solution (10 seconds), rinsed in distilled water and immersed in formalin solution (10%) for 2 minutes. Sections were then fixed in 2% sodium thiosulphate solution, rinsed in distilled water and counterstained with neutral red. Slides were dehydrated in ethanol (50-100%) and xylene and mounted on glass cover slips with aqueous Permount™ mounting media (Fischer Scientific, Loughborough, UK).

2.4 Immunohistochemistry

Immunohistochemistry was performed on formalin-fixed paraffin-embedded 3μM sections mounted on glass slides (Thermo-Fischer, Loughbourgh, UK). Primary and secondary antibodies were used at different concentrations (Appendix 1). For some targets, an antigen retrieval step was required to unmasked epitopes hidden by cross-linking formed during the fixation process.

2.4.1 General immunohistochemistry protocol with paraffin sections

Immunohistochemistry was carried out at room temperature unless otherwise stated. Formalin-fixed and paraffin embedded sections were de-paraffinised twice in xylene (for 5 min each time) and rehydrated in ethanol (50-100%) and distilled water. Antigen retrieval (if required) was performed at this stage (Appendix 1) and the sections were then washed 3 x 5 min in phosphate buffered saline solution (PBS). Endogenous peroxidise activity was blocked by incubation with hydrogen peroxide (2%) solution in PBS for 10 minutes. Slides were then washed 3 x 5 minutes in PBS. Slides were then mounted into Shandon Sequenza slide racks (Thermo-Fischer, Loughbourgh, UK). An endogenous avidin-biotin block (Vector Laboratories, Peterborough, UK) was performed by applying 3 drops of avidin solution to each slide for 15 min. Slides were then washed 3 x 5 min in PBS, then 3 drops of biotin reagent were applied for a further 15 min. Sections were then washed 3 x 5 min in PBS. Non-specific protein-binding was inhibited by incubation with blocking buffer containing species-specific serum diluted (1:5) in PBS for 30 min. Species-specific serum was chosen to match the species in which the relevant secondary antibody was raised. Without washing, samples were then incubated with a primary antibody solution (appropriately diluted in blocking buffer) for 1 hour at room temperature (Appendix 1). Slides were then washed 3 x 5 min in PBS. A secondary antibody solution appropriate to

each primary antibody was made by appropriate dilution (Appendix 1) of secondary antibody in blocking solution. Samples were incubated with secondary antibody solution for 1 hour and then washed 3 x 5 min in PBS. Slides were then treated with 3 drops of streptavidin ABC-horseradish peroxidise (HRP) reagent (DAKO, Ely, UK) for 30 min and then washed 3 x 5 min in PBS. A chromogen solution containing 3, 3'-diaminobezidine (DAB) (Invitrogen, Paisley, UK) was applied to each slide for between 1-5 min, until a colour change was observed. The slides were washed in PBS solution 3 x 5 min. Slides were then counterstained in Harry's haematoxylin solution (10 seconds), rinsed in running tap water and immersed in Scott's tap water (10 seconds). Sections were then rinsed in running tap water and dehydrated in graded ethanol solutions (50-100%) and xylene for 5 minutes each. Slides were then mounted on glass cover slips with aqueous Permount™ mounting media.

Negative controls were performed in all immunohistochemistry experiments. First, the primary antibody was replaced by a relevant isotype control antibody chosen to match the concentration, species and immunoglobulin class of the primary antibody. In a second control, the primary antibody was simply omitted.

2.4.2 Pimonidazole-adduct immunohistochemistry

Experiments to quantify tissue hypoxia were conducted using pimonidazole hydrochloride, a 2-nitroimidazole hypoxic marker that forms adducts with thiol groups in proteins, peptides and amino acids under hypoxic conditions ($PaO_2 < 1.3kPa$). Animals were injected with pimonidazole (60mg/kg) (Hypoxyprobe Inc, Burlington, USA) by intraperitonial injection 30 minutes prior to sacrifice. Liver specimens were harvested and fixed in formalin solution (12 hours) and embedded in paraffin. Immunohistochemistry for pimonidazole adducts was performed on 3μM sections in accordance with our standard immunohistochemistry protocol (as previously described). Tissue was subjected to microwave antigen retrieval (15 minutes) in a Tris-ETDA solution (pH9.0). Non-specific binding was minimised by incubating tissue sections in proprietary blocking solution (DAKO, Ely, UK). Hypoxyprobe-1™ OMNI anti-pimonidazole adduct primary antibody (Hypoxyprobe Inc, Burlington, USA) was used at a 1:200 dilution. Swine anti-rabbit secondary antibody was used at a dilution of 1:200. Positive staining was detected with Vector ABC reagent (Vector, Peterborough, UK) and 3, 3-diaminobenzidine (DAB) substrate (DAKO, Ely, UK).

2.4.3 Immunohistochemistry on human HCC specimens

Human HCC tissue from surgical resection specimens was obtained from archived tissue held by Tayside Tissue Bank and the Department of Pathology, University Medical Centre Hamburg-Eppendorf with appropriate ethical approval (UK-LREC: TR000216). Immunohistochemistry was performed as described above in collaboration with Rebecca Aucott. The primary antibodies and antigen retrieval regimes used were anti-pFAK (pY397) (Invitrogen, Paisley, UK/ Microwave pH9) and anti-β1-integrin (Abcam, Cambridge, UK/ Microwave pH9). Negative controls with isotype immunoglobulins (Santa Cruz, Heidelberg, Germany) and species-specific serum alone showed no specific staining.

2.5 Microscopy and histological analysis

Microscopic examination of tissue specimens was performed using an inverted Zeiss Axiovert-200 microscope and Axiovision image acquisition software (Zeiss, Heidenheim, Germany).

2.5.1 Digital image analysis of immunostained sections

Quantification of αSMA immunostaining in liver specimens was quantified by digital image analysis (Photoshop, Adobe, San Francisco, USA), of 20-30 randomly-selected and blinded high magnification (x200) photomicrographs per section. Values are expressed as the mean percentage area of positive staining per high power field (x200 magnification) from 3-8 independent samples. Detection thresholds were set for the brown colour of DAB from an area of intense staining and an arbitrary colour threshold range was applied.

2.5.2 Hepatic progenitor cell (HPC) quantification in immunostained sections

HPC numbers in rat/ mouse livers were quantified by direct cell counting from sections immunostained for the HPC marker cytokeratin-19 (CK-19). CK19 staining and cell counting was undertaken by Dr Andrew Robson. Cell counts were made using Image J (Nation Institute of Health, USA) from 40-60 randomly selected and blinded high power (x320 magnification) photomicrographs. Cell counts are expressed as the mean number of non-bile-duct-associated CK-19-positive cells per 60 high power portal vein fields from 2-6 independent samples.

2.5.3 Macrophage quantification in immunostained sections

Macrophage numbers in mouse livers were quantified by direct cell counting from sections immunostained for the macrophage marker F4/80. Cell counts were made using Image J from 10 randomly selected and blinded high power (x200 magnification) photomicrographs of portal vein fields. Cell counts are expressed as the mean number of F4/80-positive cells per high power portal vein field from 6-8 independent samples.

2.6 Shear rheometry measurements with rat liver tissue

Rheometry measurements were made by Prof Rebecca Wells (University of Pennsylvania) as previously described (135). Briefly, cylindrical samples were prepared from the posterior lobe of freshly removed liver using a scalpel and 25mm-diameter stainless-steel punch (McMaster-Carr, New Brunswick, USA). Samples with a thickness of 3mm (measured with a micrometer built into the rheometer) were placed between two 25mm serrated steel plates. Shear storage modulus (G') values were measured within 30 minutes of the tissue cores being cut. Control experiments had previously shown that G' measurements were unchanged for several hours of liver storage in HBSS and did not change with the plane of dissection used for disc construction. In addition, there was minimal variation in G' measurements taken from different lobes from a single animal. Perfusions of livers with heparin did not alter G' values in control experiments and therefore experiments were conducted without prior perfusion.

Shear storage modulus (G') measurements were made using a Rheometrics RFS-3 controlled strain rheometer (Rheometric Scientific, Piscataway, USA) and are reported in Pascals (Pa). G' measured by oscillatory deformation is dependent upon the frequency of oscillation and magnitude of deformation (strain). The liver samples were found to be only weakly dependent on the frequency of deformation, but G' decreased with increasing deformation. G' was measured at a frequency of 1 rad/second over a range of strain values. The G' Vs strain plot was linear to 2% strain. Reported values were recorded for 2% strain. In order to minimise drying and ageing of the samples, a moisture trap enclosed the test area and recording time was limited to 3 minutes.

2.7 Multiplex cytokine assay

2.7.1 Sample preparation for multiplex cytokine assay

Protein samples for multiplex cytokine assays were prepared from snap frozen whole liver samples. Small pieces (~0.1cm^3) of frozen tissue were added to 300µl of proprietary Tissue Protein Extraction Reagent (TPER) (Pierce, Rockford, USA). The tissue was disrupted by repeated passage through a 2ml syringe and 19 gauge needle, sonicated and centrifuged (12,000rpm at 4^{o}C) for 10 minutes. The supernatants were transferred to sterile 1.5ml tubes and assayed to establish protein concentration. Prior to use, protein samples were then diluted to a final concentration of 500µg/ml.

2.7.2 Bradford protein determination assay

The protein concentration of tissue lysates or cell extracts was determined using a modification of the Bradford Protein Assay (206). Briefly, 5µl of protein extract was added to 150µl of Bradford Reagent (Sigma, Poole, UK) diluted (1:1) in distilled water in a 96-well plates. Parallel standards were made using bovine serum albumin (Sigma, Poole, UK) (0-1000µg/ml) Absorbance was measured at 595nm using a Biotek Synergy HT microplate reader (Biotek, Potton, UK). A standard curve was plotted and the protein concentration determined from the standard curve equation using Excel software (Microsoft, Redmond, USA).

2.7.3 General multiplex cytokine assay protocol

Multiplex cytokine assays were performed on a Bio-Plex 200 Suspension Array system and Bio-Plex Pro Wash Station (Bio-Rad, Hemel Hempstead, UK). Multiplex cytokine assays for MCP-1, MIP-2, IL-6 and VEGF were performed using a Bio-Plex Pro Magnetic Cytokine Assay kit and proprietary standards. Cytokine assays were performed in accordance with the manufacturer's instructions using a modification of the method described by Molls *et al* (207). The cytokine assay plate layout consisted of eight standards in duplicate (32000-1.95pg/ml), two blank wells (for fluorescence background subtraction) and sample wells. The multiplex cytokine assay uses a flow-based microbead protein detection system based on Luminex X-MAP technology. The surface of each fluorescently-coded bead is coated with specific antibodies directed against a specific cytokine or growth factor. Each supernatant sample (50µl) is incubated (30 min, room temperature) with a

mixture of microbeads, each conjugated to a specific capture antibody. Samples are washed three times (100µl) in proprietary Wash buffer (Bio-Rad, Hemel Hempstead, UK). The samples are then incubated (30 min, room temperature) with a mixture of secondary biotinylated antibodies, each directed against a specific secondary epitope on each target molecule. The samples are then washed three times in wash solution and incubated with a streptavidin-conjugated phycoerythrin (PE) reporter for 10 min at room temperature. The samples are then washed three times in wash solution and following the final wash step the samples are resuspended in proprietary Assay buffer (Bio-Rad, Hemel Hempstead, UK). The samples are then subjected to flow cytometric analysis on a Bio-Plex 200 Suspension Array system. This system uses fluidics, laser excitation, fluorescence detection and digital signal processing for identification and scanning of individual microbeads. Each individual microbead is identified on the basis of its internal fluorescence (defining the target molecule) and the PE reporter signal associated with each bead is quantified, which is in turn dependent upon the concentration of target molecule present in each sample. The data is analysed using Bio-Plex Manager 3.0 software (Bio-Rad, Hemel Hempstead, UK) and the concentration of each target molecule calculated against the standard curve. The final concentration of each cytokine/ growth factor is expressed in pg/mg liver tissue.

2.8 RNA methods

2.8.1 Prevention of contamination

All consumables and equipment used in RNA work was DNAse/ RNAse-free. All buffer solutions were either certified as DNAse/ RNAse-free or made using DNAse/ RNAse-free water. All surfaces and equipment was treated with RNAseZap™, RNAse decontamination solution (Applied Biosystems, Warrington, UK), prior to use.

2.8.2 RNA extraction for real-time quantitative PCR

RNA extraction was performed using an RNeasy Mini-kit protocol (Qiagen, Crawley, UK).

For RNA extraction from cultured cells, culture media was aspirated from cultured cells and the cells were washed twice in ice-cold PBS. An appropriate aliquot of RLT lysis buffer containing β-mercaptoethanol (10µl/ml) was added to each culture dish and the cells harvested with a cell scraper into a sterile 1.5ml Eppendorf microfuge tube. Samples were

vortexed for 30 seconds and homogenised using QIShredder microfuge columns (Qiagen, Crawley, UK).

For RNA extraction from animal tissue, small (~0.1cm^3) pieces of frozen tissue were added to an appropriate aliquot of RLT lysis buffer containing β-mercaptoethanol (10µl/ml). The tissue was disrupted by repeated passage through a 2ml syringe and 19 gauge needle. Samples were vortexed for 30 seconds and homogenised using QIShredder microfuge columns.

The homogenised extracts were then loaded onto RNeasy Mini-kit microfuge columns and RNA purification performed according to the manufacturer's instructions. The purified RNA was then eluted from each column into an appropriate volume (30µl) of RNAse-free water. The concentration and purity of extracted RNA was quantitated by measuring absorbance at 260nm and 280nm, using a Nanodrop ND-1000 Spectrophotometer (Thermo-Scientific, Wilmington, USA). Samples were stored at -80^{o}C until use.

2.8.3 Preparation of cDNA from total RNA-reverse transcription

Total RNA was extracted from liver homogenates or cultured cells as described. Reverse transcription was performed using a Superscript-II kit (Invitrogen, Paisley, UK) according to the manufacturers instructions. RNA was thawed on ice and briefly vortexed prior to use. Briefly, 0.1-1µg of template RNA was added to a 0.2ml microcentrifuge tube containing 0.8µl DNAse I solution, 1µl 10x DNAse I Reaction Buffer and DNAse/ RNAse-free water to a final volume of 8.2µl. The tubes were incubated at room temperature for 15 min and 0.8µl of 25mM EDTA solution was added to the reaction mixture. The tubes were then incubated at 65°C for 10min. 2µl of random primers (1µg/µl) (Invitrogen, Paisley, UK) was then added to each tube, which was then incubated at 70°C for 10min then chilled on ice. A mastermix was prepared containing:

Reagent	**Volume per reaction**	**Final Concentration**
5X RT Buffer	4µl	1X
10mM dNTP mix	0.5µl	0.5mM
0.1M DTT	2µl	5mM
Superscript II	0.5µl	10 units/ 20µl
RNAse Inhibitor	0.5µl	20 units/ 20µl
DNAse/ RNAse-free water	1.5µl	
Template RNA	11µl	
Total Volume	**20µl**	

Mastermix (9µl) was then to each tube to give a final volume of 20µl. Samples were incubated at 37°C for 60 min. cDNA was stored at -20°C prior to use.

2.8.4 Reverse transcription-polymerase chain reaction (RT-PCR)

2.8.4.1 Principles of SYBR-Green RT-PCR

A PCR reaction can be divided into three phases; an exponential phase, a linear phase and a plateau. During the exponential phase of the PCR run there should be an exact doubling of product at each cycle (assuming 100% reaction efficiency). This phase of the reaction is very specific and precise. Theoretically, there is a quantitative relationship between the

amount of starting target sample and the amount of PCR product at any given cycle number, this relationship being most consistent during the exponential phase of the PCR reaction.

Real-time PCR measures the accumulation of amplicons during the PCR reaction, with data being measured during the exponential phase. SYBR-Green RT-PCR is a method of real-time PCR that relies upon the fluorescence properties of the cyanine dye SYBR-green. SYBR-green binds to the minor groove of double stranded DNA. The binding of SYBR-green to DNA in this manner results in an increase in the intensity of fluorescent emission. Thus, with each thermal cycle, as more double stranded amplicons are produced the intensity of the SYBR-green signal increases. When the fluorescence signal increases to a detectable level it can be displayed as an amplification plot. The threshold line (ΔRn) is the level of detection at which a reaction reaches a set fluorescent intensity above background, and is set within the exponential phase of the PCR reaction. The cycle at which the sample reaches this threshold is the cycle threshold (Ct). Through this method Ct values can be determined for target genes and reference housekeeping genes in each sample. Standard curves are then produced by plotting Ct values for known cDNA standards against Log of cDNA concentration. Comparative changes in cDNA concentrations can then be calculated by extrapolation from standard curves.

2.8.4.2 SYBR-Green RT-PCR protocol

PCR work was undertaken in a protective hood and all equipment was UV irradiated prior to use. Template cDNA was diluted in DNAse/ RNAse-free water prior to use. 2-20ng of first strand cDNA was used per reaction. A standard curve (S1-7) was produced by serial dilution of a high standard (S1), which was obtained by pooling equal amounts of cDNA from each sample into a single tube. A reaction mixture consisting of 5µl SYBR-Green master mix, 0.2µl primers, 0.8µl DNAse/ RNAse-free water and 4µl cDNA was made up, giving a final reaction volume of 10µl. Samples were added to a 96-well optical plate. The optical plate was covered with a protective film and the plate was briefly centrifuged. All reactions were carried out using an Applied Biosystems 7700 Sequence Detection System.

The following reaction conditions were used:

Fast DNA polymerase activation:	95°C for 20 seconds	**1 cycle**
Denature:	95°C for 3 seconds	**40 cycles**
Anneal/ extend:	60°C for 30 seconds	

The expression of each gene of interest was determined relative to the expression of the housekeeping ribosomal 18S gene. All reactions were undertaken in triplicate. Standard curves were produced for each gene by plotting Ct values for each standard against Log of cDNA concentration. After determination of the threshold cycle (Ct) for each target gene and 18S for each sample, comparative change in each sample was calculated by extrapolation from the standard curves using Excel software (Microsoft, Redmond, USA). Primer specificity was confirmed using melt curve analysis.

2.8.5 Primer design

Custom designed primers for mouse albumin, cytochrome 7A1 (CYP7A1), cytokeratin-19 (CK-19), aquaporin and gamma glutamyl transferase (γGT) were purchased directly from Qiagen (Crawley, UK). Custom designed primers for human Oct4, NANOG and the eukaryotic housekeeping gene 18S were purchased directly from Applied Biosystems (Warrington, UK). Other primer sequences were designed using the Primer3 plus program with the assistance of Dr Antonella Pellicoro (University of Edinburgh). Specifically designed primers were purchased from Eurogentec Ltd (Southampton, UK). Primer and probe sequences are provided in Appendix 2.

Primer characteristics used in design:

- Amplicon size of 100-200bp
- Primer size 18-27bp
- Primer CG percentage of 20-80%
- Maximum number of mononucleotide repeats: 5
- Primer temperature of 57-63°C
- Primer sequences were matched to the original amplicon sequence in the 5'-3' orientation.

2.9 Western blotting

Western blotting experiments were undertaken in collaboration with, and under the supervision of Dr Joerg Schrader (University of Edinburgh)

2.9.1 Protein extraction for Western blotting

An appropriate volume of cell lysis buffer was prepared (see Appendix 3.1). Biochemical reagents were purchased from Sigma (Poole, UK) unless stated. A mixture of protease and phosphatase inhibitors was added to the cell lysis buffer immediately prior to use: benzamidine (10mM); orthovanodate (2mM); leupeptin (2µg/ml); aprotinin (3.4µg/ml); and phenylmethanesulfonyl fluoride (PMSF) (1mM).

For protein extraction from cultured cells, culture media was aspirated from cultured cells and the cells were washed twice in ice-cold PBS. An appropriate aliquot of cell lysis buffer (150µl/ 50mm dish) was added to each culture dish and cells harvested with a cell scraper into a sterile 1.5ml Eppendorf microfuge tube. Samples were kept on ice. Each sample was sonicated and centrifuged (12,000rpm at 4^{o}C) for 10 minutes. The supernatants were transferred to sterile 1.5ml Eppendorf microfuge tubes, stored at -80^{o}C and assayed to establish protein concentration prior to use (Bradford protein determination assay, as described earlier).

For protein extraction from animal tissue, small (~0.1cm^{3}) pieces of frozen tissue were added to an appropriate aliquot of cell lysis buffer (200µl). The tissue was disrupted by repeated passage through a 2ml syringe and 19 gauge needle, sonicated and centrifuged (12,000rpm at 4^{o}C) for 10 minutes. The supernatants were transferred to sterile 1.5ml Eppendorf microfuge tubes, stored at -80^{o}C and assayed to establish protein concentration prior to use.

Following determination of protein concentration, protein concentration was standardised (0.1-2µg/µl) in cell lysis buffer. Samples were prepared for sodium dodecyl sulphate polyacrylamide gel electrophoresis (SDS-PAGE) with the addition of an appropriate volume of 5X Laemmli buffer (see Appendix 3.2). Samples were stored at -20^{o}C. Samples were defrosted and boiled for 10 minutes prior to use.

2.9.2 Sodium dodecyl sulphate (SDS) gel electrophoresis

SDS polyacrylamide gels were cast using a Mini Protean 3 Gel Casting Chamber (Bio-Rad, Hemel Hempstead, UK). Single percentage gels were produced by the sequential introduction to the casting chamber of resolving (10-12%) and stacking (5%) monomer solutions to which had been added 10% ammonium persulfate (APS) and tetramethlyethylenediamine (TEMED) (see Appendix 3.3). Polyacrylamide gels are left to polymerise at room temperature for 30 minutes prior to disassembly of the casting apparatus.

Following gel polymerisation, an upright Mini Protean 3 Gel Electrophoresis Tank (BioRad, Hemel Hempstead, UK) was assembled and filled with 1X running buffer (see appendix 3.4). Equal quantities of protein were loaded (2-40µg) were carefully pipetted into submerged wells. Additionally, 5µl of precision plus protein kaleidoscope standard (BioRad, Hemel Hempstead, UK) was loaded into a separate well. Electrophoresis was run at 100 volts (V) for ~2 hours. The equipment was then disassembled and the stacking gel removed.

2.9.3 Western transfer

Western transfer was performed using a Mini-Trans-Blot Cell (BioRad, Hemel Hempstead, UK). Two pieces of high grade filter paper and two transfer sponges were soaked in 1x transfer buffer (see appendix 3.4). An appropriately-sized piece of Optitran^{TM} nitrocellulose membrane (Whatman GmbH, Dassel, Germany) was also soaked in 1x transfer buffer. A transfer 'sandwich' was assembled consisting of: transfer sponge, filter paper, polyacrylamide electrophoresis gel, nitrocellulose membrane, followed by a second filter paper and transfer sponge. The transfer 'sandwich' was inserted into a cassette and loaded into the Mini-Trans-Blot Cell. An ice-block was inserted into the tank and the reservoir filled with 1x transfer solution. The transfer apparatus was connected to a power supply and the transfer run at 300mA for 1 hour. The equipment was then disassembled and the nitrocellulose membrane removed. Successful transfer was indicated by visualisation of the Bio-Rad Kaleidoscope marker protein ladder (BioRad, Hemel Hempstead, UK).

2.9.4 Membrane protein detection

Following successful transfer, the membrane was air dried at room temperature for 30 minutes and transferred to a 50ml tube. Approximately 10ml of 5% milk solution (Marvel,

UK) in Tris buffered saline solution with 0.1% Tween-20 (TBS-T) was then added to each 50ml tube to block non-specific protein binding and tubes were then placed on a rotator for 1 hour at room temperature. The blocking solution was then decanted and the membranes washed once in 5ml TBS-T solution for 5 minutes on a rotator. The wash solution was then decanted and 5ml of primary antibody solution (appropriately diluted in 5% milk solution/ TBS-T) was added and the tubes placed on a rotator overnight at 4^{o}C. The primary antibody solution was then removed and the membranes washed 3 times in TBS-T solution (as described above). A comprehensive list of primary antibodies and the concentrations used for immunoblotting is provided in Appendix 4. A secondary antibody solution appropriate to each primary antibody was made by 1:2000 dilution of a species-specific horseradish peroxidase (HRP) conjugated antibody (Cell Signalling, Danvers, USA) in 5% milk/ TBS-T solution. The wash solution was then decanted and 5ml of secondary antibody solution was added to each membrane and the tubes placed on a rotator for 1 hour at room temperature. The secondary antibody solution was then discarded and the membranes washed 3 times in TBS-T solution (as described above).

Signal detection was performed using Immobilon Western chemoluminescent HRP substrate (Millipore, Watford, UK). Each nitrocellulose membrane was placed on a clean transparent acetate sheet. The detection solution was prepared by mixing an equal volume of HRP substrate peroxide solution to the HRP substrate luminol solution (400µl/membrane). The detection solution was then carefully pipetted over each nitrocellulose membrane. A second transparent acetate sheet was placed on top of the membrane and taped down, ensuring no air bubbles were present. The membranes were placed inside a film cassette. In a dark room, a sheet of photographic film (Fuji, Bedfordshire, UK) was placed on top of the membrane and exposed for 30 seconds prior to being developed in a developer unit. The duration of subsequent exposures was varied according to the appearance of the initial film. For quantification, blots from a minimum of three independent experiments were scanned at high resolution and the resulting images analyzed by densitometry (ImageJ).

2.9.5 Western blotting membrane stripping protocol

Nitrocellulose membranes were stripped prior to repeated immunoblotting by incubation at 65^{o}C for 15 minutes in a stripping buffer containing; 1g SDS, 2ml β-mercaptoethanol and 0.75g Trizma Base in 100ml distilled water, pH6.7. Membranes were then washed 6 times in TBS-T prior to incubation with blocking solution (as described above).

2.10 Production of matrix-coated polyacrylamide (PA) gel supports for tissue culture

PA gels of variable stiffness were prepared on glass coverslips using a modification of the method initially described by Pelham and Wang (95). In brief, glass coverslips were soaked in 0.1N sodium hydroxide and air dried. A small aliquot of 3-aminopropyltrimethoxysilane (APTMS) (Sigma, Poole, UK) is spread across each coverslip and the coverslips are extensively washed in distilled water and then soaked in 0.5% glutaraldehyde (Sigma, Poole, UK) in PBS. The coverslips are then coated in a thin layer of gel containing a mixture of 7.5% acrylamide and 0.01-0.3% bis-acrylamide (National Diagnostics, UK). In each case, the shear modulus (G') of the resulting PA gels has been determined by our collaborators in the University of Pennsylvania (see Appendix 5) (195). The gels are then washed in 50mM HEPES (Sigma, Poole, UK) and sufficient 50mM sulfosuccinimidyl 6 (4'-azido-2'-nitrophenylamido) hexanoate (Sulfo-SANPAH) (Perbio, Cramlington, UK) to fully cover the gel surface. The coverslips are then exposed to UV light for 5 minutes to facilitate cross-linker activation. Excess Sulfo-SANPAH is removed by extensive washing in 50mM HEPES. A thin layer of collagen-I, collagen-IV, fibronectin (Sigma, Poole, UK) and laminin (R&D, UK) is then cross-linked to the gels at room temperature for 90 minutes. Collagen-I and Collagen-IV (Sigma, Poole, UK) were dissolved in 0.1M acetic acid at a stock concentration of 1mg/ml and then diluted to a final concentration (0.1mg/ml) in distilled water. Laminin was dissolved in PBS at a stock concentration of 20µg/ml, and used at this concentration in PBS. Fibronectin was dissolved in PBS at a stock concentration of 0.1mg/ml, and further diluted to a final concentration (50µg/ml) in PBS. Adhesion of ECM proteins to PA gels may be increased by the addition of a layer of poly-D-lysine (Sigma, Poole, UK). Poly-D-lysine is dissolved in distilled water to a stock concentration of 0.1mg/ml, and further diluted to a final concentration of 10µg/ml. It can then be cross-linked to PA gels at room temperature for 90 minutes. Excess poly-D-lysine is washed off prior to the addition of ECM proteins. Excess ECM is then washed off and any remaining cross-linker is blocked with 1% ethanolamine (Sigma, Poole, UK) in 50mM HEPES for 30 minutes at 4^{o}C. Gels are then soaked in serum free culture media overnight before plating of cells.

Figure 2.1: Schematic representation of the structure of ligand-coated polyacrylamide gel (PA) supports

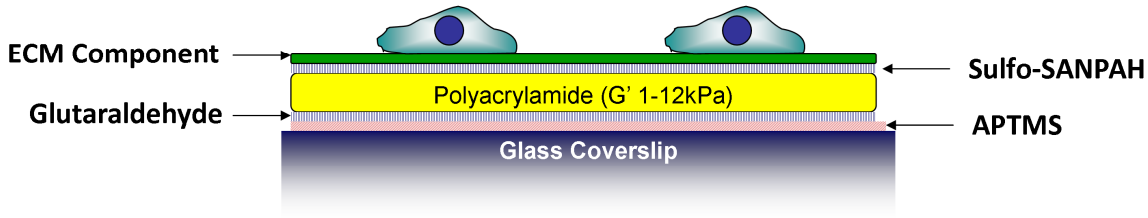

Figure 2.1 Schematic representation of a ligand-coated PA gel support. A multistep process is employed in which glass coverslips are treated with APTMS, an alkoxysilane that binds to hydroxyl groups in glass. This, in turn, is linked to glutaraldehyde, an amine reactive cross-linker that binds covalently to a thin layer of polyacrylamide (100µm thickness). The stiffness of the polyacrylamide layer can be altered (1-12kPa) by changing the concentration of bis-acrylamide cross-linker in the polyacrylamide matrix. The polyacrylamide is then treated with Sulfo-SANPAH. This is a UV-activated bivalent cross-linker that covalently links the polyacrylamide gel matrix to extracellular matrix components (e.g. collagen-I, collagen-IV, laminin or fibronectin).

2.11 Cell culture techniques

2.11.1 Culture of human epithelial cell lines

HCC cell lines Huh7 and HepG2 were kindly provided by Prof S. Wigmore (University of Edinburgh, UK). Human cell lines MCF7, MDA and LNCap were kindly donated by Dr P. Saunders (University of Edinburgh, UK). The human lung cancer cell line A549 was kindly donated by Prof T. Sethi (University of Edinburgh UK). Cell culture and chemical reagents were purchased from Sigma (Poole, UK), unless otherwise stated.

The Huh7 is a well-differentiated hepatocyte-derived cellular carcinoma-derived cell line taken from a 57-year-old Japanese male (208). The HepG2 is a well-differentiated liver carcinoma-derived cell line taken from a 15-year-old Caucasian man (209). The MCF7 is a breast adenocarcinoma cell line derived from a 69-year-old Caucasian woman (210). The MDA is believed to be a breast adenocarcinoma cell line, which was derived from a malignant pleural effusion in a 31-year-old woman (211). However, the MDA cell line has been shown to produce both breast-differentiation-specific proteins and melanocyte-specific proteins (212). There has been some debate as to whether the MDA cell line is a breast

epithelial cell line that has undergone lineage infidelity or may be of melanocyte origin (213). The A549 is an alveolar cell-derived adenocarcinoma cell line isolated from a 57-year-old Caucasian male (214). The LNCap is an androgen-sensitive human prostate adenocarcinoma derived from a left supraclavicular node metastasis in a 50-year-old Caucasian male (215).

The Huh7, HepG2, MCF7, MDA and A549 cell lines were maintained in Dulbecco's Modified Eagle Medium (DMEM) (Gibco, Paisley, UK) supplemented with 10% foetal calf serum (FCS), penicillin/streptomycin and L-glutamine, LNCap cells were cultured in Roswell Park Memorial Institute media (RPMI) (Gibco, Paisley, UK). In all experiments cells were plated at semi-confluent density in 1% FCS. Cells were cultured in a humidified atmosphere with 5% CO_2 at 37 °C.

Transforming growth factor-beta (TGFβ) and hepatocyte growth factor (HGF) (Peprotech, London, UK) were used at concentrations of 5ng/ml and 10ng/ml, respectively. Anti-β1-integrin, clone 6S6 (Millipore, Watford, UK) and control IgG1 immunoglobulin (AbD Serotec, Oxford, UK) were used for cell culture experiments at 50μg/ml. Echistatin (Tocris, Bristol, UK) was solubilised in PBS and used in cell culture experiments at a concentration of 100nM. Mitomycin c was solubilised in PBS and used in cell culture experiments at a concentration of 100μM-10mM. The ROCK inhibitor Y-27632 was solubilised in water and used in cell culture experiments at a concentration of 10-50mM. The chemical FAK inhibitor, PF573228 (Tocris, Bristol, UK) was solubilized in dimethyl-sulfoxide (DMSO) and used for cell culture experiments at a concentration of 1-5μM. The myosin-II inhibitor (blebbistatin) was solubilised in DMSO and used in cell culture experiments at a concentration of 10-50μM.

2.11.2 Culture of murine hepatic progenitor cell (HPC) lines

The bi-potential murine oval cell line (BMOL) was kindly donated by Dr B. Knight (University of Edinburgh). The BMOL is a clonally derived, spontaneously immortalised cell line that was derived from primary murine progenitor cells following prolonged maintenance in culture using a "plate and wait" strategy (216). Briefly, primary murine progenitor cells (HPCs) were isolated from male C57 BL6 mice that had been fed with a choline-deficient ethanolamine-supplemented diet for 2-3 weeks to promote HPC expansion. Following initial plating, epithelioid colonies were selected, trypsinized and replated.

Visually verified single cell cloning was carried out by serial dilution and inoculation into a 96-well plate. After initial growth inhibition, some cells overcame crisis and formed colonies. These were expanded, replated at low density and clonally derived cell lines established. The cells were passaged weekly until the cell line became stable, displaying consistent morphology and growth. BMOL cells express markers of both hepatocyte and biliary differentiation. They retain the ability to differentiate towards either a hepatocyte or biliary lineage. They differ from primary murine HPCs in a number of important respects. As immortalised cells they can be maintained indefinitely in cell culture. In comparison to primary HPCs they are more homogeneous in respect to their morphology and demonstrate higher rates of cell proliferation. The genetic alterations underlying their spontaneous immortalisation have not been characterised. As such care should be taken in extrapolating the results of experiments conducted in BMOL cells to hepatic progenitor cells more generally.

BMOL cells were maintained in specialised media containing: DMEM (50%), Ham's F10 media (50%) supplemented with 10% FCS, gentamicin, L-glutamine, sodium pyruvate, hydrocortisone and insulin. In all experiments cells were plated at semi-confluent density in 1% FCS. Cells were cultured in a humidified atmosphere with 5% CO_2 at 37 °C.

2.11.3 Isolation and culture of primary murine hepatic stellate cells (HSCs)

Primary hepatic stellate cells (HSC) were isolated as previously described (217). Briefly, mouse livers (4-6 per cell preparation) were flushed with Hank's buffered salt solution (HBSS) following cannulation of the hepatic portal vein. The livers are then dissected, mechanically disrupted and suspended in HBSS containing 0.05% DNAse (Roche Diagnostics, West Sussex, UK). The resulting cell suspension was transferred to a solution containing 0.05% Collagenase (Roche Diagnostics, West Sussex, UK), 0.3% Pronase (Sigma, Poole, UK) and 0.02% DNAse. This was then agitated/ incubated on an orbital rocker for 20 minutes at 37^{o}C at 120rpm. The cell suspension is then passed through a fine nylon mesh and then centrifuged at 1800rpm for 5 minutes. The resulting cell pellet is resuspended in 9ml HBSS and 6ml Optiprep (Sigma-Aldrich, Poole, UK) to a final volume of 15ml. The resulting cell suspension in divided between two tubes and carefully layered over Optiprep (7.5ml). A layer (0.5ml) of HBSS is then carefully layered over the cell suspension prior to centrifugation at 2500ml at 4^{o}C for 20 minutes. The upper pale cellular band, containing HSCs was carefully aspirated from each tube and resuspended in HBSS

prior to centrifugation at 1800rpm for 7 minutes. The supernatant was discarded and the cell pellet resuspended prior to plating. HSCs were maintained in DMEM media supplemented with FCS (20%), sodium pyruvate, L-glutamine, penicillin and gentamicin, In all experiments, cells were plated at semi-confluent density in 1% FCS and only low passage cells were employed (P1-3). Cells were cultured in a humidified atmosphere with 5% CO_2 at 37 °C.

2.11.4 Isolation and culture of primary murine hepatic progenitor cells (HPCs)

Primary murine HPCs were isolated in collaboration with Dr L Boulter (University of Edinburgh). HPC isolation and culture from C57BL/6 mice was performed as previously described (216, 218). Briefly, 4-week-old male mice were maintained on a choline deficient, ethionine-supplemented (CDE) diet for 2-3 weeks. Mice were anaesthetised and HPCs isolated by modification of a two-step perfusion protocol (219). The livers were perfused via the portal vein with EGTA buffer (0.5 mM EGTA, 137mM NaCl, 4.7mM KCl, 1.2mM KH_2PO_4, 0.65mM $MgSO_4$ and 10.07 mM HEPES, pH7.4) followed by collagenase buffer (67 mM NaCl, 6.7 mM KCl, 4.76 mM $CaCl_2$, 100.7 mM HEPES, 0.035% collagenase type I, pH 7.6). The livers were then mechanically disrupted into William's E media (Gibco, Paisley, UK) and dissociated by pipetting. The cell suspension was then centrifuged (1800rpm, 5 minutes). The resulting cell pellet was transferred to a flask containing 0.1% collagenase type VIII, 0.09% Pronase (Roche Diagnostics, West Sussex, UK), 0.025% trypsin/0.01% EDTA (Invitrogen, Paisley, UK), 0.004% DNase in PBS. The cell suspension was incubated for 50 min at 37 °C prior to the addition of an equal volume of William's E media containing 2% FCS. The cell suspension was passed through a 40μM BD Falcon™ cell strainer (BD Biosciences, Oxford, UK). The cells were centrifuged at 50g for 3 minutes to pellet any hepatocytes or large clumps that may have passed through the filter. The supernatant was removed and this step was repeated, following which the supernatant was centrifuged at 160g for 10 minutes. The resulting cell pellet was resuspended in 5-10ml of ammonium chloride cell lysis buffer (8.26g ammonium chloride, 1g potassium bicarbonate and 0.036g EDTA in 1 litre sterile water) and left on ice for 5 minutes. Following this 10ml of PBS was added and cells pelleted by centrifugation at 160g for 10 minutes. The cell pellet was washed three times in PBS and the resulting cell pellet was resuspended in William's E media and underlayed with 20% and 50% Percoll™ (Amersham Biosciences) in PBS. HPCs were purified by density gradient centrifugation at 1400g for 20 minutes, with the resulting cell band collected and transferred to a tube containing an equal volume of

William's E media supplemented with 2% FCS. The cells were pelleted by centrifugation (160g, 5 minutes) and washed twice in PBS. Trypan-blue excluding HPCs were counted prior to plating. HPCs were maintained in oval cell media consisting of DMEM (50%), Ham's F10 media (Gibco, Paisley, UK) supplemented with L-glutamine, gentamicin, sodium pyruvate, 10% FCS and insulin (10μg/ml). Cells were cultured in a humidified atmosphere with 5% CO_2 at 37 °C. In proliferation experiment cells were cultured at semi-confluent density in oval cell media containing 1% FCS. As primary cells, primary HPCs have a limited lifespan in culture and in all experiments passage 1 (P1) cells were used exclusively.

2.11.5 Isolation and culture of primary murine hepatocytes

Experiments using primary murine hepatocytes were kindly performed by Dr Joerg Shrader (University Medical Center Hamburg-Eppendorf). Hepatocytes isolation and culture from male C57BL/6 mice was performed as previously described (220). Briefly, mouse livers were perfused via the portal vein with 0.05% collagenase solution in DMEM. The liver tissue was then dissected/ mechanically disrupted and suspended in DMEM. The cell suspension was centrifuged (30g for 3 minutes) and the supernatant discarded. Following resuspension of the cell pellet, residual non-hepatocyte cells were removed by incubation with anti-CD8, anti-F4/80, anti-CD13, anti-CD45R, anti-CD11B, MAR18.5 (anti-B-lymphocyte) monoclonal antibodies and rabbit complement for 20 minutes at 37^{o}C. The cell suspension was then centrifuged (30g x 3 minutes) and hepatocytes were resuspended in DMEM containing 10% FCS. In proliferation experiments, identical numbers of cells (1 x 10^5) were plated onto 24mm collagen-I-coated PA gel supports and maintained in culture for 48 hours. The cells were then fixed in 4% paraformaldehyde solution and immunostaining undertaken for the Ki67 antigen. A total of 25 low power fields (x50 magnification) were counted for Ki67 positive cells for each slide (n=3).

2.12 Microscopy and digital image analysis of cultured cells

Microscopic examination and representative photomicrographs (x200 magnification) of cells in culture was performed using an inverted Zeiss Axiovert-200 microscope and Axiovision image acquisition software (Zeiss, Heidenheim, Germany). Cell spreading measurements were obtained by quantifying the mean projected surface area from 50 cells visualized by phase-contrast microscopy (ImageJ, National Institutes of Health, USA). Stress fibre orientation was quantified by digital image analysis. Stress fibre orientation was defined as

the mean angle of intersection between a line representing the predominant direction of stress fibre organisation in a single cell and a line representing the direction of applied uniaxial stress. In each experiment digital image analysis was undertaken using fully blinded and randomised images. Confocal microscopy was performed using an inverted Leica SP5C spectral confocal laser scanning microscope and image acquisition via LASAF software (Leica Microsystems GmbH, Wetzlar, Germany). DAPI, Alexafluor 488 and Alexafluor-546 were detected using band paths of 430-470, 495-540 and 550-600 for 405, 488 and 546nm lasers respectively.

2.13 Uniaxial cyclical strain application to cultured cells using Flexcell™ apparatus

HSCs were cultured at sub-confluent density on collagen-I-coated deformable silicon membranes and subjected to uniaxial mechanical strain for 4-24 hours using Flexcell FX-2000 apparatus (Flexcell International Corporation, Hillsborough, USA). The Flexcell™ system allows cells to be cultured on deformable silicon membranes in 6 well plates, which are mounted on a sealed vacuum-base unit that is attached to a computer controlled vacuum pump. Each membrane is suspended above a central arctangular™ support. Negative pressure applied to the base of each well from a computer controlled vacuum pump leads to indrawing of the peripheral (unsupported) section of each well. This results in uniaxial deformation of the central (supported) section and the cell monolayer (CM) adherent to this region (Figure 5.15B). Computer settings determine the extent of uniaxial stain imposed on the flexible-bottomed wells (expressed as a percentage). The apparatus is calibrated to produce cyclical (1Hz) uniaxial strain in the range 2.5-10%. The cell culture plates and base unit are maintained in a custom-modified incubator at 37^{o}C with atmosphere containing 5% CO_2. In experiments with primary murine HSCs, cells were cultured in collagen-I-coated Flexcell plates for 48 hours in standard HSC media containing 20% FCS. The cells were then transferred to serum free media and exposed to uniaxial strain (2.5-10%) for 4-24 hours. Cells were then either fixed in 1% paraformaldehyde for immunofluorescent staining or harvested for RNA analysis.

2.14 Immunofluorescent staining

2.14.1 General immunofluorescent staining protocol of cultured cells

Immunofluorescent staining was carried out at room temperature unless otherwise stated. Media was aspirated from culture plates and cells were washed twice in PBS. Cells were fixed in 4.5% paraformaldehyde for 10 minutes and then aspirated to dryness. Culture plates were rinsed twice in PBS and cells permeabilised with 0.2% Triton X-100 in PBS for 5 minutes. The cells were then rinsed twice with PBS. Non-specific staining was blocked by incubation with 10% bovine serum albumin solution (BSA) in PBS for 30 minutes. Without washing, samples were then incubated with a primary antibody solution (appropriately diluted in a blocking buffer containing species-specific serum) for 1 hour. (Appendix 6). Species-specific serum was chosen to match the species in which the relevant secondary antibody was raised. Cells were then washed 3 x 5 minutes in PBS. A secondary antibody solution appropriate to each primary antibody was made by appropriate dilution of secondary antibody in blocking solution. Cells were incubated with secondary antibody solution for 1 hour and then washed 3 x 5 minutes in PBS. Nuclear DNA was counterstained with 4', 6'-diamidino-2-phenyl-indole dihydrochloride (DAPI) in hard setting mounting media (Dako, Ely, UK). Slides were mounted on glass coverslips and sealed with transparent nail varnish (Rimmel, London, UK). In each experiment antibody-conjugated fluorophores were carefully chosen to avoid overlap between excitation and emission spectra.

2.14.2 Actin stress fibre staining

Actin stress fibre staining was performed using a modification of the general immunofluorescent staining protocol. Cells were fixed and permeabilised as outlined above. Non-specific binding was blocked by incubation with 10% BSA in PBS. Without washing, cells were then incubated in a solution containing Alexa 488-phalloidin (Invitrogen, Paisley, UK) in PBS (1:40 dilution) for 30 minutes and then washed 3 x 5 minutes in PBC. Nuclear DNA counterstaining and slide mounting was performed as outline above (section 2.14.1). In selected experiments, actin stress fibre staining was included in a dual staining protocol. In this setting, following the removal of the secondary antibody solution, cells were washed 3 x 5 minutes in PBS prior to incubation with the Alexa 488-phalloidin solution. Slides were then washed 3 x 5 minutes in PBS prior to proceeding to nuclear DNA counterstaining and mounting.

2.14.3 Ki67 immunostaining and cell proliferative index measurement

Ki67 immunostaining was performed using a modification of the general immunofluorescent staining protocol with polyclonal rabbit anti-Ki67 primary antibody (1:200 dilution) and Alexa 568-labelled goat anti-rabbit secondary antibody (1:400 dilution). Nuclear DNA was counterstained using DAPI hard-setting mounting media as described above. Ki67 antigen is present within the cell nucleus during all active phases of the cell cycle, but is absent from resting cells. Cellular proliferative index (Ki67 positive cells/ total cells) was calculated by direct cell counting from 15 randomly selected high magnification photomicrographs from Ki67- and DAPI-stained slides (n=3).

2.15 MTT cell assay

Assays utilising the reduction of the tetrazolium salt 3-(4, 5-Dimethylthiazol-2-yl)-2, 5-diphenyltetrazolium bromide (MTT) were employed as a marker of viable cell numbers in proliferation and chemotherapy experiments. The MTT reagent was purchased from Sigma (Poole, UK). MTT solution (5mg/ml) in PBS was freshly prepared prior to each experiment. At the end of the culture period, an appropriate volume of MTT solution was added to the cell culture media and incubated with the cells for a further 90 minutes. The culture media was then aspirated and cells washed twice in PBS. The formazan end product was then solubilised in an appropriate volume of dimethyl-sulfoxide (DMSO). The absorbance of the insoluble reduced formazan end product was measured at 590nm using a Biotek Synergy HT microplate reader (Biotek, Potton, UK).

2.16 Gene silencing with siRNA transfection

Specific gene silencing in Huh7 and HepG2 cells was achieved by transient transfection with gene targeting siRNA. Targeting and non-targeting siRNA pools (siGENOME Smartpool) were purchased from Dharmacon (Lafayette, USA). Each siRNA pool consisted of 4 annealed double-stranded RNA oligonucleotide sequences designed to silence specific target genes or function as non-targeting (control) siRNA. Transfection of siRNA was performed using DharmaFECT 4 (Dharmacon, Lafayette, USA) according to the manufacturer's instructions. Briefly, HCC cell lines were plated in DMEM media supplemented with 10% FCS and penicillin/ streptomycin (Huh7: 1.5 x 10^4cells/ cm^2 and HepG2: 3 x 10^4 cells/ cm^2). The cells were then cultured overnight in standard culture conditions. In each siRNA

experiment, cells were transfected using DharmaFECT 4 (Huh7: 0.05µ/100µl and HepG2: 0.4µl/ 100µl) and siRNA at a final concentration of 50nM in antibiotic-free media. Transfection media was replaced after 12 hours with standard antibiotic-containing media. For each experiment cells were trypsinized and transferred to PA gel supports after 48 hours and experiments terminated at 72 hours following transfection. Gene silencing at 72 hours was assessed by Western blot analysis of cell lysates using antibodies specific for FAK and β1-integrin (as previously described in section 2.9).

2.17 Clonogenic Assays

Clonogenic assays were performed using HepG2 and Huh7 cell lines. In each experiment cells were plated at semi-confluent density onto PA gels in DMEM supplemented with 1% FCS. After 48 hours in culture, cells either received cisplatin (HepG2 10µM/ Huh7 20µM) or 5-fluorouracil (5FU 25µM), or were left untreated in plating medium. After 24 hours, the medium was changed to normal culture medium and the cells were incubated for a further 48 hours, for a total of 5 days of culture. Cells were then retrieved by trypsinization, counted and plated at clonal density (10,000 cells/well) into 12-well plates in normal culture medium. Cells were fixed at between 5 and 10 days in 4% paraformaldehyde and stained with 0.5% crystal violet solution. The plates were subsequently imaged with a VersaDoc system (BioRad, Hercules, USA) and the numbers of individual quantities counted automatically using Quantify-One software (BioRad, Hercules, USA).

2.18 Flow cytometric analysis

Flow cytometry experiments were undertaken under the supervision of Dr Joerg Schrader (University of Edinburgh). Flow cytometry was performed on Huh7 and HepG2 that had been cultured on PA gel supports. Cells were dissociated from PA gel supports by incubation with EDTA (5mM) and subsequent trypsinization. A single cell suspension was generated by passing cells through a 40µM cell strainer. Non-specific antibody staining was blocked by incubating cells with PBS containing 10% FCS for 30 minutes on ice. Cells were then washed in 1ml PBS containing 0.1% FCS prior to centrifugation (1300rpm, 5 minutes). The resulting cell pellet was resuspended in a primary antibody solution diluted in PBS with 0.1% FCS and incubated on ice for 30 minutes. The following phycoerythrin-conjugated (PE) antibodies/ dilutions were used: CD44-PE (1:50), CD117-PE (c-kit) (1:50), CD133-PE (1:10), CD184-PE (CXCR-4) (1:10) and corresponding PE-labelled isotype controls. All

antibodies were purchased from E-Biosciences (Hatfield, UK). Each sample was then subjected to centrifugation (1300 rpm, 5 minutes) and washed three-times in 1ml PBS containing 0.1% FCS. The cells were then fixed for 5 minutes in 1% paraformaldehyde solution. The cells were then centrifuged (1300 rpm, 5 minutes) and resuspended in PBS with 0.1% FCS. After staining and fixation cells were analysed on a FACScan analyser (BD Biosciences, Franklin Lakes, USA). Data analysis was performed using FlowJo software (Tree-Star Inc, Ashland, USA).

2.19 Statistical analysis

Statistical analysis was performed using GraphPad Prism™ (GraphPad Software, La Jolla, USA). Mean (±standard error of mean) were calculated for each variable. Statistical differences between mean values were compared using unpaired two-way student t-tests for parametric and Mann-Whitney test for non-parametrically distributed variables. The unpaired student t-test is used for comparing the means of two unmatched groups, assuming normal distribution. In contrast a Mann-Whitney test is used for comparing the means of two unmatched groups, where the variables are non-normally distributed. Conventionally, a p value of less than 0.05 is used to define results of statistical significance. For purposes of clarity, the number of samples/ replicates (n) used in each experiment and in calculations of statistical significance is clearly described in the results sections. Similarly, the nature of each statistical test used is stated in the legend of relevant figures in the results chapters. Statistical correlations between variables were made using Spearman correlation co-efficient (R). The correlation co-efficient provides a measure of the degree of correlation between two variables. A value of 1.0 indicates a perfect correlation, whereas a value of minus 1.0 indicates a perfect negative or inverse correlation. A value of zero indicates that the two variables do not vary together at all. A D'Agostino-Pearson normality test was used to determine whether the variables were normally distributed. In each case where a correlation co-efficient was required the data was found to be non-normally distributed and the non-parametric Spearman correlation co-efficient was used. In tests of correlation, the p-value answers the null hypothesis; if there is no correlation between two variables, what is the probability that a random sampling would result in a correlation co-efficient as far from zero as that observed in the experiment. Conventionally, a p value of less than 0.05 is used to define results of statistical significance.

Chapter 3: Studies to determine the effect of changes in stiffness on the phenotype of hepatocellular carcinoma (HCC) cells

3.1. Introduction

Hepatocellular carcinoma (HCC) is a tumour that develops within the high stiffness environment that characterises liver fibrosis/ cirrhosis (2). Studies using transient elastography have demonstrated that increased liver stiffness is a strong predictor of HCC development (117, 118). In a cohort of patient with chronic HCV infection, the cumulative incidence for HCC development in patients with a low baseline liver stiffness measurement (LSM) [<10kPa] was only 0.4% after 3 years follow-up (118). In contrast, patients with a moderately elevated LSM [10.1-15kPa] had a 10% risk of HCC development over this same period. HCC risk increases further at higher LSM. Liver stiffness has conventionally been employed as a surrogate marker for liver fibrosis. It is unclear whether alterations in liver stiffness (or the presence of liver fibrosis) are mechanistically important in promoting HCC development and aggressiveness (167). Liver stiffness may in itself simply be a surrogate marker for chronic inflammation with its antecedent risk of DNA damage and genomic instability. Previous studies have indicated that pathophysiologically relevant increases in matrix stiffness disrupt tissue organisation, enhance growth and promote tumour formation in murine models of mammary gland carcinoma (46, 155). Similarly, increased matrix stiffness has been shown to enhance *in vitro* cell migration and proliferation in transformed glioma cells (184). It has been suggested that the natural history of cancer progression, from tumour growth through to tumour invasion and metastasis, is accompanied by changes in both the mechanical properties of the cancer cell niche and intrinsic contractility of cancer cells (131). Furthermore, changes in the mechanical properties of cancer cells and their surroundings throughout this 'force journey' may regulate multiple facets of cancer cell biology. HCC is ideally suited as a model in which to explore the link between tissue stiffness and cancer development. Studies utilising transient elastography and atomic force microscopy have closely defined the range of stiffness values that would be encountered by cells during the development of liver cirrhosis and hepatocarcinogenesis. It was the aim of this initial work to investigate the effect of pathophysiologically-relevant changes in matrix stiffness on HCC cell behaviour. Ligand-coated PA supports were used to investigate the effect of changes in matrix stiffness on the morphology, differentiation and proliferation of HCC cells. Ligand-coated PA gels are a valuable experimental tool, allowing separation of the biochemical and physical characteristics of the cell culture environment. For the

purposes of these studies matrix stiffness (expressed as shear modulus G') was modelled across the range 1-12kPa, corresponding to the physical characteristics of liver tissue during the transition from a normal to a cirrhotic liver.

A further aim of these studies was to investigate whether alterations in the stiffness of the cancer cell niche might influence susceptibility to chemotherapeutic agents. A diagnosis of HCC continues to impose a poor prognosis, with a mean survival from diagnosis of less than 12 months (9-11). This is a reflection of both late presentation and a lack of available treatments. Tumour recurrence, occurring months or years following resection of a primary tumour, limits the effectiveness of both hepatic resection and liver transplantation (12-14). Chemotherapy has been shown to be ineffective in the treatment of disseminated HCC and in an adjuvant/ neoadjuvant setting for eradication of disseminated (dormant) tumour cells. The mechanisms responsible for chemotherapy resistance in HCC are incompletely characterised. While, it has been demonstrated that the composition of the ECM can enhance chemotherapy resistance in a range of epithelial cancers, the influence of matrix stiffness has not been addressed (183, 221). It was therefore my intention to undertake preliminary studies to assess whether pathophysiologically-relevant changes in matrix stiffness may influence chemotherapy response in HCC cells.

3.1.1. Hypotheses

- Changes in matrix stiffness across a pathophysiologically-relevant range will modulate HCC cell morphology and cytoskeletal organisation.
- Increases in matrix stiffness will promote HCC cell proliferation.
- Changes in matrix stiffness will modulate the activity of cytokine-mediated signalling pathways, including ERK, PKB, Akt and STAT3.
- Changes in matrix stiffness will modulate chemotherapy-resistance in HCC cells.
- Alterations in matrix stiffness will modulate the frequency of stem cell marker expression in HCC cell lines.

3.2. Changes in matrix stiffness modulate cell morphology in HCC cells

In experiments conducted in both Huh7 and HepG2 cells, a consistent morphological response was observed in response to changes in support stiffness. HCC cells cultured on soft (1kPa) supports were small and rounded. In contrast HCC cells on stiff (12kPa)

supports were flattened and well-spread with prominent cellular processes (Figure 3.1). The effect of support stiffness on cell spreading was quantified with detailed measurement of projected cell surface area across a range of stiffness values (1-12kPa). For the purpose of comparison, measurements were also taken on cells cultured on identically-treated collagen-I-coated glass coverslips. This is a relevant control as matrix-coated glass is conventionally employed for the purpose of cell culture. The physical characteristics of matrix-coated glass are highly non-physiological, with shear modulus expressed in the gigapascal range.
In Huh7 cells, mean projected surface area increased from 870μm^2 on 1kPa supports to 1413μm^2 on 12kPa supports ($p<0.001$). Similarly, HepG2 projected surface area on 1kPa supports was 322μm^2, rising to 648μm^2 on 12kPa supports ($p<0.001$). In each case, maximal cell spreading was observed for cells cultured on collagen-I-coated glass. However, the incremental component of the increase in cell spreading that was observed as a quasi-linear function of increasing support stiffness, occurred across a pathophysiologically-relevant range (1-12kPa).

The results for projected surface area (value ± SEM) in Huh7 cells are: 1kPa, 870 ± 11.6μm^2; 2.5kPa, 1104 ±62.6 μm^2; 12kPa, 1413 ± 85.0 μm^2; and glass, 1480 ± 151 μm^2. For HepG2 cells the values were: 1kPa 322 ± 17.8 μm^2; 2.5kPa 387 ± 19.3 μm^2; 12kPa, 648 ± 34.0 μm^2; and glass, 857 ± 81.0 μm^2.

Figure 3.1: The effect of PA support stiffness on cell spreading in Huh7 and HepG2 cells

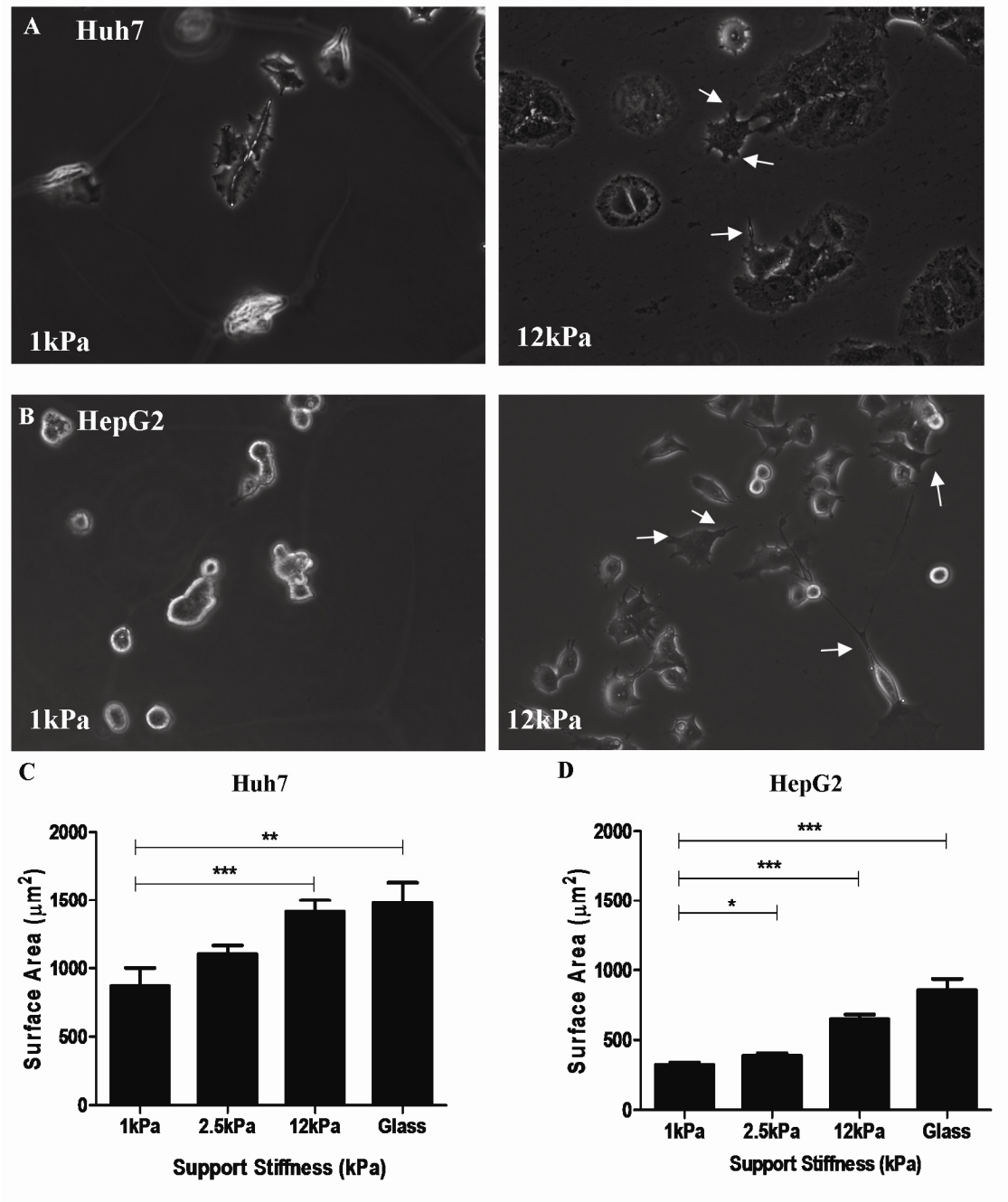

Figure 3.1: Phase contrast photomicrographs (x200 magnification) demonstrating the effect of changes in PA support stiffness (1-12kPa) on cellular morphology in (A) Huh7 and (B) HepG2 cells. Prominent cellular processes of cells on 12kPa gels are indicated by the white arrows. The projected surface area (square microns) of (C) Huh7 and (D) HepG2 cells was calculated by digital image analysis of phase contrast images of cells on collagen-I-coated PA supports and collagen-I-coated glass coverslips. In each case, the bars represent the mean (±SEM) of measurements from 50 cells (n=50) randomly selected from photomicrographs of cells cultured from PA gels in three independent experiments. Mean measurements were compared using an unpaired student t test (*$p<0.05$, **$p<0.01$ and ***$p<0.001$).

A time-course analysis of cellular spreading was performed in Huh7 and HepG2 cells plated onto 1kPa and 12kPa supports (Figure 3.2). Differences in cell spreading, as a function of support stiffness, develop rapidly (within 1 hour). The results for cell spreading (value ± SEM) in Huh7 cells are: 1 hour, 1kPa 408 ± 24.5μm^2 / 12kPa 1749 ± 165.4μm^2; 6 hours, 1kPa 828 ± 65.2μm^2 / 12kPa 2453 ±199.1μm^2; 24 hours, 1kPa 773 ± 49.4/ 12kPa 2610 ± 220.6. In HepG2 cells, a similar trend is seen: 1 hour, 1kPa 200 ± 10.8μm^2 / 12kPa 305 ± 23.6μm^2; 6 hours, 1kPa 214 ± 8.3μm^2 / 12kPa 498 ±28.9μm^2; 24 hours, 1kPa 230 ± 11.7μm^2/ 12kPa 680 ± 35.8μm^2. In order to assess whether differences in cell proliferation might be sufficient to account for the observed differences in cell spreading between PA supports, cell spreading was measured in the presence of low dose mitomycin c (100-200nM). The dose of mitomycin c used (Huh7 100nM/ HepG2 200nM) was informed by dose finding experiments (data not shown). No change in the relationship between cell spreading and support stiffness was observed following pharmacological inhibition of cell division with mitomycin c. For Huh7 cells mean projected surface area after 24 hours in the presence of mitomycin c was: 1kPa 698 ± 50.0 μm^2 / 12kPa 2614±223.2μm^2. In HepG2 cells mean projected surface area after 24 hours in the presence of mitomycin c was: 1kPa 219 ± 6.9 μm^2 / 12kPa 668 ± 32.1μm^2.

Figure 3.2: Time-course analysis of Huh7/ HepG2 cell spreading on PA supports

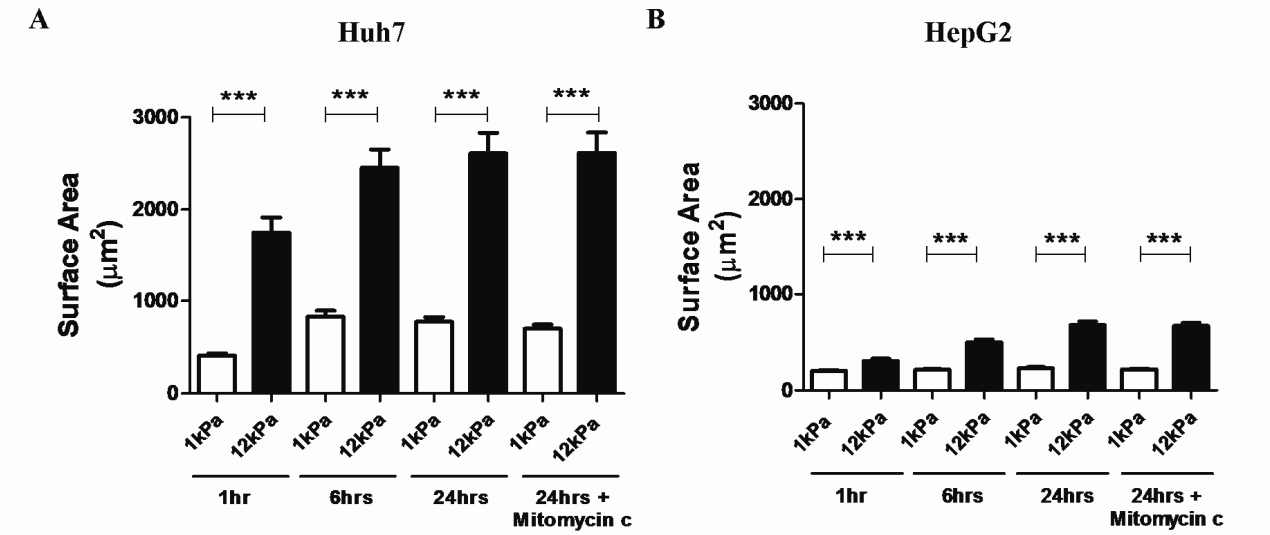

Figure 3.2 Graphs showing a time-course analysis of cell spreading of (A) Huh7 and (B) HepG2 cells plated on 1kPa and 12kPa collagen-I-coated PA supports in low serum conditions. In each case, the projected surface area (square microns) of the cells was measured by digital image analysis of phase-contrast images of cells on PA supports. In each case, the bars represent the mean (±SEM) of measurements from 50 cells (n=50) randomly selected from photomicrographs of cells cultured from PA gels in three independent experiments. Mean measurements were compared using an unpaired student t test. In control experiments, cell spreading was measured in the presence of mitomycin c (as indicated) at concentrations sufficient to inhibit cell division (Huh7 100nM/ HepG2 200nM).

3.3. Increased matrix stiffness promotes epithelial-mesenchymal transition in HCC cells

Confocal microscopy was employed to investigate the effect of changes in matrix stiffness on cytoskeletal organisation. Increasing matrix stiffness was associated with formation of prominent actin stress fibres terminating in mature (vinculin-positive) focal adhesions in both Huh7 and HepG2 cells (Figure 3.3). These features are absent in HCC cells cultured on 1kPa supports. In Huh7 cells stress fibres (green) terminate in discreet focal adhesions (red). This is less obvious in the smaller HepG2 cells that do not form prominent stress fibres. Co-localisation of actin-positive stress fibres and vinculin is indicated by overlapping (yellow) staining.

The appearance of stress fibres has been linked to the acquisition of a mesenchymal phenotype (epithelial-mesenchymal transition). To investigate this further, immunoblot analysis was performed against a panel of markers of epithelial-mesenchymal transition (Figure 3.4). HCC cells cultured on 12kPa supports showed upregulation of the mesenchymal markers N-cadherin (Huh7/ HepG2) and vimentin (Huh7) in comparison to cells maintained on 1kPa supports. HepG2 cells did not express vimentin under either condition. There was no difference in the expression of the epithelial marker E-cadherin. Huh7/ HepG2 cells maintained on 1kPa supports had higher expression of albumin, hepatocyte nuclear factor-4α (HNF4α), α1-antitrypsin and alpha-fetoprotein (AFP) than cells from stiff supports. Overall, the results suggest that alterations in environmental stiffness may be important in regulating differentiation in HCC cells. A soft environment, modelling the physical characteristics of the normal liver, promotes a differentiated hepatocyte phenotype. In contrast, increasing support stiffness is associated with loss of differentiated epithelial cell function and a transition towards a mesenchymal phenotype.

Figure 3.3: The effect of PA support stiffness on stress fibre and focal adhesion organisation in Huh7 and HepG2 cells

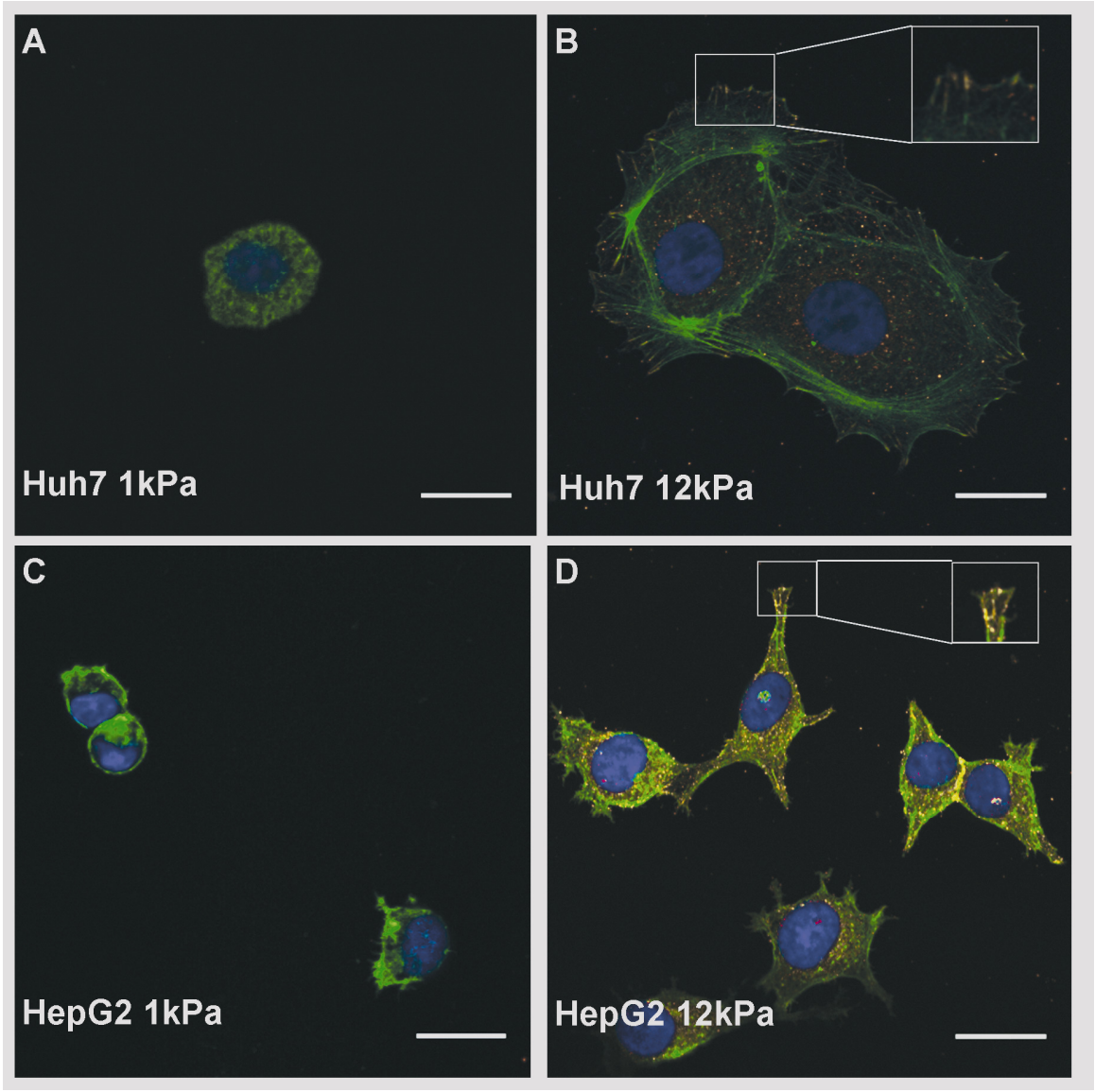

Figure 3.3: Confocal photomicrographs (x320 magnification) of (A/B) Huh7 and (C/D) HepG2 cells cultured on 1kPa and 12kPa collagen-I-coated PA supports, as indicated. Cells have been stained for the presence of actin stress fibres (phalloidin-green), mature focal adhesions (anti-vinculin-red) and nuclear DNA (4',6'-diamidino-2-phenyl-indole dihydrochloride (DAPI)-blue). The merged images are reconstructed from stacked images to demonstrate the spatial relationship between actin stress fibres and mature focal adhesions. Inserts show high magnification images of cells cultured on 12kPa supports, highlighting the insertion of stress fibres (green) into mature (vinculin-positive) focal adhesions (blue). This is less convincingly demonstrated in the HepG2 cells. In each image, the scale bar represents 20 microns.

Figure 3.4: Western blot analysis demonstrating the effect of changes in PA stiffness on Huh7/ HepG2 differentiation

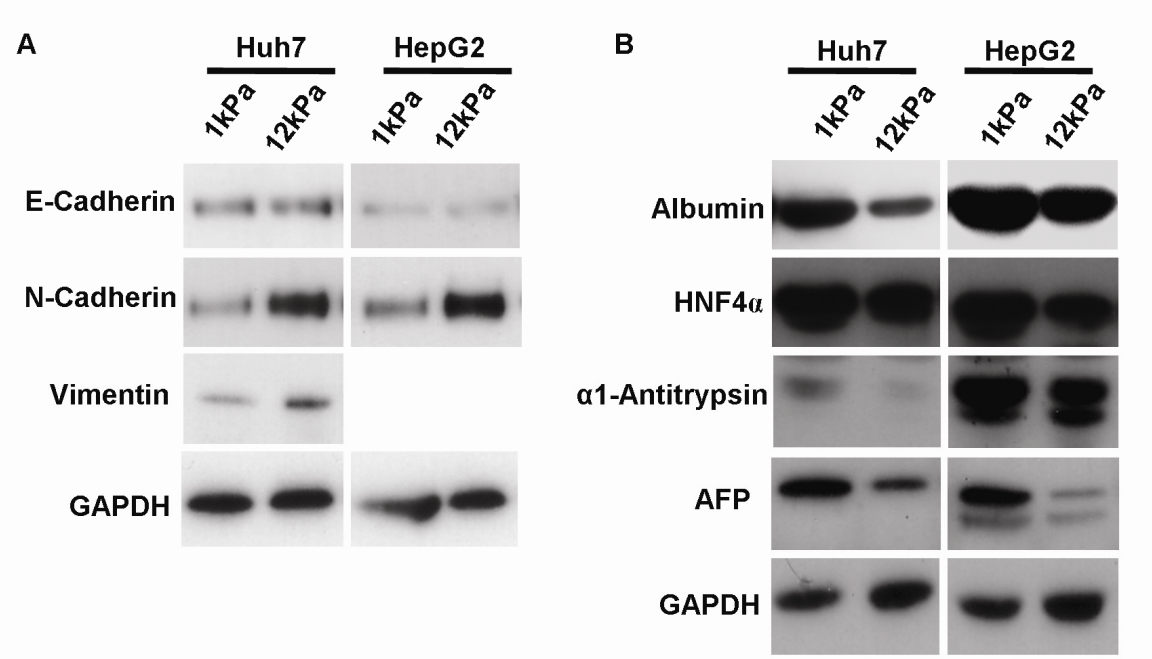

Figure 3.4: (A) Western blots from whole cell lysates showing expression of E-cadherin, N-cadherin and vimentin in Huh7/ HepG2 cells cultured on 1kPa and 12kPa collagen-I-coated PA supports (as indicated). (B) Western blots from whole cell lysates showing expression of albumin, HNF4α, α1-antitrypsin and AFP in Huh7/ HepG2 cells. In each Western blot equal quantities of protein were loaded and equal loading confirmed in relation to glyceraldehyde-3-phosphate dehydrogenase (GAPDH) expression. The immunoblots shown are representative examples from 3 independent experiments.

It has been proposed that epithelial-mesenchymal transition (EMT) is an important process in the development and progression of cancer. EMT is associated with alterations in cells that contribute to cell migration and metastasis (222). Transforming growth factor-β (TGFβ) has been implicated in both the initiation and maintenance of EMT (223). Experiments were therefore performed to investigate whether matrix stiffness regulated TGFβ-induced Smad signalling in HCC cells. Huh7 cells were plated on soft (1kPa) and stiff (12kPa) collagen-I-coated PA supports. After 48 hours of culture in low serum conditions, the cells were treated with TGFβ (5ng/ml). Cell lysates were then harvested for immunoblot analysis at baseline, 1 hour and 48 hours. Huh7 cells cultured on stiff supports demonstrated increased basal activity of the TGFβ signalling pathway, as indicated by increased Smad3 phosphorylation. Furthermore, following TGFβ stimulation there was enhanced Smad2 and Smad3 phosphorylation in cells from stiff supports. However,

densitometry analysis did not demonstrate any statistically significant difference between TGFβ-induced pSMAD2 and pSMAD3 (relative to GAPDH staining) on 1kPa and 12kPa supports at the time points analysed.

Figure 3.5: Time-course analysis of Smad2/3 signalling in response to TGFß stimulation as a function of PA support stiffness in Huh7 cells

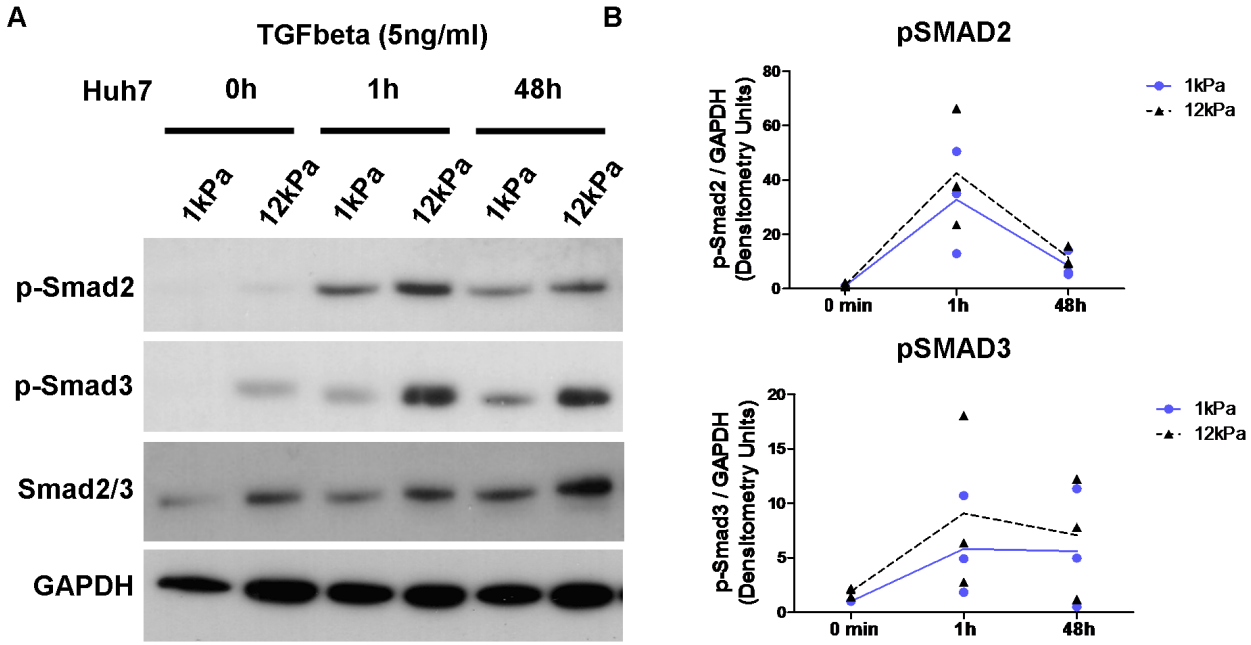

Figure 3.5: (A) Western blots from whole cell lysates of Huh7 cells showing the expression of phosph-Smad2, phospho-Smad3 and total Smad2/3 following stimulation with TGFβ (5ng/ml). In each Western blot, equal quantities of protein were loaded and equal loading was confirmed in relation to GAPDH expression. The Western blots shown are representative examples from 3 independent experiments. (B) Line graphs showing schematic representation of phosphorylated Smad2 and Smad3, expressed relative to GAPDH. Each line represents the mean of 3 independent experiments. The dot plots show the densitometry values of pSMAD2 and pSMAD3 staining relative to GAPDH in individual experiments (blue circles – 1kPa / black triangles – 12kPa). There were no significant differences between TGFβ-induced pSMAD2 and pSMAD3 upregulation on the 1kPa and 12kPa supports (unpaired student t-test).

3.4. Increased matrix stiffness promotes proliferation in HCC cells

In both Huh7 and HepG2 cells, increases in matrix stiffness regulate cell proliferation (Figure 3.6). The proliferative index of HCC cells was assessed by nuclear localisation of Ki67 antigen. The proliferative index of HCC cells increased as a function of increasing support stiffness. The proliferative index (value ±SEM) for Huh7 cells on supports of different stiffness were: 1kPa, 0.220 ± 0.015; 2.5kPa, 0.477 ± 0.035; 12kPa, 0.587 ± 0.007; and glass, 0.687 ± 0.028. The proliferative index (value ±SEM) for HepG2 cells on supports of different stiffness were: 1kPa, 0.054 ± 0.003; 2.5kPa, 0.557 ± 0.008; 12kPa, 0.156 ± 0.003; and glass, 0.692 ± 0.011. In Huh7 and HepG2 cells respectively, the proliferative index was 2.7-fold ($p<0.001$) and 12.2-fold ($p<0.001$) higher when cells were cultured on 12kPa versus 1kPa supports. Mean measurements were compared using an unpaired student t test (n=3). Maximal proliferation was observed when cells were cultured on collagen-I-coated glass. However, the major part of the observed increase in cell proliferation occurred across a pathophysiological range of stiffness values, as would be encountered by cells during the development of liver fibrosis. In parallel experiments, Huh7 and HepG2 cells were cultured on PA supports of defined stiffness (1-12kPa) for 5 days at identical initial plating density. MTT assay confirmed that there was an increase in total cell number/ viability as a function of increasing support stiffness. The absorbance measurement (580nm) was standardised to the value obtained in experiments conducted on 1kPa supports. In Huh7 cells the absorbance ratios (value ± SEM) were: 1kPa, 1.000 ± 0.034; 2.5kPa, 1.600 ± 0.072; 12kPa, 1.480 ± 0.052; and glass, 2.047 ± 0.106. In HepG2 cells the absorbance ratios (value ± SEM) were: 1kPa, 1.000 ± 0.037; 2.5kPa, 1.384 ± 0.135; 12kPa, 1.702 ± 0.136; and glass, 1.802 ± 0.143. Mean measurements were compared using an unpaired student t test (n=9).

Figure 3.6: The effect of changes in PA support stiffness on proliferation in Huh7 and HepG2 cells

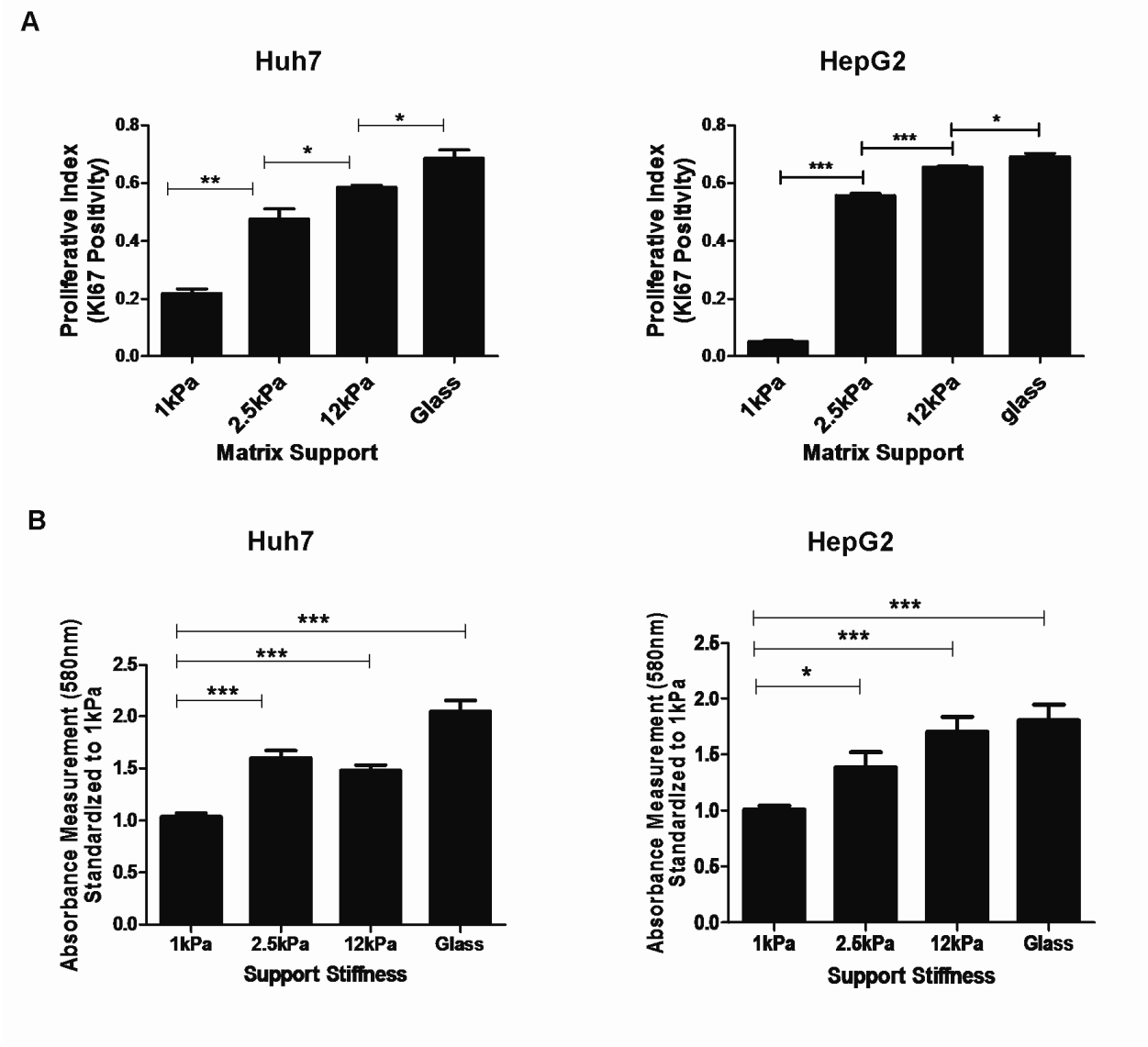

Figure 3.6: (A) Bar graphs showing the mean proliferative index (Ki67 positivity) of Huh7 and HepG2 cells cultured on collagen-I-coated PA supports across a pathophysiologically-relevant range (1-12kPa), as indicated, and collagen-I-coated glass (n=3). Mean measurements from 3 experiments were compared using an unpaired student t test. The cell counting data from which these graphs are derived is from presented in Appendix 7. (B) Bar graphs showing MTT assay measurements (representative of total cell number/ viability) of Huh7 and HepG2 cells cultured for 5-days on collagen-I-coated PA supports and collagen-I-coated glass (n=9). Mean measurements from 9 experiments (n=9) were compared using an unpaired student t test. Error bars are SEM, *p<0.05, **p<0.01 and ***p<0.001.

Experiments were also performed to investigate whether the effect of cell plating density on the stiffness-dependent regulation of cell proliferation (Figure 3.7). In both Huh7 and HepG2 cells, differences in proliferative index (Ki67-positivity) as a function of matrix stiffness were seen across a wide-range of plating densities (1000-25000 cells/cm^2). The values for proliferative index (value ± SEM) for Huh7 cells at different plating densities were: 1000 cells/mm^2, 1kPa 0.175 ±0.025/ 12kPa 0.368 ±0.024; 5000 cells/mm^2, 1kPa 0.106 ±0.019/ 12kPa 0.442 ±0.044; and 25000 cells/mm^2, 1kPa 0.210 ±0.028/ 12kPa 0.533 ±0.003. The values for proliferative index (value ± SEM) for HepG2 cells at different plating densities were: 1000 cells/mm^2, 1kPa 0.161 ±0.032/ 12kPa 0.595 ±0.028; 5000 cells/mm^2, 1kPa 0.250 ±0.031/ 12kPa 0.672 ±0.007; and 25000 cells/mm^2, 1kPa 0.332 ±0.014/ 12kPa 0.639 ±0.024.

Figure 3.7: The effect of cell plating density on the stiffness-dependent regulation of Huh7/ HepG2 cell proliferation

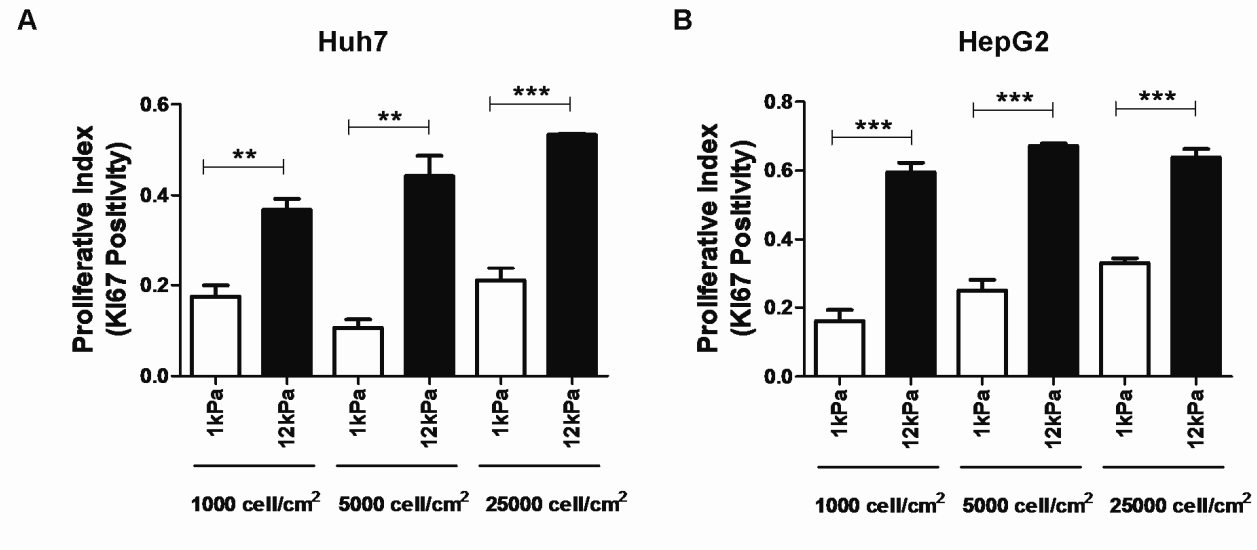

Figure 3.7: Graphs showing the effect of initial cell plating density on the mean proliferative index (Ki67-positivity) of (A) Huh7 and (B) HepG2 cells cultured on 1kPa (white) and 12kPa (black) collagen-I-coated PA supports. In these experiments, both Huh7 and HepG2 cells were plated at 3 initial plating densities (1000-25000 cells/cm^2), as indicated. The proliferative index was calculated following 48 hours culture (n=3 for each condition). Mean measurements were compared using an unpaired student t test. Error bars represent SEM, **p<0.01 and ***p<0.001. The cell counting data from which these graphs are derived is presented in Appendix 8.

Experiments were subsequently performed to investigate whether differences in the biochemical composition of the ECM altered the fundamental relationship between cell proliferation and support stiffness. This was necessary in order to exclude the possibility of a specific effect related to collagen-I. Both Huh7 and HepG2 cells were therefore cultured on PA supports coated with a range of matrix proteins including: collagen-I, collagen-IV, laminin and fibronectin. In both cell types, minor differences were observed in respect to cellular morphology and spreading between supports of defined stiffness coated with different matrix proteins (Figure 3.8). In Huh7 cells the values for projected surface area (value ± SEM) for the different support stiffness and matrix proteins were: collagen-1, 1kPa 829 ± 61μm^2/ 12kPa 1556 ± 92μm^2; collagen-IV, 1kPa 970 ± 62μm^2/ 12kPa 2109 ± 128μm^2; laminin, 1kPa 1007 ± 51μm^2/ 12kPa 2632 ± 151μm^2; and fibronectin, 1kPa 1038 ± 59μm^2/ 12kPa 1604 ± 125μm^2. In HepG2 cells the values for projected surface area (value ± SEM) for the different support stiffness and matrix proteins were: collagen-1, 1kPa 377 ± 24μm^2/ 12kPa 501 ± 36μm^2; collagen-IV, 1kPa 327 ± 20μm^2/ 12kPa 569 ± 29μm^2; laminin, 1kPa 283 ± 18μm^2/ 12kPa 667 ± 32μm^2; and fibronectin, 1kPa 214 ± 13μm^2/ 12kPa 381 ± 28μm^2.

Figure 3.8: The effect of ECM composition on Huh7/ HepG2 cell spreading on ligand-coated PA supports

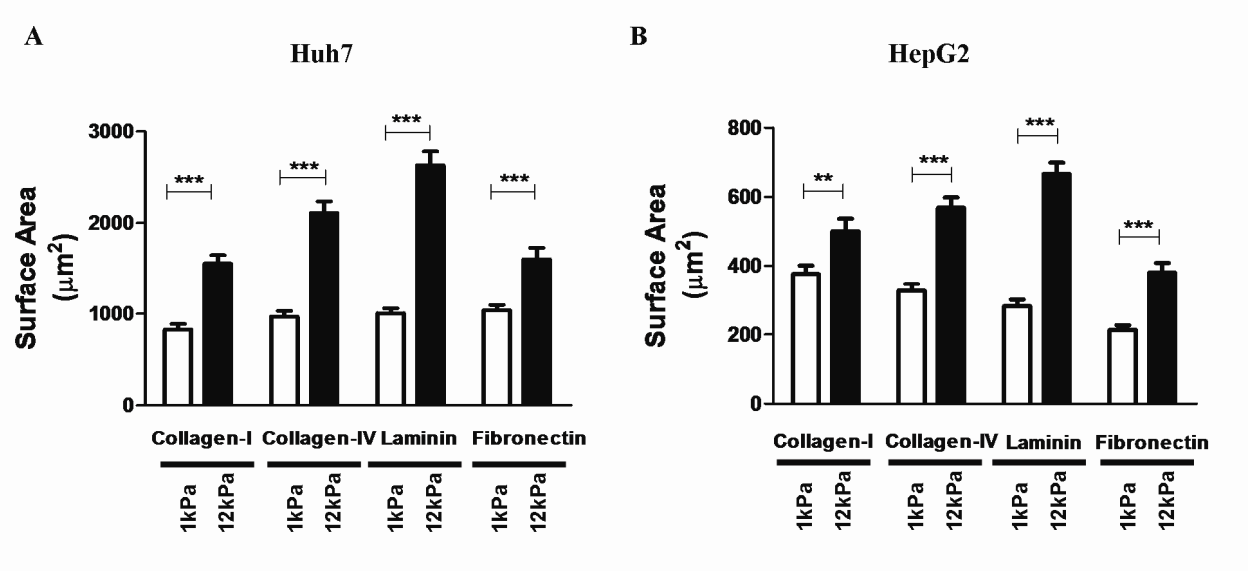

Figure 3.8: The effect of ECM composition on HCC cell spreading. Graphs showing the projected surface area (square microns) of (A) Huh7 and (B) HepG2 cells cultured on 1kPa (white) and 12kPa (black) PA supports coated with collagen-I, collagen-IV, laminin and fibronectin (as indicated). Projected surface area was calculated by digital image analysis of phase contrast images. In each case the bars represent the mean (±SEM) of measurements from 50 cells (n=50) randomly selected from photomicrographs of cells cultured from PA gels in three independent experiments. Mean measurements were compared using an unpaired student t test. Error bars represent SEM, **p<0.01 and ***p<0.001.

The biochemical composition of the surface ligand did not significantly alter the stiffness-dependent regulation of cell proliferation (Figure 3.9). Across the range of matrix proteins tested, it was the physical rather than the biochemical properties of the PA gels that exerted the predominant effect on cell proliferation. In Huh7 cells the values for proliferative index (value ± SEM) for the different support stiffness and matrix proteins were: collagen-1, 1kPa 0.297 ± 0.030/ 12kPa 0.659 ± 0.026; collagen-IV, 1kPa 0.251 ± 0.046/ 12kPa 0.637 ± 0.017; laminin, 1kPa 0.316 ± 0.017/ 12kPa 0.774 ± 0.022; and fibronectin, 1kPa 0.283 ± 0.001/ 12kPa 0.762 ± 0.031. In HepG2 cells the values for proliferative index (value ± SEM) for the different support stiffness and matrix proteins were: collagen-1, 1kPa 0.128 ± 0.001/ 12kPa 0.641 ± 0.006; collagen-IV, 1kPa 0.105 ± 0.005/ 12kPa 0.637 ± 0.008; laminin, 1kPa 0.111 ± 0.005/ 12kPa 0.642 ± 0.008; and fibronectin, 1kPa 0.156 ± 0.007/ 12kPa 0.651 ± 0.007.

Figure 3.9: The effect of ECM composition on Huh7/ HepG2 proliferation on ligand-coated PA supports

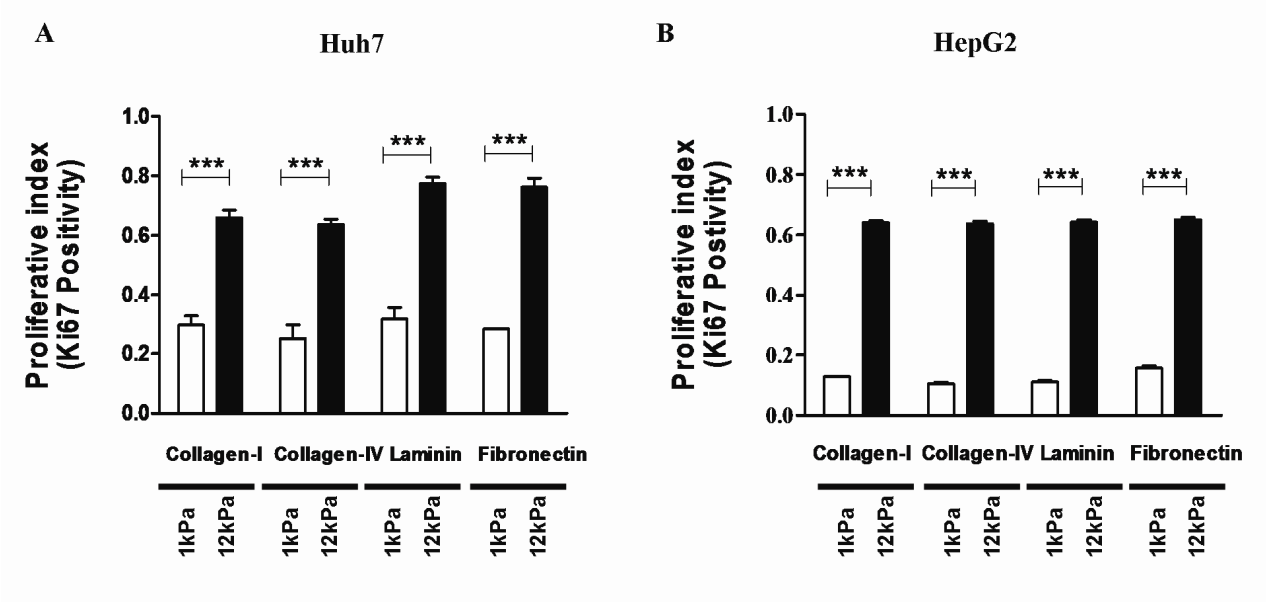

Figure 3.9: The effect of ECM composition on HCC cell proliferation as a function of support stiffness. Graphs showing the mean proliferative index (Ki67-positivity) of (A) Huh7 and (B) HepG2 cells on 1kPa (white) and 12kPa (black) PA supports coated with collagen-I, collagen-IV, laminin and fibronectin (n=3). Mean measurements were compared using an unpaired student t test. Error bars represent SEM, **p<0.01 and ***p<0.001. The cell counting data from which these graphs are derived is presented in Appendix 8.In each case error bars represent SEM and ***p<0.001. The cell counting data from which these graphs are derived is presented in Appendix 9.

It was my hypothesis that stiffness-dependent regulation of cell proliferation may be a fundamental mechanism in promoting tumour development across a range of epithelial malignancies. Experiments were therefore performed to establish the effect of changes in support stiffness on cell morphology and proliferation across a range of epithelial cancer cell lines, including prostate, breast and lung adenocarcinoma cell lines (Figure 3.10). In each case, increasing matrix stiffness promoted enhanced cell spreading and proliferation.

In respect to cell spreading, the values (mean ± SEM) for projected surface area between 1kPa and 12kPa supports in different cell lines were: LNCAP, 1kPa 225 ± 12μm^2/ 12kPa 451 ± 15μm^2; A549, 1kPa 183 ± 9 μm^2/ 12kPa 530 ± 31μm^2; MCF7, 1kPa 223 ± 10μm^2/12kPa 687 ± 63μm^2; MDA, 1kPa 301 ± 13μm^2/ 12kPa 881 ± 50μm^2; HepG2, 1kPa 322 ± 18μm^2/ 12kPa 648 ± 34μm^2; and Huh7, 1kPa 869 ± 134μm^2/ 12kPa 1413 ± 85μm^2.

In respect to proliferation, the values (mean ± SEM) for proliferative index between 1kPa and 12kPa supports in different cell lines were: LNCAP, 1kPa 0.144 ± 0.036/ 12kPa 0.687 ± 0.086; A549, 1kPa 164 ± 0.008/ 12kPa 0.783 ± 0.058; MCF7, 1kPa 0.147 ± 0.037/12kPa 0.793 ± 0.416; MDA, 1kPa 0.083 ± 0.011/ 12kPa 0.650 ± 0.021; HepG2, 1kPa 0.054 ± 0.003/ 12kPa 0.656 ± 0.003; and Huh7, 1kPa 0.220 ± 0.015/ 12kPa 0.587 ± 0.007.

Figure 3.10: The effect of PA support stiffness on cellular spreading and proliferations in a range of epithelial cancer cell lines

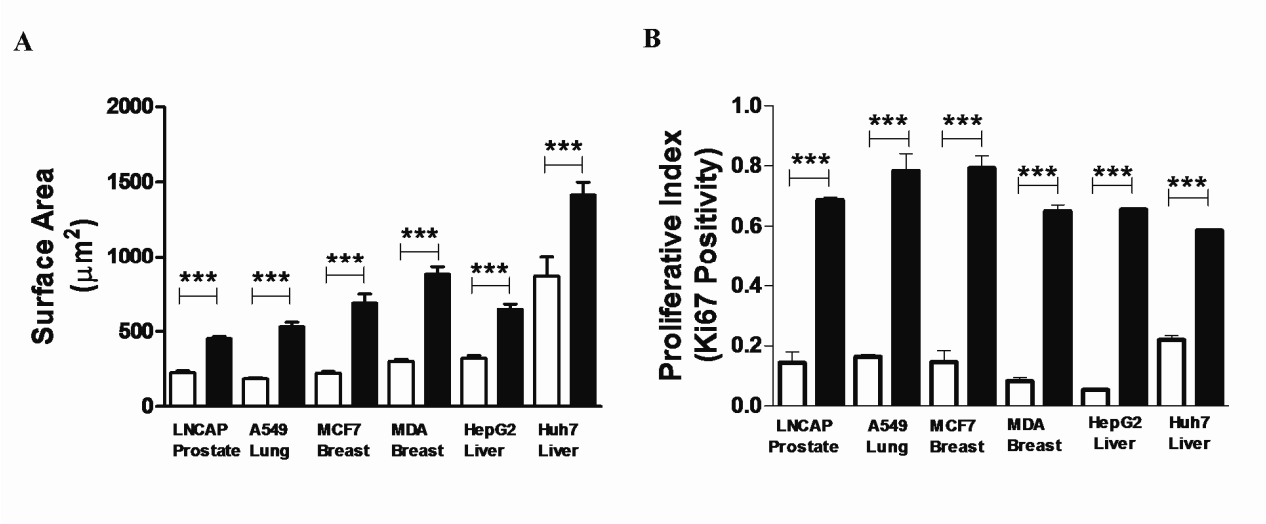

Figure 3.10: (A) Graph showing the effect of changes in PA support stiffness on cell spreading in LNCap (prostate), A549 (lung adenocarcinoma), MCF7 (breast), MDA (breast), HepG2 (HCC) and Huh7 (HCC) epithelial cancer cells. Cancer cells were cultured on 1kPa (white) or 12kPa (black) collagen-I-coated PA supports. Cell spreading (projected surface area) was calculated by digital image analysis of phase contrast images. In each case, the bars represent the mean (±SEM) of measurements from 50 cells (n=50) randomly selected from photomicrographs of cells cultured from PA gels in three independent experiments. Mean measurements were compared using an unpaired student t test (n= 50). (B) Graph showing the mean proliferative index (Ki67-positivity) of human epithelial cancer cell lines as a function of PA support stiffness (as detailed above). In each case, values represent the mean (±SEM) of measurements from three independent experiments. Mean measurements (n=3) were compared using an unpaired student t test (***$p<0.001$). The cell counting data from which these graphs are derived is presented in Appendix 10.

3.5 The effect of matrix stiffness on cell cycle regulation in HCC cells

Having established that physiological changes in matrix stiffness regulate HCC cell proliferation, experiments were undertaken to investigate the effect of changes in matrix stiffness on the expression of cell cycle regulators of G1 progression (Figure 3.11). Immunoblot analysis revealed a strong reduction in the expression of cyclin D1 and cyclin-D3 in Huh7/ HepG2 cells cultured on 1kPa versus 12kPa supports. The reduction in cell proliferation seen in Huh7 and HepG2 cells maintained on 1kPa supports was not accompanied by upregulation of the cyclin-dependent kinase inhibitors $p21^{cip}$ or $p27^{kip}$. Indeed, a modest downregulation of $p27^{kip}$ was observed for both cell lines when maintained on 1kPa versus 12kPa supports. Overall, the results suggest that physiological stiffness (modelling that encountered in the normal liver) is inhibitory to cell cycle progression. Conversely, increased matrix stiffness promotes G1 progression with an associated increased in cyclin D1/D3 expression. Induction of terminal senescence on 1kPa supports was excluded by showing that on transfer to a stiff environment (tissue culture plastic) cells resumed proliferation to levels comparable to cells initially cultured on 12kPa supports (Figure 3.12). In Huh7 cells, the values for proliferative index on tissue culture plastic (value ± SEM) for cells pre-cultured on 1kPa and 12kPa supports were: 1kPa, 0.645 ± 0.019 and 12kPa, 0.631 ±0.033, $p = 0.73$). In HepG2 cells, the values for proliferative index on tissue culture plastic (value ± SEM) for cells pre-cultured on 1kPa and 12kPa supports were: 1kPa, 0.639 ± 0.012 and 12kPa, 0.608 ±0.026, $p = 0.34$). The differences between mean values for proliferative index in each cell type were compared using an unpaired student t-test (n=3).

Figure 3.11: The effect of changes in matrix stiffness on cell cycle regulator expression

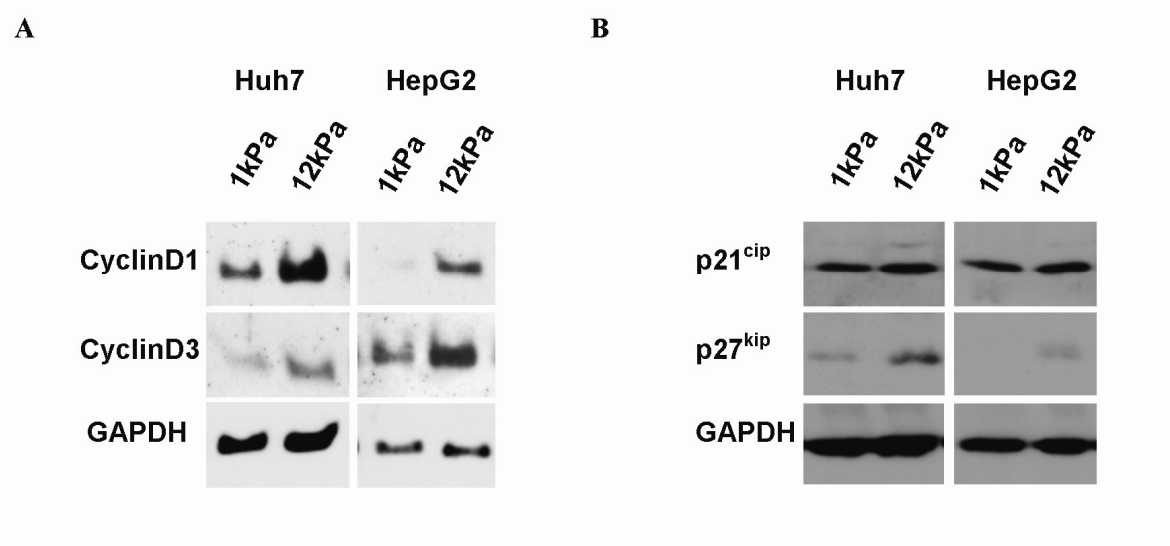

Figure 3.11: Western blots from whole cell lysates showing expression of (A) Type D cyclins (cyclin D1 and D3) and (B) cyclin-dependent kinase inhibitor ($p21^{cip}$/ $p27^{kip}$) in Huh7 and HepG2 cells cultured on soft (1kPa) and stiff (12kPa) supports, as indicated. In each Western blot, equal quantities of protein were loaded and equal loading confirmed in relation to GAPDH expression. The immunoblots displayed are representative examples from 3-6 experiments.

Figure 3.12: The reduction in cell proliferation observed in cells cultured on soft PA supports is reversible on transfer to a stiff substrate

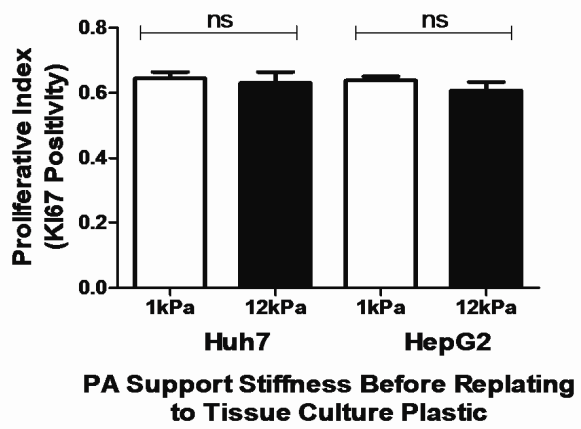

Figure 3.12: Graph showing the mean proliferative index (Ki67-positivity) of Huh7 and HepG2 cells re-plated to tissue culture plastic following 5-days culture on either 1kPa (white) or 12kPa (black) collagen-I-coated PA supports (n=3). Proliferative index (Ki67-postive cells/ total cells) was measured 2-days after re-plating. In each case, error bars represent SEM. Mean measurements (n=3) were compared using an unpaired student t test (ns indicates lack of statistical significance). Upon transfer to stiff tissue culture plastic, HCC cells initially cultured on a 1kPa support resume proliferation to levels comparable to cells coming from a 12kPa support. The cell counting data from which these graphs are derived is presented in Appendix 11.

3.6 Changes in matrix stiffness regulate morphology and proliferation in primary murine hepatocytes

Experiments were conducted with primary hepatocytes to investigate the effect of changes in support stiffness on cellular morphology and proliferation. Primary hepatocytes cultured on stiff supports showed morphological features of de-differentiation with acquisition of a mesenchymal morphology with prominent cell processes, in contrast to the more polygonal morphology of cells maintained on 1kPa supports. There was a trend towards increased proliferation of hepatocytes when cultured on 12kPa versus 1kPa supports, but this result was not statistically significant (Figure 3.13). The values for the number of Ki67-positive hepatocytes per low power field (value ± SEM) on 1kPa and 12kPa supports were: 1kPa, 1.10 ± 0.22 and 12kPa, 2.50 ± 0.60, p=0.09).

Figure 3.13: The effect of PA support stiffness on cell morphology and proliferation in primary murine hepatocytes

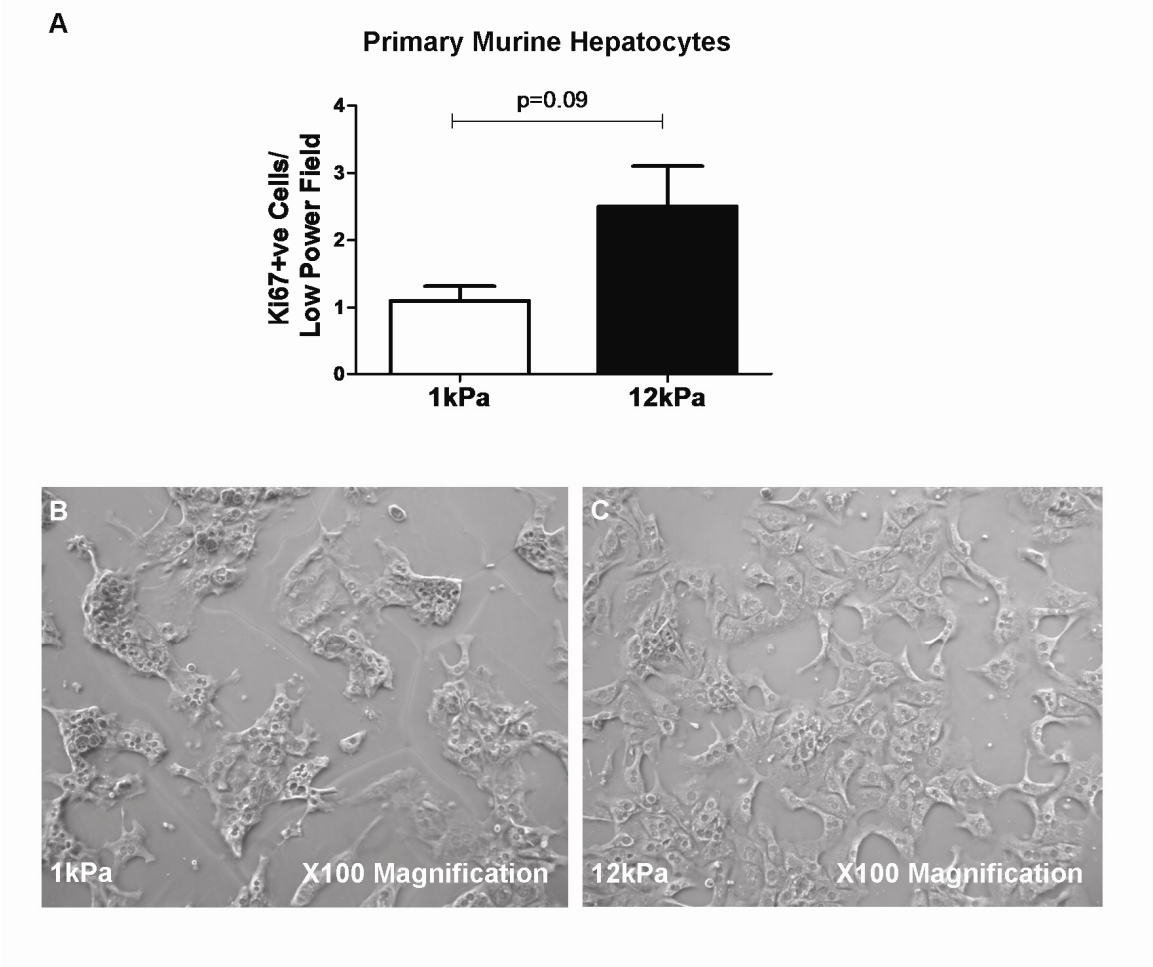

Figure 3.13 Primary murine hepatocytes were cultured on 1kPa (white) and 12kPa (black) collagen-I-coated PA supports. The bar graph (A) shows the effect of matrix stiffness on the proliferation of primary murine hepatocytes. Proliferation was assessed by the mean number of Ki67 positive cells per low power field after 48 hours in culture. Mean measurements (n=3) were compared using an unpaired student t test. Error bars are SEM, p values are as indicated. The photomicrographs displayed show phase contrast images of primary murine hepatocytes cultured on (B) 1kPa and (C) 12kPa supports.

3.7 Matrix stiffness regulates basal and HGF-induced signalling responses

It has previously been demonstrated that increasing matrix stiffness promotes growth factor-induced ERK activation in an *in vitro* model of murine mammary cancer (155). Experiments were therefore undertaken to determine whether matrix stiffness might regulate growth factor-induced mitogenic signalling in HCC cells. Huh7 and HepG2 cells were cultured on 1kPa and 12kPa collagen-I-coated PA supports for 24 hours in low serum conditions. Western blot analysis of whole cell lysates was then undertaken to investigate stiffness-dependent differences in the basal activity of critical mitogenic pathways, including FAK, STAT3 and PKB/Akt. In comparison to cells maintained on 1kPa supports, HCC cells cultured on 12kPa supports demonstrated increased basal levels of FAK, STAT3 and PKB/Akt phosphorylation (Figure 3.14 A).

Subsequent experiments were undertaken to investigate whether matrix stiffness modulates cyclin D1 expression following hepatocyte growth factor (HGF) stimulation. Huh7 and HepG2 cells were cultured on 1kPa and 12kPa PA supports for 24 hours in the presence or absence of HGF (10ng/ml). Western blot analysis was then used to assess cyclin D1 expression. In each cell type, HGF stimulation was associated with increased cyclin D1 expression, but the magnitude of cyclin D1 upregulation was substantially higher in cell cultured on 12kPa supports (Figure 3.14 B).

Figure 3.14: The effect of matrix stiffness on mitogenic signalling in Huh7 and HepG2 cells

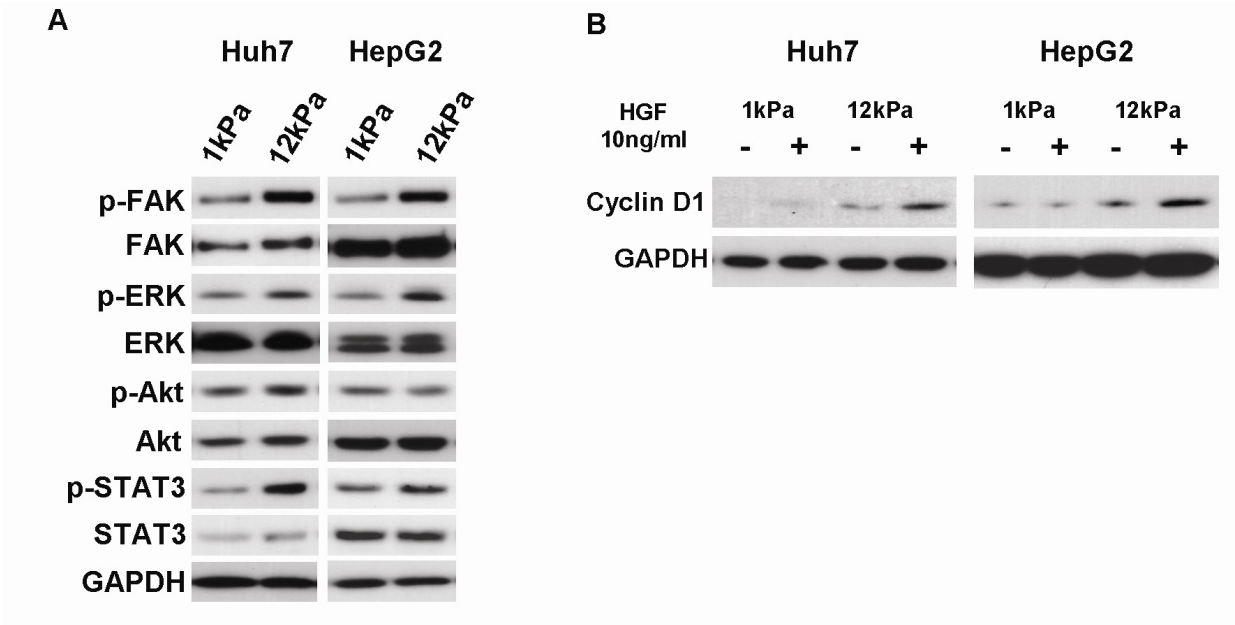

Figure 3.14: (A) Western blots showing basal expression of phosphorylated and total focal adhesion kinase (FAK), extracellular-regulated kinase (ERK), protein kinase B (PKB/Akt) and signal transducer and activator of transcription 3 (STAT3) in Huh7 and HepG2 cells cultured for 24 hours in low serum conditions on 1kPa and 12kPa collagen-I-coated PA supports, as indicated. (B) Western blots showing cyclin D1 expression in Huh7 and HepG2 cells cultured for 24 hours on PA supports (1-12kPa) in the presence (+) and absence (-) of HGF (10ng/ml).

Experiments were then performed to investigate how support stiffness might regulate growth factor-induced mitogenic signalling in response to HGF stimulation. HCC cells were cultured on 1kPa and 12kPa supports for 24 hours and then subjected to HGF stimulation (10ng/ml). An increase in the magnitude of ERK, STAT3 and PKB/Akt phosphorylation following HGF stimulation was observed in both Huh7 (Figure 3.15) and HepG2 cells (Figure 3.16) cultured on 12kPa versus 1kPa supports. These results would suggest that the mechanical properties of a cells environment regulate its response to a defined biochemical stimulus.

Figure 3.15: The effect of matrix stiffness on HGF-induced mitogenic signalling in Huh7 cells

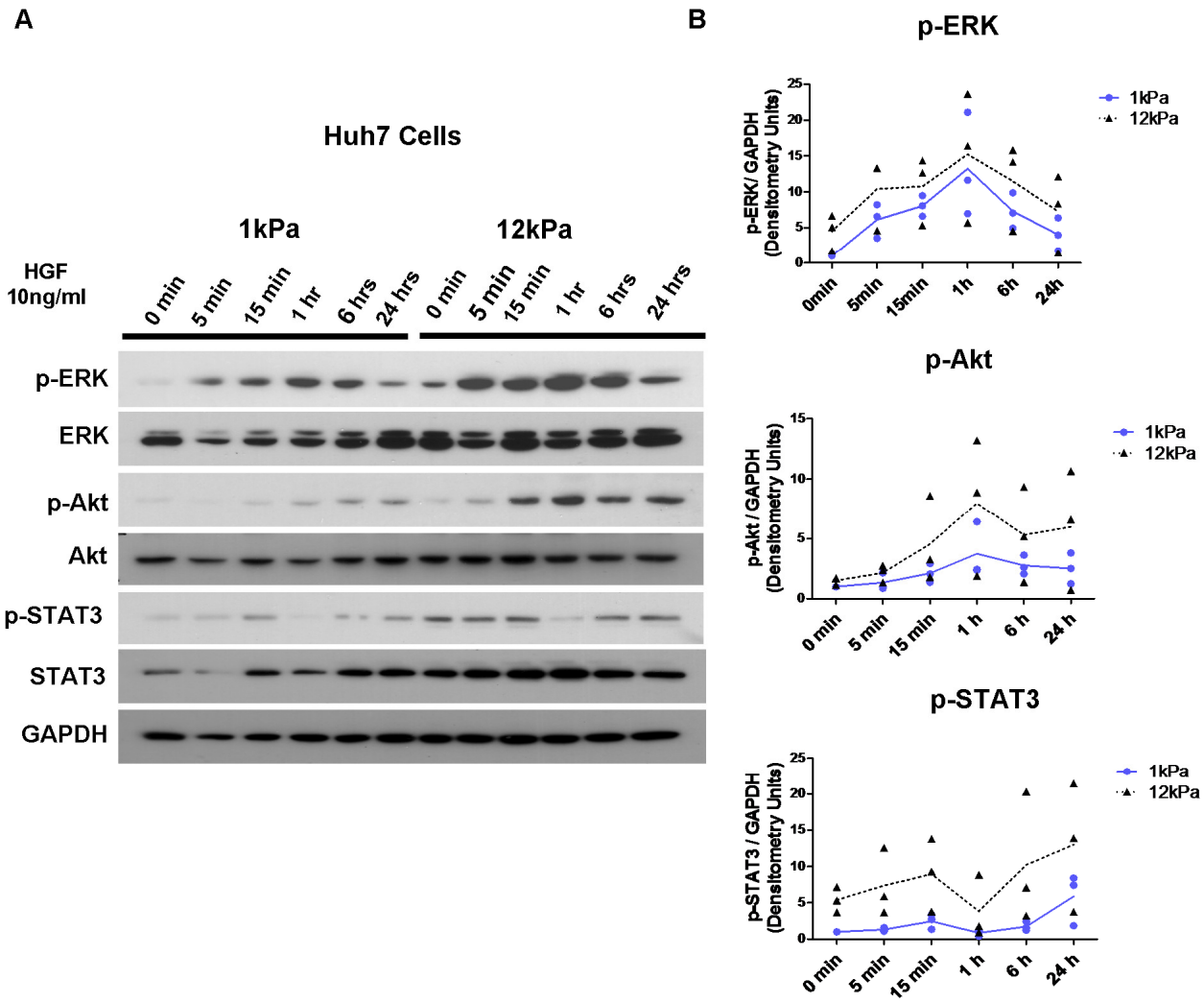

Figure 3.15: Western blots showing a time-course analysis for expression of phosphorylated and total ERK, PKB/Akt and STAT3 in Huh7 cells cultured on 1kPa and 12kPa collagen-I-coated PA supports. Whole cell lysates were harvested at baseline and specific time points (as indicated) following the addition of HGF (10ng/ml) to culture media. The line graphs (right panel) showing densitometry analysis of phosphorylated ERK, PKB/Akt and STAT3 expression relative to GAPDH. Individual replicates are represented as blue circles (1kPa) and black triangles (12kPa). The line (blue continuous- 1kPa/ black dotted- 12kPa) represents the mean of the 3 independent experiments (n=3). At each time point, there was no significant difference between pSMAD2 and pSMAD3 expression (relative to GAPDH) between 1kPa and 12kPa supports (unpaired student t-test).

Figure 3.16: The effect of matrix stiffness on HGF-induced mitogenic signalling in HepG2 cells

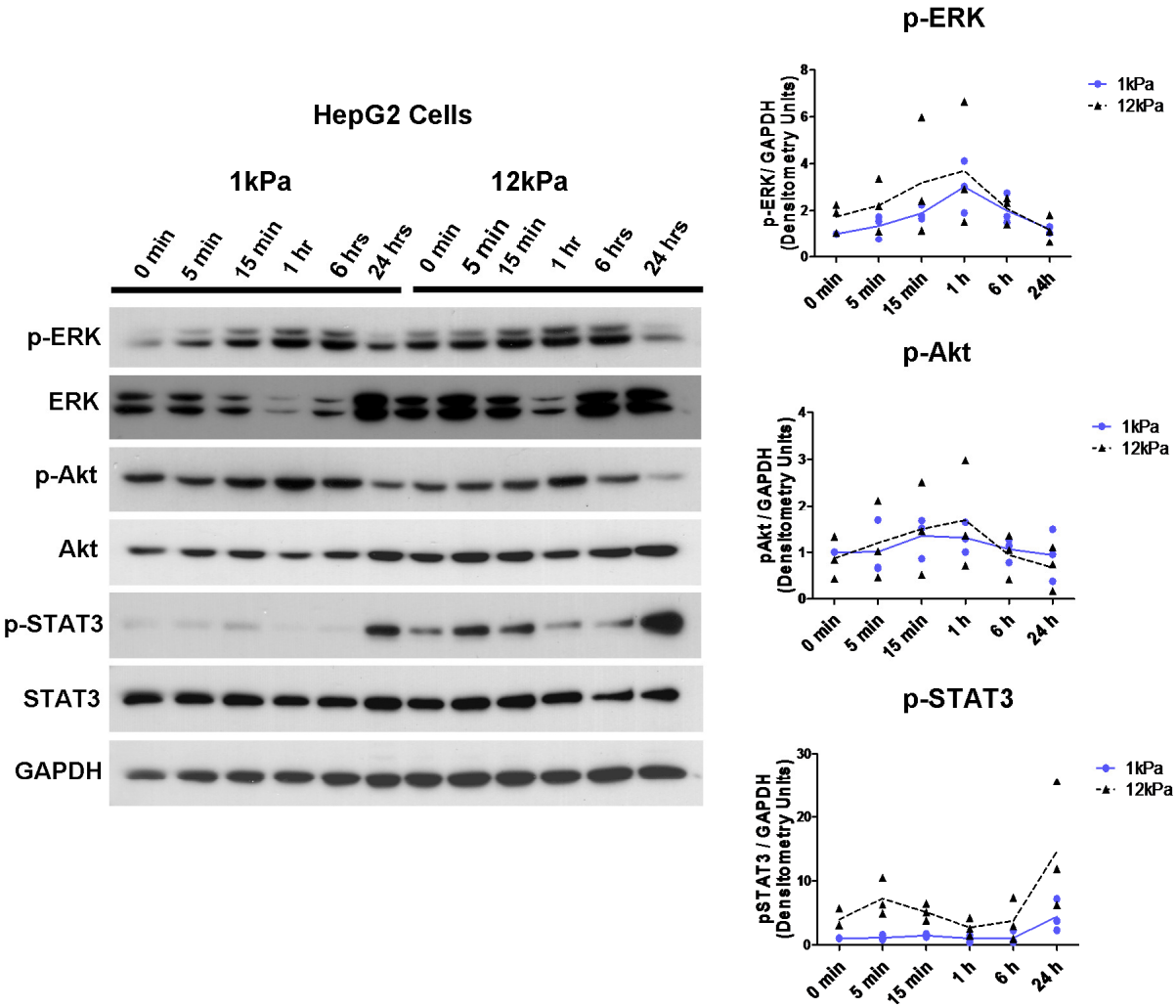

Figure 3.16: (A) Western blots showing a time-course analysis for expression of phosphorylated and total ERK, PKB/Akt and STAT3 in HepG2 cells cultured on 1kPa and 12kPa collagen-I-coated PA supports. Whole cell lysates were harvested at baseline and specific time points (as indicated) following the addition of HGF (10ng/ml) to culture media. (B) The line graphs (right panel) showing densitometry analysis of phosphorylated ERK, PKB/Akt and STAT3 expression relative to GAPDH. Individual replicates are represented as blue circles (1kPa) and black triangles (12kPa). The line (blue continuous- 1kPa/ black dotted- 12kPa) represents the mean of the 3 independent experiments (n=3). At each time point, there was no significant difference between pSMAD2 and pSMAD3 expression (relative to GAPDH) between 1kPa and 12kPa supports (unpaired student t-test).

3.8 Beta-1 integrin and phospho-FAK^{Tyr397} are expressed in human HCC and regulate the proliferation of HCC cells *in vitro*

FAK, the canonical mediator of integrin-based signalling, is implicated in multiple aspects of cancer development. FAK activation has been linked to the modulation of multiple downstream signalling pathways including ERK, PKB/ Akt, Rho and Rac (177, 224). Experiments were undertaken to investigate the prevalence of β1-integrin and phospho-FAK^{Tyr397} expression in HCC specimens. Immunohistochemistry studies were performed on an unselected cohort of 15 human HCC specimens (Tayside Tissue Bank), obtained at the time of tumour resection or biopsy (Figure 3.17). β1-integrin was expressed in 15/15 of the specimens tested. There was increased phospho-FAK^{Tyr397} staining in tumour tissue, relative to the surrounding liver parenchyma in 8/15 (53%) of the HCC specimens. These results are consistent with published histological studies that have analysed patterns of β1-inetgrin and FAK expression in HCC (225, 226).

Figure 3.17: The expression of β1-integrin and phospho-FAK^{Tyr397} in human HCC specimens

A

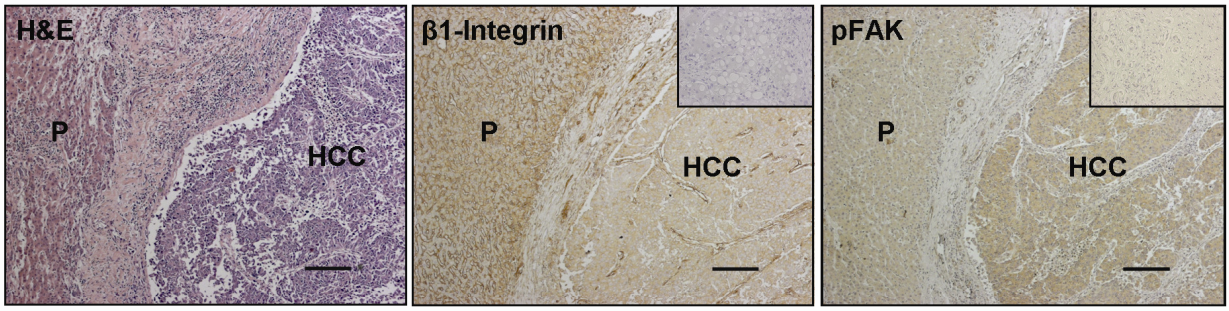

B

	Number of Positive HCC Samples	Number of Negative HCC Samples	Indeterminate	Percentage Positive (%)
β1-Integrin	15	0	0	100
Phospho-FAK	8	4	3	53

Figure 3.17: β1 Integrin and phospho-FAK^{Tyr397} are expressed in human HCC specimens. (A) Low lower (x50 magnification) photomicrographs of HCC specimens stained with haematoxylin and eosin (left panel), anti-β1-integrin (centre panel) and anti-phospho-FAK^{Tyr397} (right panel). Negative control (isotype) staining is represented by the indented images in the top right corner of each image. β1-integrin is expressed in both the tumour tissue (HCC) and surrounding normal parenchyma. Phospho-FAK^{Tyr397} is strongly expressed in the tumour tissue relative to parenchyma (P). Scale bar represents 200 microns. (B) Table showing the prevalence of β1-integrin and phospho-FAK^{Tyr397} immunostaining in HCC tumour tissue in a cohort of human HCC resection/ biopsy specimens (n=15).

Experiments were subsequently conducted to determine the effect of inhibition of β1-integrin and FAK function on the proliferation of Huh7 and HepG2 cells *in vitro*. β1-integrin was disrupted using a function blocking anti-β1-integrin antibody (6S6) and the dysintegrin, echistatin (Figure 3.18). Treatment with both the anti-β1-integrin (6S6) and echistatin promoted cellular rounding in Huh7 and HepG2 cells cultured on collagen-I-coated 12kPa PA supports. Cell proliferation was assessed by determination of proliferative index after Ki67 immunohistochemistry (Ki67-positivity).

In Huh7 cells (Figure 3.18A), the values for proliferative index (value ±SEM) under each experimental condition were: untreated control, 0.413 ± 0.019; isotype control, 0.426 ± 0.026; echistatin (100nM), 0.293 ± 0.060; and 6S6 (50μg/ml), 0.265 ± 0.043. Huh7 proliferation was reduced by treatment with both 6S6 antibody (38% reduction, $p<0.05$) and echistatin (29% reduction, $p=0.07$) relative to relevant controls.

In HepG2 cells (Figure 3.18B), the values for proliferative index (value ±SEM) under each experimental condition were: untreated control, 0.624 ± 0.010; isotype control, 0.658 ± 0.024; echistatin (100nM), 0.495 ± 0.022; and 6S6 (50μg/ml), 0.078 ± 0.019. In HepG2 cells, cell proliferation was reduced by both 6S6 antibody (92% reduction, $p<0.001$) and echistatin (21% reduction, $p<0.01$).

The effect of FAK on HCC cell proliferation was investigated in experiments conducted with the small molecular FAK inhibitor PF573228. PF573228 binds to the ATP-binding pocket of FAK and effectively blocks FAK catalytic activity (227). Treatment of cells with PF573228 inhibits the auto-phosphorylation of tyrosine 397 and downstream activities of FAK. There are conflicting reports as to the effect of FAK inhibition on cancer cell proliferation (227-229).

Treatment of Huh7 and HepG2 cells with PF537228 (1-5μM) resulted in a demonstrable reduction on FAK phosphorylation at tyrosine 397 (Figure 3.18C). Similarly, treatment of both Huh7 and HepG2 cells with PF537228 (1-5μM) was associated with a reduction in cell proliferation. In Huh7 cells under each experimental condition (Figure 3.18A), the values for proliferative index (value ± SEM) were: DMSO control, 0.393 ± 0.035; PF537228 (1μM), 0.338 ± 0.033; and PF537228 (5μM), 0.228 ±0.026. In HepG2 cells under each experimental condition (Figure 3.18B), the values for proliferative index (value ± SEM) were: DMSO control, 0.680 ± 0.021; PF537228 (1μM), 0.465 ± 0.010; and PF537228

(5μM), 0.373 ±0.013. Treatment of cells cultured on 12kPa supports with PF563228 (Figure 3.18) at a concentration of 5μM was associated with a reduction in proliferation for both Huh7 (42% reduction, $p<0.01$) and HepG2 cells (45% reduction, $p<0.001$).

These results suggested that inhibition of either β1-integrin or FAK function attenuated HCC cell proliferation. In order to corroborate these findings proliferation assays were performed on Huh7 and HepG2 cells after siRNA-dependent knockdown of β1-integrin and FAK. Western blotting was used in each cell type to confirm the efficiency of siRNA knockdown of β1-integrin and FAK protein expression (Figure 3.19A/B). In Huh7 cells, the values for proliferative index (value ± SEM) for each experimental condition were: 1kPa untreated, 0.092 ± 0.021; 12kPa untreated, 0.536 ± 0.019; scrambled siRNA, 0.546 ± 0.036; β1-integrin siRNA, 0.455 ± 0.039; and FAK siRNA, 0.469 ± 0.023. In HepG2 cells, the values for proliferative index (value ± SEM) for each experimental condition were: 1kPa untreated, 0.124 ± 0.008; 12kPa untreated, 0.704 ± 0.022; scrambled siRNA, 0.734 ± 0.006; β1-integrin siRNA, 0.482 ± 0.051; and FAK siRNA, 0.566 ± 0.025. In each cell type, transfection with scrambled siRNA did influence β1-integrin or FAK expression relative to controls. In HepG2 cells (Figure 3.19D), a reduction in proliferative index was observed following siRNA-dependent knockdown of both β1-integrin (34% reduction, $p<0.01$) and FAK (23% reduction, $p<0.001$). In Huh7 cells (Figure 3.19C), a trend towards reduced cell proliferation was seen following siRNA-dependent knockdown of β1-integrin and FAK, but in each case this was not statistically significant.

Figure 3.18: Inhibition of β1-integrin and focal adhesion kinase (FAK) activity reduces Huh7 and HepG2 cell proliferation *in vitro*

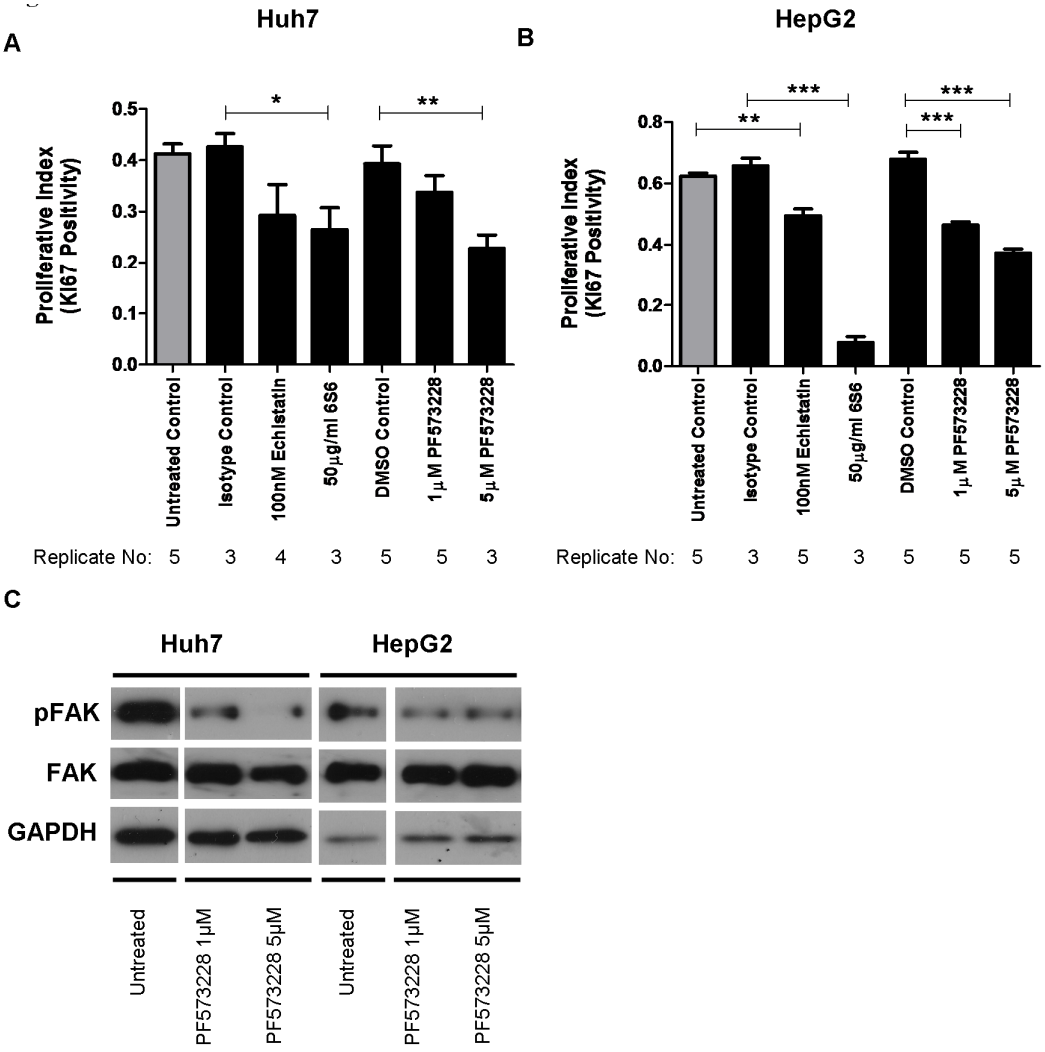

Figure 3.18: Graphs showing the mean proliferative index (Ki67-positivity) of (A) Huh7 and (B) HepG2 cells cultured on collagen-I-coated 12kPa PA supports. Cells were treated with echistatin (100nm), anti-β1-integrin antibody (6S6) (50µg/ml), isotype control IgG1 antibody (50µg/ml), PF573228 (1µM), PF573228 (5µM), DMSO (vehicle control) or left untreated in media (untreated control) for 24 hours. The number of replicates (n) for each condition is indicated beneath the x-axis of each graph. Mean measurements were compared using an unpaired student t test. Error bars are SEM, *$p<0.05$, **$p<0.01$, and ***$p<0.001$. (C) Western blots showing phospho-FAK^{Tyr397} expression in Huh7 and HepG2 cells, either left untreated or treated with PF573228 (1-5µM), as indicated. In each immunoblot, equal amounts of protein were loaded and equal loading confirmed in relation to GAPDH expression. The cell counting data from which these graphs are derived is presented in Appendix 12.

Figure 3.19: Inhibition of β1-integrin and FAK expression with siRNA reduces proliferation of Huh7 and HepG2 cells on stiff PA supports

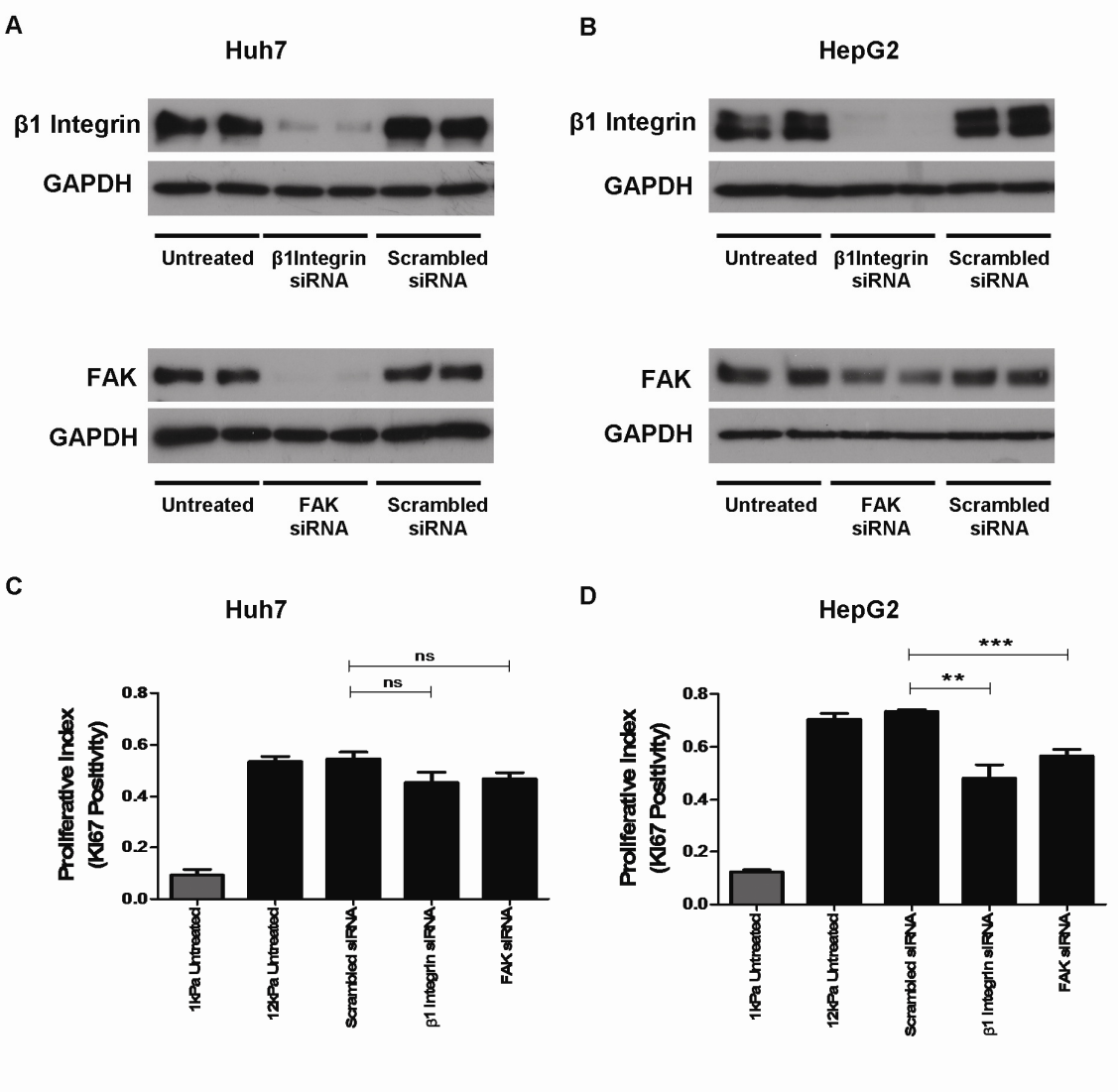

Figure 3.19: Western blots showing the expression of β1-integrin and FAK protein in (A) Huh7 and (B) HepG2 cells that were left untreated or transfected with siRNA for β1-integrin, FAK or control (scrambled sequences). Western blots show levels of protein expression 72 hours following transfection. Graphs show the mean proliferative index (Ki67-positivity) of (C) Huh7 and (B) HepG2 cells cultured on 1kPa and 12kPa collagen-I-coated PA supports following the transfection procedure. Transfected cells and untreated controls were trypsinized and transferred to PA supports 48 hours following the transfection procedure. Cells were fixed at 72 hours and proliferation determined by nuclear localisation of Ki67 antigen (n=5). Mean measurements were compared using an unpaired student t test. Error bars are SEM, ns = not significant, **p<0.01 and ***p<0.001. The cell counting data from which these graphs are derived is presented in Appendix 13.

3.9. Matrix stiffness regulates chemotherapeutic response in HCC cells

HCC is characterised by a resistance to conventional chemotherapeutic agents (9, 10). It has previously shown that chemotherapy resistance in HCC is regulated by Rho pathway signalling. Rho is an important regulator of cell morphology and the actin cytoskeleton that has been implicated in mediating cancer cell responses to changes in matrix stiffness (155). Experiments were conducted to determine whether alterations in matrix stiffness might regulate chemotherapy responses in HCC cells. Huh7 and HepG2 cells were cultured on collagen-I-coated PA supports (1-12kPa) and subjected to treatment with cisplatin for up to 24 hours. HCC cell apoptosis was assessed by immunoblot analysis for poly-ADP-ribose polymerase (PARP) cleavage in whole cell lysates (Figure 3.20A). In each cell line, increased susceptibility to apoptosis (PARP cleavage) was observed in cells cultured on soft (1kPa) supports. In addition, there was a non-significant trend towards increased numbers of surviving cells following cisplatin treatment on 12kPa supports (data not shown).

It has been suggested that tumour-initiating stem cells (TISCs) may play an important role in HCC development (230, 231). TISCs have been defined in relation to four criteria : high efficiency self-renewal, differentiation along at least two independent lineages, chemotherapy-resistance and the ability to form tumours that recapitulate the original tumour phenotype (clonogenic potential) (232). Clonogenic assays were used to investigate whether alteration in matrix stiffness might influence the survival and behaviour of TISCs following chemotherapy (Figure 3.20B). Cells were cultured for 48 hours on PA supports (1-12kPa). The cells were then either left untreated, treated with cisplatin [HepG2 10μM/ Huh7 20μM] or 5FU [25μ] for 24 hours prior to a media change. After a further 48 hours, cells were trypsinized and equal numbers of viable (trypan-blue excluding) cells were replated at clonal density in 12-well plates. Clonogenic capacity was calculated by direct counting of the resulting colonies. The results are expressed as the percentage colony formation relative to the number of colonies obtained from 1kPa supports.

In Huh7 cells, the values for percentage colony formation (value ± SEM) under each experimental condition were: untreated, 1kPa 100 ± 8.4/ 12kPa 85.6 ± 7.6; cisplatin (20μM) 1kPa 100 ± 8.8/ 12kPa 40.6 ± 8.8; and 5FU (25μM), 1kPa 100 ± 17.7/ 12kPa 27.8 ± 2.7. In HepG2 cells, the values for percentage colony formation (value ± SEM) under each experimental condition were: untreated, 1kPa 100 ± 5.0/ 12kPa 103.9 ± 7.1; cisplatin (10μM) 1kPa 100 ± 17.0/ 12kPa 44.5 ± 8.7; and 5FU (25μM), 1kPa 100 ± 19.5/ 12kPa 53.9 ± 8.4.

Amongst surviving viable cells following cisplatin treatment, there was an increased frequency of clone-initiating cells for both Huh7 (2.2-fold, $p<0.05$) and HepG2 cells (2.4-fold, $p<0.001$) cultured on 1kPa versus 12kPa supports (Figure 3.20B). In addition, there was a non-significant trend towards an increase in the total number of clone-forming cells derived from 1kPa versus 12kPa supports (data not shown). The validity of these findings was tested in repeat experiments with a second unrelated chemotherapeutic agent, 5-flurouracil (5FU). Following 5FU chemotherapy, there was an increased frequency of clone-initiating cells from Huh7 (1.9-fold, $p<0.05$) and HepG2 (3.6-fold, $p<0.001$) cultured on 1kPa versus 12kPa supports. In control experiments there was no difference in the frequency of clone-initiating cells in untreated Huh7 or HepG2 cells cultured on 1kPa versus 12kPa supports. These results are intriguing. The increase in PARP cleavage in cells cultured on soft (1kPa) supports might suggest that these cells are more susceptible to chemotherapy-induced apoptosis. However, the clonogenic assays indicate that HepG2 and Huh7 cells gown on 12kPa PA supports form fewer colonies than cells grown on 1kPa supports. This suggests that HepG2 and Huh7 are more sensitive to chemotherapy when maintained on a 12kPa support.

Figure 3.20: The effect of matrix stiffness on HCC cell apoptosis and clonogenic potential following treatment with chemotherapeutic agents

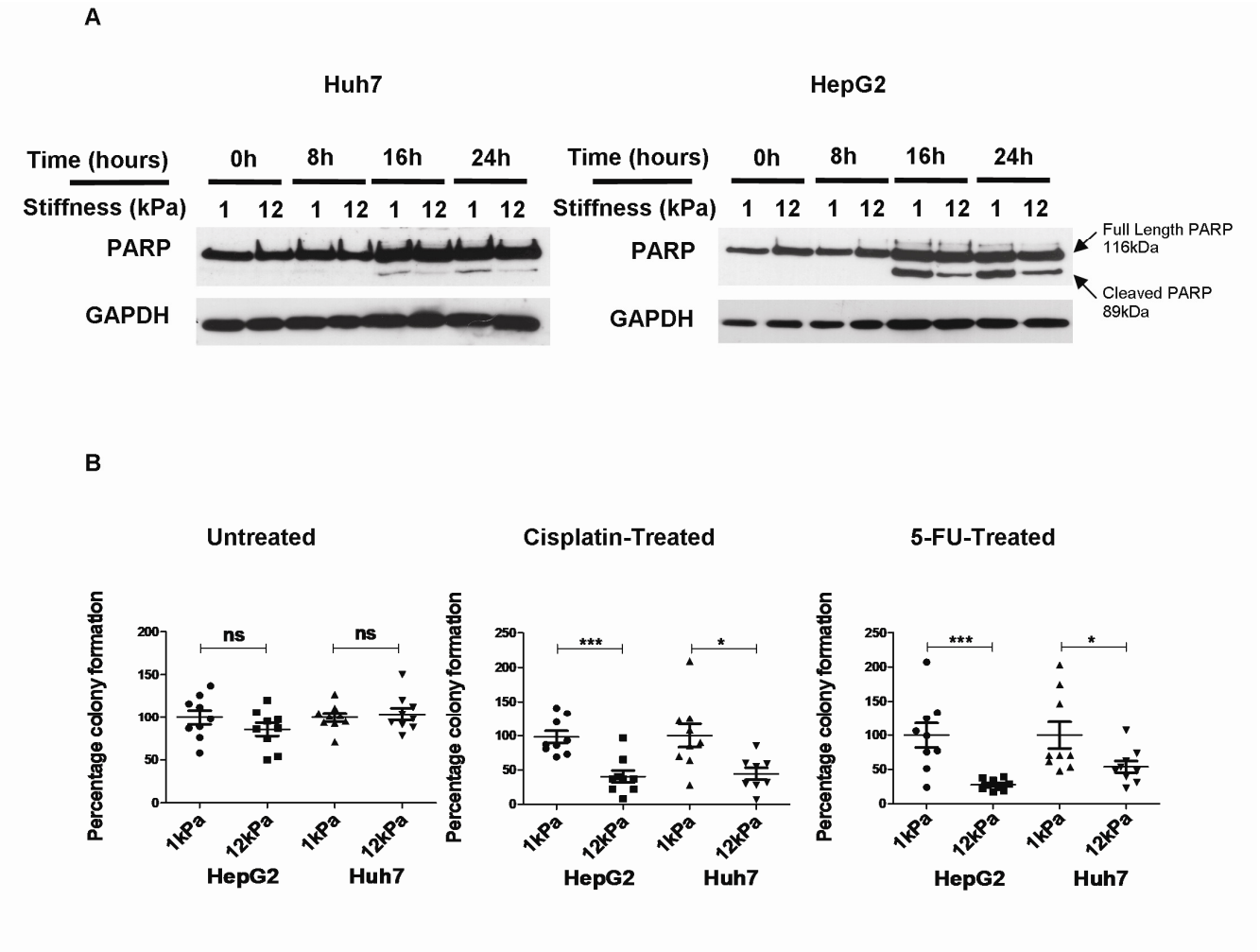

Figure 3.20: (A) Western blot showing full length (116kPa) and cleaved poly-ADP-ribose polymerase (PARP) (89kDa) following treatment with cisplatin [HepG2 10μM/ Huh7 20μM] on collagen-I-coated PA supports (1-12kPa), as indicated. The Western blots shown are representative examples from three independent experiments. (B) Graphs showing the frequency of clone-forming Huh7 and HepG2 cells following chemotherapy. Huh7 and HepG2 cells were cultured for 48 hours on PA supports (1-12kPa). Cells were then either left untreated (left panel) or treated with cisplatin [HepG2 10μM/ Huh7 20μM] (middle panel) or 5FU [25μM] (right panel) for 24 hours prior to a media change. After a further 48 hours, cells were trypsinized and equal numbers of viable (trypan-blue excluding) cells were replated at clonal density in 12-well plates. Clonogenic capacity was calculated by direct counting of the resulting colonies. The results are expressed as the percentage colony formation relative to the number of colonies obtained from 1kPa supports in 3 independent experiments (n =9). Mean measurements were compared using an unpaired student t test. Error bars are SEM, *$p<0.05$, ***$p<0.001$.

3.10 Matrix stiffness regulates cancer stem cell marker expression in HCC cells

The increase in the clone-initiating capabilities of Huh7 and HepG2 cells from a low stiffness environment following chemotherapy might be explained by selective enrichment for clone-initiating cells with stem cell characteristics. Experiments were therefore performed to investigate whether cisplatin treatment was associated with alteration in the frequency of stem cell marker expression. Flow cytometric analysis was performed on HepG2 cells cultured on collagen-I-coated PA supports (1-12kPa), both without and following cisplatin chemotherapy (Figure 3.21A).

The values for CD133 expression (percentage ± SEM) under each experimental condition were: untreated, 1kPa 3.27 ± 0.08/ 12kPa 2.17 ± 0.09; and cisplatin treated, 1kPa 5.10 ± 0.32/ 12kPa 1.80 ± 0.58. The values for c-kit expression (percentage ± SEM) under each experimental condition were: untreated, 1kPa 0.087 ± 0.057/ 12kPa 0.067 ± 0.033; and cisplatin treated, 1kPa 1.377 ± 0.186/ 12kPa 0.200 ± 0.058. The values for CD44 expression (percentage ± SEM) under each experimental condition were: untreated, 1kPa 1.50 ± 0.10/ 12kPa 0.23 ± 0.09; and cisplatin treated, 1kPa 2.53 ± 0.12/ 12kPa 0.43 ± 0.03. The values for CXCR4 expression (percentage ± SEM) under each experimental condition were: untreated, 1kPa 10.70 ± 0.87/ 12kPa 3.67 ± 0.24; and cisplatin treated, 1kPa 12.09 ± 0.99/ 12kPa 4.60 ± 1.00. Culture on 1kPa versus 12kPa supports was associated with enrichment for the cell surface markers CD133 (2.9-fold, $p<0.001$), c-kit (1.3-fold, $p=0.78$), CD44 (6.4-fold, $p<0.001$) and CXCR4 (2.9-fold, $p<0.01$). Cisplatin chemotherapy (10μM) increased the prevalence of CD44 (1.7-fold, $p<0.01$), CD133 (1.6-fold, $P<0.01$) and c-kit (15.8-fold, $p<0.01$) cells when cells were maintained on 1kPa but not 12kPa supports. Furthermore, quantitative PCR demonstrated upregulation of stem cell-associated transcription factors OCT4 and NANOG in HepG2 cells on 1kPa versus 12kPa supports, both in untreated controls (OCT4 2.0-fold increase, $p<0.05$; NANOG 2.7-fold increase, $p<0.05$) and following cisplatin chemotherapy (OCT4 2.0-fold increase, $p<0.05$; NANOG 3.4-fold, $p<0.05$) (Figure 3.21B). Cisplatin treatment alone did not have any demonstrable effect on the expression of either OCT4 or NANOG, regardless of support stiffness. The values for Oct4 mRNA expression (values ± SEM) relative to expression of the housekeeping gene 18S under each experimental condition were: untreated, 1kPa 3.70 ± 0.52/ 12kPa 1.82 ± 0.20; and cisplatin treated, 1kPa 3.71 ± 0.67/ 12kPa 1.89 ± 0.35. Overall, these results show an increase in cells displaying stem cell markers when maintained on soft (1kPa) versus stiff (12kPa) supports.

This suggests that HCC cells maintained in a low stiffness environment may display a clinically more aggressive phenotype.

Figure 3.21: The effect of matrix stiffness and cisplatin treatment on stem cell marker expression in HepG2 cells

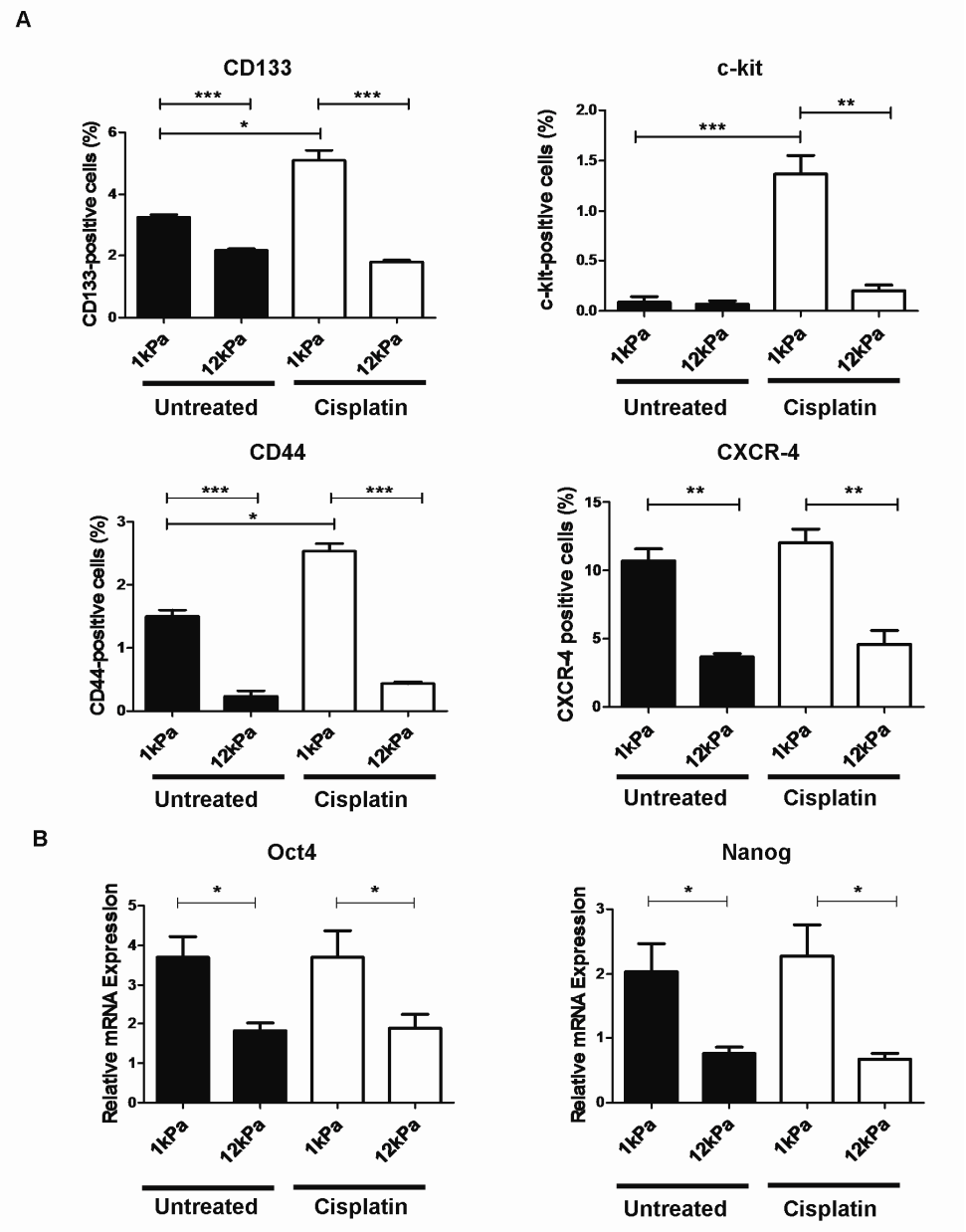

Figure 3.21: (A) Graphs showing quantification by flow cytometry of cancer stem cell markers CD133, c-kit, CD44 and CXCR-4 in HepG2 cells. (B) Graphs showing quantitative PCR analysis for OCT4 and NANOG expression in HepG2 cells. Gene of interest expression is relative to the 18S housekeeping gene. In each experiment HepG2 cells were cultured for 5 days on collagen-I-coated PA supports (1-12kPa). Cells were either left untreated (black) or treated for 24 hours with cisplatin [10μM] (white). Mean measurements were compared using an unpaired student t test (n=3). Error bars are SEM, *p<0.05, **p<0.01 and ***p<0.001.

3.11 Discussion

The results of these experiments demonstrate that the stiffness of the sub-cellular matrix can regulate cell morphology, proliferation and chemotherapy resistance in HCC cells *in vitro*. Increases in matrix stiffness promote HCC cell proliferation. Importantly, the major part of the increase in cell proliferation occurs across a pathophysiologically-relevant range (1-12kPa) corresponding to the range of stiffness values encountered during the transition from a normal to a cirrhotic liver. Previous epidemiological studies demonstrated a close relationship between increases in liver stiffness and prospective risk of HCC development (117, 118). The data presented here provide evidence for a potential mechanism that may underlie these epidemiological findings and the results of previous *in vivo* studies demonstrating that the induction of liver fibrosis was associated with accelerated tumour growth following orthotopic HCC implantation (121, 122). Overall, there is now a considerable body of evidence that suggests that increases in matrix stiffness associated with the development of liver fibrosis are mechanistically important in promoting HCC development. The counter to this observation is equally significant. A reduction in the stiffness of the cancer cell niche, as encountered by disseminated tumour cells entering an unaffected secondary site, might be sufficient to promote reversible cellular quiescence.

The results of experiments in both Huh7 and HepG2 cells demonstrates that increases in matrix stiffness are associated with an increase in cell proliferative index. Where the proliferative index increases, total cell number is also observed to increase, confirming that the increased proliferative index does indeed represent a higher number of cells in cycle , which is not balanced by increased rates of cell death.

Physiological alterations in matrix stiffness have broad and pervasive effects in relation to both mitogenic signalling and cell cycle regulation. The findings presented in this chapter are consistent with published results in non-transformed epithelial and mesenchymal cells, indicating that a moderate increase in matrix stiffness is associated with the induction of cyclins D1 and D3 (127, 128). Conversely, the reduction in proliferation observed in HCC cells maintained on soft supports is associated with a downregulation of cyclin D expression without concurrent upregulation of cyclin-dependent kinase inhibitors, $p21^{cip}$ and $p27^{kip}$. The expression profile of cell cycle regulators in HCC cells cultured on soft supports is in keeping with a quiescent G0 state. In contrast to previous studies in which mammary epithelial cells (233) and fibroblasts (129) were cultured on soft collagen gel substrates, the stiffness-dependent reduction in cellular proliferation was not associated with an

upregulation of cyclin-dependent kinase inhibitors. Overall, these findings confirm those of previous publications that suggest that physiological stiffness is inhibitory to cell cycle progression.

I had postulated that alterations in mitogenic signalling responses, modified by matrix stiffness, may account for stiffness-dependent regulation of cellular proliferation. Cyclin D1 expression is strongly dependent upon the organisation of the actin cytoskeleton. Across a physiological range, cells adjust the stiffness of the cytoskeleton to match that of their substrate (86). A high tensional state is characterised by actin stress fibre formation. The Rho-Rho kinase pathway promotes actin polymerisation and cellular contractility, thus promoting stress fibre development. It has recently been suggested that G1 phase cyclin D1 expression can be resolved into two distinct phases on the basis of cytoskeletal organisation (234). Early-G1 expression of cyclin D1 (absent in mesenchymal cells) is regulated by the Rho-family GTPase, Rac. Rac activation is inhibited by Rho-Rho kinase pathway activation, can proceed in a low tensional environment in the absence of cytoskeletal organisation and sustained ERK activation, but is insufficient to promote S-phase entry. In contrast, mid-G1 expression of cyclin D1 (occurring in epithelial and mesenchymal cells) sufficient to promote cell cycle progression is dependent upon co-ordinated Rac and ERK pathway activation. Sustained ERK activation requires adequate intracellular tension that is in turn dependent upon both matrix stiffness and Rho-Rho kinase pathway activation. In hepatoma cells, increasing matrix stiffness promoted the formation of both actin stress fibres and vinculin-containing focal adhesions in hepatoma cells. This was associated with enhanced basal autophosphorylation of FAK and ERK pathway activation. Indeed, it has previously been demonstrated in mammary epithelial cells that increasing matrix stiffness promotes both ERK and Rho activation, and that crosstalk between these pathways drives a positive feedback loop to further increase cytoskeletal tension. However I believe that this model represents an over-simplification in relation to the stiffness-dependent regulation of cyclin D1 in particular, and cancer cell behaviour more generally.

The results presented here show consistent evidence for the stiffness-dependent regulation of multiple signalling pathways implicated in the regulation of cyclin D1 expression, including FAK, ERK, PKB/ Akt and STAT3. In other words, matrix stiffness modulates cellular responses to growth factor stimulation across a wide-range of signalling pathways. Stiffness-dependent regulation of the STAT3 pathway has not previously been described. The data points towards a critical role for matrix stiffness and the cytoskeleton in regulating STAT3

expression. STAT3 is frequently activated in malignant cells and plays a key role in regulating the expression of genes involved in cancer-associated inflammation (235). Downstream targets of STAT3 include genes involved in multiple aspects of cancer biology, including proliferation (e.g. cyclin D1, c-myc), anti-apoptosis (e.g. Bcl-2, MCL-1) and angiogenesis (e.g. VEGF). The magnitude of STAT3 activation in response to HGF is regulated by matrix stiffness. Indeed I would propose a model in which cellular behaviour is regulated by a network of molecular interactions, with extensive cross-talk between multiple signalling pathways. Interactions between pathways conveying information from both soluble mediators and the extracellular matrix is integrated at the level of the cytoskeleton. In this context, the role of cytoskeletal tension has been likened to a cellular rheostat, acting to dampen or augment the responses of multiple signalling pathways to external stimuli (155, 172). Matrix stiffness determines the level at which a mitogenic stimulus can elicit a growth response.

Both β1-integrin and FAK are important in mediating HCC proliferation. In accordance with previous histological studies I have confirmed that both β1-integrin and phospho-FAK^{Tyr397} are upregulated in HCC specimens *in vivo* (225, 226). It has previously been shown that FAK expression in HCC correlates significantly with clinically meaningful endpoints including tumour size and disease-free survival (225). FAK expression also correlates to invasive potential in a range of human malignancies (236-238). In colorectal cancer, FAK expression in liver metastases is higher that that in primary colorectal tumours, suggesting that FAK activation may be important in the development of metastases. (238). The results in this chapter demonstrate that increased matrix stiffness promotes FAK activation. Furthermore, inhibition of FAK is associated with a reduction in HCC cell proliferation *in vitro*. This is consistent with a large body of evidence that FAK is important in cancer development and the progression of malignancy (228). Expression of a dominant negative mutant form of FAK, lacking kinase activity (FRNK) reduces the proliferation of mammary cancer cells *in vitro* and reduces tumour growth following transplantation into syngeneic rats (239). Similarly, inhibition of FAK with siRNA reduces colony formation in soft agar and inhibits migration in human lung cancer cells (240). However, a similar strategy in murine breast cancer cells failed to produce a reduction in cell proliferation, although cells showed reduced invasion through Matrigel and following transplantation to mice formed fewer metastases (241). The effects of FAK inhibition with the small molecular inhibitors have been similarly contradictory (227-229). Experiments have also been undertaken using conditional FAK knockout in transgenic mice. In mice heterozygous

for FAK, tumour formation following the topical application of carcinogens is reduced as compared to wild-type mice (242). Furthermore, conditional knockout of FAK after benign skin tumour formation inhibits malignant progression (243). While it is quite clear that FAK is important in mediating cancer development and progression, it is equally clear that FAK inhibition does not produce a consistent and reproducible phenotype in cancer cells. The results presented here add to this existing body of evidence. In the HCC cells tested, FAK inhibition using either siRNA or small molecular inhibition attenuated cell proliferation. However, it is likely that tumour-dependent variables will modify the response to FAK inhibition in different cancer cells. Indeed, in a significant proportion of the HCC specimens I tested, there was no evidence of enhanced FAK activation relative to the surrounding liver parenchyma. Thus while activation of FAK may promote cancer progression, it is not a consistent feature in HCC.

It has been demonstrated that matrix stiffness affects both proliferation and differentiation in HCC cells. A low stiffness environment promotes hepatocyte differentiation, as demonstrated by expression of hepatocyte markers, including: albumin, HNF4α, α1-anti-trypsin and AFP. This is consistent with previous reports investigating the effect of matrix stiffness on hepatocyte morphology and differentiation (142, 143, 146). This would suggest that in order to maintain hepatocyte function *in vitro*, cells should be cultured in a biophysical environment that recapitulates the stiffness characteristics of the native liver. This has clear implications in respect to the development of bio-artificial livers, where the goal is to maintain hepatocytes in prolonged culture while preserving hepatocyte function. However, achieving a better understanding of the relationship between matrix stiffness and differentiation is also important in respect to cancer biology.

Epithelial-mesenchymal transition (EMT) describes the process by which polarized epithelial cells, which normally interact with the basement via its basal surface, undertake a phenotypic shift to assume characteristics of mesenchymal cells (244, 245). These include increased migratory capacity, resistance to apoptosis, invasiveness and increased production of matrix components. Mesenchymal cells have the ability to invade and migrate through the ECM to create dramatic cell transpositions. EMT was originally described in relation to embryogenesis (classical EMT) (244, 246). Following fertilisation, the developing embryo undergoes gastrulation. Gastrulation proceeds from the formation of the primitive streak from a furrowed invagination in the epiblast layer. The epithelial cells in this region initially express E-cadherin and demonstrate apical-basal polarity. Through a process of invagination

the epiblast cells at the primitive streak separates to form the mesoendoderm, which subsequently separates through an EMT to form the mesoderm and endoderm. Definite mesenchyme with the potential to give rise to muscle and connective tissue arises from the epithelial mesoderm at the same time as neural crest mesenchyme develops from the ectoderm. EMT is subsequently employed in embryogenesis to remodel unwanted epithelial, for example that if the medial edge of the palate. These are considered prototypical examples of classical EMT. However, the use of the term EMT has subsequently been expanded to a range of situations, including cultured cells. In a seminal paper EMT was first described in a three-dimensional culture model of corneal epithelial cells as epithelial-mesenchymal transformation (247). In this model, epithelial cells derived from the adult and embryonic anterior lens, when cultured in collagen gels developed pseudopodia and filopodia characteristic of migratory cells and developed morphological and ultrastructural features indistinguishable from mesenchymal cells.

It has been proposed that EMT is encountered in distinct biological settings (244, 245). Type 1 EMT describes the form of EMT associated with implantation, embryo formation and organ development. Type 2 EMT describes processes associated with tissue injury that generates fibroblasts and other cell types associated with wound injury and tissue regeneration (248, 249). Type 3 EMT is described in relation to neoplastic cells that have undergone genetic and epigenetic changes promoting tumour development (222). Through this process neoplastic epithelial cells develop the ability to invade the basement membrane and give rise to distant metastases. EMT is associated with loss of proteins associated with the polarized epithelial phenotype and the acquisition of proteins associated with the mesenchymal, migratory phenotype of transitioning cells (245). Cells undergoing EMT lose expression of E-cadherin, syndecan-1 and zona occludens 1, while increasing expression of cytoskeletal proteins, including N-cadherin, vimentin, collagen-I and collagen-II. Additional proposed markers for EMT include increased nuclear expression of transcription factors (including CBF-A and β-catenin) and new expression of the transcription factors (including Snail, Slug and Twist). Mesenchymal cells lose cell polarity and develop spindle shaped morphology with redistribution of stress fibres. Loss of E-cadherin is thought to be a crucial step in the process of EMT, both within embryogenesis and in pathological situations in the adult. However, it has been shown that loss of E-cadherin is not a necessity for EMT in human breast cancer cells (250).

The results presented in this chapter suggest that human HCC cells cultured on stiff substrates demonstrate some features of classical EMT, which may represent a transition to a proliferative or migratory phenotype and contribute to cell behaviours associated with chronic disease processes, including tumorigenesis and malignant progression/ metastatic spread. During the process of cancer development and tumour dissemination, cancer cells are believed to acquire mesenchymal properties, enabling them to migrate through and invade surrounding tissues, eventually entering the lymphatics and bloodstream (147, 251). Thus the process of EMT is believed to facilitate cancer progression. However, at secondary sites, tumour cells are recognised by their epithelial characteristics and developing metastases usually recapitulate in part the epithelial phenotype of the primary tumour (252). At present there is limited understanding of this reverse process of mesenchymal to epithelial transition (MET). The results presented in this chapter demonstrate that HCC cells lose mesenchymal features; including stress fibres, N-cadherin and vimentin expression, and up-regulate hepatocyte markers when cultured in a soft environment. This is consistent with previous studies showing that non-transformed mammary epithelial cells cultured on compliant PA supports revert to an organised epithelial phenotype (155). Similarly, hepatocytes retain an epithelial phenotype when cultured on soft collagen gels (141). It has previously been shown that FAK signalling is required for induction of EMT in hepatocytes in response to TGFβ (253). Our results suggest that the interlinked processes of EMT and MET are directly and reversibly regulated by changes in environmental stiffness.

It is likely that changes in matrix stiffness might regulate multiple facets of cell behaviour throughout the natural history of a tumour. Thus while increases in tissue stiffness, as encountered in liver fibrosis, may promote tumour development, we should also consider the effect of changes in matrix stiffness on disseminated tumour cells and potential links to tumour dormancy. Cancer cell dormancy describes a state of reversible cellular quiescence in cells that have the potential upon reactivation to form micrometastases (254). Solitary tumour cells may persist in a quiescent state for many years prior to initiating metastatic tumour growth (255). Furthermore, chemotherapeutic agents that target actively dividing cells have proven ineffective in treating these solitary dormant cells (256). It has been proposed that the ECM is a critical regulator of cellular dormancy (257); however the role of matrix stiffness in regulating this process has not been specifically addressed. The growth, invasion and dissemination of tumour cells are accompanied by dramatic changes in the mechanical properties (stiffness) of the cancer cell niche. The bone marrow, a common reservoir site for disseminated tumour cells (258), will provide a microenvironment with

stiffness significantly lower than would be encountered by cells in most epithelial tumours. Animal models of cancer cell dormancy have established inflammation and surgical trauma as mechanisms for the reactivation of dormant cells (259, 260). The induction of lung fibrosis, accompanied by type I collagen deposition is associated with the development of lung metastases in a murine model of disseminated mammary gland carcinoma (261). Furthermore, using a 3D-culture system to model cancer cell dormancy, it was shown that collagen-I promotes the proliferation of previously dormant cancer cells though β1-integrin activation of SRC and FAK. Blockade of β1-integrin, ERK and myosin light chain kinase (MLCK) using both siRNA and pharmacological techniques inhibited cytoskeletal reorganisation and proliferation. This strongly suggests that collagen-I deposition may be important in facilitating the proliferation of dormant tumour cells. The role of changes in matrix stiffness in mediating this effect was not addressed in this study.

Our findings suggest that a reduction in the stiffness of the cancer cell niche would be sufficient to promote reversible cellular quiescence (dormancy). Furthermore, an increase in environmental stiffness (as may occur with inflammation, surgery or stromal reaction to tumour) or alteration in the stiffness-sensing machinery of the cell (occurring due to genomic instability) might facilitate reactivation of dormant cells. Barkan and colleagues used a 3D *in vitro* culture system reconstituted from basement membrane to recapitulate solitary tumour dormancy and the transition to proliferation *in vitro* (262). In this study, tumour cells with dormant behaviour *in vivo* remained growth arrested in 3D culture. In contrast, tumour cells with marked *in vivo* tumour-forming capacity transitioned into cellular proliferation, a process that was accompanied by cytoskeletal reorganisation/ actin stress fibre formation. Importantly, both cell lines proliferated rapidly when cultured on 2D plastic substrates. The effect of matrix stiffness on both the induction of cellular dormancy and transition to cellular proliferation was not addressed. Both collagen-gel and Matrigel-based substrates have stiffness values that are substantially lower than those encountered in many physiological tissues and many orders of magnitude lower than that of plastic substrates (263). Indeed, the major deficiency of existing models of cancer cell dormancy has been a failure to consider the effect of matrix stiffness on cellular behaviour. Hence, the PA support with its precise regulation of both stiffness and ligand density provides what has been hitherto unavailable, a tractable *in vitro* model of cancer cell dormancy.

HCC demonstrates a high rate of chemotherapy resistance, which explains in part the poor prognosis of patients with HCC. The majority of HCC develop within the context of liver

fibrosis (a high stiffness environment). In addition, tumour growth is associated with further stiffening of the ECM. The results presented here suggest that increasing matrix stiffness reduces chemotherapy-induced apoptosis in HCC cells. The mechanism for this observation requires further investigation. The clinical effectiveness of systemic chemotherapy is also limited by a failure of adjuvant/ neoadjuvant chemotherapy to eradicate disseminated tumour cells that are responsible for tumour recurrence following surgery or liver transplantation (264, 265). HCC recurrence occurs in 10-60% of patients following liver transplantation (12, 14). The mean time to recurrence is in the range of 1-2 years, but very late recurrence is also described (14). The results presented in this chapter demonstrate an increase in clone-initiating capability following chemotherapy from cells maintained in a low stiffness environment. There was no difference in the frequency of clone-initiating cells derived from soft or stiff supports not treated with chemotherapy. I have shown that the expression of cancer stem cell markers is influenced by changes in matrix stiffness. Culture on soft substrates is associated with an increase in the proportion of cells expressing cancer stem cell markers (CD44, CD133 and CXCR-4). CD44, CD133 and CXCR4 have previously been shown to define populations of cells with cancer stem cell properties in HCC (266-269). The defining properties of cancer stem cells include the ability to self-renew; differentiate; and initiate tumour formation. Both immunogenic markers and functional properties (e.g. chemotherapy resistance) are used to identify cancer stem cells. However, due to the inherent heterogeneity of carcinogenesis, it is unlikely that a single marker can be reliably used to define cancer stem cell populations. I have demonstrated that chemotherapy is associated with an increase in the expression of a number of cancer stem cell markers, particularly for cells in a low stiffness environment. It remains unclear whether the enrichment for cells with a cancer stem cell phenotype following chemotherapy is due to positive selection or active induction of cancer stem cell characteristics. It has previously been reported that chemotherapy can lead to propagation of cancer stem cells (232, 270). In lung cancer, chemotherapeutic agents, including doxorubicin, cisplatin and etoposide, have been used to select drug-surviving cells (DSCs) (270). These cells are enriched for the expression of the cancer stem cell marker CD133 and demonstrate loss of markers of cell differentiation. The DSCs maintained their self-renewal capacity and ability to differentiate. Differentiation was associated with loss of CD133 expresssion and re-acquisition of chemotherapy-sensitivity. Importantly, DSCs demonstrate higher tumorigenic and metastatic potential upon inoculation into immunodeficient mice, consistent with a stem cell phenotype.

The process of metastasis requires cells to migrate through the ECM into blood vessels and lymphatics prior to extravasation at secondary sites and initiation of tumour formation. As discussed, both EMT and MET are believed to play a critical role in this process (271). Disseminated tumour cells that give rise to metastases are thought to be synonymous with cancer stem cells. Both stem cell and epithelial-mesenchymal transition markers are frequently over-expressed in disseminated tumour cells (272). Furthermore the expression of cancer stem cell markers is strongly associated with poor prognosis in HCC patients (273, 274). Attempts have been made to define a cancer stem cell signature in metastatic HCC. Yang and colleagues demonstrated that all HCC specimens tested and most blood samples from these patients contained highly tumourigenic $CD90^{+}$/ $CD45^{-}$ cell populations which were absent from normal and cirrhotic livers (275). The co-expression of both CD90 and CD45 defined an even more aggressive tumourigenic population. Furthermore, the haematopoietic marker c-kit, which is not typically expressed in primary HCC , is abundantly expressed in metastatic HCC deposits in association with CD90 (57, 276). These studies suggest that disseminated cancer stem cells are responsible for the development of metastases. However, the mechanisms and signals responsible for the growth of disseminated tumour cells into clinically significant metastases are incompletely characterised. It has been shown that cancer stem cells are regulated by a number of environmental factors (277). However, to the best of my knowledge, the results presented in this chapter are the first to suggest that matrix stiffness regulates stem cell marker expression in cancer cells. The results provide a potential mechanism for the long-term survival and clone-initiating capability of disseminated tumour cells in a soft environment (e.g. bone marrow or transplanted liver). They also suggest that increases in matrix stiffness (as would be encountered in acute inflammation or fibrosis) may be sufficient to promote the activation and outgrowth of these cells.

In this chapter I have investigated the effect of changes in matrix stiffness on the proliferation, differentiation and chemotherapeutic responsiveness of two unrelated HCC cells lines. While the results of experiments conducted in highly passaged cells lines should be interpreted with some caution, the results presented here are consistent with a large body of evidence that suggests that matrix stiffness is important in regulating cancer development. Overall, these results suggest that increases in matrix stiffness encountered in liver fibrosis may foster HCC progression by promoting cell proliferation and mesenchymal phenotype, whilst also enhancing chemotherapeutic resistance. In contrast, a reduction in the stiffness of the cellular environment (as might be encountered by disseminated tumour cells) induces

cellular dormancy, a stem cell phenotype and enhanced clonogenic capacity following chemotherapy.

Chapter 4: Studies to determine the effect of changes in stiffness on hepatic progenitor cell behaviour

4.1. Introduction

Hepatic progenitor cells (HPCs) are tissue resident bi-potential stem cells that have the potential to differentiate into either hepatocytes or cholangiocytes (278). Under normal conditions, both hepatocytes and cholangiocytes retain the ability to proliferate following liver injury. However, in cirrhosis and other conditions in which the regenerative capacity of hepatocytes is overwhelmed, regeneration is achieved by proliferation and differentiation of HPCs. HPCs are believed to reside in a stereotyped stem cell compartment or niche (28). The anatomical location of this stem cell compartment is believed to be the canals of Hering, which are remnants of the foetal ductal plates (29, 30). The properties of this stem cell compartment are responsible for regulating stem cell behaviour, maintaining an appropriate balance between stem cell quiescence, proliferation and differentiation. The hepatic progenitor cell niche has both cellular and extracellular components (28). Cellular components of the HPC niche include macrophages and activated hepatic MFBs. Following liver injury, macrophages cluster at sites of HPC proliferation. Similarly, activated MFBs are intimately associated with streaming cords of HPCs, forming an almost continuous layer adjacent to the progenitor cell compartment. More recently it has been demonstrated that different forms of liver injury differentially affect the cellular composition of the HPC niche, and thus may direct hepatic progenitor cell fate (218). Biliary injury results in a marked accumulation of αSMA-positive MFBs which express the Notch ligand Jagged1 and are responsible for the deposition of large amounts of fibrillar collagen. Adjacent HPCs demonstrate Notch pathway activation and express cholangiocyte-associated transcription factors. The acquisition of this biliary phenotype can be suppressed by treatment with a Notch inhibitor. In contrast, following hepatocyte injury, WNT3a-expressing macrophages localise close to HPCs which it can be shown demonstrate WNT pathway activation. This results in activation of downstream transcriptional targets of the WNT pathway including the Notch pathway inhibitor, Numb. This in turn leads to suppression of Notch pathway activation in these HPCs, favouring a hepatocyte phenotype. Through this mechanism, the cellular elements of the HPC niche may direct stem cell fate.

Extracellular components of the HPC niche are dominated by the presence of a laminin-rich matrix. Both the basement membrane and ECM that surrounds the bile ducts is principally

composed of type-IV collagen and laminin (17, 21, 22). Immunohistological studies in a range of animal models have demonstrated that HPCs are always surrounded by a laminin-rich matrix or sheath (28, 279). Laminin gene expression has been demonstrated in a number of non-parenchymal liver cells, including HSCs and endothelial cells. However, it has also been shown that laminin can be produced by HPCs, both in respect to an immortalised rat HPC cell line (28) and primary murine HPCs *in vitro* (Dr M Williams: personal communication). Using *in vitro* culture of primary murine HPCs, it has previously been demonstrated that laminin markedly up-regulates progenitor (DLK1) and biliary (GGT, Aquaporin-1) gene expression in freshly isolated primary murine HPCs, while suppressing expression of the early hepatocyte gene (CEBP/a). Thus it is thought that laminin may play an important role in maintaining HPCs in an undifferentiated phenotype. This would be consistent with results which suggest that laminin isoforms are effective at maintaining undifferentiated growth of human embryonic stem cells *in vitro* (280).

HPCs are characterised histologically as small round cells with an oval nucleus and scanty cytoplasm (281). A number of immunohistochemical markers have been used that identify HPCs. The most widely recognised markers include cytokeratin-7 (CK-7) and cytokeratin-19 (CK-19), which are components of intermediate filaments (282, 283). Both CK-7 and CK-19 are expressed both by HPCs and mature cholangiocytes. Additional immunohistochemical markers for HPCs include EpCAM (284), OV-6 (285) and E-cadherin (286). HPCs can also express markers in common with mature hepatocytes (albumin, cytokeratin-8), foetal hepatoblasts (AFP), haematopoietic stem cells (c-kit, CD133) and neuro-epithelial cells (neural cell adhesion molecule [NCAM]) (281, 285, 287). The expansion of the HPC compartment and the differentiation of these cells towards mature hepatocytes, is characterised by the appearance of trans-amplifying cell populations with histological features intermediate between HPCs and mature hepatocytes (281). This is accompanied by progressive loss of the CK-7 and CK-19 expression. In contrast, mature cholangiocytes retain expression of both CK-7 and CK-19, although the expression of neuroendocrine markers such as NCAM is lost.

HPC proliferation has been described in a number of human liver diseases, characterised by damage and impaired regeneration of either cholangiocytes or hepatocytes. HPC proliferation is described histologically as the “ductular reaction”, which is characterised by anastomosing strands of proliferating of HPCs that may differentiate into either hepatocytes or cholangiocytes (288). While it has been established that both the cellular and extracellular

components of the HPC niche may be important in regulating HPC fate, relatively little is known regarding the effect that changes in the biomechanical properties of the niche might have in regulating HPC responses (289). As previously discussed, an increase in the stiffness of the liver is typically seen in association with acute tissue injury and the subsequent development of liver fibrosis and cirrhosis. HPC proliferation is often seen in association with the development of liver fibrosis. This is particularly true during biliary regeneration, in which HPCs are closely associated with activated MFBs expressing copious amounts of fibrillar collagen (218). A prominent ductular reaction is a feature of fibrosing cholestatic hepatitis (28). This condition is frequently seen as a complication of active HCV infection in immunosuppressed patients following liver or renal transplantation (290, 291). It is characterised histologically by prominent HPC proliferation, in association with more rapid development of liver fibrosis and cirrhosis. Detailed histological analysis reveals that there is close topographical alignment between HPCs and activated MFBs. This is an important finding as hepatic MFBs are believed to be the predominant source of fibrillar collagen production in chronic liver disease (38). Furthermore, it has been shown that increased matrix stiffness is required for MFB activation (133, 134, 292). It has previously been demonstrated that (in the absence of known hepatocyte inhibitors) oval cell proliferation is enhanced in a carbon tetrachloride model of rat liver fibrosis (289). Furthermore, both the number of CK19 positive and Ki67 positive HPCs were higher with more advanced stages of fibrosis. This would suggest that factors associated with liver fibrosis may promote HPC responses.

Kallis *et al* investigated the functional role of ECM degradation in regulating HPC responses (293). Using the collagen 1α1 (r/r) mouse, which synthesises a mutated form of collagen-I that is resistant metalloproteinase-mediated degradation, they demonstrated that following repeated injury with CCl4, r/r mice had markedly attenuated HPC responses, This was accompanied by persistence of collagen-I and a failure to deposit ECM laminin. Similar results were obtained in experiments with r/r mice given the CDE diet, a further model of HPC response. This has been interpreted as showing that impairment of ECM remodelling following fibrotic liver injury may inhibit HPC response/ migration. These results, which appear to emphasise the importance of ECM remodelling in facilitating HPC response would be consistent with data showing the existence of clonal proliferative units within the liver, with a probable origin in the periportal region (294). The spatial organisation of these clonal units would be in keeping with migration of either HPCs themselves, or their progeny, from the periportal region to the hepatic veins. Such cellular migration would necessitate

significant ECM remodelling. What is less certain is whether the results obtained in the r/r mouse are mechanistically informative in respect to determining the relationship between liver fibrosis and HPC responses. The impairment of r/r collagen degradation and consequent increase in collagen-I accumulation following liver injury, may both independently modulate HPC responses. Importantly it remains unclear whether physical factors associated with liver fibrosis (including alterations in liver stiffness) influence the HPC response. Thus further studies are required to more closely characterise this aspect of the HPC-matrix relationship.

The aim of this chapter was to more fully characterise the temporal relationship between the development of liver fibrosis, parenchymal stiffness and HPC responses in animal models of chronic liver injury. In addition I aimed to undertake detailed *in vitro* experiments to more fully characterise the effect of alterations in environmental stiffness on HPC morphology, proliferation and differentiation.

4.1.1 Hypotheses

- Increases in matrix stiffness, in the context of acute inflammation and chronic liver fibrosis will promote HPC proliferation.
- HPC response should be closely correlated both the development of liver fibrosis and changes in matrix stiffness in animal models of progressive liver fibrosis.
- Increases in matrix stiffness should precede HPC proliferation in animal models of liver fibrosis.
- Increases in matrix stiffness, across a pathophysiologically-relevant range will promote HPC proliferation *in vitro*.
- Changes in matrix stiffness will modulate HPC differentiation and may be involved in directing stem cell fate.

4.2. The relationship between liver fibrosis and HPC response in animal models of chronic liver disease

4.2.1. Liver fibrosis and HPC response in a rat thioacetamide (TAA) model of liver fibrosis

A thioacetamide model of liver fibrosis was used to more closely characterise the temporal relationship between the development of liver fibrosis and HPC response in chronic liver disease. Liver fibrosis was induced by oral administration of low dose TAA (0.03%) in drinking water in male SD rats. Animals were sacrificed and liver tissue analysed at 4, 8, 10, 14, 18, 20 and 26 weeks. Comparison was made to tissue derived from untreated control animals. Histological analysis of PSR-stained sections from TAA-treated rats revealed evidence of bridging fibrosis from 20 weeks. In rats treated with 26 weeks TAA there was evidence of established cirrhosis, with dense bridging fibrosis and regenerative nodules. Liver fibrosis was quantified by digital image analysis of PSR-stained sections (Figure 4.1A). Values for percentage PSR-staining (value ± SEM) were: control untreated, 0.57 ± 0.04; 4 weeks, 0.61 ± 0.10; 8 weeks, 0.65 ± 0.19; 10 weeks, 0.95 ± 0.26; 14 weeks, 0.68 ± 0.36; 20 weeks, 0.95 ± 0.14; and 26 weeks, 3.59 ± 0.46. Prior to week 20, there was no significant increase in liver fibrosis in comparison to untreated control animals. Following 20 weeks of low dose TAA treatment there was a modest but significant increase in PSR-staining (1.7 fold, $p=0.01$). However, at week 26 there was a marked increase in PSR-staining (6.3-fold, $p<0.0001$) relative to untreated controls. HPC response was assessed by direct cell counting of CK-19-positive cells (Figure 4.1B). Values for HPC numbers per 20 high power fields (value ± SEM) were: control untreated, 65.4 ± 17.9; 4 weeks, 131 ± 26.0; 8 weeks, 118.3 ± 15.7; 10 weeks, 136.8 ± 5.6; 14 weeks, 133.0 ± 12.9; 20 weeks, 175.8 ± 24.4; and 26 weeks, 1676.0 ± 659.5. A modest increase in HPC numbers (relative to untreated controls) was seen from 4 weeks (2.0 fold, $p=0.07$). The increase in HPC numbers in TAA-treated animals was statistically significant from week 10 (2.1-fold, $p=0.01$). HPC response, as assessed the numbers of CK-19-positive cells, was markedly increased following 26 weeks of TAA (25.6-fold, $p=0.03$), in comparison to untreated control animals. The major expansion in HPC numbers at 26 weeks corresponds to a similar increase in PSR-staining at this time point. Further analysis reveals a positive correlation between HPC numbers and PSR staining in the TAA model of liver fibrosis ($R=0.665$, $p<0.001$) (Figure 4.1C). However, the more modest early increase in HPC numbers from week 4 onwards occurred prior to the development of significant liver fibrosis.

Figure 4.1: Liver fibrosis and HPC responses in a TAA model of rat liver fibrosis

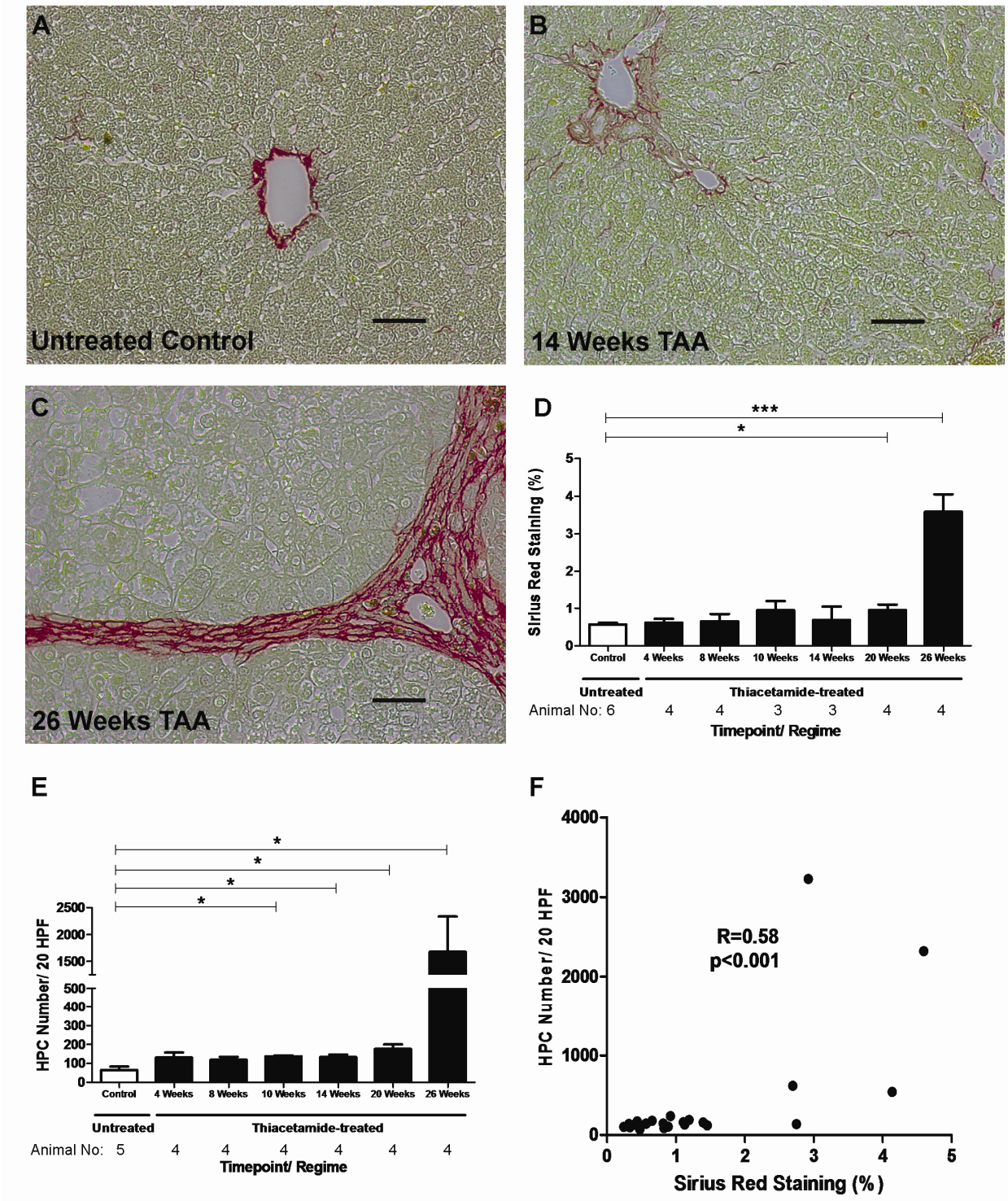

Figure 4.1 Quantification of liver fibrosis and HPC response in a TAA model of rat liver fibrosis. (A-C) Photomicrographs showing representative high power (x200) images of PSR-stained liver sections from (A) untreated control rats (B) 14 week TAA-treated rats and (C) 26 week TAA-treated rats. (D) Quantification of pico-sirius red staining by digital image analysis of liver sections derived from rats treated with low dose (0.03%) TAA sacrificed at the time points indicated (4-26 weeks). Comparison is made to liver tissue derived from untreated control animals. Each bar represents the mean percentage area of PSR-staining per high power (x200) field (HPF). The number of replicates (n) at each time point is indicated beneath the x-axis of the graph. The 4-20 week time points show only a modest increase in periportal PSR-staining. After 26-weeks TAA-treatment there is a more dramatic increase in PSR-staining with evidence of bridging fibrosis/ cirrhosis. Statistical comparisons between mean values are made using an unpaired student t-test. (E) Quantification of CK-19-positive HPCs in liver sections in the low dose TAA model. Each bar represents the mean number of non-bile duct associated CK-19 positive cells per high power (x320) field from 3-6 animals. The precise number of animals (n) at each time point is indicated beneath the x-axis of the graph. Statistical comparisons between mean values are made using an unpaired student t-test. (F) Graph showing the statistical correlation between HPC number and liver fibrosis (percentage PSR staining) in the low dose TAA model of liver fibrosis (n=23) (R= Spearman correlation co-efficient). In each case error bars represent SEM, *$p<0.05$, **$p<0.01$, ***$p<0.001$.

4.2.2. Liver fibrosis and HPC response in a rat carbon tetrachloride (CCL_4) model of liver fibrosis

A CCl_4 model of liver fibrosis was used as confirmatory model in order to characterise the relationship between liver fibrosis and HPC response. Liver fibrosis was induced by twice weekly intra-peritoneal injection of 0.2ml/100g of a 1:1 mixture of CCL_4 in olive oil. After 2 weeks the dose of this mixture was reduced to 0.1ml/ 100g. Animals were sacrificed and liver tissue analysed (including rheometry measurements) at 7, 14, 28, 42, 56 and 70 days. Both vehicle-injected (olive oil alone) and uninjected animals were used as controls (135). Liver fibrosis was quantified by digital image analysis of PSR-stained sections (Figure 4.2A). Early liver fibrosis was characterised by portal tract expansion, with subsequent development of portal bridging fibrosis. Digital image analysis reveals a progressive increase in PSR-staining with increasing duration of injury. The values for percentage PSR-staining (value ± SEM) were: 7 days, control 1.27 ± 0.40/ CCl_4 0.54 ± 0.17; 14 days, control 0.41 ± 0.19/ CCl_4 1.46 ± 0.30; 28 days, control 0.31 ± 0.21/ CCl_4 4.75 ± 0.71; 42 days, control 0.45 ± 0.05/ CCl_4 6.11 ± 0.68; 56 days, control 0.49 ± 0.02/ CCl_4 10.13 ± 2.49; control 0.46 ± 0.18/ CCl_4 8.08 ± 0.89. At 28 days, PSR-staining was increased 15.6-fold ($p=0.03$) relative to vehicle treated controls, increasing to 17.6-fold ($p=0.004$) at 70 days.

The pattern of MFB activation in this model, as assessed by digital image analysis of αSMA-staining, has previously been quantified (135). The values for percentage αSMA-staining (value ± SEM) were: 7 days, control 0.04 ± 0.01/ CCl_4 0.38 ± 0.10; 14 days, control 0.06 ± 0.01/ CCl_4 0.33 ± 0.07; 28 days, control 0.55 ± 0.04/ CCl_4 1.23 ± 0.41; 42 days, control 0.05 ± 0.01/ CCl_4 1.52 ± 0.51; 56 days, control 0.06 ± 0.01/ CCl_4 1.65 ± 0.31; control 0.07 ± 0.03/ CCl_4 5.11 ± 1.82. There is a modest early increase in MFB activation from as early as 7 days (Figure 4.2B). The majority of the increase in αSMA staining occurs at later time points (28-70 days).

HPC response was assessed by direct cell counting of CK-19-positive cells (Figure 4.2C). The values for HPC numbers per 60 high power fields (value ± SEM) were: 7 days, control 28.5 ± 7.5/ CCl_4 78.5 ± 13.5; 14 days, control 41.5 ± 24.5/ CCl_4 93.6 ± 12.8; 28 days, control 39.0 ± 4.0/ CCl_4 56.5 ± 1.5; 42 days, control 26.0 ± 2.0/ CCl_4 116.0 ± 24.4; 56 days, control 40.0 ± 11.0/ CCl_4 156.0 ± 30.0; control 18.0 ± 3.0/ CCl_4 492.2 ± 179.7. Overall, HPC numbers are increased in animals treated with CCl_4 ($p< 0.05$, two-way ANOVA), however absolute differences at each time point relative to vehicle-treated controls were not

statistically significant (unpaired student t-test). There is a trend towards an early increase in HPC numbers at 7 days (2.8-fold, $p=0.09$) relative to vehicle-treated controls. However, the majority of the increase in HPC numbers appears to occur after 70 days of treatment (27.3-fold, $p=0.17$). HPC numbers are positively correlated to both PSR staining ($R=0.65$, $p<0.05$) and αSMA staining ($R=0.78$, $p<0.001$) (Figure 4.3).

Figure 4.2: Liver fibrosis, αSMA expression and HPC response in a CCl_4 model of rat liver fibrosis

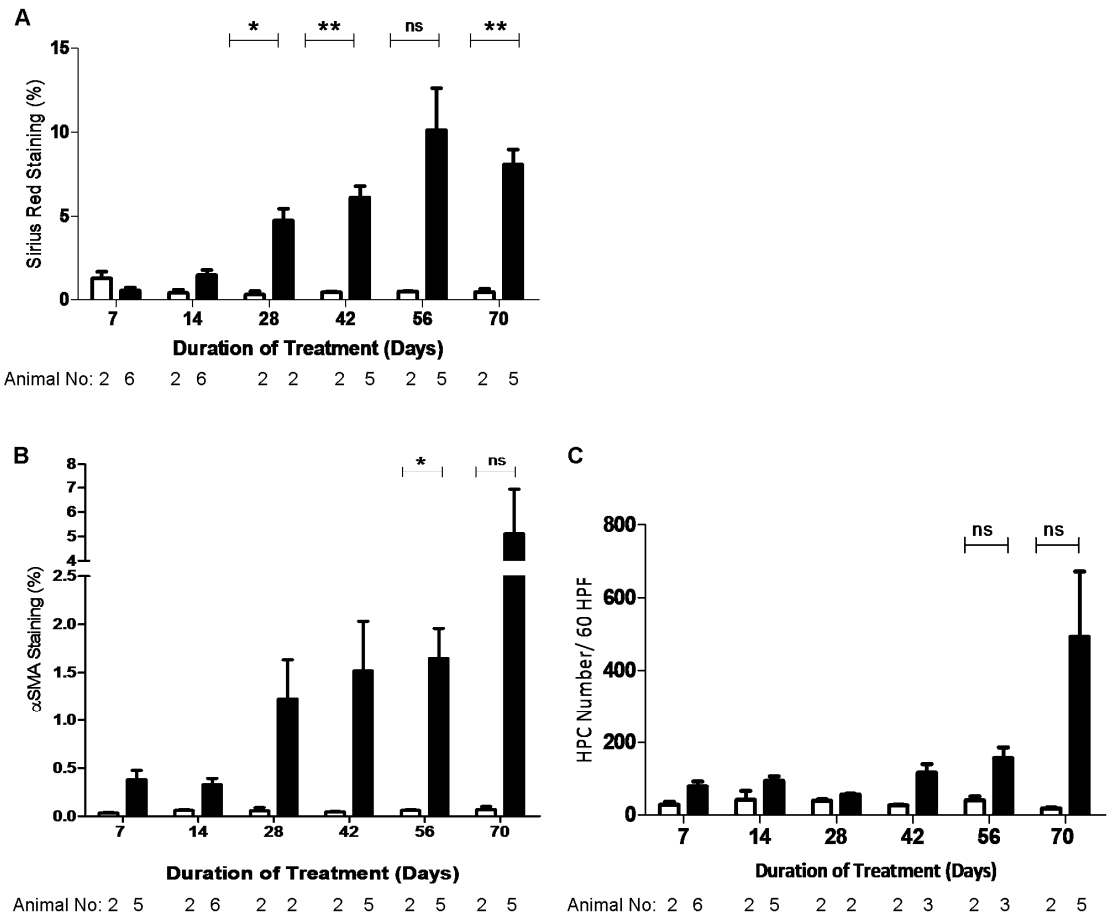

Figure 4.2 Quantification of liver fibrosis, MFB-activation and HPC response in a CCl_4 model of rat liver fibrosis. (A) Quantification of PSR staining by digital image analysis of liver sections derived from rats treated with twice weekly CCl_4 injection (black) (7-70 days). Comparison is made to liver tissue derived from vehicle (olive oil) treated control animals (white bars). Each bar represents the mean percentage area of PSR-staining per high power (x200) field (HPF) from 2-6 animals. (B) Quantification of MFB activation as assessed by digital image analysis of αSMA-stained liver sections in the rat CCl_4 model. Each bar represents the mean percentage area of PSR-staining per high power (x200) field (HPF) from 2-6 animals. The number of animals used (n) in each analysis is indicate below the x-axis of each graph. (C) Quantification of CK-19-positive HPCs in liver sections in the CCL_4 model. Each bar represents the mean number of non-bile duct associated CK-19 positive cells per 60 high-power (x320) fields from 2-6 animals. The differences between mean measurements were compared using a student t test. In each case error bars represent SEM, *p<0.05, **p<0.01, ***p<0.001, ns= not statistically significant. The number of animals used (n) in each analysis is indicate below the x-axis of each graph.

Figure 4.3: Statistical correlation of HPC numbers to PSR and αSMA-staining in a CCL_4 model of rat liver fibrosis

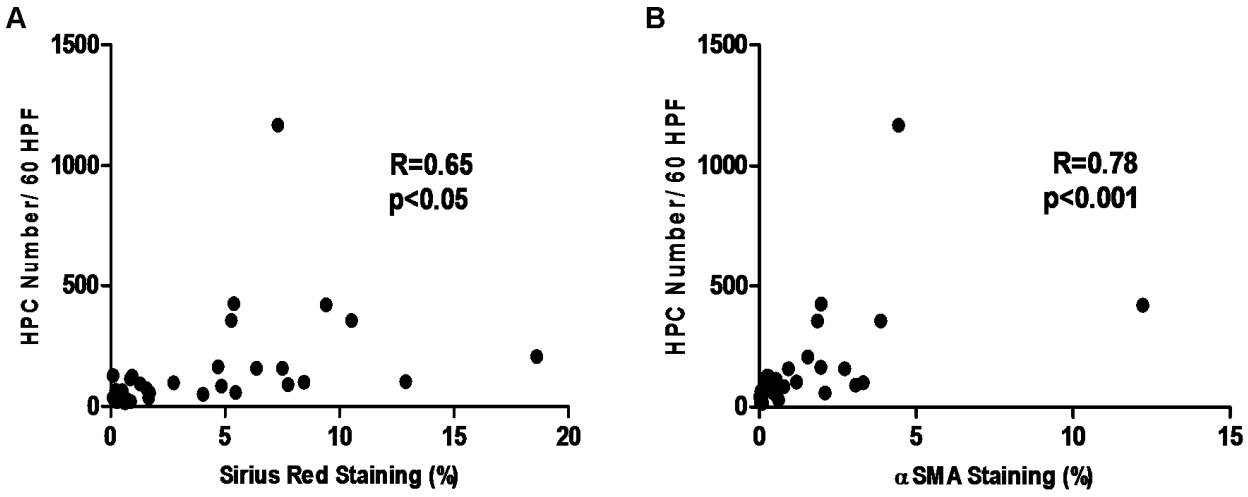

Figure 4.3 Graphs showing the statistical correlation between mean HPC numbers (non-bile duct-associated CK-19 positive cells/ 60 high power fields) and (A) liver fibrosis [PSR-staining] and (B) myofibroblast activation [αSMA-staining] in a CCl_4 model of rat liver fibrosis. In each case R= Spearman correlation co-efficient and p values are as indicated (n= 37).

4.2.3 Relationship between changes in liver stiffness and HPC response in a rat CCl_4 model of liver fibrosis

It has previously been demonstrated that liver stiffness increases with duration of CCl_4 administration in a rat model of liver fibrosis (Figure 4.4 A) (135). The values liver stiffness (G') in rats untreated control animals, olive oil controls and CCl4 treated animals (value ± SEM) were: untreated baseline control, 374.1 ± 49.7Pa; 7 days, olive oil control 413.5 ± 2.2Pa/ CCl_4 763.6 ± 84.2Pa; 14 days, olive oil control 532.7 ± 73.0Pa/ CCl_4 642.8 ± 28.0Pa; 28 days, olive oil control 587.3 ± 30.9Pa/ CCl_4 829.6 ± 51.3Pa; 42 days, olive oil control 637.5 ± 29.8Pa/ CCl_4 1349.0 ± 61.9Pa; 56 days, olive oil control 548.9 ± 24.5Pa/ CCl_4 1471.0 ± 251.2Pa; olive oil control 425.7 ± 54.6Pa/ CCl_4 1504 ± 150.2Pa. Liver stiffness (G') is increased after 7 days of CCl_4 treatment (2.0-fold, $p<0.001$), relative to untreated controls. G' continues to increase to day 42 of CCl_4 treatment (3.6-fold, $p<0.0001$) and then stabilises. The values for HPC numbers per 60 high power fields with increasing duration of CCl4 treatment were: day 7, 78.5 ± 13.5; day 14, 76.0 ± 7.5; day 28, 54.0 ± 4.0, day 42, 116.0 ± 24.4; day 56, 196.2 ± 43.0; and day 70, 492.2 ± 179.7. There is positive correlation between liver stiffness and HPC numbers ($R=0.79$, $p<0.0001$) (Figure 4.4 B). It is evident that the major increase in liver stiffness (G') precedes the major expansion in HPC numbers in this CCl_4 model of rat liver fibrosis (Figure 4.4 C).

Figure 4.4: Relationship between changes in liver stiffness and HPC response in a CCl_4 model of rat liver fibrosis

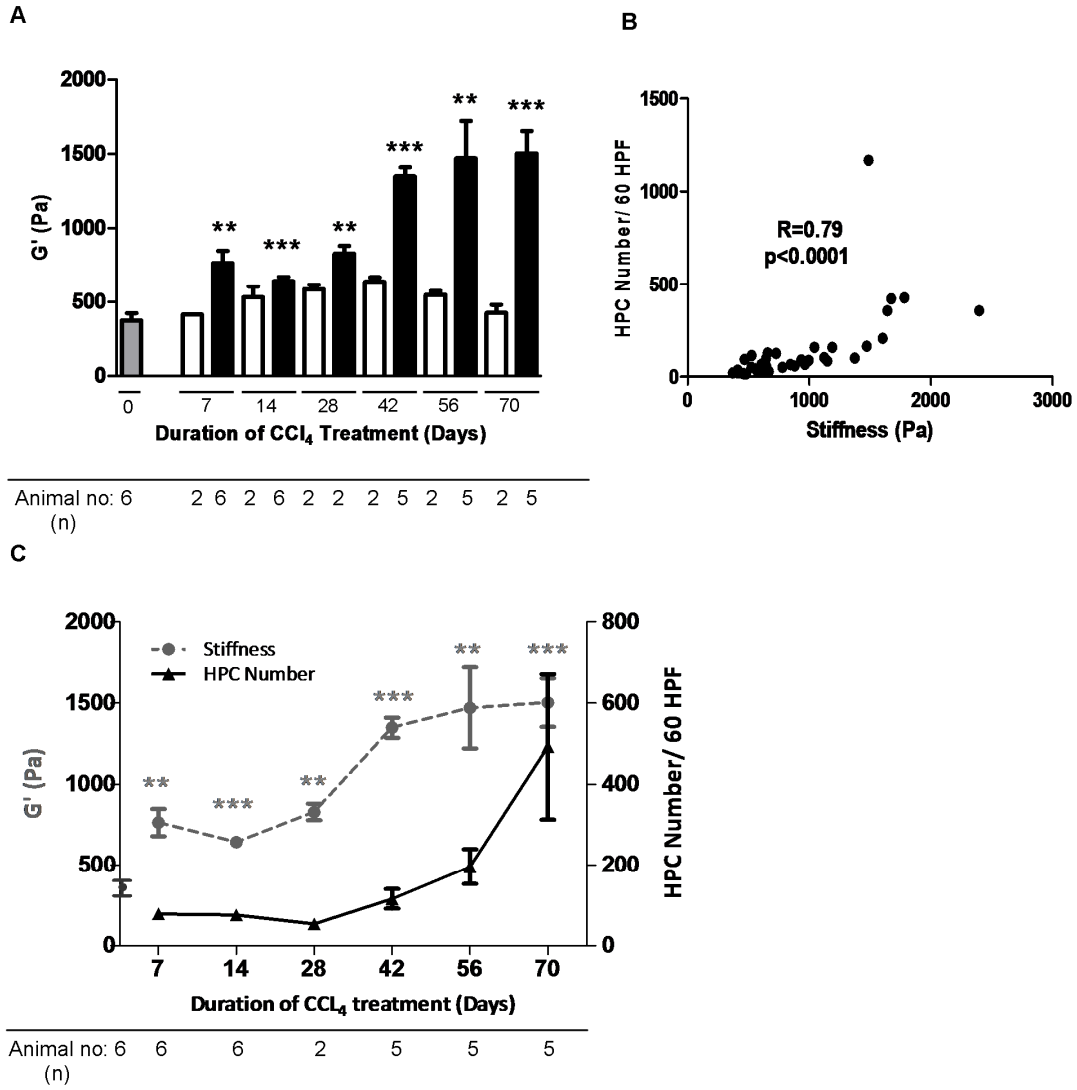

Figure 4.4: Graphs showing the relationship between liver stiffness (G') and HPC numbers in a CCl_4 model of liver fibrosis. (A) Liver stiffness increases with duration of CCl_4 administration (black bars) relative to untreated control animals (grey bars) and vehicle-treated controls (white bars). The precise number of animals (n) represented by each bar is indicated below each graph. (B) There is a positive correlation between mean liver stiffness measurements and mean HPC numbers (assessed by direct cell counting of non-bile-duct-associated CK19-positive cells per 60 high-power fields). (C) Graph showing the relationship between G' (grey line) and HPC numbers (black line) in this CCl_4 model of rat liver fibrosis. In respect to liver stiffness, statistical comparison to the baseline liver stiffness in untreated animals is made using an unpaired student t test. In each case error bars represent SEM, *p<0.05, **p<0.01, ***p<0.001, ns= not statistically significant and R= Spearman correlation co-efficient.

4.2.4. The effect of BAPN on liver stiffness and HPC response in a rat CCl_4 model of liver fibrosis

It has been shown, both *in vitro* and *in vivo,* that enhanced collagen cross-link formation may increase collagen stiffness (G') independent of collagen deposition (44-47)**.** As previously discussed, LOX is a copper-dependent amine oxidase that initiates intra- and inter-molecular cross-linking of collagen. LOX is upregulated early after liver injury and has been shown that reducing LOX activity with β-aminopropionitrile (BAPN) attenuates tissue stiffness and prevents liver fibrosis in a rat model of liver fibrosis (135). In these experiments liver fibrosis was induced by twice-weekly injection of 0.2ml/100mg of a 1:1 mixture of CCl_4 in olive oil. A second cohort of rats also received treatment with BAPN (2mg/ml in drinking water) for the duration of CCl_4 injury. Both vehicle-treated (olive oil alone), non-injected and non-injected/ BAPN treated animals were used as controls. It has previously been shown that CCl_4-treated animals have increased liver stiffness (G') in comparison to normal (uninjured) and vehicle-treated control animals (135). It has also been demonstrated that BAPN treatment of CCl_4-injured rats results in a marked blunting of the early increase in liver stiffness. In rats receiving CCl_4-treatment the mean liver stiffness (G') after 14 days treatment was 506Pa compared to a liver stiffness value of 359Pa in CCl_4/ BAPN-treated animals ($p= 0.003$). HPC response in this model was subsequently assessed by direct cell counting of CK-19-positive cells (Figure 4.5). The values for HPC number per 60 high power fields were: day 0, uninjected, 42.5 ± 8.5; day 6, CCl_4 76.8 ± 11.4/ CCl_4 + BAPN 66.5 ± 4.0; day 14, CCl_4 99.2 ± 17.0/ CCl_4 + BAPN 81.2 ± 12.4/ BAPN alone 37.8 ± 6.4.

Overall there was a trend towards a reduction in HPC numbers in CCl_4/ BAPN-treated animals in comparison to those receiving CCl_4 alone, but this difference was not statistically significant. In our earlier CCl_4-model of rat liver fibrosis, it was shown that the major expansion in HPC numbers does not occur until after 42 days of injury. Therefore it might be expected that a longer duration of injury would be required in order to evaluate whether BAPN-treatment might attenuate HPC responses in CCl_4-induced liver injury.

Figure 4.5: The effect of BAPN on HPC response in a 2 week CCl_4 model of rat liver fibrosis

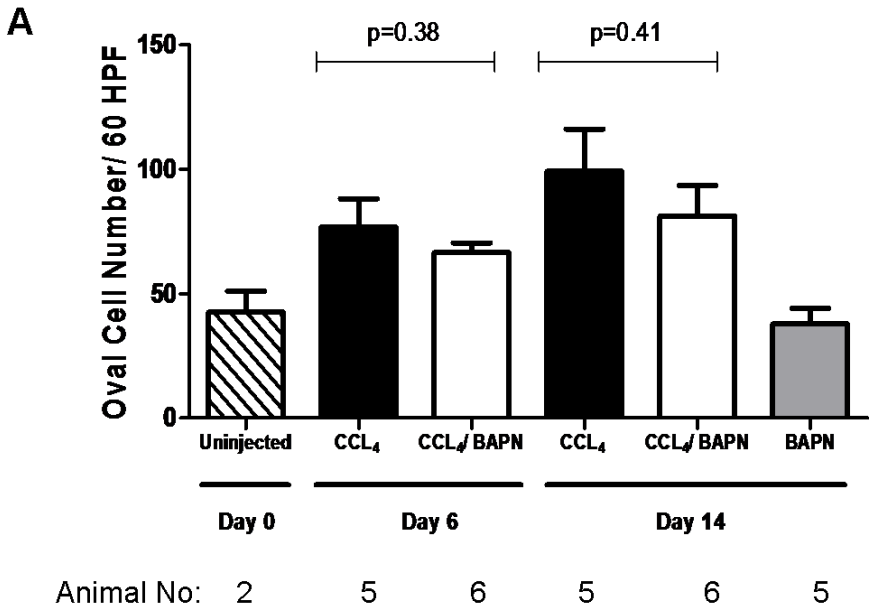

Figure 4.5: The effect of BAPN treatment on HPC response in a CCl_4 model of rat liver fibrosis. Quantification of CK-19 positive HPCs in liver sections from rats treated for between 6 and 14 days with either CCl_4-alone (black bars) or CCl_4/ BAPN (white bars), as indicated. Comparison is made to non-injected (hatched bar) and non-injected/ BAPN-treated control animals (grey bar). Each bar represents the mean number of non-bile duct associated CK-19 positive cells per 60 high-power (x320) fields from 2-6 animals. The number (n) of animals represented by each bar is indicated below the x-axis of the graph. Comparison between mean measurements was made using a student t test. In each case error bars represent SEM and p values are as indicated.

4.3. Changes in environmental stiffness regulate HPC morphology and cytoskeletal organisation *in vitro*

In order to investigate how changes in the stiffness of the cellular microenvironment might affect HPC responses, experiments were undertaken in which HPCs were cultured on matrix-coated PA supports of defined stiffness. The stiffness of the PA supports was modelled across a pathophysiologically relevant range (1-12kPa) corresponding to changes in stiffness that would be encountered by cells in the transition from a normal to a fibrotic (or cirrhotic) liver. Initial experiments were undertaken using an immortalised bi-potential murine oval cell line (BMOL). It has previously been shown that in proliferating culture conditions BMOL cells express abundant oval cell and biliary cell markers (including CK-19) (216). However under conditions favouring differentiation, BMOL cell up-regulate markers of hepatocyte differentiation. BMOL cells were cultured on PA gel supports of defined stiffness that were coated with either laminin or collagen-IV. The effect of changes in support stiffness on the organisation of the actin cytoskeleton was assessed following staining with fluorescently-labelled phalloidin (Figure 4.6). Cells cultured on laminin-coated 1kPa supports were generally small and rounded with homogeneously distributed F-actin staining. In contrast, cells cultured on laminin-coated 12kPa supports demonstrated enhanced cell spreading and prominent F-actin stress fibre formation. A similar trend in respect to cytoskeletal organisation was seen when BMOL cells were cultured on collagen-IV-coated PA supports (data not shown). Changes in cell spreading as a function of support stiffness were quantified by digital image analysis of phase contrast photomicrographs. Cell spreading was measured in relation to projected cell surface area (μm^2). In BMOL cells cultured on laminin-coated PA supports, values for projected surface area (value ± SEM) were: 1kPa, 379 ± 21μm^2; 2.5kPa, 531 ± 26μm^2; 12kPa, 687 ± 47μm^2; and laminin-coated glass, 1808 ± 95μm^2. In BMOL cells cultured on collagen-IV-coated PA supports, values for projected surface area (value ± SEM) were: 1kPa, 709 ± 26μm^2; 2.5kPa, 904 ± 45μm^2; 12kPa, 1008 ± 66μm^2; and laminin-coated glass, 1808 ± 128μm^2. In BMOL cells cultured on both laminin- and collagen-IV-coated PA supports, projected surface area increased as a function of increasing support stiffness (Figure 4.6 C). Cell spreading was maximal when cells were cultured on matrix-coated glass, which has a supra-physiological stiffness (giga-pascal range).

Figure 4.6: The effect of PA support stiffness on cytoskeletal organisation and cell spreading in BMOL cells

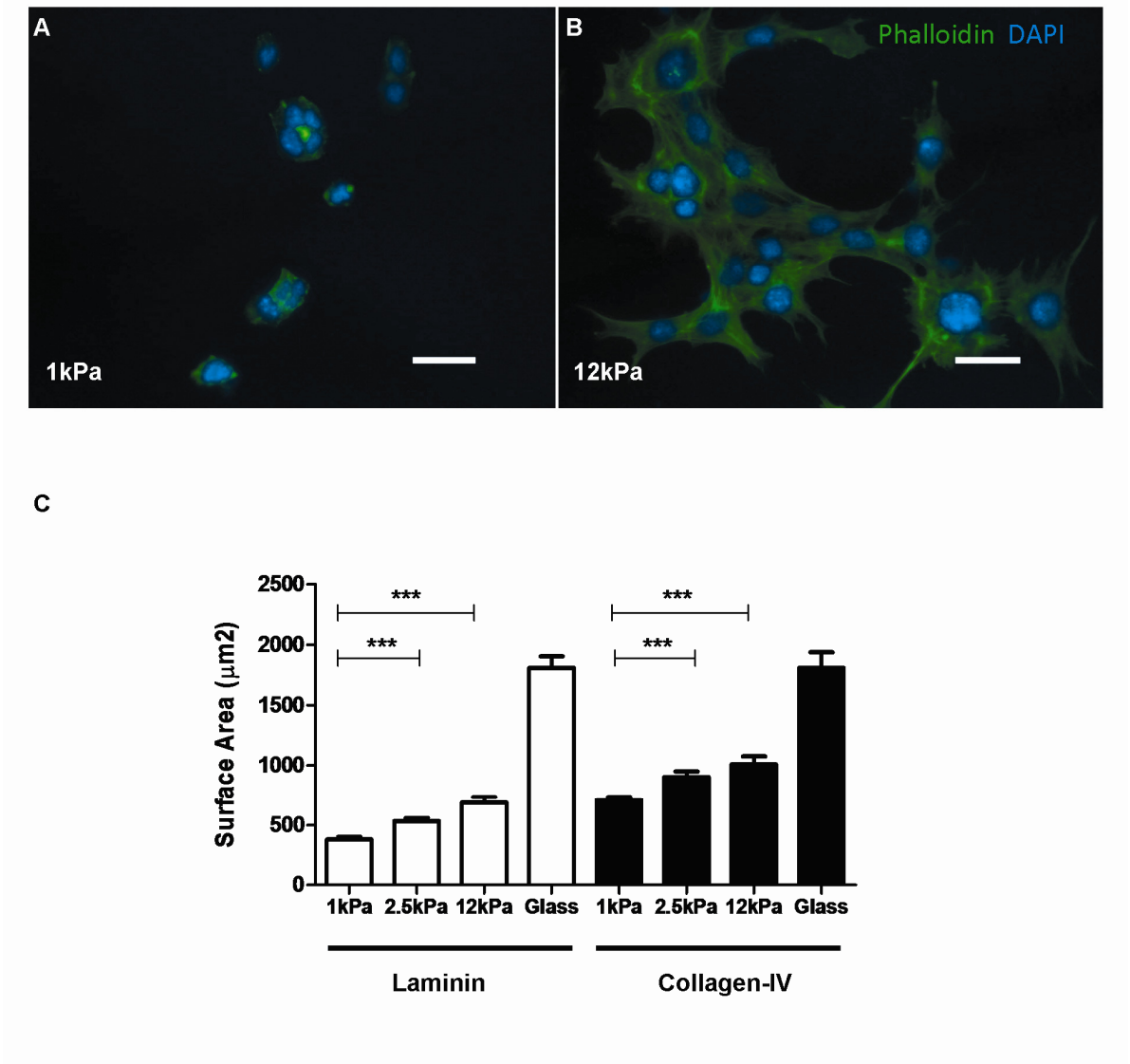

Figure 4.6 (A/B) Photomicrographs (x 320 magnifications) showing BMOL cells cultured on soft (1kPa) and stiff (12kPa) laminin-coated PA supports and stained for the presence of actin stress fibres (phalloidin-green) and nuclear DNA (4', 6'-diamidino-2-phenyl-indole dihydrochloride) (DAPI-blue). The scale bar indicates 200 microns. (C) Graph showing the relationship between cells spreading and polyacrylamide support stiffness for BMOL cells cultured on laminin (white) and collagen-IV (black) coated supports. Comparison is made to cells cultured on matrix-coated glass supports. Cell spreading is expressed as projected surface area (μm^2) calculated by digital image analysis of phase contrast photomicrographs. In each case, the bars represent the mean (±SEM) of measurements from 50 cells (n=50) randomly selected from photomicrographs of cells cultured from PA gels in three independent experiments. Mean measurements were compared using an unpaired student t test (***$p<0.001$).

4.4 Increases in support stiffness promote HPC proliferation *in vitro*

Increasing substrate stiffness enhances cell proliferation in BMOL cells (Figure 4.7A). In a series of experiments BMOL cells were cultured on matrix-coated PA supports of defined stiffness (1-12kPa) coated with either laminin or collagen-IV. In BMOL cells cultured on laminin-coated PA supports, values for proliferative index (value ± SEM) were: 1kPa, 0.025 ± 0.005; 2.5kPa, 0.178 ± 0.045; 12kPa, 0.298 ± 0.057; and laminin-coated glass, 0.467 ± 0.267. In BMOL cells cultured on collagen-IV-coated PA supports, values for proliferative index (value ± SEM) were: 1kPa, 0.040 ± 0.013; 2.5kPa, 0.245 ± 0.063; 12kPa, 0.315 ± 0.045; and laminin-coated glass, 0.560 ± 0.019. In cells cultured on laminin-coated supports, the proliferative index of BMOL cells (assessed by nuclear localisation of Ki67 antigen) was 11.7-fold ($p<0.001$) higher when cells were cultured on 12kPa versus 1kPa supports. Similarly, in cells cultured on collagen-IV-coated PA supports, the proliferative index of BMOL cells was 8.0-fold ($P<0.001$) higher when cells were cultured on 12kPa versus 1kPa supports. In each case, the proliferative index of BMOL cells was maximal when cells were cultured at supra-physiological stiffness on matrix-coated glass (laminin or collagen-IV). Across a pathophysiologically relevant range (1-12kPa), there was no significant difference in the proliferative index of BMOL cells as a function of surface ligand identity (laminin Vs collagen-IV). These results would suggest that in the culture conditions employed in these experiments, it is the physical (as opposed to the biochemical properties) of the PA supports that exerts the dominant effect on BMOL proliferation. In each experiment, BMOL cells were plated at constant initial plating density. Direct cell counting of adherent cells 1 hour after plating confirmed that there was no significant difference in the initial adherance of cells as a function of PA support stiffness (data not shown). The results of proliferation experiments were replicated in experiments in which an MTT- assay was used to confirm that increasing matrix stiffness was associated with an increase in MTT conversion (as a proxy for total cell number) after a period of culture on laminin- or collagen-IV-coated supports (data not shown).

Experiments were subsequently undertaken using freshly isolated primary cells to confirm that increasing support stiffness promotes cell proliferation in primary murine HPCs (Figure 4.7B). Freshly isolated primary murine HPCs were cultured on matrix-coated PA supports of defined stiffness (1-12kPa) coated with either laminin or collagen-IV. The values for mean proliferative index (value ± SEM) in primary HPCs cultured on laminin-coated supports were: 1kPa, 0.044 ± 0.007; and 12kPa, 0.075 ± 0.005. The values for mean

proliferative index (value ± SEM) in primary HPCs cultured on collagen-IV-coated supports were: 1kPa, 0.037 ± 0.008; and 12kPa, 0.087 ± 0.011. In cells cultured on laminin-coated supports, the proliferative index (Ki67 positivity) of primary HPCs was 1.7-fold higher ($p<0.05$) in cells cultured on 12kPa versus 1kPa supports. Similarly, on collagen-IV-coated supports, the proliferative index of primary HPCs was 2.4-fold higher ($P<0.05$) when cells were cultured on 12kPa versus 1kPa supports.

Immunoblot analysis of cell lysates from BMOL cultured on laminin- and collagen-IV-coated PA supports demonstrates that increasing support stiffness promotes upregulation of cyclin D1 (Figure 4.8). The values from densitometry analysis (arbitrary units) of cyclin D1 expression (value ± SEM) relative to GAPDH expression are: collagen-IV, 1kPa 1.0, 2.5kPa 2.98 ± 0.10, 12kPa 6.24 ± 0.75, and collagen-IV-coated glass 9.13 ± 0.90; and laminin, 1kPa 1.0, 2.5kPa 1.77 ± 0.62, 12kPa 2.32 ± 0.99, and laminin-coated glass 2.04 ± 0.87. All results are expressed relative (standardised) to cyclin D1 expression on the relevant 1kPa support. Cyclin D1 expression is 6.2-fold higher ($p<0.01$) in BMOL cells cultured on collagen-IV-coated 12kPa versus 1kPa supports. Similarly cyclin D1 expression is 2.3-fold higher ($p=0.26$) on laminin-coated 12kPa versus 1kPa supports. Similar results have been obtained in respect to cyclin D3 (data not shown).

Figure 4.7: Effect of changes in PA support stiffness on proliferation in BMOL cells and primary murine HPCs

A

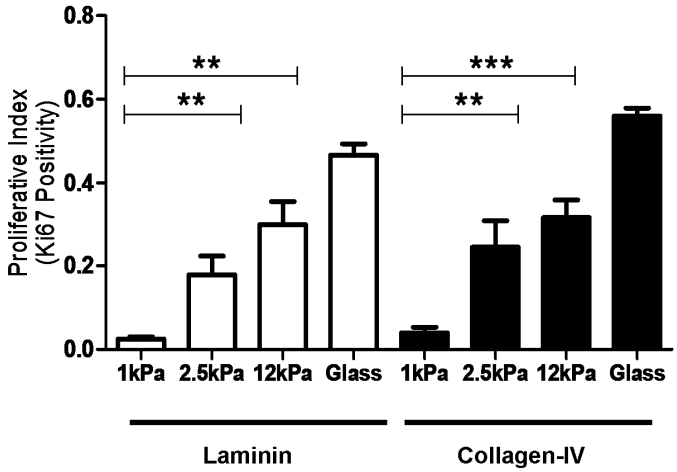

B

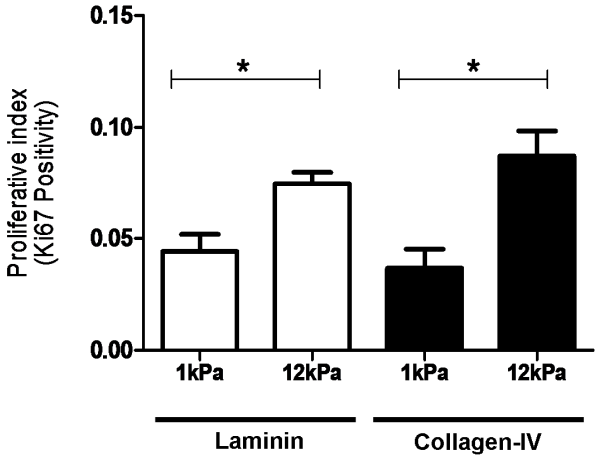

Figure 4.7 (A) Graph showing the effect of changes in support stiffness (kPa) on the proliferative index (Ki67-positivity) of BMOL cells. Experiments were conducted on laminin (white) and collagen-IV-coated (black) PA gel supports (1-12kPa) and matrix-coated glass, as indicated. (B) Graph showing the effect of changes in support stiffness on the proliferative index of primary murine HPCs. In each case, values reflect the mean (±SEM) of measurements from 3 independent experiments (*$p<0.05$, **$p<0.01$ and ***$p<0.001$). Statistical comparisons between mean measurements were made using a student t-test (n=3). The cell counting data from which these graphs are derived is presented in Appendix 14.

Figure 4.8: The effect of matrix stiffness on cyclin D1 expression in BMOL cells

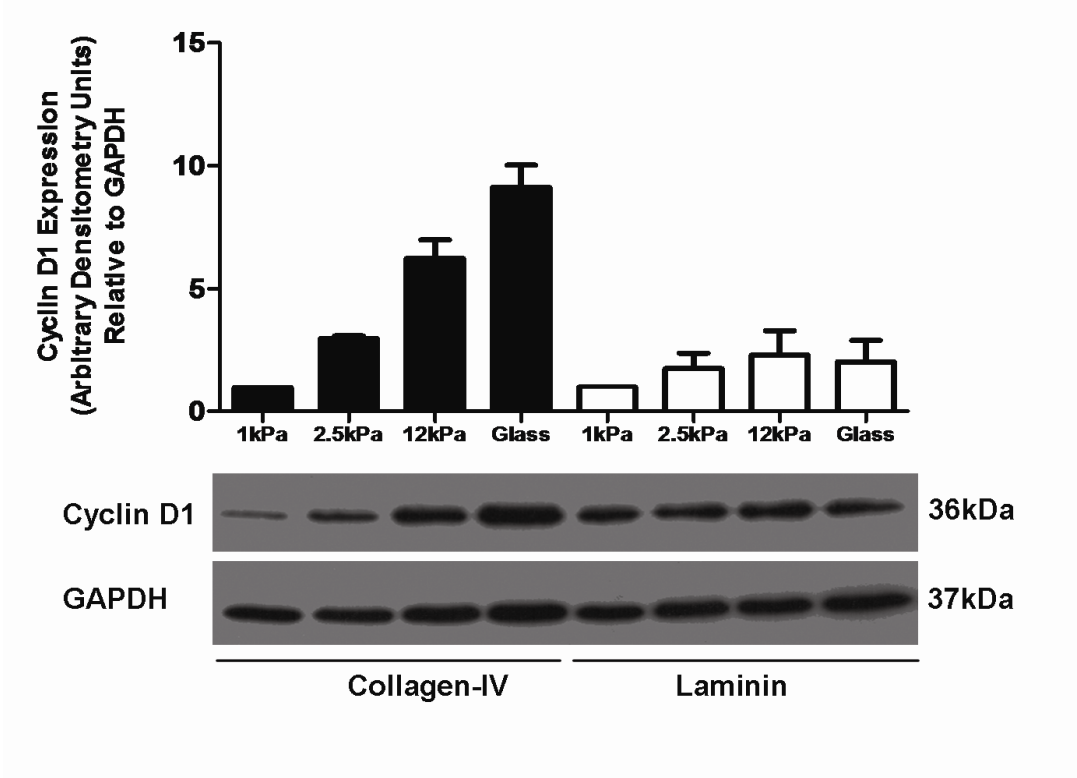

Figure 4.8 Western blot analysis of cyclin D1 expression in BMOL cells cultures on collagen-IV (black) and laminin-coated (white) PA gels of defined stiffness (1-12kPa) and collagen-IV-coated glass. In each western blot equal quantities of protein were loaded and equal loading confirmed in relation to glyceraldehyde-3-phosphate dehydrogenase (GAPDH) expression. The bar graph shows the results of densitometry analysis of cyclin D1 expression relative to GAPDH. In each case, values represent the mean (±SEM) of measurements from 3 independent experiments (n=3). Results are standardised to expression of cyclin D1/ GAPDH in cell cultured on 1kPa supports.

4.5 Changes in support stiffness modulate cell differentiation in HPCs

Experiments were undertaken to assess whether changes in matrix stiffness might modulate HPC differentiation (progenitor cell fate). BMOL cells were cultured in low serum conditions on either 1kPa or 12kPa laminin-coated polyacrylamide supports. After six days in culture, cells were harvested for mRNA. The effect of support stiffness on cell differentiation was assessed by real-time quantitative PCR against a panel of progenitor cell, biliary and hepatocyte-specific markers (Figure 4.9). The values for mRNA expression (value ± SEM) of selected genes (expressed as fold induction standardised to GAPDH relative to expression of gene of interest on 1kPa supports) are: albumin, 1kPa 1.00 ± 0.05/ 12kPa 0.66 ± 0.06; Cyp7A1, 1kPa 1.00 ± 0.06/ 12kPa 0.62 ± 0.04; cytokeratin-19, 1.00 ± 0.07/ 12kPa 1.57 ± 0.20; aquaporin, 1.00 ± 0.08/ 12kPa 0.96 ± 0.14; gamma-glutamyl transferase, 1kPa 1.00 ± 0.16/ 12kPa 0.90 ± 0.11. BMOL cells cultured on 12kPa supports down-regulated the expression of hepatocyte-specific markers including albumin (1.5-fold, $p<0.01$) and CYP7A1 (1.6-fold, $p<0.01$), in comparison to cells grown on 1kPa supports. In contrast, expression of cytokeratin-19, a marker of biliary and progenitor cell differentiation, was up-regulated (1.6-fold, $p<0.01$) in cells maintained on 12kPa supports, relative to cells on 1kPa supports. There was no significant difference in the expression of the biliary epithelial markers aquaporin and gamma-glutamyl transferase (γGT) in BMOL cells as a function of support stiffness.

Figure 4.9: The effect of PA support stiffness on BMOL differentiation

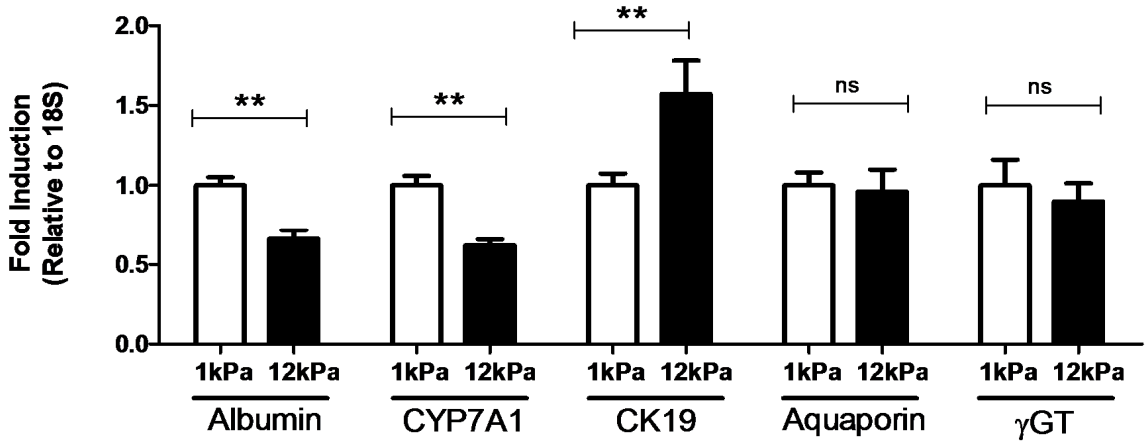

Figure 4.9 Graph showing the effect in BMOL cells of changes in support stiffness on mRNA expression of a panel of progenitor cell, biliary and hepatocyte markers. BMOL cells were cultured for 6 days in low serum conditions on either 1kPa (white) or 12kPa (black) laminin-coated PA supports. For each gene of interest mRNA expression, relative to the 18S housekeeping gene, was measured using real-time quantitative PCR. Values are expressed as fold-induction relative to mRNA expression in cells cultured on 1kPa supports. Statistical differences between mean values (n=6) were determined using an unpaired student t-test (**$p<0.01$, ns = not significant).

4.6 FAK, ROCK and myosin-II regulate cell proliferation in HPCs *in vitro*

Immunofluorescent staining of BMOL cells cultured on laminin-coated PA supports demonstrates that increasing support stiffness promotes FAK activation. BMOL cells cultured on 12kPa demonstrate strong staining for phospho-FAK^{Tyr397}, which is absent from cells cultured on 1kPa supports (Figure 4.10). FAK, ROCK and myosin-II have previously been identified as being important mediators of mechanotransduction and stiffness-sensing responses. BMOL cells were cultured on both laminin- and collagen-IV-coated tissue culture plastic, in the presence and absence of small molecular inhibitors of FAK [PF573228], ROCK [Y-27632] and myosin-II [blebbistatin] (Figure 4.11). Experiments were performed in low serum conditions in the presence of supplemental epithelial growth factor (EGF) [20mg/ml]. An MTT assay was employed to assess cell proliferation. MTT conversion is a measure of cell viability and is an indirect measure of cell number. In each case, the addition of contractile inhibitors significantly reduced BMOL cell numbers/ proliferation. In experiments in which BMOL cells were cultured on laminin-coated tissue plastic the values for MTT conversion (value ± SEM) were: water control, 0.206 ± 0.001; Y-27632 (10mM), 0.156 ± 0.008; Y-27632 (50mM), 0.127 ± 0.006; DMSO control, 0.174 ± 0.010; PF-573228 (1mM), 0.095 ± 0.005; PF-573228 (5mM), 0.081 ± 0.059; blebbistatin (10μM), 0.152 ± 0.007; blebbistatin (50μM), 0.128 ± 0.005. BMOL proliferation (as assessed by MTT measurement) was reduced by treatment with PF573228 both at 1μM (46% reduction , $p<0.001$) and 5μM (54% reduction, $p<0.0001$), relative to suitable vehicle controls (DMSO). Similarly, BMOL proliferation was reduced by treatment with Y-27632 both at 10μM (24% reduction, $p<0.01$) and 50μM (39% reduction, $p<0.001$) relative to vehicle control (water). Treatment with blebbistatin was associated with more modest reductions in BMOL proliferation both at 10μM (13% reduction, $p<0.001$) and 50μM (26% reduction, $p<0.001$), relative to vehicle control (DMSO).

A similar trend was seen in MTT experiments conducted in BMOL cells cultured on collagen-IV-coated tissue culture plastic. Values for MTT conversion (value ± SEM) were: water control, 0.185 ± 0.008; Y-27632 (10mM), 0.145 ± 0.003; Y-27632 (50mM), 0.125 ± 0.008; DMSO control, 0.166 ± 0.011; PF-573228 (1mM), 0.093 ± 0.003; PF-573228 (5mM), 0.078 ± 0.004; blebbistatin (10μM), 0.118 ± 0.016; blebbistatin (50μM), 0.095 ± 0.006. BMOL proliferation was reduced by FAK inhibition with PF573228 at both at 1μM (44% reduction, $p<0.001$) and 5μM (53% reduction, $p<0.001$). ROCK inhibition with Y-27632 reduced BMOL proliferation at 10μM (22% reduction, $p<0.001$) and 50μM (32% reduction,

p<0.001). Similarly, myosin-II inhibition with blebbistatin reduced BMOL proliferation at both 10μM (29% reduction, p<0.05) and 50μM (43% reduction, p<0.001).

Figure 4.10: Immunofluorescent staining showing the effect of PA stiffness on FAK activation in BMOL cells

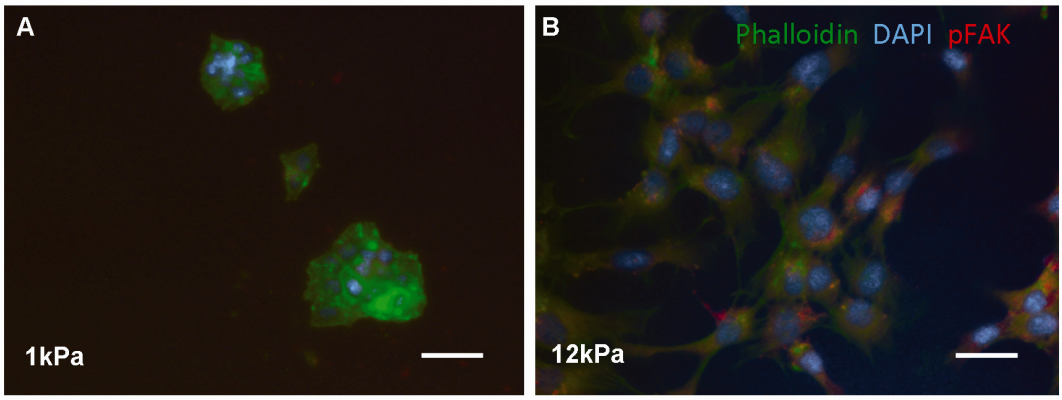

Figure 4.10 Photomicrographs (x 320 magnifications) showing BMOL cells cultured (A) soft (1kPa) and (B) stiff (12kPa) laminin-coated polyacrylamide supports and stained for the presence of phospho-FAK^{Tyr397} (red), actin stress fibres (phalloidin-green) and nuclear DNA (4',6'-diamidino-2-phenyl-indole dihydrochloride) (DAPI-blue). Cells cultures on the stiffer (12kPa) supports demonstrate strong staining for activated FAK, which is absent from cells cultured on softer (1kPa) supports. The scale bar indicates 200 microns.

Figure 4.11: The effect of small molecular inhibitors of FAK, ROCK and myosin-II on proliferation in BMOL cells

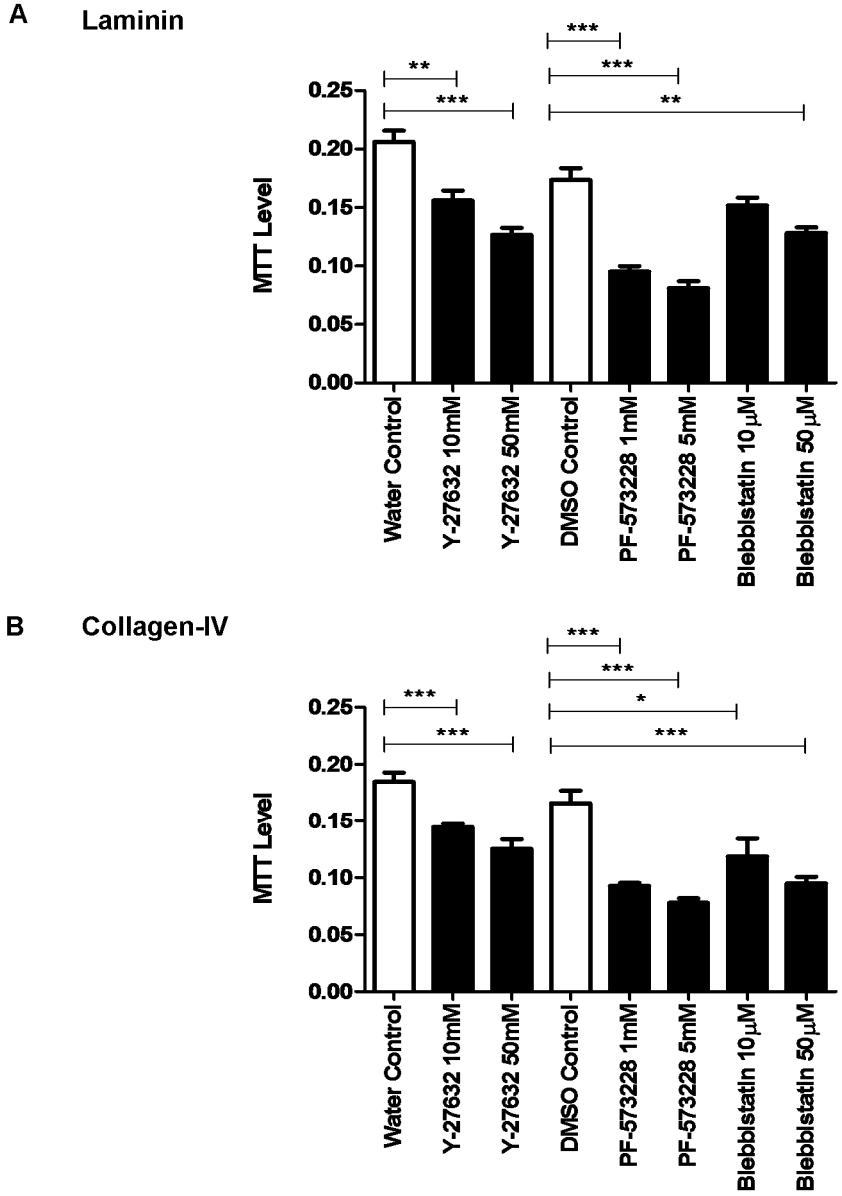

Figure 4.11 Graphs showing the effect of contractile inhibitors on MTT conversion (reflecting cell number/ viability) in BMOL cells. BMOL cells were cultured in low serum conditions for 120 hours on (A) laminin-coated plastic and (B) collagen-IV-coated plastic, in the presence and absence of small molecular inhibitors of FAK (PF573228), ROCK (Y-27632) and myosin-II (blebbistatin) at the concentrations indicated. Comparison is made to suitable vehicle controls corresponding to the solvent used in the solubilisation of the small molecular inhibitors [Y-27632 (water) and PF573228/ blebbistatin (DMSO)]. In each case, bars represent the mean (±SEM) from 3 experiments (*$p<0.05$, **$p<0.01$ and ***$p<0.001$). Statistical comparisons between means (n=3) were made using an unpaired student t-test.

4.7 Discussion

The results of these experiments suggest that alterations in the stiffness of the extracellular environment may be important in regulating HPC responses in chronic liver disease. Normally following liver injury, cell loss is restored through the replication of mature hepatocytes and cholangiocytes, as illustrated following bile duct ligation or partial hepatectomy (281). The HPC compartment represents a reserve compartment that is activated when mature hepatocytes or cholangiocytes are subjected to chronic or repeated injury, or where the regenerative capacity of these cells is overwhelmed following severe tissue damage. This can be demonstrated experimentally in animal models where hepatocyte injury (e.g. choline-deficient diet or partial hepatectomy) is accompanied by the administration of substances that inhibit the replicative capacity of hepatocytes (e.g. ethionine or 2-acetylaminofluorine) (279, 295). The choline-deficient ethionine supplemented (CDE) diet has become established as a reliable model of hepatocellular regeneration with marked HPC expansion (295). Similarly, a dramatic expansion in HPC numbers has been observed in transgenic models in which hepatocyte regeneration is inhibited by conditional over-expression of the cell cycle inhibitor p16 (296). As previously discussed, oval cell proliferation is also enhanced in animal models of liver fibrosis in the absence of known hepatocyte inhibitors (289). However, it is unclear whether factors associated with liver fibrosis may promote HPC proliferation, or whether the severity of liver fibrosis is simply a surrogate marker for hepatocyte damage and impairment of hepatocyte-mediated regeneration. Our results in both the TAA and CCl_4 models of rat liver fibrosis demonstrate a close association between HPC expansion and liver fibrosis severity. In both models, the major expansion in HPC numbers corresponds temporally to a similar large increased in scar tissue deposition. However, more modest early increases in HPC numbers occur prior to the development of significant fibrosis.

We have proposed that changes in liver stiffness may be important in regulating HPC behaviour. It has previously been shown that liver stiffness increases with both the duration and severity of liver fibrosis (135). However, the early increase in liver stiffness precedes the major increase in scar deposition. Similarly, in our model of CCl_4-induced liver fibrosis, increases in liver stiffness precede the major expansion in HPC numbers. The factors responsible for this early increase in liver stiffness are uncertain but may include interstitial oedema due to acute inflammation or early increases in collagen fibril cross-linking. This is the first study to explicitly explore the relationship between hepatic stiffness and HPC

response *in vivo*. Our *in vivo* observations demonstrate a close association between liver stiffness measurements and HPC expansion, suggesting that alterations in the mechanical properties (stiffness) of the stem cell niche may be important in regulating HPC proliferation. This is backed up by detailed *in vitro* experiments that demonstrate that increases in environmental stiffness, across a pathophysiologically-relevant range (1-12kPa) promote HPC proliferation. These results were obtained in both an immortalised rat oval cell line (BMOL) and primary murine HPCs. In each case, it is the physical characteristics, rather than the biochemical composition of the matrix, that exerts the dominant effect on HPC proliferation. Our results suggest that increasing matrix stiffness promotes cell cycle progression with increased expression of cyclin D1. This would be consistent with published results showing that physiological stiffness is inhibitory to cell cycle progression (97). Conversely, increases in the stiffness of the stem cell niche, as occur following tissue injury and liver fibrosis may be mechanistically important in promoting HPC proliferation. Further experiments are required to more closely characterise the effect of changes in matrix stiffness on other regulators of cell cycle progression, including the cyclin-dependent-kinase inhibitors p21 and p27.

If increased matrix stiffness is an important factor in promoting HPC proliferation, then it would be expected that therapeutic interventions to either attenuate increases in ECM stiffness, or disrupt mechanotransduction responses, would impair HPC proliferation. It has previously been shown that BAPN can attenuate increases in both liver stiffness and liver fibrosis in a CCL_4 model of rat liver fibrosis (135). This is believed to be due to inhibition of LOX-mediated collagen cross-linking. Using liver tissue derived from this two-week CCl_4 model we demonstrated a trend towards a reduction in HPC numbers in CCl_4/ BAPN-treated animals in comparison to those receiving CCl_4-alone. This difference was not statistically significant. We have previously shown in a more protracted model of CCl_4 injury that the major expansion in HPC numbers did not occur until 42 days of twice weekly CCl_4 administration. As such, we would anticipate that a longer duration of injury would be required in order to properly assess whether BAPN can attenuate HPC responses in CCl_4-induced liver injury, and so reduce the probability of type II statistical error. Further experiments with a more protracted model of fibrotic liver injury are required.

Our *in vitro* experiments with matrix-coated PA gels show a close relationship between support stiffness and HPC proliferation. We have shown that increases in matrix stiffness, across of pathophysiologically-relevant range (1-12kPa), promotes FAK activation. FAK

activation is a pivotal event in integrin-mediated signalling. Our experiments in HPCs maintained on stiff substrates show that biochemical inhibition of FAK reduces cell proliferation. This is consistent with previous studies which have shown that FAK activation promotes cell cycle progression/ cellular proliferation (297, 298). Similarly, biochemical inhibition of ROCK and myosin-II (critical mediators of mechanotransduction responses) attenuate HPC proliferation on stiff substrates. ROCK and FAK are known to interact with each other through multiple signalling molecules. It has also been shown that ROCK is required for FAK activation (tyr^{397} phosphorylation) in response to mechanical stretch (299). Inhibition of mechanotransduction responses (stiffness-sensing) may therefore represent an effective method of modulating HPC proliferation.

The effects of changes in ECM stiffness on HPC differentiation remain poorly characterised. Our results suggest that a low stiffness environment, with characteristics similar to that of the normal liver, promotes a modest up-regulation of hepatocyte-specific markers in BMOL cells. Conversely, HPCs exposed to stiffer substrates demonstrated up-regulation of the biliary/ progenitor cell marker CK-19. These results are consistent with published results in hepatocytes and our own results looking at the effect of matrix stiffness on HCC differentiation. Hepatocytes maintained on softer substrates demonstrate higher levels of albumin excretion and differential responses to growth factor stimulation, indicative of a more differentiated phenotype (142). Similarly, Lozoya *et al* investigated the effect of matrix stiffness on foetal-derived human hepatic stem cell differentiation in three-dimensional hyaluronic acid (HA) based hydrogels (300). They demonstrated that changes in hydrogel stiffness affected the both viability of hepatic stem cells and levels of urea, albumin and AFP secretion (hepatic metabolism). The effect of changes in matrix stiffness on BMOL differentiation *in vitro*, are less pronounced. This may in part relate to the specific properties of the BMOL cell line.

Overall, these results are consistent with a biomechanical model of HPC regulation. It is proposed that a low stiffness environment, as encountered in the normal liver, may be important in maintaining HPC quiescence. In contrast, pathophysiological increases in niche stiffness that would be encountered in the context of acute inflammation or liver fibrosis, would promote progenitor cell expansion. Further experiments are required to explore the effect of changes in matrix stiffness on mitogenic signalling in HPCs.

Finally, it is important to consider to the extent to which results may provide insight into the pathogenesis of HCC. HCC may be derived from at least four distinct lineages, including hepatocytes, mature cholangiocytes, HPCs and periductular cells (50, 53). It has previously been demonstrated that increasingly matrix stiffness promotes tumour develop in a murine model of breast cancer (46). I have also shown that alterations in matrix stiffness modulate proliferation and stem cell characteristics in HCC (chapter 3). Our results demonstrate that increasing matrix stiffness, as would be encountered in the cirrhotic liver, promotes proliferation in HPCs. As such, alterations in the biochemical properties of the HPC niche associated with acute inflammation and liver fibrosis may be important in promoting hepatocarcinogenesis.

Chapter 5: Studies to characterise the effect of chronic passive congestion on liver fibrogenesis

5.1 Introduction

Hepatic injury as a consequence of cardiac dysfunction is a commonly encountered clinical syndrome that remains incompletely characterised. The term cardiac hepatopathy describes the spectrum of pathological changes occurring in the liver as a consequence of cardiac dysfunction. The principle histological features observed in this context are chronic passive congestion (CPC) and centrilobular necrosis (CLN) (301). These are distinct morphological entities that are frequently observed concurrently. CPC is regarded as a consequence of elevated hepatic venous pressure, as will occur in right-heart failure. In contrast, CLN (or ischaemic hepatitis) is commonly seen in the context of severe hypotension due to cardiogenic shock or circulatory collapse. A number of studies have suggested the existence of reciprocal potentiation of CPC and CLN, whereby local alterations resulting from one lesion may enhance the underlying pathological features of the other (301-303).

Longstanding cardiac dysfunction is associated with the development of liver fibrosis (304). Histological studies in humans have defined the pattern of morphological changes in the liver resulting from chronic hepatic congestion. In mild hepatic congestion, liver histology is minimally disrupted, with a normal reticulin pattern. Progressive hepatic congestion results in centrilobular reticulin condensation, with loss of hepatocytes from the centrilobular region resulting in collapse of the reticulin stroma. This is followed by *de novo* centrilobular fibrosis with pronounced thickening of the centrilobular vein wall and variable extension of fibrous tissue spurs outward into the parenchyma. In severe heart failure there is progressive liver fibrosis with bridging fibrosis connecting adjacent central veins (reversed lobulation). This histological pattern is described as cardiac cirrhosis. The portal tracts are initially unaffected in this condition but may become involved in advanced disease and liver progenitor cell (oval cell) proliferation has been described in this context (304). Cardiac cirrhosis remains a rare condition, reflecting the low prevalence of and poor prognosis associated with prolonged heart failure (305).

The effect of chronic hepatic congestion on the development of liver fibrosis has been investigated in patients with chronic right heart failure occurring secondary to specific forms of congenital heart disease (306-309). The Fontan procedure was developed as a palliative

treatment for tricuspid atresia (310). The classical Fontan procedure involves the formation of a direct connection between the right atrium and pulmonary arteries. The circulation is supported by left ventricular contraction, with passive flow of blood into the lungs. This operation has been superseded by total cavo-pulmonary anastomosis, which avoids long-term complications related to right atrial enlargement and subsequent cardiac arrhythmias (atrial tachycardia). However, both operations result in chronic central venous hypertension, depressed dynamic cardiac output and late ventricular dysfunction. The long-term consequences of the Fontan procedure include alterations in the hepatic microvasculature with central venous hypertension, sinusoidal arterialisation, portal hypertension and progressive liver fibrosis. Liver fibrosis and cirrhosis are common complications of the Fontan procedure. Indeed, in an autopsy study, cirrhosis was present is all four long-term survivors of the Fontan procedure (306). In a detailed morphological study Kendall *et al* demonstrated that the histological features in the livers of Fontan patients are similar to those encountered in cardiac cirrhosis (307). In these patients, the liver is exposed to high venous pressure, with superimposed deep intra-hepatic reflux secondary to atrial contraction. Sinusoidal dilation is a prominent feature. Liver fibrosis was centred on the perivenular region with fibrous spurs extending outward into the parenchyma. Perisinusoidal fibrosis – similar to that typically encountered in steatohepatitis – was also prominent. Interestingly, inflammation (as defined by the presence of a lymphocytic infiltrate) was not a prominent feature in this cohort. The authors postulated that liver fibrosis in patients with the Fontan circulation might develop independently of inflammation. This effect may be mediated as a response to chronic hypoxia or mechanical stretch of the hepatic sinusoids and consequently the cells surrounding them. Sinusoidal dilation is a consequence both of elevated central venous pressure and intra-hepatic reflux secondary to atrial contraction. It has been shown in a related study that the extent of cirrhosis is positively correlated with hepatic vein pressures (308). Furthermore, there is a positive correlation between the duration of central venous hypertension and liver fibrosis score. However, it is also the case that inflammatory changes may be present prior to time of biopsy or may not be represented in the biopsy material (due to sampling error). In a large autopsy study of patients with both right- and left-sided congestive cardiac failure, CPC and CLN (with an associated inflammatory cell infiltrate) were frequently observed concurrently (301).

The precise aetiological factors responsible for the pathogenesis of liver fibrosis in cardiac hepatopathy remain poorly characterised. These may include: (1) Impaired cardiac output and diminished hepatic blood flow resulting in decreased hepatic oxygen delivery; (2)

Perisinusoidal oedema restricting diffusion of oxygen and nutrients; (3) Elevated central venous pressure (CVP) resulting in sinusoidal dilatation and hepatocyte plate compression; and (4) Cellular responses to alterations in matrix stiffness and cellular tension. A more detailed understanding of the sequence of pathological events contributing to liver fibrosis in chronic passive congestion requires the development of tractable animal models of cardiac hepatopathy. I have therefore undertaken studies to characterise the sequence of histological events in the liver in two unrelated models of murine dilated cardiomyopathy, with the intention that this would permit characterisation of the early events in the congested liver that contribute to the development of liver fibrosis. In particular, I wished to investigate the extent to which mechanical factors may promote the initiation and progression of liver fibrosis.

5.1.1 Hypotheses

- Chronic hepatic congestion, as encountered in murine models of dilated cardiomyopathy, may provide a model system analogous to the situation observed in human patients following the Fontan procedure.
- Mechanical factors, including alterations in matrix stiffness and cell strain consequent upon sinusoidal dilatation may promote liver fibrosis.
- Increases in matrix stiffness, across a pathophysiologically-relevant range, will enhance profibrotic gene expression in hepatic MFBs *in vitro*.
- Repetitive uniaxial stretch will enhance profibrotic gene expression in hepatic MFBs *in vitro*.

5.2 Murine models of cardiac hepatopathy

5.2.1 The python model of cardiac hepatopathy

The python model of dilated cardiomyopathy (DCM) was generated by Prof Neil Dear (University of Leeds) using N-ethyl-N-nitrosurea (ENU) mutagenesis, as previously described (203). The phenotype is inherited in an autosomal dominant fashion with complete penetrance in both sexes. Features of congestive cardiac failure included shallow rapid breathing, piloerection, subcutaneous oedema, ascites and pleural effusions. The median onset of overt symptoms on a C3H/ HeN genetic background is 83 days for males and 91 days for females. The pattern of cardiac histology and haemodynamic changes

occurring in the python model has been extensively characterised (203). At the time that mice demonstrate overt evidence of congestive cardiac failure (CCF) there is gross dilatation of both the right and left atria and ventricles.

Detailed haemodynamic measurements in male python mice on a C3H/ HeN background aged 71-78 days (Table 5.1) were undertaken by Dr Craig Lygate (MRC Centre for Human Genetics, Oxford), i.e. approximately 2 weeks prior to the onset of overt congestive cardiac failure (203). Left ventricular catherisation demonstrated impaired left ventricular systolic pressure (value ± SD) in python mice relative to littermate controls (75±3 versus 97±8 mmHg, $p<0.001$). In addition, left ventricular end-diastolic pressure (LVEDP) was significantly higher in python mice (17.7±2 versus 3.8±1.1 mmHg, $p<0.01$) indicating impaired left ventricular contractility. Mean arterial pressure was also significantly lower in python mice relative to controls (60±6 versus 75±9 mmHg, $p<0.01$). At this time point, there was no difference in central venous pressure between the two groups (1.6±0.8 versus 1.8±2.0 mmHg, $p=0.83$).

Positional cloning has identified the python mutation as a single missense mutation in the dynamin-like gene (dnm1l) on chromosome 16. The python mutation results in a replacement of a cysteine residue by a phenylalanine at position 452 in the dmn1l protein. This C452F mutation is in a highly conserved region of M domain of the dnm1l protein. This mutation has been shown to alter protein interactions in a yeast two-hybrid system suggesting that the residue may affect intramolecular interactions within the dnm1l monomer (203). Dnm1l is a member of the dynamin family of large GTPases implicated in tubulation and fission events in peroxisomes and mitochondria (311-314). Homozygosity for the python mutation (Py/Py) results in an embryonic lethal phenotype. Mouse embryonic fibroblasts (MEFs) from Py/Py homozygous embryos survive poorly in culture and have grossly abnormal mitochondria. In contrast, skin fibroblasts from heterozygous python mice (Py/+) have less pronounced abnormalities in mitochondrial morphology. The mitochondria in Py/+ skin fibroblasts are highly elongated in comparison to wild type (+/+) controls, but there is no difference in total cellular mitochondrial volume. The phenotype observed in the python (Py/+) mouse is, at a gross level, restricted to the cardiac myocytes. Indeed, with the exception of the development of congestive cardiac failure, the python mice do not demonstrate any other features of mitochondrial cytopathy, i.e. neurological, skeletal muscle and metabolic abnormalities. This is believed to be a consequence of the peculiar nature of the python mutation (203). In contrast, a previous report of a mutation in the M region of the

DLP1 gene, the human homologue of dnm1l, described a severe phenotype characterised by abnormal brain development, persistent lactic acidosis and elevated levels of long-chain fatty acids (314). Defects in energy metabolism in the python mouse show considerable tissue specificity. Adenosine triphosphate (ATP) production – the endpoint of respiratory chain function – was measured in 10 week-old mice and littermate controls (203). Both ATP and total adenine nucleotide (TAN) levels were reduced by 50 percent in python hearts. Importantly, both ATP and TAN levels in liver (and brain) tissue were similar in python mice and littermate controls. While these findings are reassuring, the nature of the germline mutation responsible for the python phenotype must raise concerns in relation to the utility of the python mouse as a model of cardiac hepatopathy. However, the apparent tissue specificity of the observed defects in energy metabolism suggests that the python model might provide some valuable insight into the pathophysiology of this condition.

5.2.1.1 Hepatic changes in the python model of cardiac hepatopathy

Preliminary experiments in male C3H/ HeN mice, undertaken by Dr Michael Cheeseman and Dr Tertius Hough (Mary Lyon Centre and Mammalian Genetics Unit, MRC Harwell, UK) found evidence of hepatic congestion concurrent with features of overt CCF. This was preceded by increases in the serum levels of the liver enzymes alanine aminotransferase (ALT) and aspartate aminotransferase (AST) (Figure 5.1). The values for ALT (U/L) expression in wild-type controls and python mice at different time points (value ± SEM) are: week 5, wild-type 33.1 ± 0.9/ python 60.7 ± 3.0; week 7, wild-type 32.4 ± 2.1/ python 48.1 ± 3.8; week 9, wild-type 36.4 ± 1.7/ python 109.0 ± 20.8; overt CCF, wild-type 32.0 ± 2.9/ python 157.6 ± 27.9. Serum ALT (value ± SEM) was significantly elevated in 5-week-old python mice relative to littermate controls (60.6±3.0 vs. 33.1±0.9, $p<0.001$). The development of overt CCF was associated with a further increase in serum ALT relative to littermate controls (157.6±27.9 vs. 32.0±2.9, $p<0.01$). A similar pattern was observed in respect to serum AST. The values for AST (U/L) expression in wild-type controls and python mice at different time points (value ± SEM) are: week 5, wild-type 58.7 ± 5.9/ python 101.5 ± 7.1; week 7, wild-type 56.2 ± 3.5/ python 94.5 ± 5.2; week 9, wild-type 53.1 ± 3.1/ python 158.9 ± 18.4; overt CCF, wild-type 45.3 ± 2.2/ python 167.1 ± 17.5. At no time points was a significant difference observed in respect to serum albumin concentration between python mice and age-matched littermate controls. The values for AST (U/L) expression in wild-type controls and python mice at different time points (value ± SEM) are: week 5, wild-type 32.9 ± 0.6/ python 32.9 ± 0.7; week 7, wild-type 35.4 ± 2.4/ python 32.7 ± 0.5; week 9, wild-type 34.2 ± 0.4/ python 32.4 ± 0.6; overt CCF, wild-type 32.7 ± 0.7/ python 32.6 ± 0.5.

Figure 5.1: Measurement of serum markers of liver damage in the python mouse

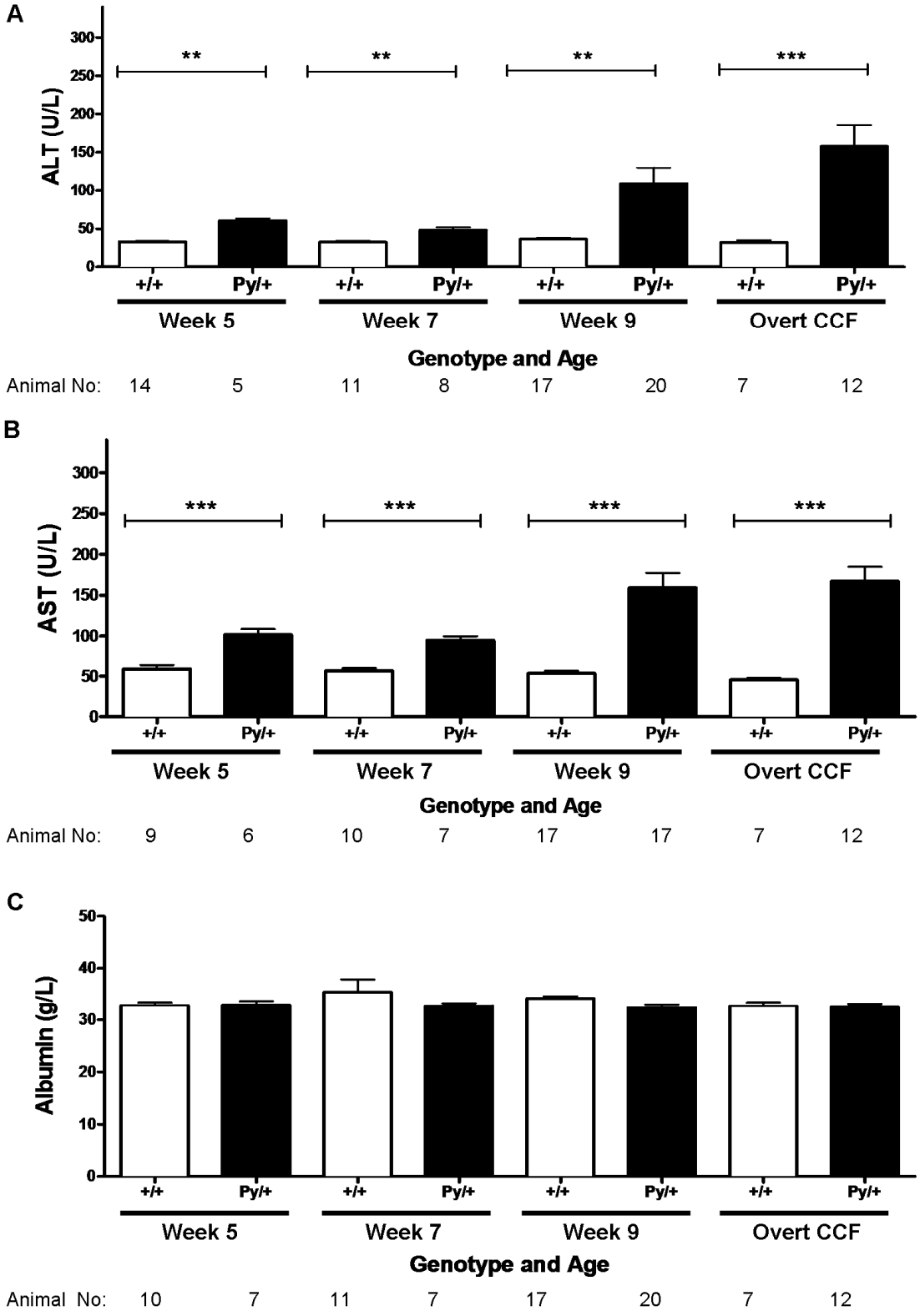

Figure 5.1 Measurement of serum markers of liver injury in the python mouse. The serum levels of the liver enzymes (A) alanine aminotransferase (ALT) and (B) aspartate aminotransferase (AST) were measured in serum taken from python (Py/+) mice and age-matched littermate controls (+/+). Serum samples were taken from mice aged 5, 7 and 9 weeks and at the time that mice developed features of overt congestive cardiac failure (CCF). In 5-week-old python mice, serum ALT was significantly elevated (1.8-fold increase, $p<0.001$) relative to controls. The development of overt CCF was associated with a further increase in ALT (4.9-fold increase, $p<0.01$) relative to controls. A similar pattern was seen in respect to serum AST. (C) No difference in serum albumin concentration was observed between python mice and littermate controls at any time point. Error bars are SEM, $^{**}p<0.01$, $^{***}p<0.001$. Statistical comparison between groups was made using an unpaired student t-test. The number of samples/ animals represented by each bar is represented below each x-axis.

Experiments were conducted to define the early events in the congested liver that may contribute to the development of liver fibrosis. Cohorts of male python (Py/+) mice and age-matched wild-type (+/+) controls were culled at 5, 7, 9 and 11 weeks, and at the development of overt features of CCF. At 5-weeks of age the python mice were macroscopically indistinguishable from age-matched control animals (Figure 5.2). At the time that python mice develop features of overt congestive cardiac failure, there is evidence of gross cardiac enlargement (Figure 5.3A) and macroscopic evidence of hepatic congestion (Figure 5.3B). Histological examination of the hearts taken from python mice manifesting features of overt CCF demonstrates dilatation of both the right and left atria and ventricles (Figure 5.3C). There was a visible increase in the size of python mice with overt CCF due to substantial peripheral oedema and ascites (Figure 5.3D).

Figure 5.2: The macroscopic appearance of 5-week-old python mice

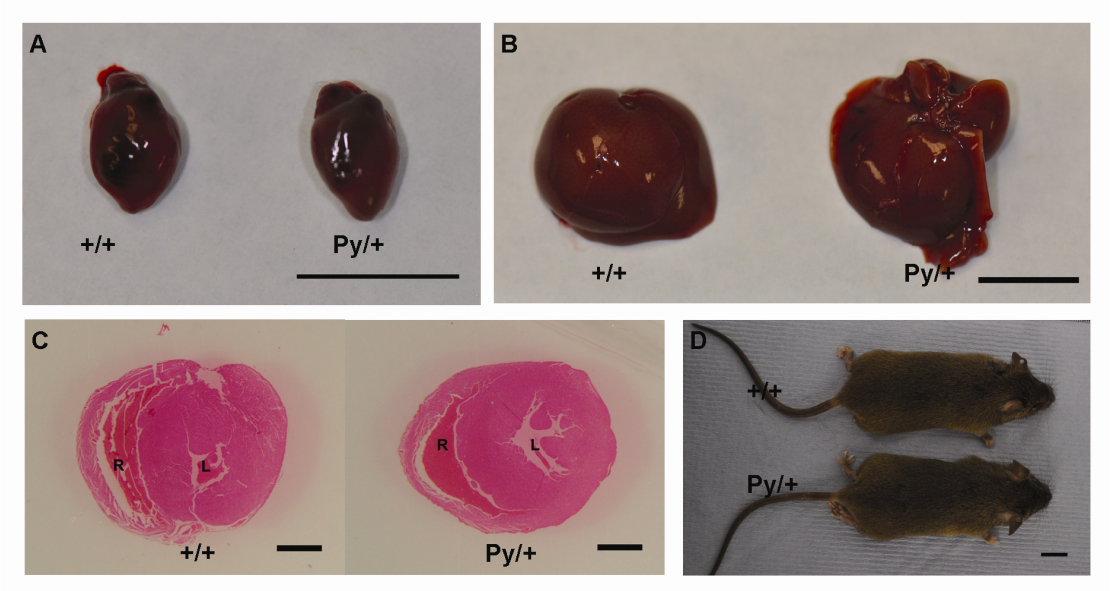

Figure 5.2 Photographs showing the macroscopic appearance of (A) hearts and (B) livers taken from 5-week-old python (Py/+) and littermate wild-type (+/+) mice on a C3H/ HeN genetic background (scale bar=1cm). (C) Photomicrographs (x10 magnification) of haematoxylin and eosin stained sections through the hearts taken from 5-week-old python (Py/+) and littermate wild-type (+/+) mice on a C3H genetic background (scale bar=1mm) showing a normal appearance of both the right (R) and left (L) ventricles. (D) Photographs showing the gross macroscopic appearance of 5-week-old python (Py/+) and wild-type mice on a C3H/ HeN genetic background (scale bar = 1cm).

Figure 5.3: The macroscopic appearance of 12-week-old python mice

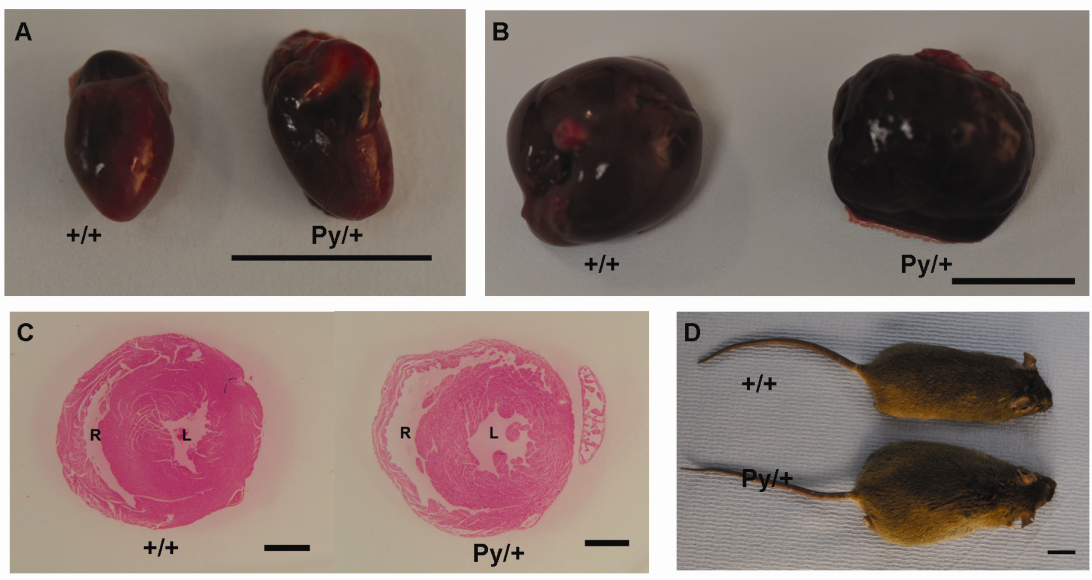

Figure 5.3 Photographs showing the microscopic appearance of (A) hearts and (B) livers taken from 12-week-old python (Py/+) and littermate wild-type (+/+) mice on a C3H/ HeN genetic background (scale bar=1cm). (C) Photomicrographs (x10 magnification) of haematoxylin and eosin stained sections through the hearts taken from a 12-week-old python (Py/+) manifesting features of CCF and an unaffected littermate wild-type (+/+) control (scale bar=1mm). The heart taken from the 12-week-old python mouse displays features of cardiomyopathy with dilatation of the right ventricle (R) and left ventricles (L) with associated thinning of the ventricular walls. (D) Photographs showing the gross macroscopic appearance of 12-week-old python (Py/+) and wild-type mice on a C3H genetic background. In the terminal phase of cardiomyopathy/ congestive cardiac failure, the python mouse develops features of right ventricular failure, including peripheral oedema and ascites.

The livers taken from 5-9 week-old python (Py/+) mice show a progressive increase in hepatocyte nuclear size in comparison to from those taken from wild-type (+/+) littermate controls in the absence of any other significant histological abnormalities. (Figure 5.4). Histological features consistent with cardiac hepatopathy were not observed in Py/+ mice until 11 weeks. This would be consistent with previous haemodynamic measurements demonstrating no significant difference in central venous pressure between python mice and wild-type controls at 10 weeks (section 5.2.1). It has been recognised that in male python mice on a C3H/ HeN background, features of cardiac decompensation develop unpredictably from around 11 weeks. This may reflect the situation observed in clinical practice with DCM whereby cardiac decompensation often occurs secondary to an unpredictable cardiac arrhythmia or thromboembolic event. Liver histology from python mice with overt features

of CCF is grossly abnormal. Within the perivenous region of 12-week-old (Py/+) mice there is marked perivenular sinusoidal congestion and dilatation/ ectasia. This is accompanied by irregular plate atrophy and hepatocyte degeneration. There are areas of vacuolation and finely granular cytoplasmic change that are thought to form part of a spectrum of hepatocyte degeneration. These changes are absent from the centrilobular region (Figure 5.4 F). There is a mild to moderate inflammatory cell infiltrate. Immunohistochemistry with lineage-specific markers confirms a mixed inflammatory cell infiltrate comprising macrophages, neutrophils, B-lymphocytes and T-lymphocytes (Appendix 15). Macrophage infiltration is concentrated around the central veins at areas of CLN (Figure 5.5). Quantification of the number of F4/80-positive cells in liver sections from python mice and age-matched controls demonstrates that increased numbers of F4/80-positive cells are not evident until such time that overt features of cardiac hepatopathy are present. The values for the number of F4/80-positive cells per high power field (value ± SEM) in wild-type and python mice, at the different time points were: 7 weeks, wild-type 47.1 ± 4.4/ python 42.9 ± 42.9; 9 weeks, wild-type 38.2 ± 2.9/ python 43.0 ± 6.3; 11 weeks, wild-type 51.7 ± 7.3/ python 102.6 ± 25.8; and at the onset of overt CCF, wild-type 55.1 ± 4.4/ python 203.1 ± 6.3. There is only a minor increase in GR1-staining (neutrophil staining) in liver sections from 12-week-old Py/+ mice, relative to age-matched controls. However, the onset of clinical features of overt CCF is accompanied by a more significant and dramatic increase in both CD3 (T-lymphocyte) and B220 staining (B-lymphocyte) in Py/+ liver section, relative to age-matched controls (Appendix 15).

Figure 5.4: Histological appearance of the python liver (haematoxylin and eosin staining)

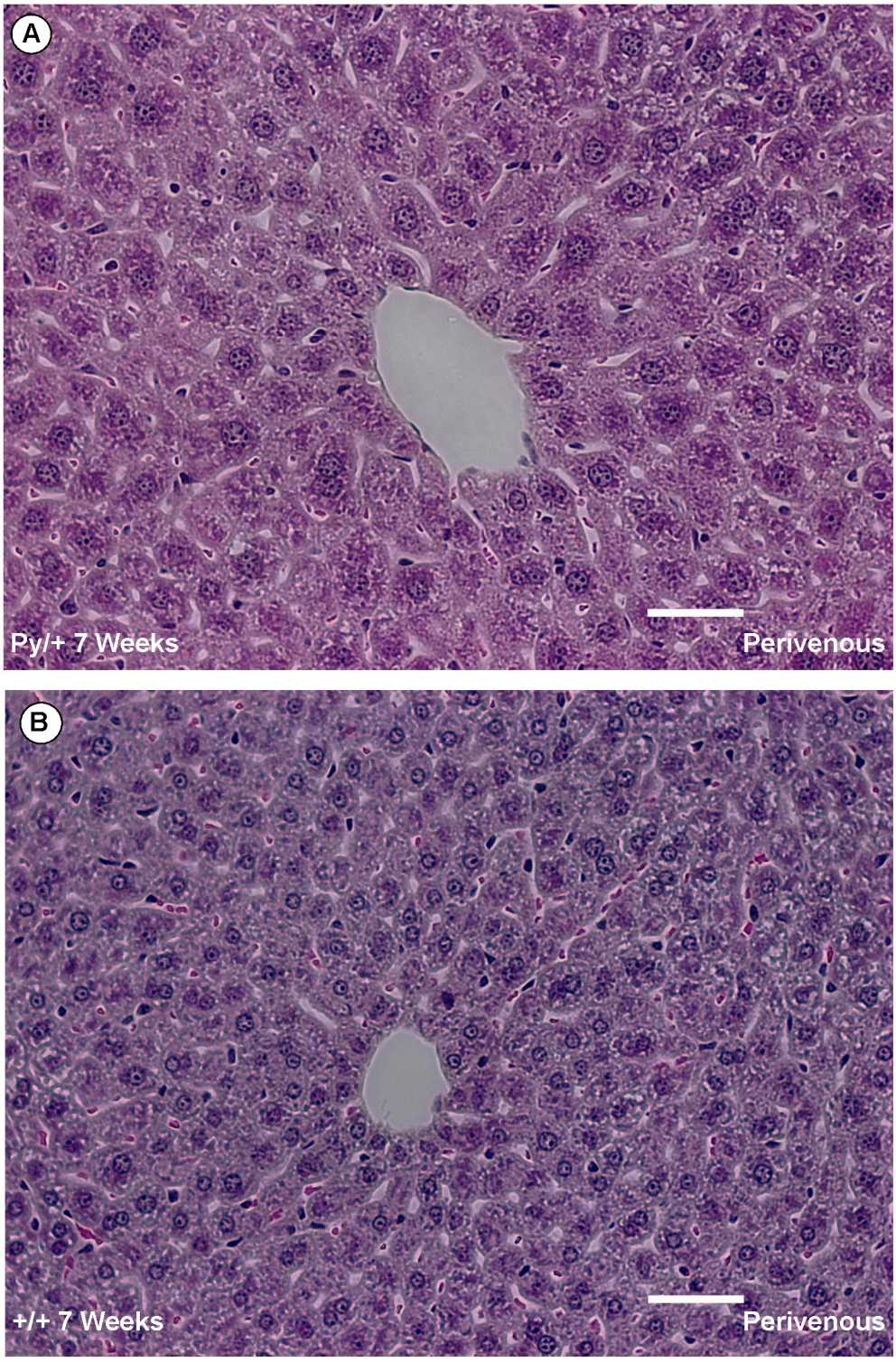

Figure 5.4: Continued

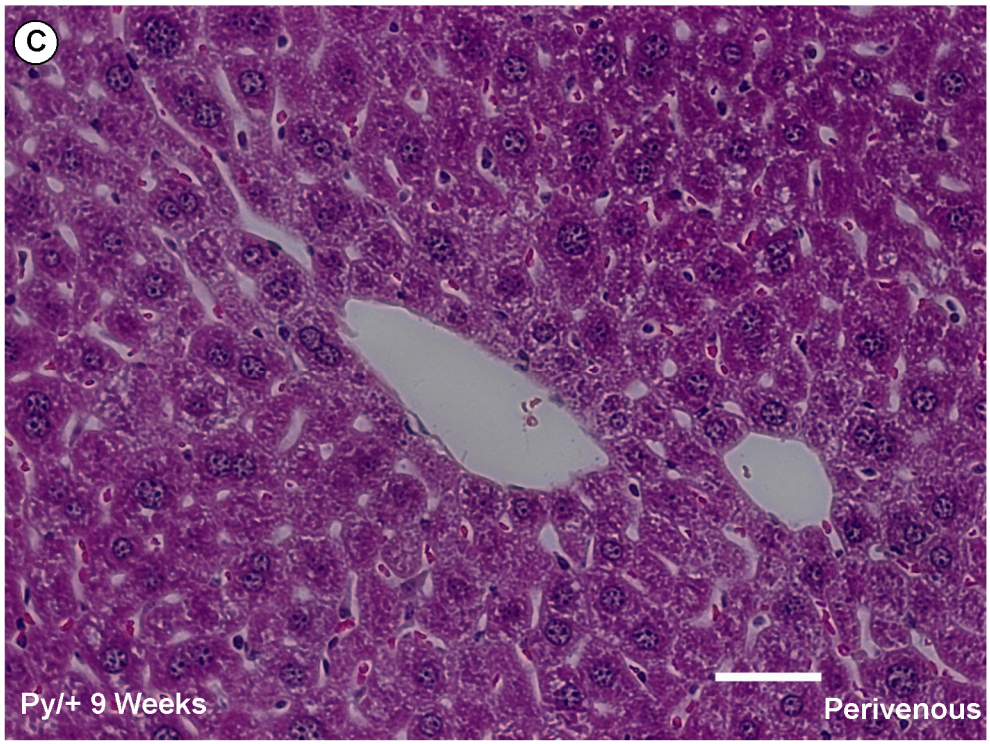

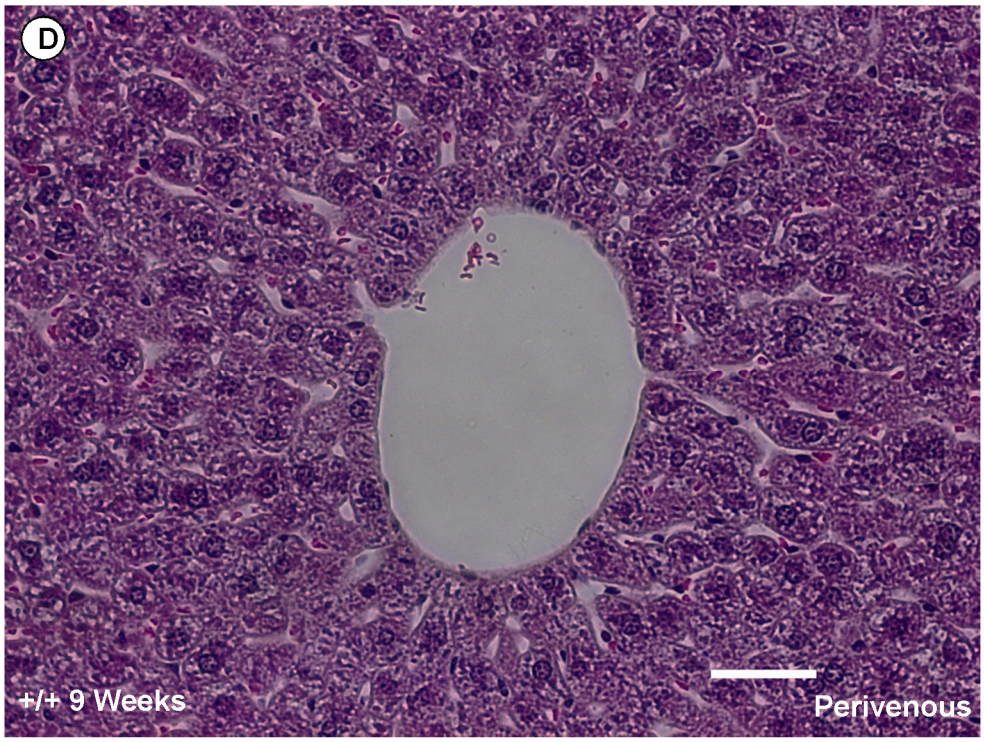

Figure 5.4: Continued

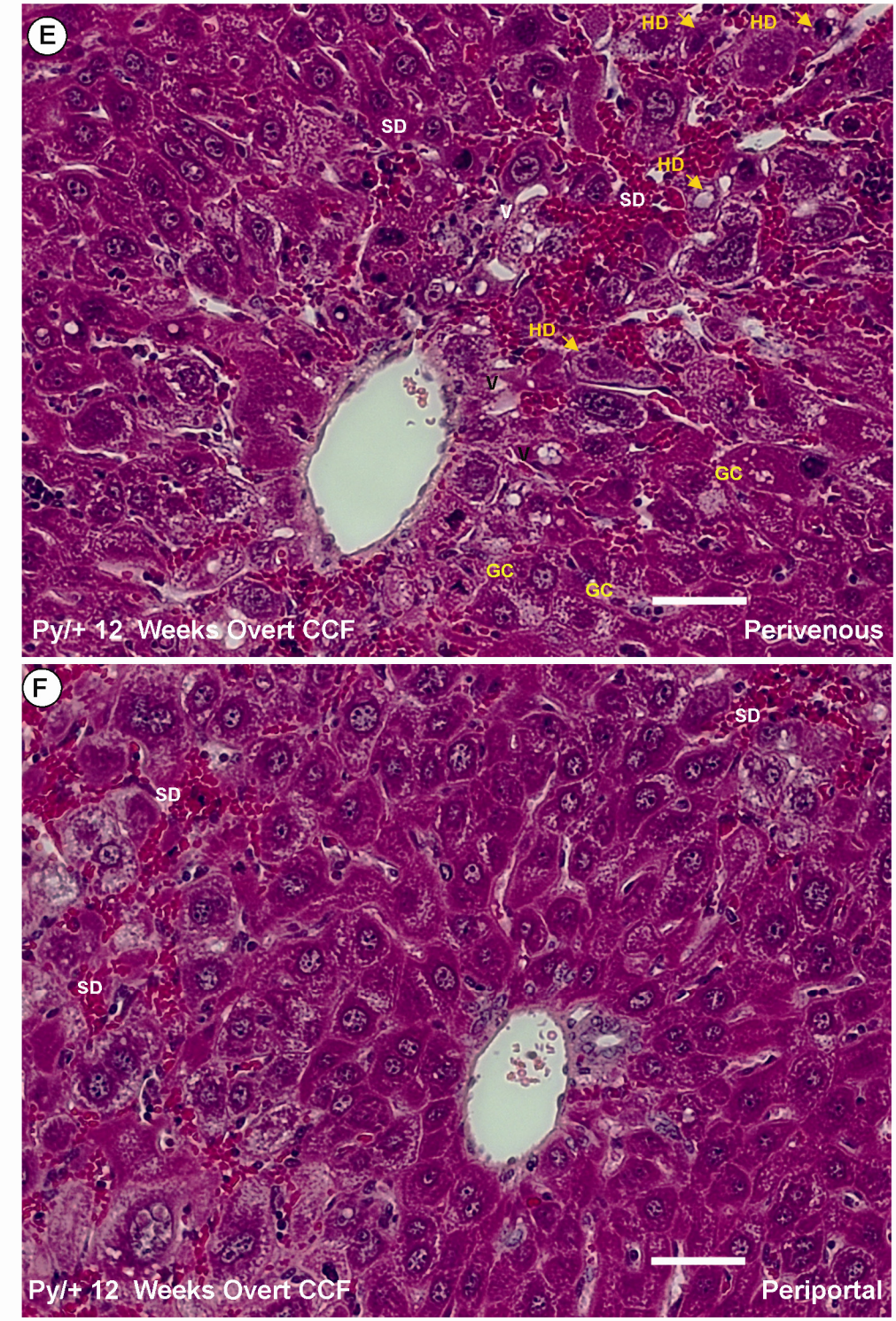

Figure 5.4: Continued

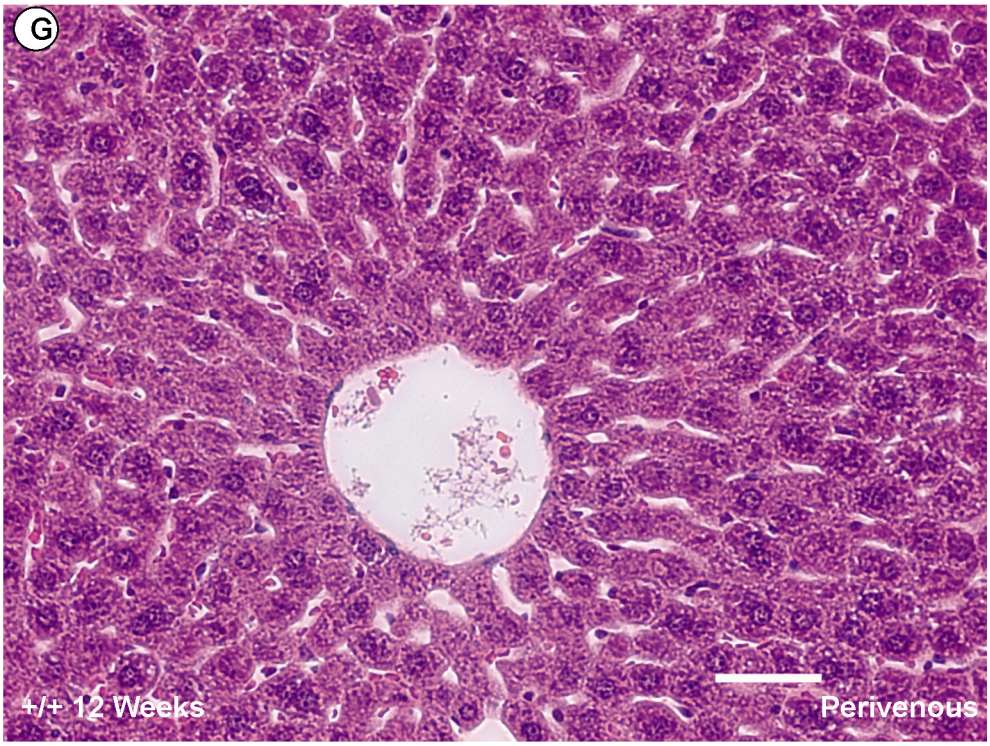

Figure 5.4 High magnification (x200) photomicrographs of haematoxylin and eosin stained liver tissue taken from (A) 7-week-old python (Py/+) mice, (B) age-matched wild-type (+/+) controls, (C) 9-week-old Py/+ and (D) age-matched (+/+) control mice. There is a clear increase in nuclear size amongst hepatocytes from 7-9-week-old Python (Py/+) mice but no other significant histological abnormalities are seen. (E/F) Liver tissue taken from 12-week-old Py/+ mice displaying clinical features of overt congestive cardiac failure have gross histological abnormalities. In the (E) perivenular region of 12-week-old Py/+ mice there is marked perivenular sinusoidal congestion and dilatation/ ectasia (SD) accompanied by irregular plate atrophy and hepatocyte degeneration (HD). Areas of hepatocyte vacuolation (V) and granular cytoplasm (GC) represent part of this degenerative process. These changes are not present in the (F) periportal zone. (G) Liver tissue from age-matched 12-week-old (+/+) mice showing normal liver histology. In each image the scale bar indicates 50 microns.

Figure 5.5: F4/80 immunohistochemistry and macrophage quantification in the python liver

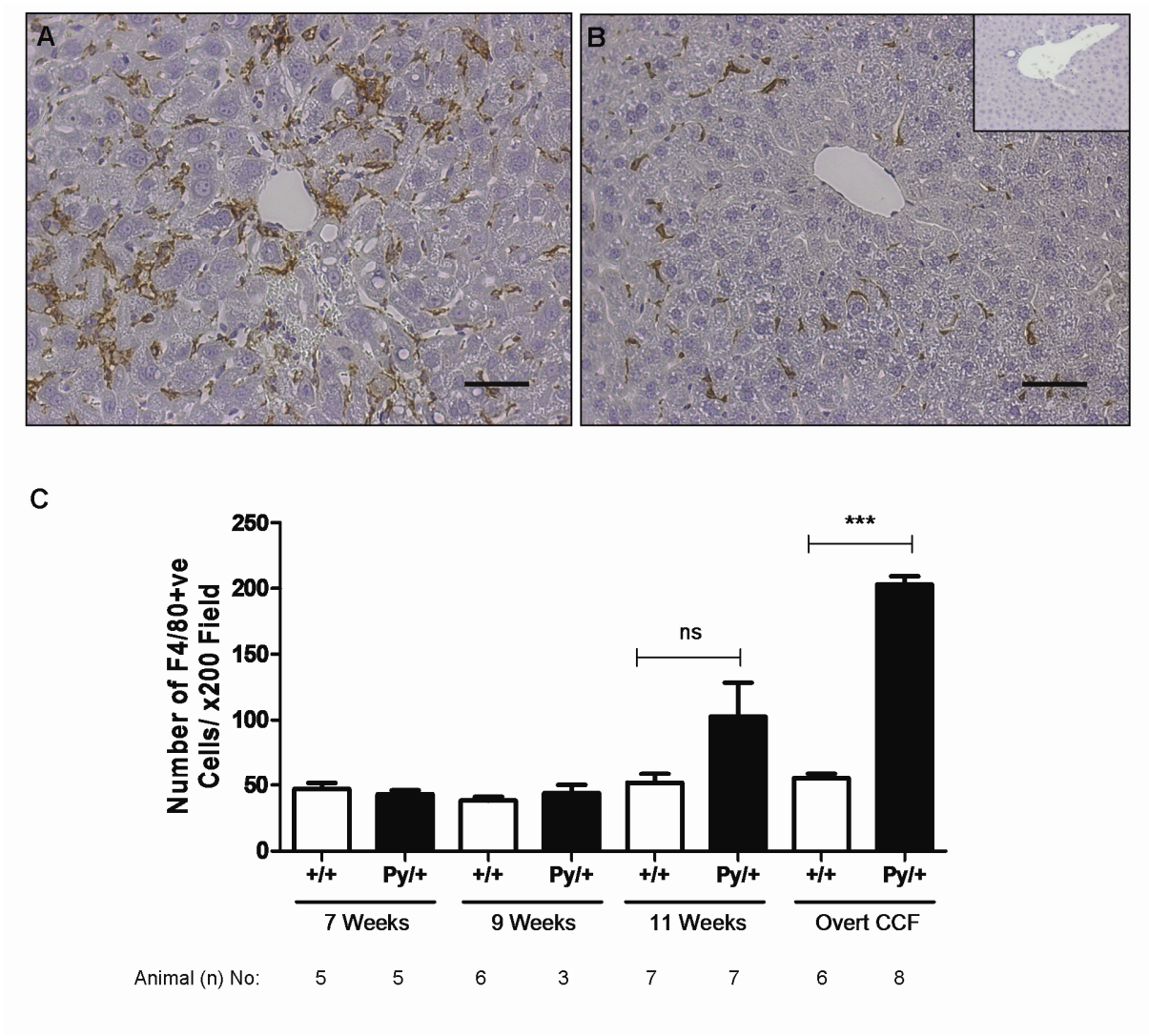

Figure 5.5 Macrophage recruitment to the liver in the python model of cardiac hepatopathy High magnification (x200) photomicrographs of F4/80-immunstained liver tissue from (A) python (Py/+) mice demonstrating features of overt congestive cardiac failure, and (B) age-matched wild-type (+/+) controls. Isotype-control staining is represented by the indented image (top right). Scale bar indicates 50 microns (C) Quantification of the number of F4/80-positive cells in liver sections taken from Py/+ mice at 7, 9 and 11 weeks, and at the development of features of overt CCF. In each case comparison is made to age-matched +/+ control animals. F4/80-positive cell numbers are expressed as the mean number of cells/ high power (x200) central vein field. Statistical comparison between means was made using a student t-test. The number of animal (n) represented by each car is indicated beneath the x-axis of the graph. Error bars indicate SEM, ***p<0.001, ns = not significant.

5.2.1.2 Fibrous tissue changes in the python model of cardiac hepatopathy

Alterations in fibrous tissue architecture in the python mouse are evident from 11-weeks (Figure 5.6). Early alterations in fibrous tissue architecture are evident as condensation of collagen fibres around the central veins. In python mice exhibiting overt feature of CCF there is extension of collagen fibrils outward into the parenchyma (fibrous spur formation). Fibrous tissue changes occur in a perivenular distribution around the central veins and in areas of more marked sinusoidal dilatation. However, even in python mice demonstrating features of advanced CCF there was no evidence of either bridging fibrosis or cirrhosis. This may reflect the acute time course of cardiac decompensation in the python model, such that there is insufficient time for advanced fibrosis, and ultimately cirrhosis to develop. The accumulation of fibrillar collagen in the python model was quantified by digital image analysis of PSR stained liver sections (Figure 5.6 D). The values percentage (%) PSR-staining (value ± SEM) in wild-type and python mice, at the different time points were: 7 weeks, wild-type 1.04 ± 0.18/ python 1.08 ± 0.22; 9 weeks, wild-type 1.41 ± 0.14/ python 1.10 ± 0.14; 11 weeks, wild-type 1.19 ± 0.14/ python 1.93 ± 0.14; and at the onset of overt CCF, wild-type 1.66 ± 0.16 / python 4.85 ± 0.52. This confirmed that prior to the onset of overt features of CCF there was no significant increase in fibrillar collagen content in the python liver relative to age-matched controls. The onset of overt CCF was accompanied by a dramatic increase (2.9-fold, $p<0.001$) in PSR staining relative to controls.

Figure 5.6: Quantification of liver fibrosis (PSR staining) in the python liver

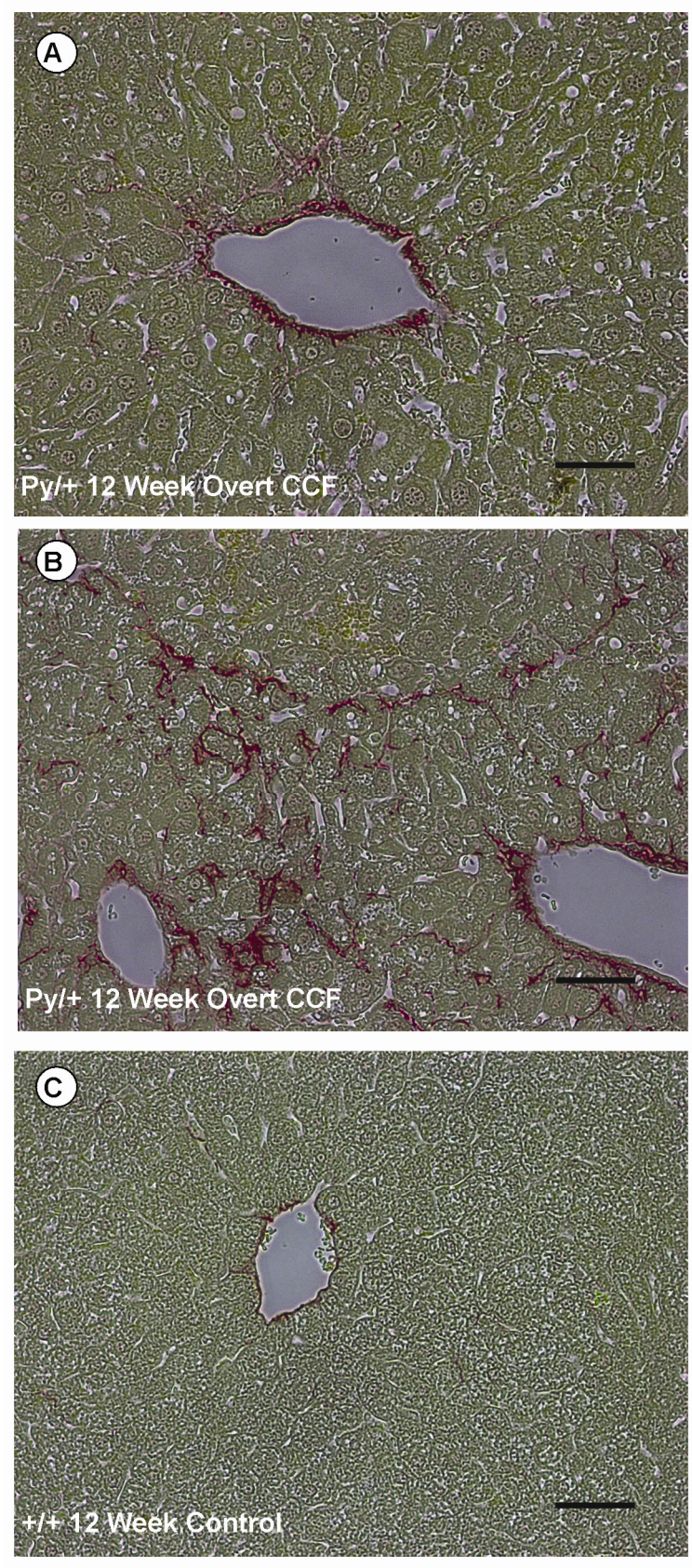

Figure 5.6: Quantification of liver fibrosis (PSR staining) in the python liver (continued)

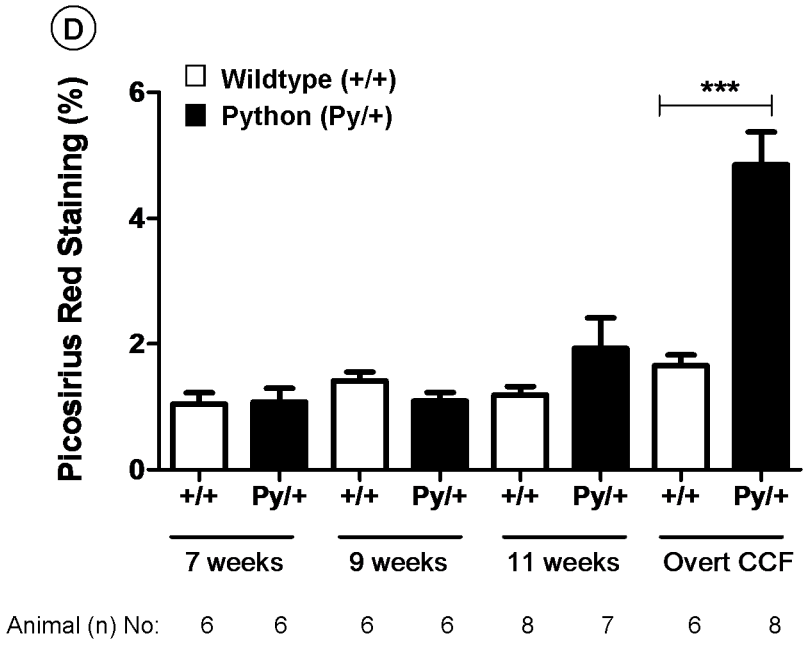

Figure 5.6 Quantification of PSR staining in the python model of cardiac hepatopathy Photomicrographs (x200magnification) of PSR stained liver sections from (A/B) 12 week-old python (Py/+) mice demonstrating overt features of CCF and (C) age-matched wild-type (+/+) littermate controls. (D) Quantification of PSR staining by digital image analysis of liver sections derived from python mice at 7, 9 and 11 weeks, and at the onset of overt symptoms of CCF. At each time point comparison is made to age-matched wild-type littermate controls. Each bar represents the mean percentage area of PSR staining per high power (x200) field. The number of animals (n) represented by each bar is indicated beneath the x-axis of the graph. Statistical comparisons between means were made using a student t-test. Error bars indicate SEM, ***$p<0.001$.

Real-time quantitative PCR of cDNA derived from whole liver lysates was used to quantify the expression profile of ECM components and profibrotic mediators, implicated in the pathogenesis of chronic liver disease (Figure 5.7). Gene expression is expressed as fold induction relative to 18S expressions. Values are standardised to expression values in 5-week-old wild-type mice. The values for fold induction of COL1A1 (value ± SEM) are: 5 weeks, wild-type 1.00 ± 0.16/ python 1.73 ± 0.34; 7 weeks, wild-type 0.32 ± 0.08/ python 0.24 ± 0.43; 9 weeks, wild-type 0.14 ± 0.02/ python 0.17 ± 0.03; 11 weeks, wild-type 0.15 ± 0.03/ python 0.61 ± 0.42; and at the onset of overt CCF in python mice, wild-type 0.08± 0.02 / python 11.98 ± 3.57. The values for fold induction of COL3A1 (value ± SEM) are: 5 weeks, wild-type 1.00 ± 0.11/ python 1.64 ± 0.17; 7 weeks, wild-type 0.42 ± 0.09/ python 0.39 ± 0.05; 9 weeks, wild-type 0.24 ± 0.03/ python 0.26 ± 0.03; 11 weeks, wild-type 0.24 ± 0.04/ python 0.37 ± 0.15; and at the onset of overt CCF in python mice, wild-type 0.15± 0.03 / python 3.67 ± 0.55. The values for fold induction of αSMA (value ± SEM) are: 5 weeks, wild-type 1.00 ± 0.19/ python 1.32 ± 0.31; 7 weeks, wild-type 0.18 ± 0.02/ python 0.13 ± 0.04; 9 weeks, wild-type 0.73 ± 0.13/ python 0.63 ± 0.09; 11 weeks, wild-type 0.67 ± 0.13/ python 1.49 ± 0.57; and at the onset of overt CCF in python mice, wild-type 0.70± 0.10 / python 70.65 ± 14.13. The values for fold induction of TIMP1 (value ± SEM) are: 5 weeks, wild-type 1.00 ± 0.10/ python 2.97 ± 0.68; 7 weeks, wild-type 0.44 ± 0.08/ python 0.56 ± 0.15; 9 weeks, wild-type 0.35 ± 0.07/ python 0.73 ± 0.06; 11 weeks, wild-type 0.44 ± 0.08/ python 2.00 ± 1.20; and at the onset of overt CCF in python mice, wild-type 0.46± 0.14 / python 17.88 ± 4.11. The values for fold induction of TIMP2 (value ± SEM) are: 5 weeks, wild-type 1.00 ± 0.06/ python 1.26 ± 0.07; 7 weeks, wild-type 0.74 ± 0.06/ python 0.88 ± 0.06; 9 weeks, wild-type 1.01 ± 0.09/ python 1.17 ± 0.10; 11 weeks, wild-type 0.77 ± 0.04/ python 0.93 ± 0.02; and at the onset of overt CCF in python mice, wild-type 0.64± 0.08 / python 2.98 ± 0.34. In python mice demonstrating features of overt CCF there is marked up-regulation of COL1A1 (142-fold, $p<0.05$), COL3A1 (25-fold, $p<0.001$), αSMA (102-fold, $p<0.01$), TIMP1 (39-fold, $p<0.01$) and TIMP2 (5-fold, $p<0.001$) mRNA, relative to controls. There is no significant difference between python mice and controls in the expression of COL1A1, COL3A1 or αSMA prior to the onset of overt CCF. However, TIMP1 gene expression in python liver is consistently upregulated relative to age-matched wild-type control liver from as early as 5 weeks (3-fold increase, $p<0.05$). The biological relevance of this observation is uncertain. Consistent with previous published findings (315), immunohistochemical examination of serial liver sections suggests that TIMP1 is derived from both macrophages and HSCs (data not shown).

Figure 5.7: Real-time PCR analysis for fibrosis marker expression in the python liver

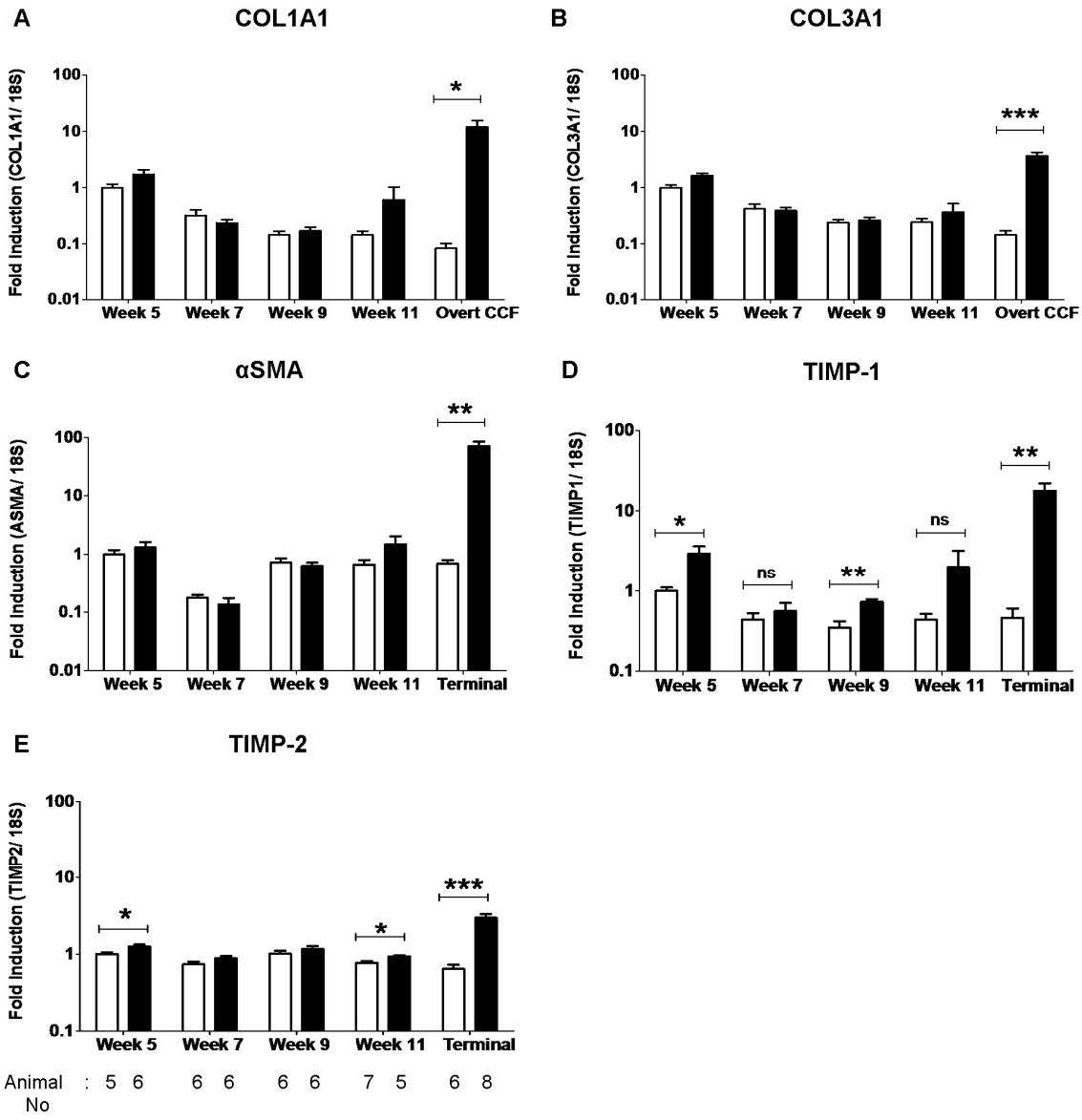

Figure 5.7 Real-time quantitative PCR analysis for (A) COL1A1, (B) COL3A1, (C) αSMA, (D) TIMP1 and (E) TIMP2 mRNA expression in whole liver lysates derived from python (Py/+) mice (black bars) at 5, 7, 9 and 11 weeks, and at the onset of overt CCF. At each time point comparison is made to mRNA from whole liver lysates derived from age-matched wild-type (+/+) control animals (white bars). In each case, target mRNA expression is calculated relative to the expression of the 18S housekeeping gene and fold-induction expressed relative to target mRNA expression in the +/+ control group at 5 weeks. Statistical comparisons between means were made using an unpaired student t-test. The number (n) of animals represented by each bar is indicated below the x-axis of graph E. In each case error bars represent SEM, *p<0.05, **p<0.01, ***p<0.001.

5.2.1.3 Myofibroblast (MFB) activation in the python model of cardiac hepatopathy

Immunohistochemical staining for the αSMA – a marker of activated MFBs – was undertaken in order to characterise the pattern of MFB activation in the python model. The development of overt features of CCF was accompanied by a marked increase in αSMA-staining in the python liver. MFB activation was centred on the central veins and dilated sinusoids radiating out into the parenchyma. The most prominent accumulations of activated αSMA-positive MFB were seen in areas of sinusoidal dilatation/ ectasia. These are the areas in which haematoxylin and eosin staining has demonstrated the presence of hepatocyte degeneration/ hepatocyte plate atrophy (Figure 5.4). The presence of activated MFBs around dilated sinusoids suggests that mechanical factors related to sinusoidal dilatation might be implicated in the activation of these cells. The portal tracts appeared relatively normal until late in the disease process. In those livers with the most florid histological changes, αSMA-positive MFBs were identified around the portal tracts. This may reflect sequential activation of MFB populations in response to progressive cardiac hepatopathy. Digital image analysis was used to quantify the pattern of αSMA-expression in the python model relative to age-matched wild-type controls (Figure 5.8). The values for percentage αSMA staining (value ± SEM) in wild-type and python mice at the different time points are: 5 weeks, wild-type 0.0010 ± 0.0006/ python 0.0054 ± 0.0052; 7 weeks, wild-type 0.0063 ± 0.0029/ python 0.0025 ± 0.0013; 9 weeks, wild-type 0.0937 ± 0.0263/ python 0.1481 ± 0.0478; 11 weeks, wild-type 0.1917 ± 0.081/ python 0.2394 ± 0.1049; and at the onset of overt CCF in python mice, wild-type 0.1797± 0.0519 / python 14.27 ± 2.840. This showed that there is no significant difference in the expression of αSMA in the python liver relative to age-matched wild-type controls prior to the onset of overt CCF in python mice. At the onset of overt cardiac decompensation there is a marked and rapid increase (79-fold, $p<0.01$) in αSMA staining, relative to age-matched wild-type controls. These results have been confirmed with Western blotting for αSMA in whole liver lysates (data not shown).

Figure 5.8 Quantification of myofibroblast activation (αSMA staining) in the python liver

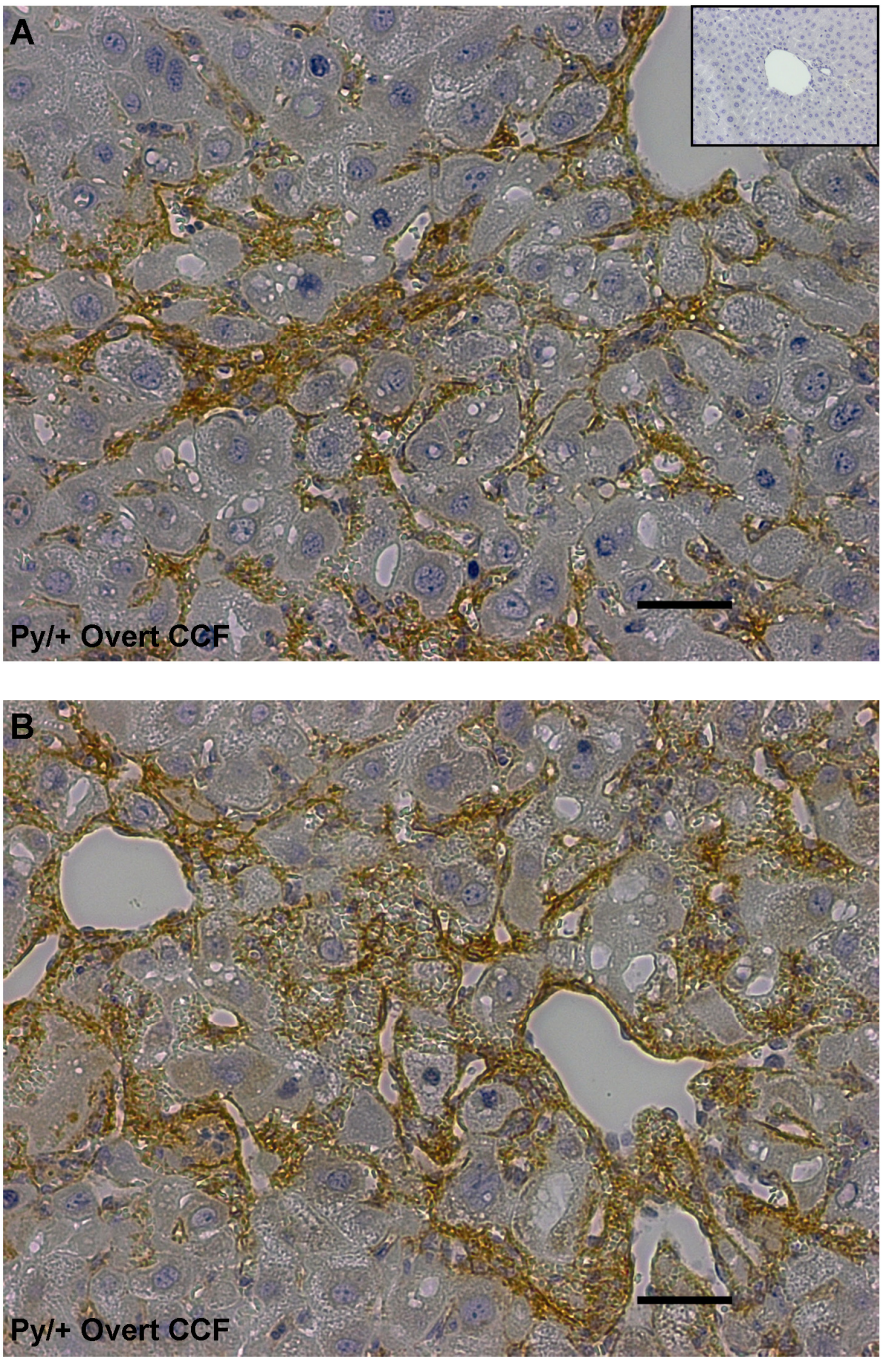

Figure 5.8 Continued

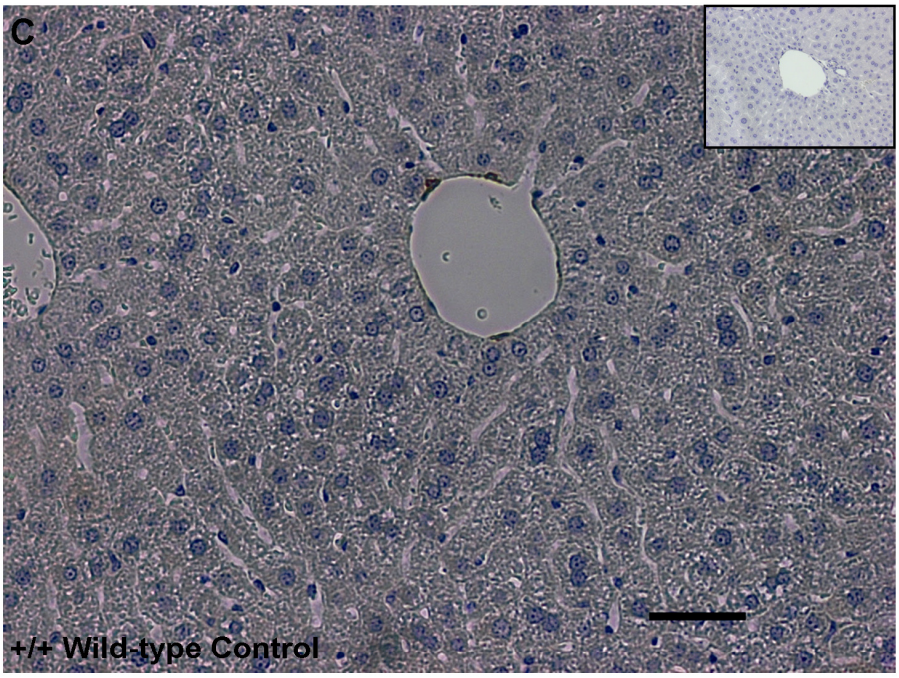

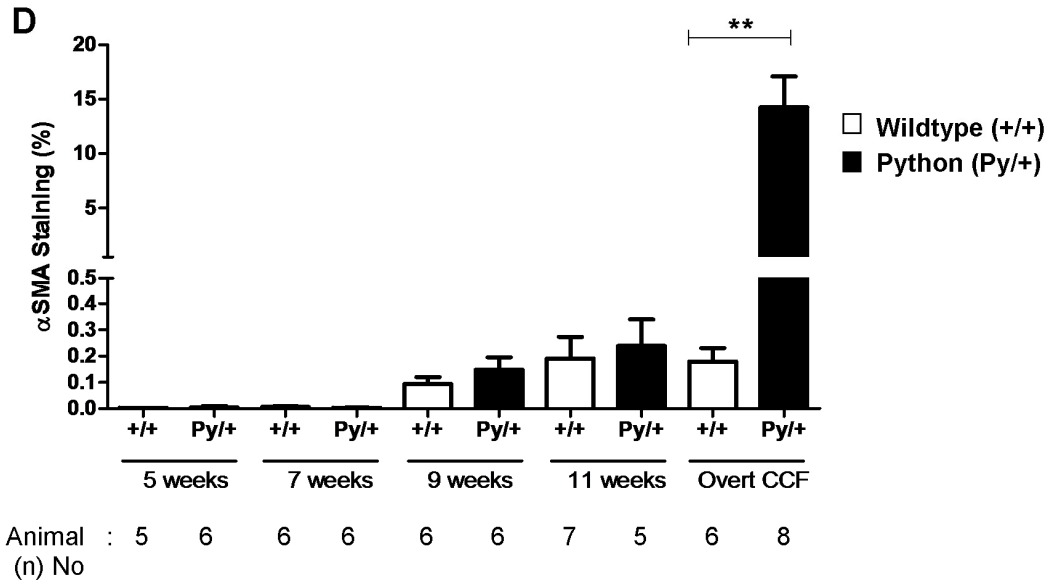

Figure 5.8 Quantification of αSMA staining in the python model of cardiac hepatopathy Photomicrographs (x200magnification) of αSMA-immunostained (brown) liver sections from (A/B) python (Py/+) mice demonstrating overt features of CCF and (C) age-matched wild-type (+/+) littermate controls. Slides stained with an isotype control primary antibody showed no significant staining (indented images) Scale bar indicates 50 microns. (D) Quantification of αSMA-immunostaining by digital image analysis of liver sections derived from python mice at 5, 7, 9 and 11 weeks, and at the onset of overt symptoms of CCF. At each time point comparison is made to age-matched wild-type littermate controls. Each bar represents the mean percentage area of αSMA-immunostaining per high power (x200) field. The number (n) of animals represented by each bar is indicated below the x-axis of the graph. Error bars indicate SEM, **$p<0.01$. Statistical comparisons are made using a student t test.

5.2.1.4 Expression of inflammatory chemokines/ cytokines in the python model of cardiac hepatopathy

Studies were undertaken to quantify levels of relevant inflammatory chemokines in whole liver lysates taken from python mice and age-matched wild-type controls (Figure 5.6). The development of overt features of CCF is associated with a 2.3-fold increase ($p<0.001$) in whole liver MCP-1 expression, relative to controls. There was no evidence of upregulation of MCP-1 in livers lysates from python mice at earlier time points. The values for MCP-1 protein expression (pg/mg tissue) in wild-type and python mice at the different time points (value ± SEM) are: 5 weeks, wild-type 73.5 ± 10.9/ python 77.6 ± 5.4; 7 weeks, wild-type 69.7 ± 5.2/ python 58.3 ± 2.8; 9 weeks, wild-type 59.5 ± 5.5/ python 65.6 ± 4.0; 11 weeks, wild-type 61.6 ± 4.0/ python 69.5 ± 7.8; and at the onset of overt CCF in python mice, wild-type 47.2± 5.3 / python 109.8 ± 9.5. Macrophage-chemoattractant-protein-1 (MCP-1/ CCL2) is an important mediator of monocyte/ macrophage recruitment in acute and chronic liver injury (316). MCP1 is produced by a range of cells; including monocytes/ macrophages, activated myofibroblasts and cholangiocytes. Furthermore, MCP-1 is released by Kupffer cells in response to ischaemia/reperfusion injury (317).

Macrophage inhibitory protein-2 (MIP2/ CXCL2) is a potent neutrophil chemoattractant and was also found to be markedly up-regulated (7.2-fold increase, $p<0.01$) in python mice demonstrating overt features of CCF. Interestingly MIP2 levels were consistently higher in python mice relative to controls from as early as 5 weeks, although this trend was not statistically significant until 11 weeks. The values for MIP2/ CXCL2 protein expression (pg/mg tissue) in wild-type and python mice at the different time points (value ± SEM) are: 5 weeks, wild-type 20.7 ± 3.5/ python 34.3 ± 5.1; 7 weeks, wild-type 10.5 ± 1.7/ python 15.4 ± 1.9; 9 weeks, wild-type 10.4 ± 1.4/ python 12.9 ± 1.5; 11 weeks, wild-type 10.1 ± 1.5/ python 16.7 ± 2.6; and at the onset of overt CCF in python mice, wild-type 8.8 ± 0.9 / python 64.1 ± 11.4. Both hepatic and serum MIP2 levels have previously been shown to correlate with the extent of necroinflammatory change in animal models of alcoholic liver disease (318). MIP2 has also been implicated in mediating responses to ischaemia/ reperfusion in the liver (319).

There was no detectable difference in hepatic IL-6 levels between python mice and wild-type mice at any time point. The values for IL-6 protein expression (pg/mg tissue) in wild-type and python mice at the different time points (value ± SEM) are: 5 weeks, wild-type 36.3 ±

5.4/ python 35.6 ± 7.3; 7 weeks, wild-type 30.5 ± 2.5/ python 20.3 ± 1.6; 9 weeks, wild-type 27.8 ± 2.4/ python 25.3 ± 1.0; 11 weeks, wild-type 31.2 ± 3.4/ python 26.8 ± 3.2; and at the onset of overt CCF in python mice, wild-type 27.9 ± 2.7 / python 26.4 ± 1.7.

Figure 5.9: Quantification of MCP1, MIP2α and IL6 expression in the python liver

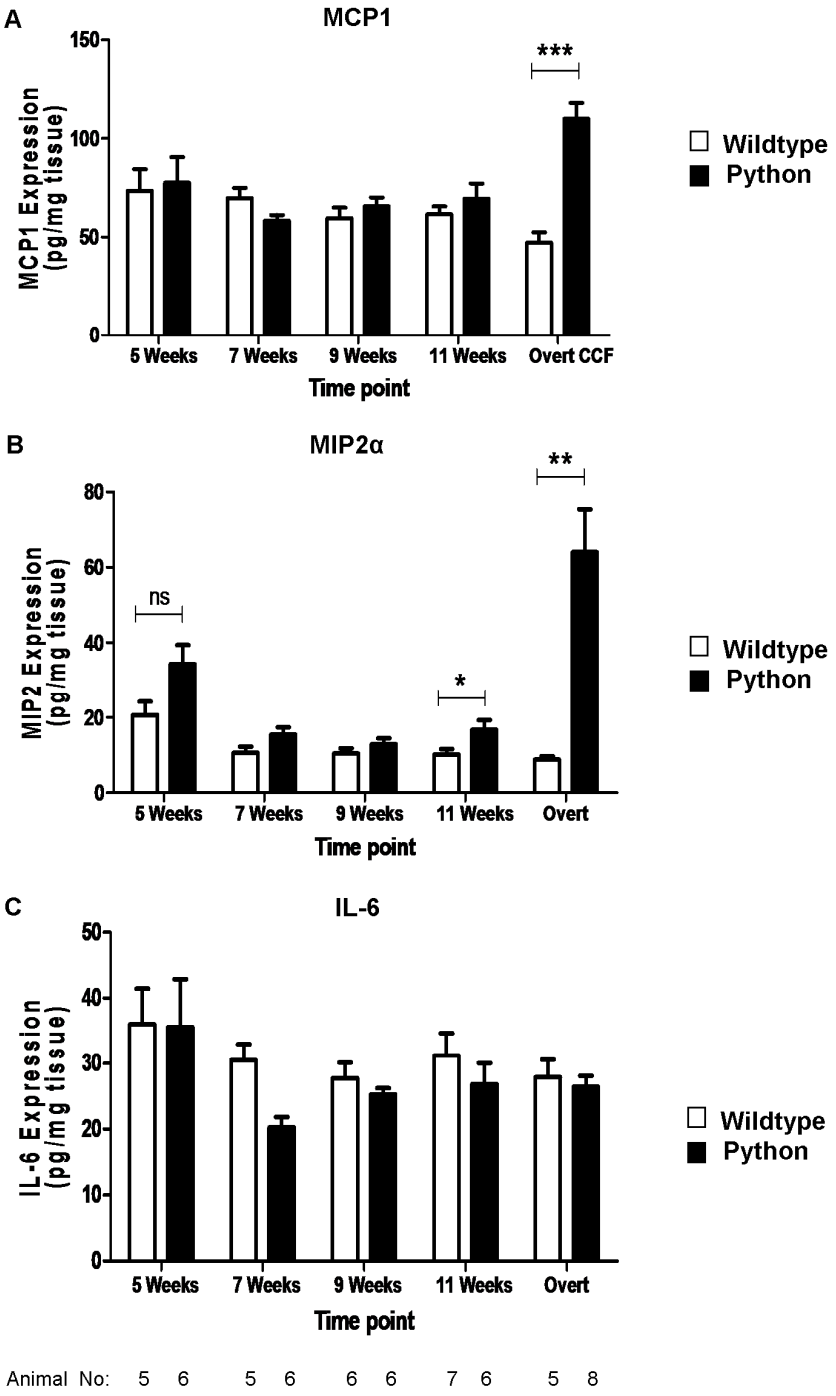

Figure 5.9 Quantification of inflammatory chemokine/ cytokine levels in the python (Py/+) liver relative to wild-type (+/+) controls at the time points indicated and at the onset of overt CCF. The concentration of the inflammatory chemokines (A) MCP-1, (B) MIP2 and (C) the cytokine IL-6 are expressed as pg/mg liver tissue. The number (n) of animals/ samples represented by each bar is indicated below the x-axis of graph C. Statistical comparisons between mean values were made using an unpaired student t-test. In each case error bars indicate SEM, *p<0.05, **p<0.01, ***P<0.001 and ns= not significant.

5.2.1.5 Quantification of tissue hypoxia in the python model of cardiac hepatopathy

It has been postulated that tissue hypoxia might be a key mechanism underlying the pathogenesis of hepatocyte injury and fibrogenesis in chronic hepatic congestion. Studies were conducted to determine the degree of liver hypoxia present in the python liver during the development of features of overt CCF. Experiments were conducted using pimonidazole hydrochloride, a 2-nitroimidazole hypoxic marker that forms adducts with thiol groups in proteins, peptides and amino acids under hypoxic conditions ($PaO_2 < 1.3$kPa). Experiments were performed in python (Py/+) mice aged 5 weeks, 9 weeks and at the onset of overt features of CCF. Control experiments were performed in age-matched littermates. Pimonidazole binding was assessed by immunohistochemical staining for the presence of pimonidazole adducts in liver tissue sections (Figure 5.10). In normal wild-type liver intense staining of pimonidazole adducts is restricted to the area immediately surrounding the central veins. A similar pattern is observed in liver sections from python mice prior to the onset of overt features of CCF. In contrast, in python mice with overt features of CCF, there is increased intensity of staining around the central veins, with extension of pimonidazole adduct formation outward into the parenchyma, bridging adjacent central vein regions.

Figure 5.10: Quantification of tissue hypoxia with pimonidazole staining in the python liver

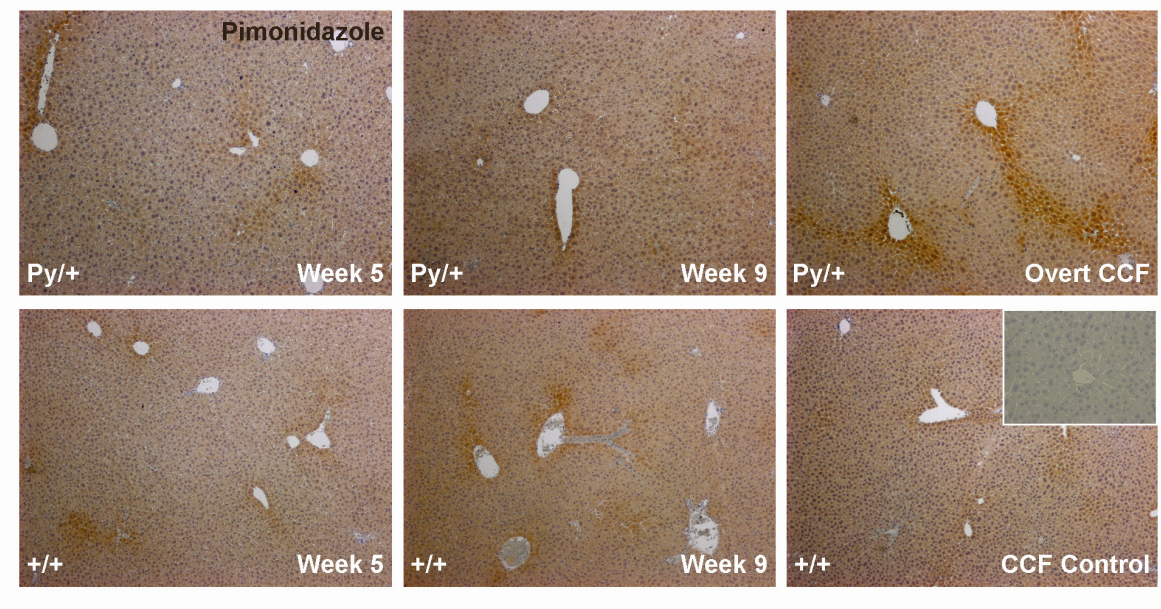

Figure 5.10 Quantification of tissue hypoxia with pimonidazole staining in the python model of cardiac hepatopathy. Photomicrographs of liver sections following immunohistochemical staining for pimonidazole-adducts (brown). Experiments were conducted in python (Py/+) mice aged 5 weeks and 9 weeks, and at the onset of overt CCF (upper panel). Control experiments were conducted with age-matched littermate controls (as indicated). Control staining with an isotype primary antibody showed no specific staining (bottom right indented image).

5.2.2 The CREB S133A model of cardiac hepatopathy

The CREB S133A is a transgenic murine model of dilated cardiomyopathy, the generation of which has previously been described (204). Signalling through cyclic adenosine monophosphate (cAMP) is known to play an important role in the pathogenesis of cardiac failure. The downstream targets of cAMP include the cAMP response element binding protein (CREB), a 43kDa leucine zipper transcription factor, which performs an important role in regulating cardiomyocyte function (320, 321). The transcriptional activity of CREB is positively regulated by phosphorylation of the CREB protein at a critical serine residue (S133). This phosphorylation event facilitates the interaction of CREB with CREB-binding protein (CBP) resulting in activation of the basal transcription complex. In the absence of S133 phosphorylation CREB binds DNA but cannot activate transcription. The mutated CREB S133A molecule, incorporating a serine to alanine mutation at position 133, is a dominant negative repressor of CREB-dependent gene transcription (322, 323). CREB S133A transgenic mice have been developed (ICR/CD1 background) that express this dominant-negative repressor of CREB-mediated signalling under the transcriptional control of the cardiac myocyte-specific alpha-myosin heavy chain (MHC) promoter (204). Expression of the CREB S133A transgene is restricted to the heart, as demonstrated by Northern blot analysis (204). It has been demonstrated that CREB S133A transgenic mice develop a form of dilated cardiomyopathy (DCM) that closely resembles idiopathic dilated cardiomyopathy in humans. Histological analysis of hearts from male CREB S133A mice demonstrates progressive four chamber dilatation. Histological changes were present in a proportion of CREB S133A mice from as early as 4 weeks, and in all animals at 8 weeks. Intracardiac thrombus formation was a common finding in animals with DCM. Echocardiography demonstrated an increase in left ventricular end-systolic and end-diastolic dimensions, in CREB S133A mice relative to littermate wild-type controls (204, 324). CREB S133A mice also had diminished left-ventricular contractility in response to beta-adrenergic stimulation (isoproterenol). Haemodynamic measurements confirm that CREB S133A mice have depressed LV systolic function in association with significant reductions in both systemic systolic and diastolic blood pressure (204, 324). CREB S133A mice develop clinical features of overt congestive cardiac failure from 8-20 weeks of age, characterised by peripheral oedema, ascites, lethargy and dyspnoea. Liver histology is reported as showing features consistent with nutmeg liver with central venous congestion and centrilobular necrosis. However, more detailed morphological studies of hepatic changes during the course of progressive cardiac failure have not been undertaken in this model.

5.2.2.1 Hepatic changes in the CREB S133A model of cardiac hepatopathy

Experiments were conducted in male CREB S133A mice in order to characterise the morphological changes occurring within the liver, during the development of progressive cardiac failure. Cohorts (n=3-5) of male CREB S133A mice (ICR/CD1 background) and age-matched wild-type controls were culled at 4, 8 and 12 weeks. In male mice there were no demonstrable histological features suggestive of cardiac hepatopathy in 8-week-old CREB S133A mice, relative to wild-type controls. Histological changes consistent with cardiac hepatopathy were present in all mice from 12 weeks of age (Figure 5.11). There was considerable heterogeneity in the time of onset of cardiac decompensation in CREB S133A mice. In some specimens, histological changes were restricted to mild CPC with sinusoidal dilatation. In mice demonstrating more severe features of congestive cardiac failure, more florid histological abnormalities were present (Figure 5.11 C/D). There was marked sinusoidal congestion and ectasia centred on the hepatic veins (perivenular region). Hepatocyte degeneration was evident with vacuolation and hepatocyte plate atrophy was seen. Apoptotic hepatocytes (acidophil bodies) could also be identified in the 12 week CREB liver, which were less conspicuous in the Python model. Areas of extra-medullary haematopoiesis were identified as areas of cohesively clustered cells, likely reflecting the systemic condition of the animals at the time of sacrifice. Liver fibrosis was not a prominent feature. In some specimens with more florid histological changes, there was extension of fibrous spurs outwards from the central vein into the hepatic parenchyma. Bridging fibrosis was not seen. Mild to moderate inflammatory changes were seen, centred in the perivenular region. Macrophage infiltration was concentrated around central veins and at sites of hepatocyte necrosis but was not present prior to 12 weeks (data not shown). MFB activation, as assessed by αSMA-staining, was evident at sites of sinusoidal dilatation centred on dilated central veins, in the vicinity of hepatocyte degeneration (Figure 5.12). The values for percentage αSMA staining (%) in wild-type and CREB S133A mouse livers (value ± SEM) at the time points investigated were: week 4, wild-type 0.011 ± 0.002/ CREB S133A 0.019 ± 0.010; week 8, wild-type 0.001 ± 0.0007/ CREB S133A 0.004 ± 0.002; and week 12, wild-type 0.005 ± 0.002/ CREB S133A 0.473 ± 0.302. These differences were not statistically significant. In CREB S133A mice with histological changes consistent with mild hepatic congestion, MFB activation was restricted to the centrilobular region with variable extension outwards into the liver parenchyma. In liver samples with the most marked histological abnormalities, αSMA-staining extended throughout the hepatic lobule in a perisinusoidal distribution. Digital image analysis of αSMA-stained sections shows a dramatic increase (92-

fold) in αSMA-staining in 12 week-old CREB S133A mice relative to wild-type controls, although this did not achieve statistical significance. This reflects the degree of heterogeneity observed in this cohort with respect to the onset of severe right-heart failure. There was no evidence of MFB activation prior to the development of overt congestive cardiac failure.

Figure 5.11: Histological appearance of the CREB S133A liver (haematoxylin and eosin staining)

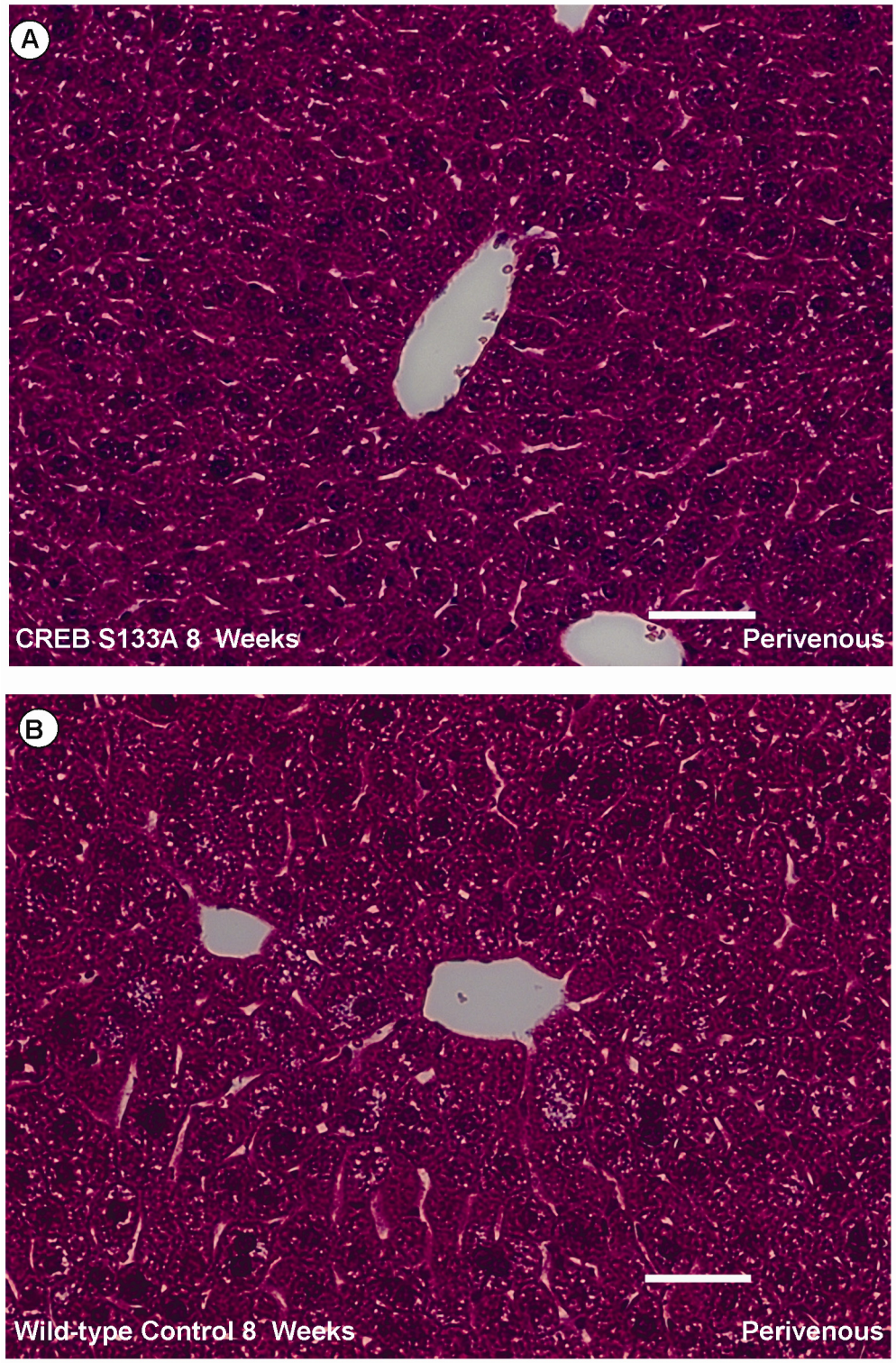

Figure 5.11 Continued

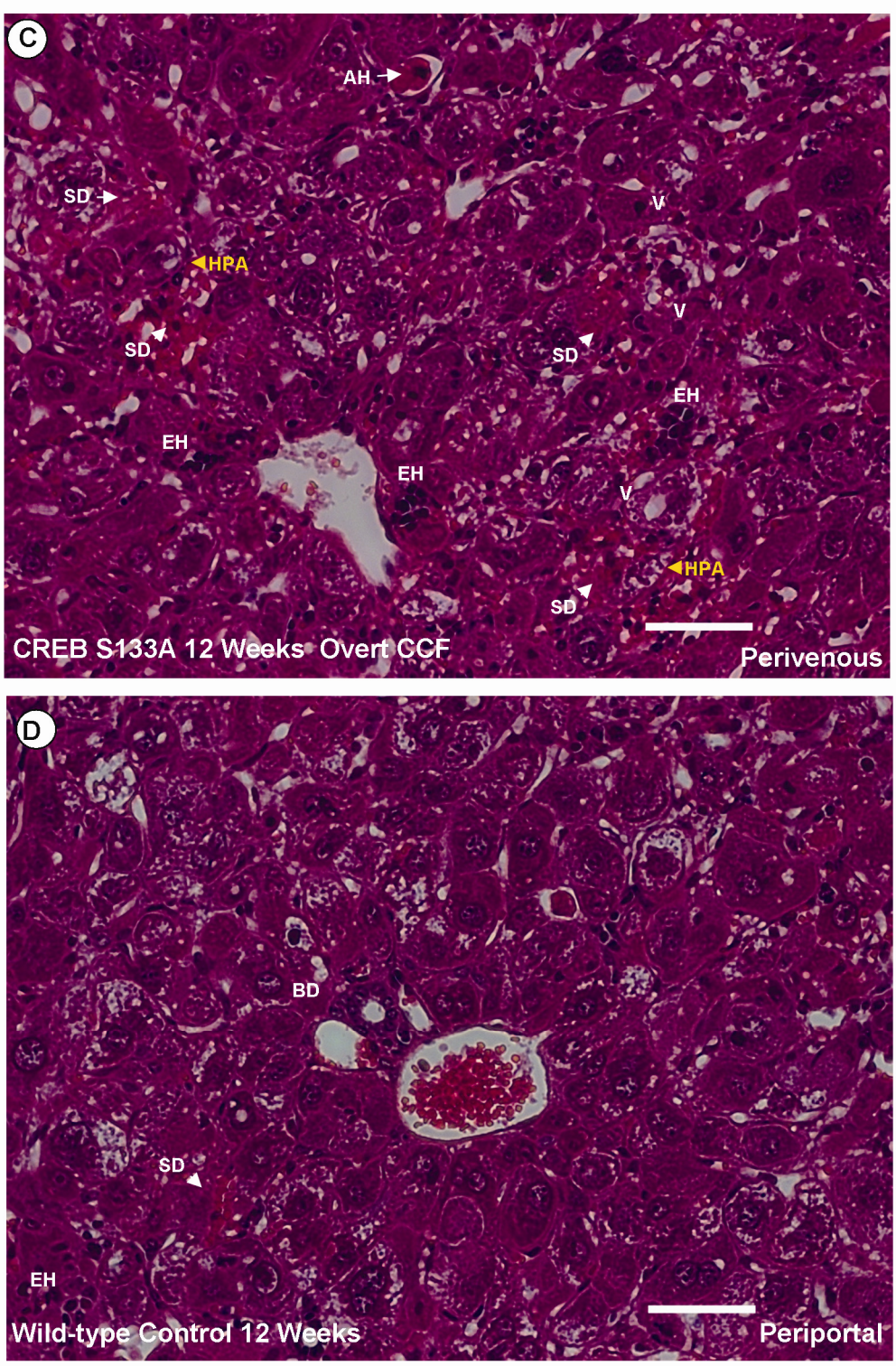

Figure 5.11 Continued

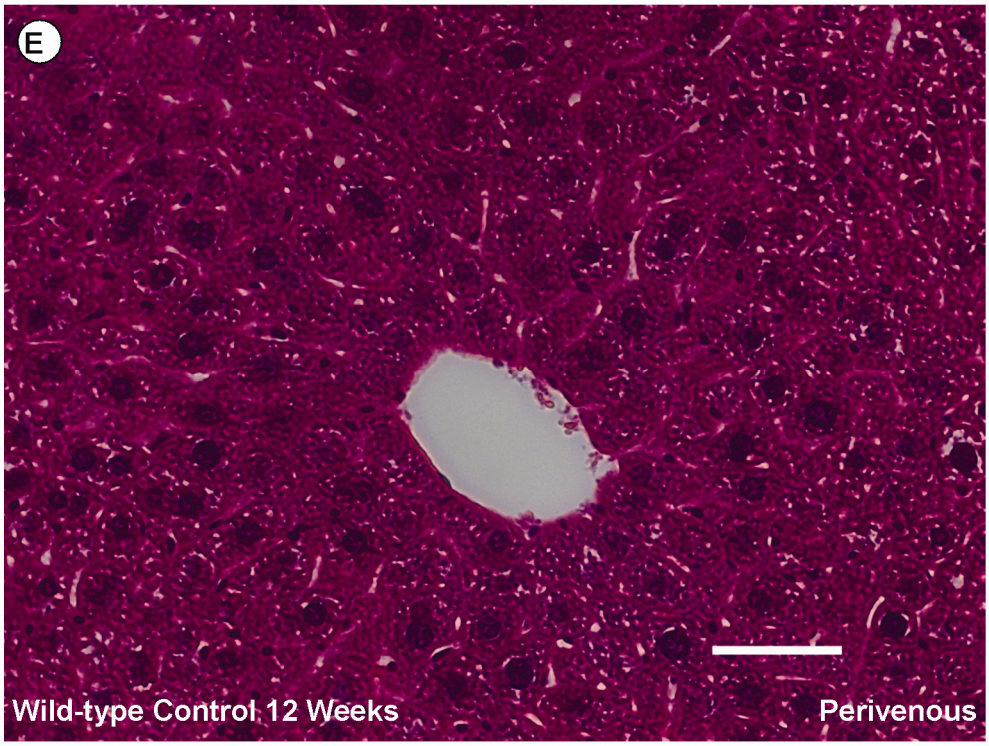

Figure 5.11 Photomicrographs (x200-magnification) of haematoxylin and eosin stained liver sections taken from CREBS133A transgenic mice and age-matched wild-type controls at various time points (as indicated). The histological appearance of the liver in (A) 8-week-old CREB S133A transgenic mice is indistinguishable from that of (B) 8-week-old wild-type control animals. Histological abnormalities consistent with cardiac hepatopathy develop from 12 weeks of age in CREB S133A animals. (C/D) Liver tissue taken from 12-week-old CREB S133A mice displaying clinical features of overt congestive cardiac failure has gross histological abnormalities. There is perivenular sinusoidal congestion and dilatation/ ectasia (SD) accompanied by hepatocyte plate atrophy (HPA) and apoptotic hepatocytes are also seen. Hepatocyte degenerative vacuolation is also seen (V). There are also areas of apparent extra-medullary haematopoiesis (EH). (D) The immediate periportal region is relatively spared. BD = bile duct. (E) Liver tissue from age-matched 12-week-old wild-type mice showed normal liver histology. In each image the scale bar indicates 50µm.

Figure 5.12 Quantification of myofibroblast activation (αSMA staining) in the CREB S133A liver

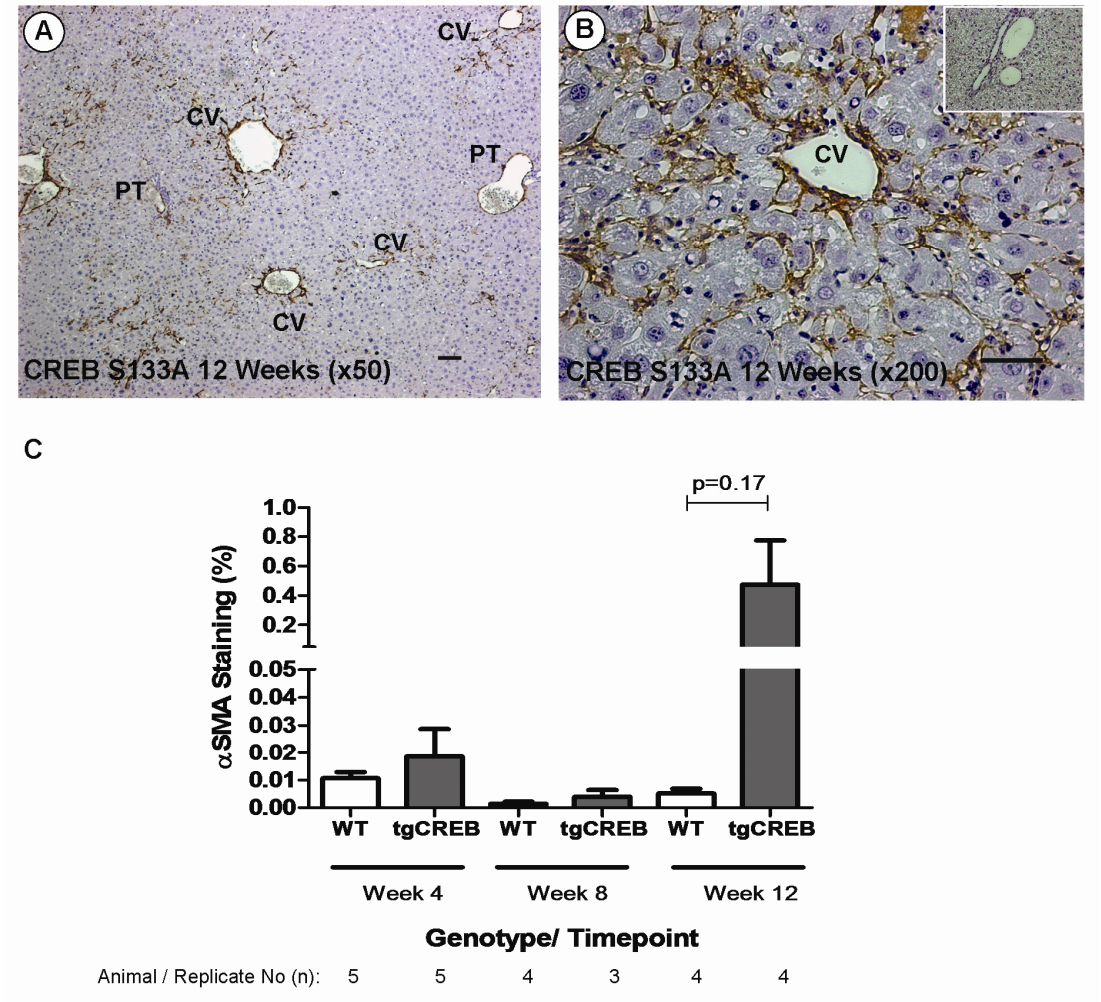

Figure 5.12. Quantification of αSMA staining in the CREB S133A model of cardiac hepatopathy. (A) Photomicrograph (x50-magnification) of αSMA stained liver tissue from a 12-week-old CREB S133A transgenic mouse with right-heart failure. MFB activation predominates in the centrilobular region with radiation outwards into the liver parenchyma. (B) Photomicrograph (x200-magnification) of αSMA stained liver tissue from a 12-week-old CREB S133A transgenic mouse with more advanced right-heart failure. Isotype control staining is represented by the indented image at the right hand corner. (C) Quantification of αSMA staining by digital image analysis of liver sections derived from CREB S133A (tgCREB) mice at 4, 8 and 12 weeks. At each time point comparison is made to age-matched wild-type (WT) littermate controls. Statistical comparisons between means were made using an unpaired student t-test. Each bar represents the mean percentage area of αSMA staining per high power (x200) field (p value as indicated). The number of animals/ samples represented by each bar is indicated below the x-axis. Abbreviations: CV, central vein and PT, portal tract.

5.2.2.2 Fibrous tissue changes in the CREB S133A model of cardiac hepatopathy

The accumulation of fibrillar collagen in the CREB S133A model was quantified by digital image analysis of PSR stained liver sections (Figure 5.13). The values for percentage PSR staining (%) in wild-type and CREB S133A mouse livers (value ± SEM) at the time points investigated were: week 4, wild-type 0.071 ± 0.035/ CREB S133A 0.071 ± 0.023; week 8, wild-type 0.172 ± 0.061/ CREB S133A 0.157 ± 0.043; and week 12, wild-type 0.364 ± 0.054/ CREB S133A 0.445 ± 0.120. In 12 week-old CREB S133A mice, there was considerable heterogeneity in the extent of fibrous tissue deposition, which reflected the variability/ severity of hepatic congestion seen. In those CREB S133A mice displaying features of overt congestive cardiac failure there was a dramatic increase in PSR staining. In these specimens, the increase in PSR staining was centred on central veins, radiating outwards into the parenchyma. However, overall, there was no significant increase in PSR staining in CREB S133A mice at 12 weeks, relative to wild-type controls. Furthermore, there was no difference in PSR staining between CREB S133A mice and wild-type controls at earlier time points.

Real-time quantitative PCR of cDNA derived from whole liver lysates was used to quantify the expression profile of ECM components and profibrotic mediators at 4, 8 and 12 weeks (Figure 5.14). Gene expression is expressed as fold induction relative to 18S expressions. Values are standardised to expression values in 5-week-old wild-type mice. The values for fold induction of COL1A1 (value ± SEM) are: week 4, wild-type 1.000 ± 0.227/ CREB S133A 1.316 ± 0.234; week 8, wild-type 0.209 ± 0.056/ CREB S133A 0.203 ± 0.052; and week 12, wild-type 0.306 ± 0.153/ CREB S133A 9.377 ± 4.202. The values for fold induction of COL3A1 (value ± SEM) are: week 4, wild-type 1.000 ± 0.178/ CREB S133A 1.256 ± 0.149; week 8, wild-type 0.335 ± 0.061/ CREB S133A 0.285 ± 0.045; and week 12, wild-type 0.230 ± 0.055/ CREB S133A 2.095 ± 0.689. The values for fold induction of TIMP1 (value ± SEM) are: week 4, wild-type 1.000 ± 0.270/ CREB S133A 1.604 ± 0.373; week 8, wild-type 0.328 ± 0.017/ CREB S133A 0.255 ± 0.031; and week 12, wild-type 1.448 ± 0.322/ CREB S133A 16.35 ± 5.862. The values for fold induction of αSMA (value ± SEM) are: week 4, wild-type 1.000 ± 0.483/ CREB S133A 1.429 ± 0.488; week 8, wild-type 2.826 ± 0.835/ CREB S133A 3.223 ± 0.470; and week 12, wild-type 0.282 ± 0.073/ CREB S133A 90.92 ± 16.22.

In 12 week-old CREB S133A mice there was marked upregulation of COL1A1 (31-fold,

$p<0.05$) COL3A1 (9-fold, $p<0.05$) and TIMP1 (11-fold, $p<0.05$) mRNA, relative to controls. Similarly, there was a dramatic upregulation in αSMA expression in 12-week-old CREB S133A mice, relative to controls. There was no significant difference between CREB S133A mice and wild-type controls in COL1A1, COL3A1, TIMP1 or αSMA expression prior to the development of overt congestive cardiac failure at 12 weeks.

Figure 5.13 Quantification of liver fibrosis (PSR staining) in the CREB S133A liver

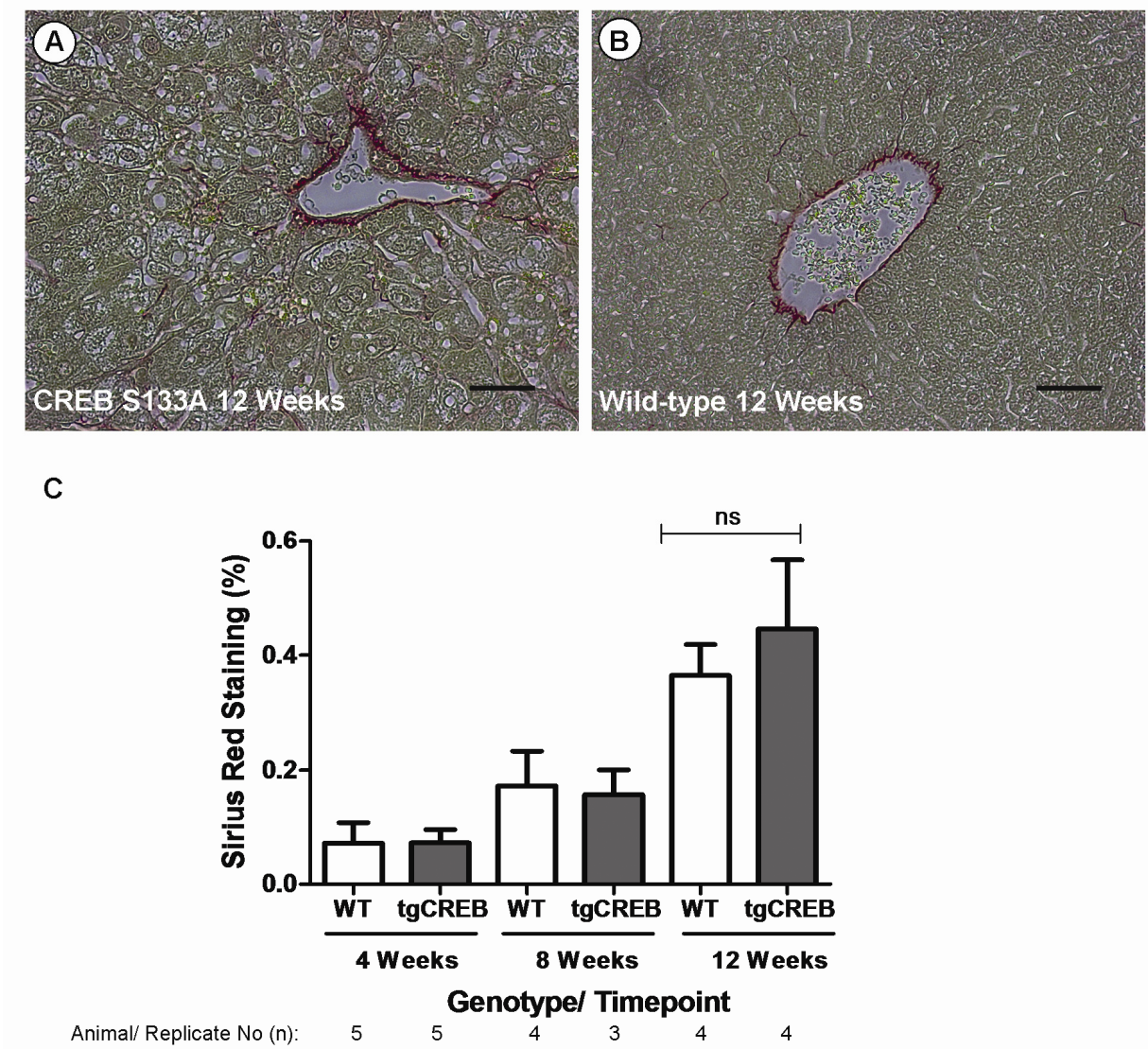

Figure 5.13 Quantification of PSR staining in the CREB S133A model of cardiac hepatopathy. Photomicrographs (x200 magnification) of PSR stained liver sections from (A) 12 week-old CREB S133A mice demonstrating overt features of CCF and (B) age-matched wild-type controls. Scale bar indicates 200µm. (C) Quantification of PSR staining by digital image analysis of liver sections derived from CREB S133A (tgCREB) mice at 4, 8 and 12 weeks. At each time point comparison is made to age-matched wild-type (WT) littermate controls. Statistical comparisons between means were made using an unpaired student t-test. Each bar represents the mean percentage area of PSR staining per high power (x200) field (ns = not significant). The number of animals/ samples represented by each bar is indicated below the x-axis.

Figure 5.14: Real-time PCR analysis for fibrosis marker expression in the CREB S133A liver

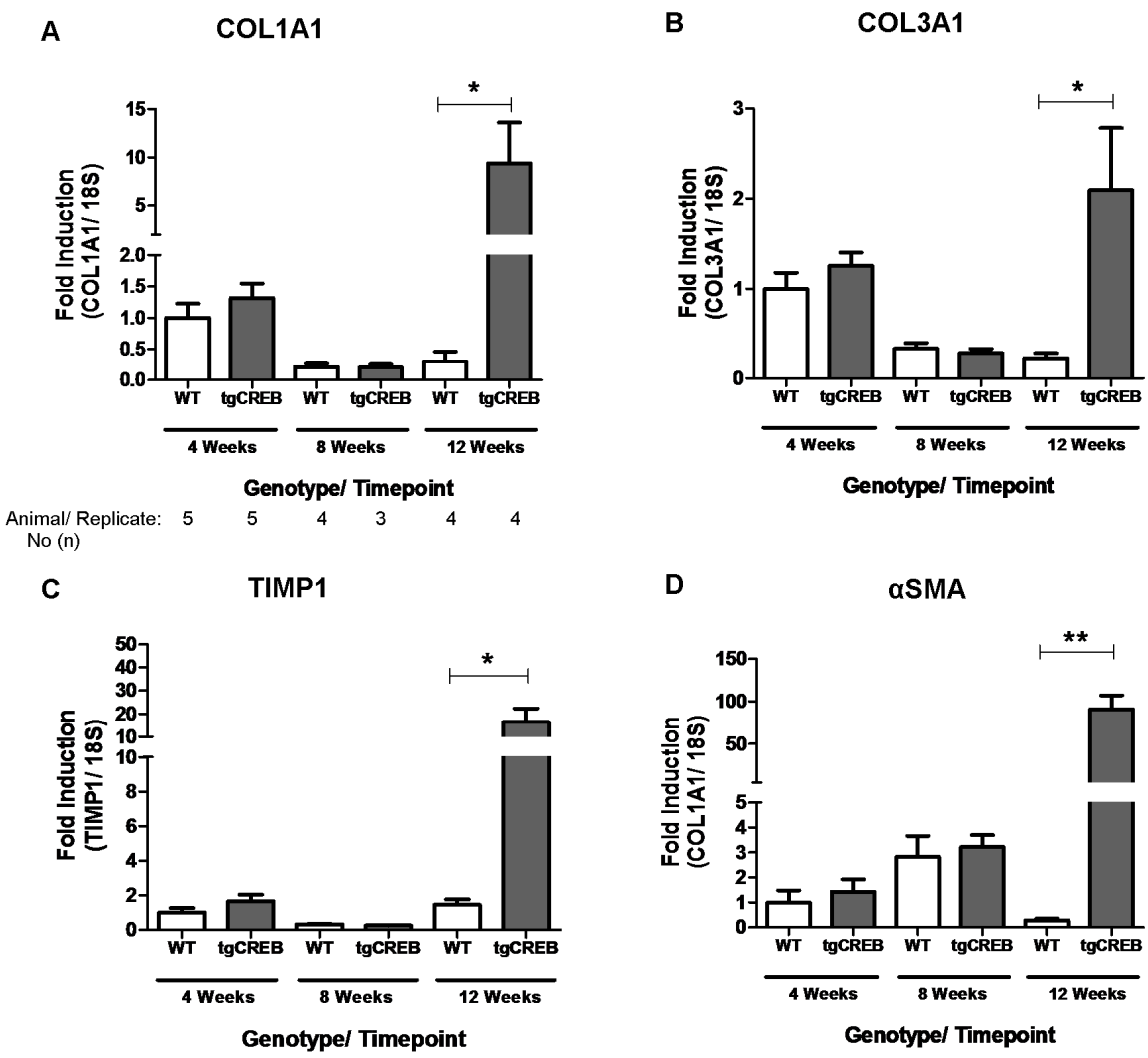

Figure 5.14 Real-time quantitative PCR analysis for (A) COL1A1, (B) COL3A1, (C) TIMP1 and (D) αSMA mRNA expression in whole liver lysates derived from CREB S133A mice (grey bars) at 4, 8 and 12 weeks (n= 3-5 per time point). At each time point comparison is made to mRNA from whole liver lysates derived from age-matched wild-type (+/+) control animals (white bars). In each case, target mRNA expression is calculated relative to the expression of the 18S housekeeping gene and fold-induction expressed relative to target mRNA expression in the +/+ control group at 5 weeks. Statistical comparisons between means were made using an unpaired student t-test. Error bars represent SEM, *p<0.05, **p<0.01, ***p<0.001. The number of animals/ replicates represented by each bar is indicated below the x-axis of graph 5.14 A.

5.3 Uniaxial strain facilitates cytoskeletal realignment and promotes a fibrogenic phenotype in HSCs *in vitro*

Physical factors, including both changes in matrix stiffness and stretch, may be important in promoting a fibrogenic phenotype in HSCs. In each murine model of congestive cardiac failure, αSMA-staining (a marker of myofibroblast activation) was observed in a perisinusoidal distribution in association with sinusoidal dilatation. It was hypothesised that uniaxial stretch, consequent upon sinusoidal dilatation, might promote a fibrogenic phenotype in HSCs. In order to investigate this hypothesis, HSCs were cultured on collagen-I-coated deformable silicon membranes and subjected to uniaxial mechanical strain for between 4 and 24 hours (Figure 5.15). Cyclical strain (1Hz) was applied to the membranes to give uniaxial strain of 2.5-10%. Cytoskeletal organisation was assessed by digital image analysis following F-actin staining with fluorescently-labelled phalloidin.

Figure 5.15

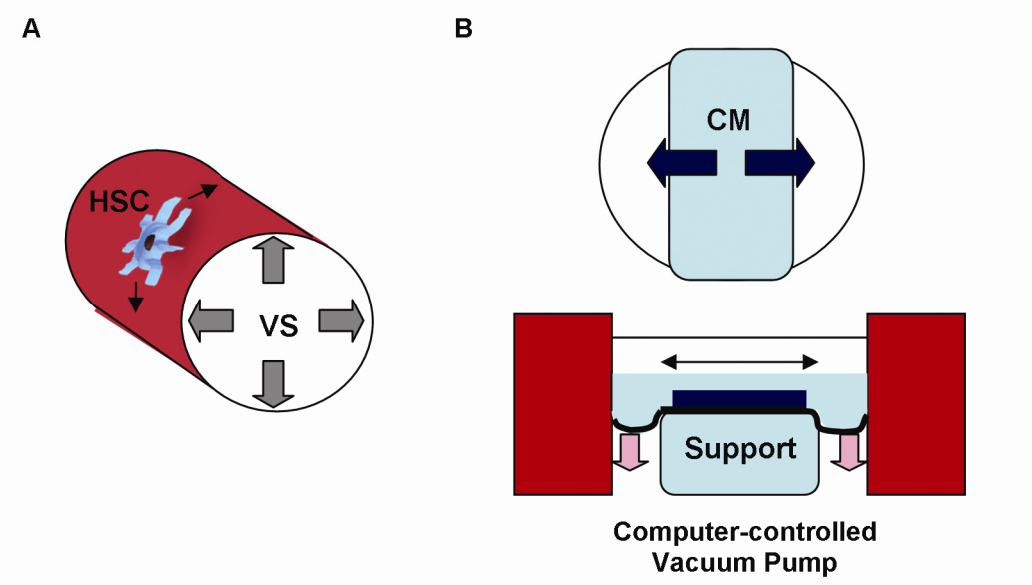

Figure 5.15 (A) Schematic representation of the relationship between vascular sinusoids (VS) and hepatic stellate cells (HSCs) *in vivo*. Sinusoidal dilatation, as encountered in hepatic congestion would result in uniaxial deformation of perisinusoidal HSCs. (B) Schematic representation of Flexcell FX2000 apparatus. HSCs are cultured in six-well plates on collagen-I-coated deformable membranes. Each membrane is suspended above a central arctangular™ support. Negative pressure applied to the base of each well from a computer controlled vacuum pump leads to indrawing of the peripheral (unsupported) section of each well. This results in uniaxial deformation of the central (supported) section and the cell monolayer (CM) adherent to this region. The apparatus is calibrated to produce cyclical (1Hz) uniaxial strain in the range 2.5-10%.

HSCs subjected to cyclical uniaxial strain in 2-dimensional culture for 4-24 hours demonstrate reorientation of their actin stress fibres parallel to the direction of applied stress (Figure 5.16). After 4 hours, the values for mean stress fibre orientation (value in degrees ± SEM) relative to the direction of applied strain for different magnitudes of strain were: control/ unstrained, 41.60 ± 2.28^{o}; 2.5% strain, 40.47 ± 2.52^{o}; 5% strain, 33.45 ± 2.86^{o}; and 10% strain, 38.40 ± 2.78^{o}. After 24 hours, the values for mean stress fibre orientation (value in degrees ± SEM) relative to the direction of applied strain for different magnitudes of strain were: control/ unstrained, 47.95 ± 2.42^{o}; 2.5% strain, 24.91 ± 2.90^{o}; 5% strain, 32.52 ± 2.21^{o}; and 10% strain, 37.93 ± 2.12^{o}.

Real-time quantitative PCR of cDNA derived from HSC cells subjected to cyclical (1Hz) uniaxial strain (2.5-10%) was used to investigate the effect of increasing strain on the expression of selected profibrotic genes including COL1A1, COL3A1, αSMA and TIMP1 (Figure 5.17). Gene expression is expressed as fold induction relative to 18S expressions. Values are standardised to expression values in cells exposed to 2.5% strain. The values for fold induction of αSMA (value ± SEM) are: 2.5% strain, 1.000 ± 0.104; 5% strain, 1.229 ± 0.130; and 10% strain, 1.030 ± 0.090. The values for fold induction of COL1A1 (value ± SEM) are: 2.5% strain, 1.000 ± 0.041; 5% strain, 1.259 ± 0.076; and 10% strain, 1.201 ± 0.071. The values for fold induction of COL3A1 (value ± SEM) are: 2.5% strain, 1.000 ± 0.085; 5% strain, 2.400 ± 0.232; and 10% strain, 3.584 ± 0.371. The values for fold induction of TIMP1 (value ± SEM) are: 2.5% strain, 1.000 ± 0.092; 5% strain, 1.466 ± 0.115; and 10% strain, 1.778 ± 0.132. An increase in the magnitude of uniaxial strain from 2.5-10%, resulted in a statistically significant increase in the expression of COL1A1 (1.2-fold, $p<0.05$), COL3A1 (3.6-fold, $p<0.001$) and TIMP1 (1.8-fold, $p<0.001$). Alterations in the magnitude of applied strain (2.5-10%) did not result in any significant alteration in αSMA expression (unpaired student t-tests).

Figure 5.16: Effect of cyclical uniaxial strain on cytoskeletal organisation and cell orientation in primary murine HSCs

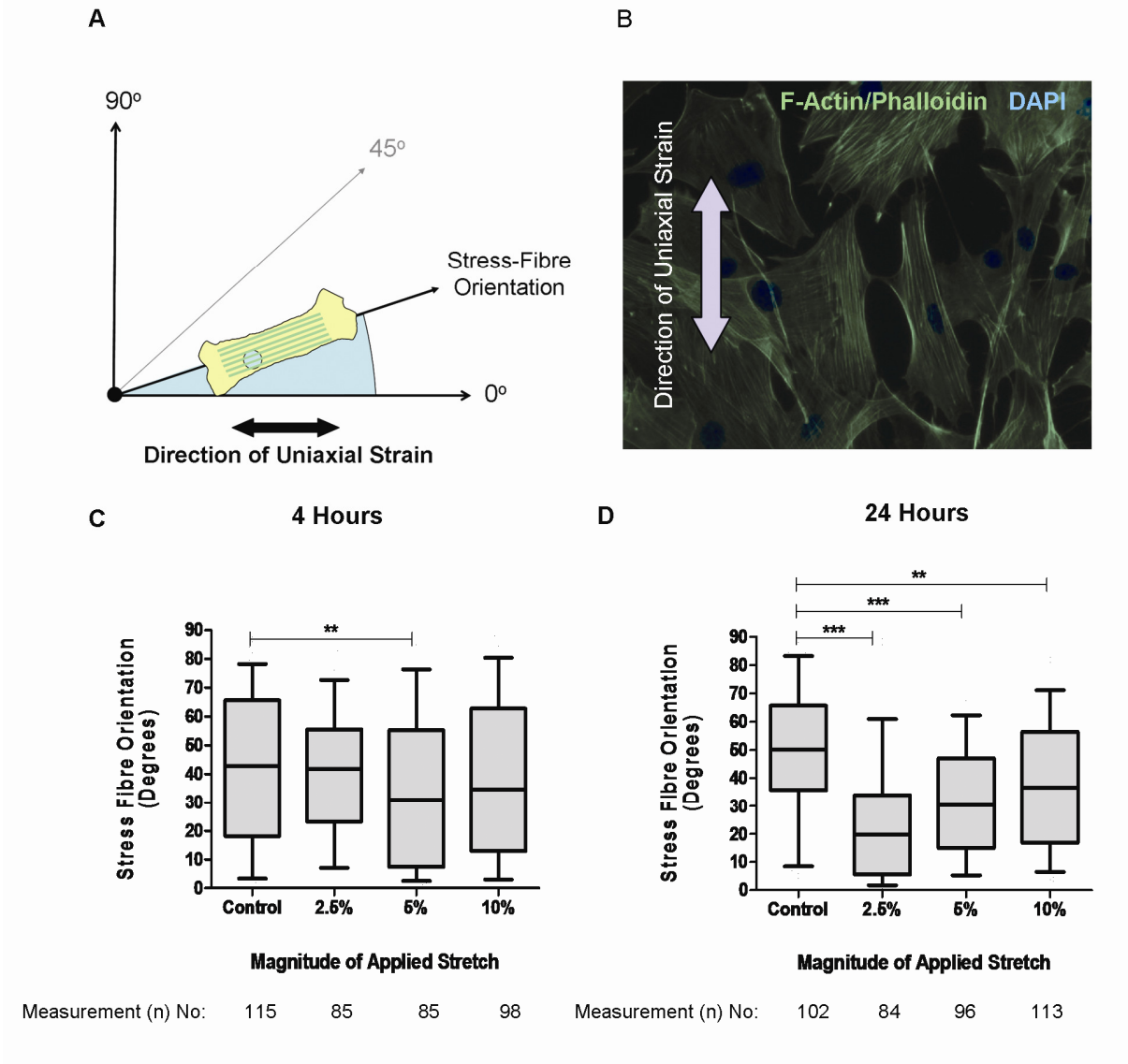

Figure 5.16 HSCs subjected to cyclical uniaxial strain (2.5-10%) demonstrate reorientation of stress fibres parallel to the direction of applied strain. (A) The orientation of actin stress fibres in HSCs was measured relative to the direction of applied uniaxial strain. (B) The predominant orientation of actin stress fibres in individual HSCs was measured by digital image analysis following immunofluorescent staining of the actin cytoskeleton with fluorescently-labelled phalloidin. The graphs show the change in mean stress fibre orientation of HSCs subjected to cyclical uniaxial strain for (C) 4 and (D) 24 hours. Values represent the mean orientation of stress fibres relative to the direction of strain. Stress fibre orientation was determined for all cells in 20 randomly selected high power (x200) fields. The number of cells represented by each bar is indicated below the x-axis of each graph. Boxes represent 25th to 75th percentiles and whiskers indicate 10th and 90th percentiles. Statistical comparisons between means were made using a Mann-Whitney test (**p<0.01 ***p<0.001).

Figure 5.17: Effect of cyclical uniaxial strain on pro-fibrotic gene mRNA expression in primary murine HSCs

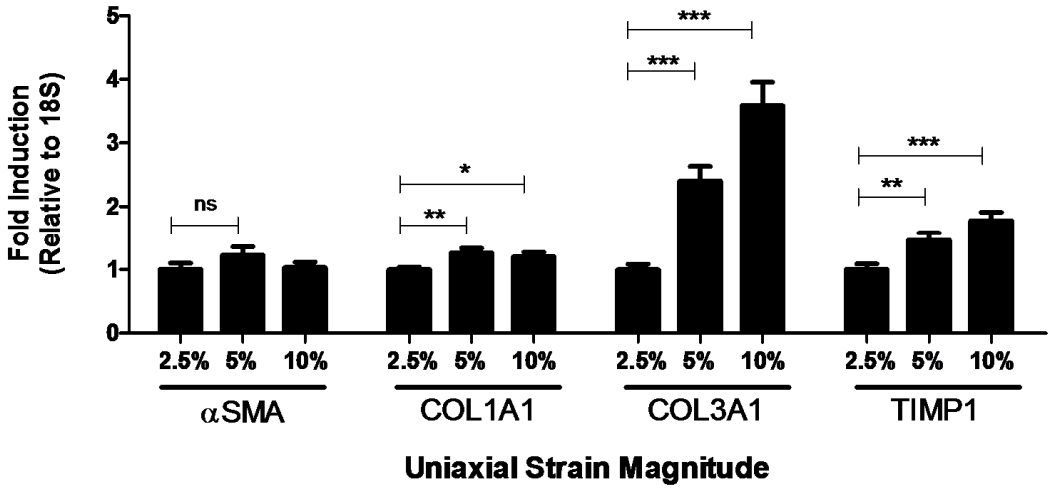

Figure 5.17 Graphs showing the mRNA expression for selected pro-fibrotic genes in HSCs subjected to cyclical (1Hz) uniaxial strain with magnitude 2.5-10% (as indicated) for a period of 24 hours. Gene expression (mRNA) was measured using SYBR-green quantitative PCR relative to the expression of the 18S housekeeping gene. Values are represented as fold-induction relative to gene expression in cells subjected to 2.5% uniaxial strain. Increasing the magnitude of uniaxial strain from 2.5 to 10% resulted in a significant upregulation of COL1A1 (1.2-fold, $p<0.05$), COL3A1 (3.6-fold, $p<0.001$) and TIMP1 (1.8-fold, $p<0.001$) expression. The results reflect the mean of 3 replicates in 3 independent experiments (n=9). Statistical comparisons between mean values were made using an unpaired student t-test. (ns = not significant, *$p<0.05$, **$p<0.01$ and ***$p<0.001$).

5.4 Increases in matrix stiffness promote cytoskeletal reorganisation and fibrogenic phenotype in HSCs *in vitro*

Experiments were conducted to determine the effect of changes in matrix stiffness on HSC morphology and cytoskeletal organisation *in vitro*. Primary murine HSCs were cultured on collagen-I-coated PA gel supports of defined stiffness (G' 1-12kPa). Cytoskeletal organisation was assessed by digital image analysis following F-actin staining with fluorescently-labelled phalloidin (Figure 5.18). HSCs cultured on soft (1kPa) supports were small and rounded with absent stress fibres. In contrast, HSCs cultured on stiff (12kPa) supports were well-spread and flattened with numerous fine cellular processes and prominent actin stress fibres. Real-time PCR was used to investigate the effect of changes in matrix stiffness on the expression of selected profibrotic genes. Gene expression is expressed as fold induction relative to 18S expressions. Values are standardised to expression values in cells cultured on 1kPa supports. The values for gene of interest expression (value ± SEM) for HSCs cultured on 1kPa and 12kPa supports are: αSMA, 1kPa 1.000 ± 0.156/ 12kPa 1.888 ± 0.230; COL1A1, 1kPa 1.000 ± 0.143/ 12kPa 1.587 ± 0.140; COL3A1, 1kPa 1.000 ± 0.152/ 12kPa 1.496 ± 0.130; and TIMP1, 1kPa 1.000 ± 0.089/ 12kPa 1.274 ± 0.090. In comparison to cells cultured on soft (1kPa) supports, HSCs on stiff (12kPa) supports upregulated expression of αSMA (1.9-fold, $p<0.05$), COL1A1 (1.6-fold, $p<0.05$) and COL3A1 (1.5-fold, $p<0.05$). There was a trend towards upregulation of TIMP1 in HSCs cultured on stiff supports but this was not statistically significant. These results are consistent with published studies demonstrating that increases in matrix stiffness across a pathophysiologically-relevant range (1-12kPa) promote myofibroblast differentiation and collagen deposition in both HSCs (134) and PFs (133).

Figure 5.18: The effect of PA support stiffness on cytoskeletal organisation and pro-fibrotic gene expression in primary murine HSCs

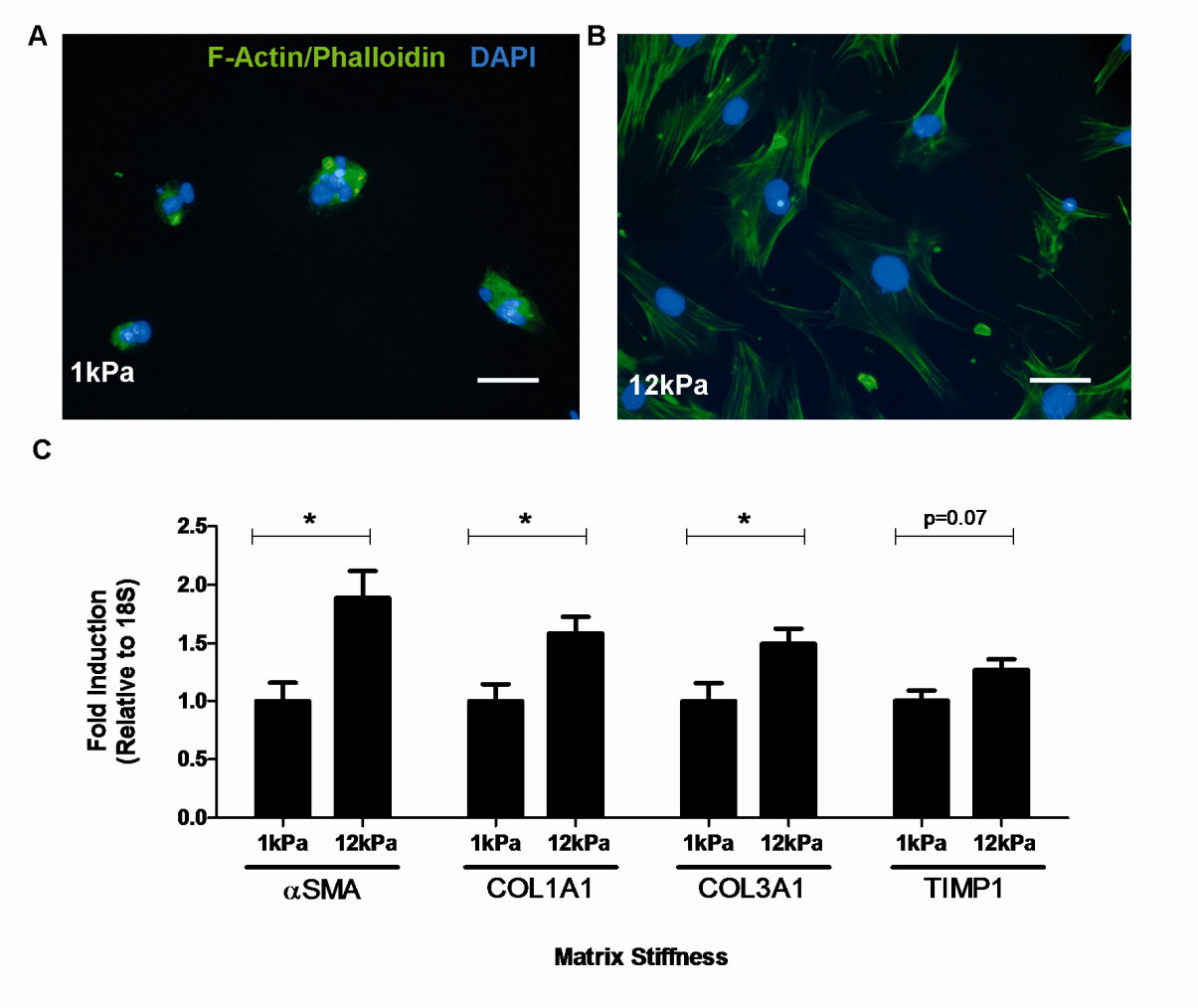

Figure 5.18 Confocal photomicrographs (x200 magnification) of primary murine HSCs cultured on 1kPa and 12kPa collagen-I-coated PA supports, as indicated. Cells have been stained for the presence of actin stress fibres (phalloidin- green), mature focal adhesions (anti-vinculin-red) and nuclear DNA (4',6'-diamidino-2-phenyl-indole dihydrochloride (DAPI)- blue). (C) Graphs showing mRNA expression for selected pro-fibrotic genes in HSCs cultured for 72 hours on 1kPa and 12kPa collagen-I-coated PA supports, as indicated. Gene expression (mRNA) was measured using SYBR-green quantitative PCR relative to the expression of the 18S housekeeping gene. Values are expressed as fold-induction relative to gene expression on 1kPa supports. The results reflect the mean of 3 replicates in 3 independent experiments (n=9). Statistical comparisons between means were made using an unpaired student t-test (*$p<0.05$).

5.5 Discussion

Cardiac hepatopathy defines a heterogeneous group of conditions that are perhaps best described in relation to the duration of cardiac dysfunction (325). Acute cardiac dysfunction is typically associated with the development of ischaemic hepatitis. This syndrome is characterised clinically by marked elevation of serum transaminase levels and histologically as acute hepatitis with centrilobular necrosis (326). In contrast cardiac fibrosis and cirrhosis has been described in relation to patients with chronic congestive cardiac failure (304). Myers *et al* published a detailed description of the clinical, haemodynamic and histological characteristics of a cohort of 83 patients presenting with cardiac hepatopathy (325). Patients were sub-divided into clinical groups based on the duration of cardiac dysfunction. Serum transaminase levels were markedly elevated in patients with either acute or acute on chronic cardiac dysfunction. In contrast, serum transaminase levels were typically within the normal range, or more modestly elevated in patients with chronic cardiac dysfunction. In respect to liver histology, centrilobular necrosis, inflammation and sinusoidal haemorrhage were more common in patients with acute, or acute on chronic cardiac dysfunction. Severe fibrosis sufficient to disrupt the normal microscopic architecture was uncommon (present in 19% of cases), and indeed was absent in all patients with acute cardiac dysfunction. Cirrhosis was present in only one patient with chronic valvular heart disease. This would suggest, as would be expected, that severe liver fibrosis and cirrhosis develops as a consequence of chronic cardiac dysfunction.

Ischaemic hepatitis is traditionally believed to occur as a consequence of acute impairment of hepatic perfusion secondary to systemic hypotension. However this model represents an oversimplification. Hypotension alone would appear to be insufficient to precipitate ischaemic hepatitis (303). Seeto *et al* published a case comparison study in which patients presenting with markedly elevated transaminase levels (>20x ULN) secondary to ischaemic hepatitis were compared to a control group of previously healthy individuals who had sustained non-hepatic trauma (303). Despite similar reductions in systolic blood pressure, no patients in the control group developed ischaemic hepatitis. Furthermore, all patients with ischaemic hepatitis had evidence of pre-existing heart disease with the overwhelming majority (94%) demonstrating features of right heart failure. These results would suggest that ischaemic hepatitis is uncommon in patients without pre-existing heart disease. This is consistent with the results of histological studies suggesting that chronic passive congestion may contribute to the development of centrilobular necrosis in the context of systemic

hypotension (301).

What then are the precise haemodynamic alterations that promote ischaemic hepatitis or liver fibrosis in patients with cardiac dysfunction? Myers *et al* reported that in patients with acute cardiac dysfunction, transaminase elevation was highly correlated with right atrial pressure (RAP), free hepatic venous pressure (FHVP) and wedged hepatic venous pressure (WHVP), but interestingly was not correlated with cardiac index (325). In patients with acute on chronic cardiac dysfunction, there was no correlation between transaminase levels and RAP, free hepatic venous pressure or wedged hepatic venous pressure. In patients with chronic cardiac dysfunction transaminase elevation was only weakly correlated to RAP. In respect to liver histology, as would be expected, elevated free hepatic vein pressure was associated with sinusoidal dilatation and patients with liver fibrosis had elevated WHVP, reflecting elevated portal pressure. Liver fibrosis was not significantly associated with any particular haemodynamic variable. These results would suggest that elevated venous pressure is an important factor in the pathogenesis of ischaemic hepatitis. However the haemodynamic variables that contribute to chronic cardiac hepatopathy are less clearly defined.

The haemodynamic changes described in patients following the Fontan procedure provide significant insight into the effects of chronic hepatic congestion. Liver fibrosis and cirrhosis are common complications of the Fontan procedure (306-308). Kiesewetter *et al* undertook detailed haemodynamic measurements in a cohort of patients assessed for surgical correction of failing Fontan circulations, the majority of which (7/12) had evidence of cirrhosis on liver biopsy (308). There was a significant correlation between the Fontan duration and the extent of liver fibrosis. More importantly the presence of cirrhosis was positively correlated with free hepatic vein pressure. As discussed previously, detailed morphological analysis of liver histology in a related cohort of Fontan patients showed histological features similar to those described in cardiac sclerosis (307). It was postulated that in these patients, the absence of inflammation or hepatocellular damage in biopsy specimens meant that fibrosis may be mediated by a non-inflammatory mechanism. This is somewhat speculative and the absence of acute inflammation in these specimens may be related to sample bias. Liver biopsies were only obtained from patients undergoing pre-operative assessment prior to surgical correction of failing Fontan circulations, whose livers would have been subject to chronically elevated right-sided pressures. The time course of histological events in the Fontan liver remains uncharacterised. Ethical considerations would prevent serial liver biopsies being taken from these patients throughout the natural history of their condition. Across a range of

inflammatory disorders, including autoimmune hepatitis and non-alcoholic fatty liver disease, it is not uncommon for liver biopsies from patients with advanced or 'burnt out' cirrhosis to demonstrate an absence of acute inflammation or hepatocellular damage. It was hoped that a murine model of congestive cardiac failure would prove a better understanding of the histological events contributing to the development of liver fibrosis in chronic cardiac hepatopathy.

The murine models described in this chapter are most appropriately defined as models of acute on chronic cardiac dysfunction. In the python model of cardiac hepatopathy, features of overt congestive cardiac failure are associated with marked elevation in serum transaminase levels (>3x ULN). Histological abnormalities in liver architecture are not present until mice demonstrate features of overt congestive cardiac failure and then develop rapidly. In each model the principle histological abnormalities observed at the context of decompensated cardiac failure are sinusoidal dilatation/ ectasia with associated hepatocyte degeneration manifested as granular cytoplasmic change, vacuolation and hepatocyte plate atrophy. Hepatocyte apoptosis was observed in the CREB S133A model but gross centrilobular necrosis was not seen. Neither of these models provides a model of progressive liver fibrosis analogous to the Fontan liver. Distinct sinusoidal pericellular αSMA immunopositivity is seen that would suggest MFB activation. However, although fibrous spur formation is present in some specimens in association with sinusoidal dilation, bridging fibrosis and liver fibrosis is not observed. However, it should be acknowledged that the natural history of cardiac failure in this model is such that there may be insufficient time for the development of organised liver fibrosis and cirrhosis. With the notable exception of TIMP1, in the python model, and to a lesser extent TIMP2, there was no significant difference in the expression of selected ECM components/ profibrotic mediators and inflammatory cytokines prior to the onset of overt cardiac failure. This would suggest that the histological changes observed in patients with overt congestive cardiac failure occur rapidly and without significant prodrome.

In the python model there is a clear and progressive increase in hepatocyte nuclear size as the mice age. It has been suggested that this may relate to impairment of nuclear fission due to the germline mutation in the dlp1 gene and a resulting increase in cell ploidy. Further work would be required to investigate this further, but this observation raises clear concerns in respect to the use of the python mouse as a model of cardiac hepatopathy. Such changes in hepatocyte nuclear appearance are not apparent in the CREB S133A model. However, a

similar pattern of histological changes is otherwise observed in the CREB S133A model of dilated cardiomyopathy. Importantly, expression of the CREB S133A transgene which disrupts CREB-related gene transcription is restricted to the heart. Therefore the similarity in histological changes observed in the liver of both the CREB S133A and python models of cardiac hepatopathy does, to some extent, allay concerns that observed phenotype in the python liver is a consequence of a more general impairment of organelle fission or mitochondrial function . Liver histology from CREB S133A mice prior to the onset of overt cardiac failure is indistinguishable from age-matched control animals.

It is probable that the histological abnormalities observed in the livers taken from mice with overt cardiac failure are a consequence of both systemic hypotension and elevated right-sided pressures. Haemodynamic measurements in 10-11 week-old python mice demonstrate a significant reduction in mean arterial pressure relative to controls. There was no difference in central venous pressure between the two groups at this time point. However, in python mice, the development of overt cardiac failure was associated with clinical features of elevated right-sided pressure including: ascites, peripheral oedema and right atrial/ ventricular enlargement. As the haemodynamic measurements obtained in the python model were taken prior to the development of advanced cardiac failure they do not properly reflect the conditions present during the evolution of hepatic dysfunction. Further haemodynamic measurements would therefore be required, in both models, to delineate the relative importance of systemic hypotension and central venous pressure in promoting hepatic dysfunction in this model.

The aim of the research presented in this chapter was to provide the first detailed characterisation of the sequence of histological events observed in murine models of cardiac hepatopathy. Neither the Python or CREB S133A models of dilated cardiomyopathy provides a model of chronic liver fibrosis comparable to that observed in livers from patients with failing Fontan circulations. Instead they represent models of acute on chronic cardiac hepatopathy, more readily comparable to the ischaemic hepatitis observed in patients with pre-existing cardiac dysfunction. In each model, the natural history of cardiac dysfunction is such that there is insufficient time for the development of organised liver fibrosis and cirrhosis. It is unclear whether, were it possible to extend the time course of cardiac dysfunction in these models, we would observe the development of bridging fibrosis and ultimately cirrhosis. It is equally uncertain whether in human patients with the Fontan circulation, liver fibrosis is a consequence of chronic liver damage secondary to persistently

elevated right-sided pressures, or repetitive injury due to recurrent episodes of systemic hypotension and hypoxaemia. These questions would be better addressed with the development of an animal model with a more protracted phase of right-sided heart failure.

The precise aetiological factors responsible for the development of liver damage and fibrosis in cardiac hepatopathy are poorly characterised. These may include: tissue hypoxia secondary to diminished hepatic perfusion; perisinusoidal oedema restricting diffusion of oxygen and nutrients; elevated central venous pressure resulting in sinusoidal dilatation and hepatocyte plate compression; and cellular responses to alteration in matrix stiffness and cellular tension. Pimonidazole-adduct immunohistochemistry was used to determine the degree of liver hypoxia associated with the development of congestive cardiac failure. In python mice with features of overt congestive cardiac failure, there was increased intenstity of staining around the central veins, with extension of pimonidazole-adduct formation outward into the liver parenchyma. This pattern of increased tissue hypoxia paralleled the pattern of hepatocyte injury and hepatic myofibroblast activation. Hypoxia is known to promote type I collagen production by activated HSCs (327) and hypoxia has been implicated as a possible aetiological factor in a range of liver diseases (328). However a full discussion as to the role of tissue hypoxia in promoting liver fibrosis is beyond the scope of this thesis.

It has been suggested that direct mechanical stimulation of liver resident cell populations consequent upon elevated central venous pressure may promote liver fibrosis. Elevated central venous pressure results in hepatic venous distension and sinusoidal dilatation. In addition, in patients with tricuspid regurgitation, atrial contraction is associated with intra-hepatic reflux resulting in cyclical sinusoidal dilatation and compression of hepatocyte cell plates (308). HSCs residing within the space of Disse would therefore be subjected to repetitive strain. The results presented in this chapter demonstrate that HSCs subjected to increasing cyclical uniaxial strain respond by up-regulation of profibrotic genes, including COL1A1, COL3A1 and TIMP1, that would be expected to promote liver fibrosis. This is consistent with the results of previous research demonstrating that cyclical mechanical stretch enhances TGFβ expression by HSCs *in vitro* (329). Another consequence of hepatic congestion is an increase in liver stiffness (115). In experiments conducted using collagen-I-coated PA gels of defined stiffness (1-12kPa) I have demonstrated that increasing matrix stiffness is associated with upregulation of markers of MFB activation and fibrillar collagen components. This confirms the results of previous *in vitro* research showing that increases in matrix stiffness across a pathophysiological range promotes MFB differentiation and matrix

deposition in both HSCs and PFs (133, 134). It is tempting to speculate that increased tissue stiffness due to oedema may render liver resident cells, including MFB precursors, more responsive to a range of factors, including inflammatory cytokines, toxins and hypoxic stimulation. However, more research is required to understand how changes in matrix stiffness/ intracellular tension might influence MFB responses to mitogenic and profibrotic stimulation.

Chapter 6: General Discussion

6.1 Overview

The principle aim of this thesis was to explore how changes in matrix stiffness observed in liver disease might influence the development of hepatocellular carcinoma. Previous research undertaken by Dr Rebecca Wells suggested that changes in matrix stiffness might be important mechanistically in the initiation and perpetuation of liver fibrosis (133-135, 292). The ability of cells to respond to changes in the mechanical properties of the ECM has been shown to be critical to the regulation of both cell proliferation and differentiation (97, 98). The stiffness of the ECM in different tissues spans several orders of magnitude (83). However, within each tissue, under normal conditions, differentiated cells are exposed to a narrow range of environmental stiffness (100). As discussed previously, matrix stiffness changes dramatically throughout embryological development and in pathological processes, including inflammation and cancer development. Understanding how cells respond to these pathophysiologically-relevant changes in matrix stiffness will greatly enhance our understanding of these disease processes. Changes in matrix stiffness associated with inflammation and fibrosis are thought to be mechanistically important in promoting cancer development. The relationship between inflammation and cancer development has long been recognised (330, 331). Cancer development involves both factors intrinsic to the cancer cells themselves (genetic instability), and extrinsic factors. These include the stromal, endothelial and inflammatory cells that contribute to a heterocellular tumour, and the biochemical and mechanical properties of the extracellular matrix.

Liver fibrosis is associated with an increased risk of cancer development (167, 168), with multiple mechanisms thought to account for this association. The abundant ECM that characterises liver fibrosis promotes integrin signalling in hepatocytes, which may enhance the growth and survival of pre-cancerous cells. Both collagen and integrin expression is closely correlated with tumour development in well-validated murine models of HCC (332). There is also extensive paracrine crosstalk between tumours and tumour-associated stromal cells. Fibroblasts are associated with tumour cells at all stages of cancer progression. Tumour-associated stromal cells produce growth factors, chemokines and ECM proteins that promote tumour growth (333). The expression profile of non-tumoral liver tissue is correlated to survival in patients with HCC (334). Genetic studies have demonstrated that a 36-gene signature originating from the non-cancerous liver tissue can accurately predict the

risk of recurrence in patients with multifocal HCC (335). The genes identified in this study were a heterogeneous group. They include the Fps/Fes proto-oncogene that it known to promote angiogenesis and which is implicated in the development and progression of thyroid and colon cancer. Another signature gene encodes oncoprotein 18, a protein that is phosphorylated in response to several extracellular signals and is highly expressed in leukaemia, breast and ovarian cancer. A number of the genes have inflammatory or immune modulating functions, including: tumour necrosis factor-α (LITAF), T cell receptor β locus, DC class II histocompatibility antigen α chain (HLA-DQA1) and immunoglobulin-binding protein 1 (IGBP1). Interestingly matrix proteins are not represented. The ECM is also thought to play a role in regulating the availability of growth factors. It has been demonstrated that growth factors, including TGFβ are sequestered in ECM that may subsequently been released in the context of inflammation, promoting tumour development (336). Furthermore, the presence of liver fibrosis may impair immune surveillance by natural killer cells facilitating the development of HCC (337). Finally, it has been proposed that changes in the mechanical properties of the ECM may promote the development of malignancy (155, 172).

Seminal research undertaken by Paszek *et al* in the breast cancer field explored the relationship between matrix stiffness and tumour development (155). As discussed previously, it was demonstrated that tumours were rigid due to both the presence of a stiff stroma and elevated cytoskeletal tension. Rho driven cytoskeletal tension promoted focal adhesion formation, disturbed tissue polarity and glandular differentiation while enhancing growth factor stimulated ERK activation. Conversely, EGF-transformed epithelia with elevated ERK and Rho activity could be induced to revert to a non-malignant phenotype if either ERK or Rho-generated contractility was inhibited or cells were cultured on soft PA supports with stiffness approximating that of non-malignant mammary tissue. These observations formed the basis of a model for tensional control of malignant transformation. Subsequent *in vivo* experiments demonstrated that a reduction in tissue stiffness through inhibition of collagen cross-linking could impede tumour growth in a murine model of breast cancer (46). The premise that matrix stiffness might regulate cancer development has been extended to other malignancies, with increasing matrix stiffness shown to promote proliferation in both transformed glioma cells (184) and lung carcinoma cells (338). However, stiffness dependent-regulation of cell proliferation is not a universal property of cancer cells. Indeed, Tilghman *et al* have shown that cancer cell lines can be segregated on the ability to proliferate on soft (<1000Pa) collagen-coated gels (338, 339). However, the

precise mechanisms underlying the biomechanical regulation of cancer cell phenotype remain incompletely characterised.

The experiments conducted in this thesis were intended to evaluate the effect of changes in matrix stiffness on proliferation, differentiation and growth factor-mediated signalling in HCC cells. I have also examined the effect of matrix stiffness on the behaviour of hepatic progenitor cells, which have themselves been implicated in hepatocarcinogenesis.

6.2 Summary of key findings and suggestions for future research

6.2.1 The effect of matrix stiffness on the pathophysiology of hepatocellular carcinoma (HCC)

The liver provides an exemplary model in which to explore the relationship between tissue stiffness and cancer development. Transient elastography and torsional rheometry have defined the range of stiffness values that would be encountered by cells during the evolution of liver fibrosis and hepatocarcinogenesis (117, 135, 340). Experiments conducted with ligand coated PA supports have been used to explore the effect of changes in matrix stiffness on cancer cell phenotype. These experiments demonstrate that increases in matrix stiffness are associated with both the development of liver fibrosis and tumour development, and enhance proliferation in HCC cells *in vitro*. These findings are consistent with the published literature which argues that physiological stiffness is inhibitory to cell cycle progression (127). Increases in matrix stiffness typically occur in the context of tissue damage or inflammation, where a loosening of cell cycle regulation may be desirable to facilitate tissue regeneration. Thus, tensional control of cell cycle progression may represent a fundamental and primitive mechanism regulating cellular proliferation. However, an undesirable consequence of such tensional homeostasis in the context of chronic inflammation might be to promote cancer development.

Alterations in matrix stiffness have broad and pervasive effects in relation to growth factor-mediated signalling. Increases in matrix stiffness are associated with more robust activation of the FAK, ERK, Akt/ PKB and STAT3 signalling pathways in response to HGF stimulation. Stiffness-dependent regulation of STAT3-signalling has not previously been described. The results are consistent with a model in which cytoskeletal tension regulates the activity of multiple signalling pathways. The cytoskeleton functions as a central rheostat or computer processor, dampening or augmenting the responses of multiple signalling pathways to external stimulation (155). β1-integrin is implicated as being an important regulator of stiffness-dependent cell proliferation. Immunohistochemical analysis confirms that both β1-integrin and phospho-FAK^{Tyr397} are upregulated in HCC specimens *in vivo*. Furthermore, *in vitro* inhibition of either β1-integrin or FAK was associated with a reduction in the proliferation of both HepG2 and Huh7 cells.

At a basic level, the results presented in this thesis provide evidence that increased matrix stiffness, as encountered in the cirrhotic liver, is mechanistically important in promoting HCC development. However, these results also suggest that a reduction in matrix stiffness is sufficient to induce reversible cellular quiescence that may be analogous to cancer cell dormancy. Genetic studies of disseminated breast cancer cells suggest that cancer cells dissemination is an early event in the natural history of many tumours (341). Dormant cancer cells are thought to represent a quiescent population of disseminated cells that exist in a state of reversible growth arrest. The mechanisms responsible for inducing cancer cell dormancy and the subsequent 'reawakening' of these disseminated cells remain poorly characterised. This is in part due to the fact that disseminated tumour cells are difficult to detect *in vivo* and there is a lack of reliable *in vitro* models of cancer dormancy. The results presented here are consistent with a model in which a reduction in the stiffness of cancer cell niche, as might be encountered by disseminated tumour cells, may be sufficient to induce reversible cellular quiescence. In a low stiffness environment, disseminated tumour cells would be expected to have low levels of cell proliferation and relative insensitivity to growth factor signalling. A subsequent increase in environmental stiffness secondary to localised inflammation, desmoplasia, or alterations in the stiffness-sensing machinery of the cell due to genomic instability, might facilitate the reactivation of dormant cells. This hypothesis remains somewhat speculative. However, it is clear that cell culture on low stiffness PA gel supports provides an interesting model of reversible cancer cell quiescence, with the potential to provide insight into mechanisms underlying cancer dormancy. Indeed, using PA supports, Tilghman *et al* have shown that rigidity-dependent cell lines exhibit lower levels of cellular ATP and protein synthesis when cultured on soft supports (339). They suggest that metabolic events may be key regulators promoting the slow growth of rigidity-dependent cells. This example illustrates that PA supports have the potential of allowing cancer cell biology to be investigated under conditions of cellular quiescence and reflecting the biomechanical environment encountered by disseminated tumour cells.

In this thesis, PA supports have also been used to investigate the effect of changes in matrix stiffness on chemotherapy resistance in HCC. The results suggest that increasing matrix stiffness, as would be encountered in the setting of cirrhosis, is associated with a reduction in chemotherapy-induced apoptosis in HCC cells. The mechanisms underlying this observation are unclear but may plausibly relate to alteration in the expression of multidrug resistance transporter proteins or increased resistance to chemotherapy due to EMT. Rather unexpectedly it was shown that following chemotherapy, there was an increase in the

frequency of clone initiating cells for cells maintained in a low stiffness environment. This phenomenon was observed in both the HepG2 and Huh7 cell line, and following treatment with both cisplatin and 5-flurouracil. Using flow cytometry it was subsequently demonstrated that culture in a low stiffness environment was associated with an increase in the frequency of stem cell marker expression, including CD44, CD133 and CXCR-4. This effect was further enhanced in the presence of chemotherapy. A process of enrichment for cells with stem cell characteristics following treatment with chemotherapy may explain the results of these clonogenic assays. However, a number of questions remain unanswered. Firstly, it is unclear whether these 'stem cell markers' accurately define the subset of cells with clone-initiating potential following chemotherapy. It is also uncertain whether the enrichment for cells with clone-initiating potential (a stem cell trait) following chemotherapy, is due to positive selection of these cells from a mixed population or active induction of stem cell characteristics. These issues require further investigation. It has previously been shown that stem cells can be regulated by the micro-environment (277). However, the results described here represent the first report that matrix stiffness regulates stem cell marker expression in cancer cells.

6.2.2 The effect of matrix stiffness on hepatic progenitor cell (HPC) response

Hepatic progenitor cells have been implicated in the pathogenesis of HCC. Genetic studies have demonstrated that HCC can be categorised into genetically distinct subgroups (342, 343). It is believed that HCC develops from a range of founder cells, from HPCs through transient-amplifying cells to fully differentiated hepatocytes (53). As previously discussed, markers of progenitor-derived HCC define a subgroup of tumours that are associated with poorer prognosis (58, 344). Factors that promote HPC proliferation may therefore be implicated in hepatocarcinogenesis. It has been demonstrated that factors associated with the progression of chronic liver disease promote HPC proliferation in both the CCl_4 and TAA models of liver fibrosis. Using tissue derived from experiments undertaken by Prof R Wells (University of Pennsylvania) in a rat model of CCl_4-induced liver injury, it has been shown that there is a close correlation between HPC numbers and liver stiffness measurements. The major expansion in HPC numbers in this model coincides with a similarly large increase in fibrous tissue deposition. Attenuation of liver stiffness in animals treated with BAPN, an inhibitor of collagen cross-linking, reduces HPC number, although this result was not statistically significant. Interestingly, an early increase in HPC number occurs in association with a more modest increase in liver stiffness, prior to the development of significant liver

fibrosis. I would hypothesise that this early increase in liver stiffness may be a consequence of interstitial oedema in the context of acute inflammation. Detailed *in vitro* experiments using PA supports demonstrate that increasing matrix stiffness promotes the proliferation of both primary murine HPCs and an immortalised HPC line. Overall, these results are consistent with a model in which increased matrix stiffness, in the context of tissue damage and fibrosis may, in concert with soluble factors and other components of the progenitor cell niche, promote HPC expansion. The development of progenitor-derived HCC may be an unfortunate consequence of this loosening in the biomechanical control of HPC proliferation.

6.2.3 Murine models of cardiac hepatopathy

Cardiac hepatopathy describes a heterogeneous group of conditions characterised by both acute and chronic liver injury. As discussed, cardiac hepatopathy is best defined in relation to the duration of cardiac dysfunction. Acute cardiac dysfunction is associated with the clinical syndrome of ischaemic hepatitis. The results of studies conducted in patients with the Fontan circulation suggested that chronic hepatic congestion resulted in progressive liver fibrosis and cirrhosis in the absence of florid inflammation and hepatocellular damage (307). We had hypothesised that tissue oedema in the context of chronic hepatic congestion might be an important factor in promoting liver fibrosis. Thus models of chronic hepatic congestion might allow us to define a common sequence of events through which cells respond to oedema and provide a model of the early changes associated with increased stiffness in an otherwise architecturally normal and non-inflamed liver. Studies were therefore undertaken to define the sequence of histological events occurring in two unrelated murine models of dilated cardiomyopathy. The murine models described in chapter 5 are most appropriately defined as models of acute on chronic cardiac dysfunction, and unfortunately do not recapitulate the histological features observed in the Fontan liver. Histological abnormalities within the liver are not present until mice develop features of overt and severe cardiac failure. However, to the best of my knowledge, this study represents the first detailed characterisation of the histological events observed in murine cardiac hepatopathy. In each case, features of chronic passive congestion (sinusoidal congestion/ ectasia) and perivenular hepatocyte injury develop concurrently. Hepatocyte damage is evident as a spectrum of injury with granular cytoplasmic change, hepatocyte vacuolation and hepatocyte plate atrophy. MFB activation is inferred by prominent αSMA – staining around dilated sinusoids that radiate outwards from the central veins. However, bridging fibrosis and cirrhosis is not present. It is uncertain whether, were it possible to

extend the time course of cardiac dysfunction, we would observe the development of progressive liver fibrosis (and ultimately cirrhosis)? What is required is an animal model with a more prolonged phase of right heart failure and elevated central venous pressure, without significant systemic hypotension that might contribute to the development of ischaemic hepatitis. A model with these characteristics may provide some insight into the sequence of histological events and factors associated with hepatic congestion that may promote cardiac cirrhosis. Multiple aetiological factors may be responsible for the pathogenesis of cardiac hepatopathy. In the python model, an increase in tissue hypoxia is observed around central veins, which parallels the pattern of hepatocyte necrosis and MFB activation seen in advanced cardiac failure. The role of mechanical factors in promoting liver fibrosis remains uncertain. However, the results of *in vitro* experiments with PA gels, confirmed that increases in matrix stiffness, as might be encountered in hepatic congestion, was associated with an upregulation of markers of MFB activation and fibrillar collagen components. Similarly, repetitive cyclical mechanical strain, as might be encountered by hepatic MFB precursors in the context of sinusoidal dilatation, was associated with similar changes in gene expression. These experiments provide evidence for the importance of biomechanical factors in regulating the development of liver fibrosis. It must be emphasised that however closely these model systems attempt to recapitulate the biomechanical properties of *in vivo* environment, they are inherently artificial, and the results of these experiments should be viewed with some scepticism. It would be extremely difficult to precisely define or replicate the complex range of mechanical stimuli to which cells are exposed within living tissues. However, the basis of our future understanding of biomechanics necessitates the use of these imperfect *in vitro* models of biomechanical cell stimulation.

6.3 Suggestions for future study

The data presented in this thesis raises questions that could form the basis of future research

6.3.1 The effect of matrix stiffness cancer cell biology: wider perspectives

The effect of changes in matrix stiffness on intracellular signalling needs further characterisation. The results presented in this thesis demonstrate that matrix stiffness regulates the activity of multiple signalling pathways including FAK, ERK, PKB/ Akt and STAT3. However, biochemical pathways do not operate in isolation. Cellular behaviour is

governed by networks of molecular interactions with extensive crosstalk between different biochemical pathways. A systems biology approach using phospho-proteomics would facilitate a global assessment of the impact of changes in cellular tension on intracellular signalling. Similarly, array-based transcriptional analysis could be used to assess the effect of changes in matrix stiffness on gene expression. A major limiting factor associated with the use of PA supports is the complex and time-consuming nature of gel fabrication. A method for the rapid fabrication of PA supports in 96- and 384-well formats has recently been reported that has the potential to allow high-throughput screening of cultured cells (338). It has been suggested that this technique could be used to more rapidly define the effect of matrix characteristics on cell growth and differentiation. It could also be used as a screening tool to assess the interaction between matrix stiffness and exogenous factors, including cytokines and matrix components.

6.3.2 *In vivo* models of cancer cell dormancy

An assessment of the importance of the cytoskeleton in regulating the behaviour of dormant cancer cells would benefit from the development of tractable models of cancer cell dormancy. Research has previously been undertaken in which mammary carcinoma cells were injected intravenously into rats that subsequently developed pulmonary metastases (260). No metastases were seen in other organs. However, the implantation of glass fragments in the liver, spleen and mesentery of these animals, prior to the inoculation of tumour cells, resulted in the development of metastases at these sites. Similarly, treatment of rats with CCl_4 for three days prior to cancer cell inoculation was associated with increased tumour localisation and growth within the liver. Comparable results have been shown in animal studies in which the induction of liver fibrosis is associated with increased tumour growth following orthotopic implantation of HCC cells (121, 122). These results are interpreted as showing that factors associated with acute inflammation and fibrosis promote tumour growth. Preliminary experiments have been undertaken in collaboration with Dr Daniel Benton (University Medical Centre Hamburg-Eppendorf) to investigate the utility of using intravenous injection of human HCC cell lines into mice as a model of cancer cell dormancy. In preliminary experiments, Huh7 cells were injected via tail vein into NOD/SCID mice. Cells were subsequently identified following immunostaining for human-specific CK18. Initial results demonstrate the presence of isolated disseminated tumour cells and developing micrometastases within the liver (data not shown). Refinement of this model would facilitate the study of disseminated tumour cells *in vivo*. Experiments could then be

undertaken to investigate factors associated with the reactivation of dormant cells, either by modification of the micro-environment (e.g. induction of liver fibrosis) or genetic modification of the transplanted cells themselves.

6.3.3 The effect of matrix stiffness on cell signalling in hepatic progenitor cells (HPCs)

The results presented in this thesis demonstrate that changes in matrix stiffness influence both proliferation and differentiation of HPCs. Increased matrix stiffness promotes BMOL proliferation and the upregulation of the biliary/ progenitor marker CK19. In contrast, a low stiffness environment, with characteristics similar to that of the normal liver, is associated with lower rates of cell proliferation and a modest upregulation of hepatocyte markers in BMOL cells. This suggests that changes in matrix stiffness may be involved in directing HPCs towards either a hepatocyte or biliary phenotype. Research undertaken in our group has implicated both WNT and Notch signalling in directing stem cell fate (218). The effect of changes in matrix stiffness on WNT and Notch signalling should be studied to assess whether changes in cytoskeletal tension associated with inflammation may modulate the activities of these critical signalling pathways.

The suggestion that matrix stiffness may be important in directing HPC fate raises interesting question in respect to how local changes in matrix stiffness might affect HPC differentiation. Techniques such as torsional rheometry and transient elastography provide a measure of the mean stiffness across the liver, but provide no indication of how stiffness might vary across the hepatic lobule. Following severe hepatocytic liver injury, the HPC cell response is evident as streaming cords of small cells emanating from their origin adjacent to the ductal tracts outwards into the liver parenchyma. During this migration they are accompanied by activated MFBs and surrounded by a laminin-rich sheath, which is lost as they transition to fully differentiated hepatocytes. The laminin-rich sheath is thought to be important in maintaining HPCs in an undifferentiated phenotype (345). However, localised changes in matrix stiffness during the migration of cells away from the portal tracts might also be important in determining cell phenotype. Preliminary discussions with investigators in the Department of Physics (University of Edinburgh) suggest that micro-indentation techniques could be developed to measure variation in stiffness across the liver at a microscopic level. Micro-indentation has previously been used to make elasticity measurements from soft tissues at sub-centimetre resolution. Levental *et al* undertook elasticity measurements from a

range of soft tissues including isolated mouse glomeruli and resected liver specimens (346). Using their micro-indentation device they demonstrated marked variation in stiffness measurements made at different points from individual livers derived from both CCl4-treated animals and oil-treated control specimens. They speculated that local variation in tissue stiffness would be expected given the structural variation in the regions of the liver at this scale, i.e. periportal, perivenous and parenchymal). Unfortunately it was not possible to identify the region of the liver probed by individual stiffness measurements. Further adaptation of this technique to incorporate microscopy is required to permit high resolution stiffness mapping of the liver parenchyma. Progress in this area would require considerable investment but would have the potential to provide insight into the biomechanical properties of the ECM across the hepatic lobule, both under normal conditions and in models of liver fibrosis.

6.4 Concluding remarks

Overall, I believe that the results presented in this thesis provide compelling evidence for the importance of changes in matrix stiffness in promoting both HCC development and HPC responses within the liver. Perhaps most importantly I believe that this work highlights deficiencies in conventional cell culture conducted on stiff substrates such as tissue culture plastic which fail to take account of the role of matrix stiffness in determining cellular responses.

Appendix 1

Primary antibodies/ antigen retrieval used in immunohistochemistry

Primary Antibody	Antigen (Ag) Retrieval	Source	Dilution	Secondary Antibody	Source	Dilution
Anti-pFAK (pY397)	Microwave Tris EDTA pH9	Invitrogen 44624G	1:200	Swine anti-rabbit IgG	DAKO	1:200
Anti-β1-integrin	Microwave Tris EDTA pH9	AbCam Ab59519	1:50	Rabbit anti-mouse IgG	DAKO	1:200
Anti-CK19	0.01% Trypsin in Calcium Chloride	Novocastra NCL-CK19	1:50	Rabbit anti-mouse IgG	DAKO	1:200
Anti-αSMA (mouse anti-mouse)	Microwave pH9	Sigma 1A4	1:3000	Rabbit anti-mouse IgG	DAKO	1:250
Anti-F4/80 (rat anti-mouse)	Microwave Na Citrate pH6	AbCam Ab6640	1:300	Rabbit anti-rat IgG	DAKO	1:300
Anti-TIMP-1(goat anti-mouse)	Microwave Na Citrate pH6	R&D Systems AF180	1:50	Rabbit anti-goat IgG	DAKO	1:200
Anti-PANCK	Microwave pH6/ Proteinase K	DAKO Z0622	1:200	Swine anti-rabbit IgG	DAKO	1:200
Anti-CD3 (rat anti-human)	Microwave EDTA pH8	Serotec McA1477	1:100	Rabbit anti-rat IgG	DAKO	1:100
Biotinylated anti-B220 (rat anti-mouse)	Microwave Vector Ag retrieval solution	BD Pharmagen 553485	1:50	-	-	-
Anti-Lys6G/ Lys6C [GR1] (Rat anti-mouse)	No Ag Retrieval	Cambridge Biosciences 108413	1:200	Rabbit anti-rat IgG	DAKO	1:300

Appendix 2

Primer sequences used in SYBR-green quantitative PCR

Target		Primer Sequence
Collagen 1A1	Forward	GATGACGTGCAATGCAATGAA
	Reverse	CCCTCGACTCCTACATCTTCTGA
Collagen 3A1	Forward	GTTCTAGAGGATGGCTGTACTAAACACA
	Reverse	TTGCCTTGCGTGTTTGATATTC
Smooth Muscle Actin	Forward	TCAGCGCCTCCAGTTCCT
	Reverse	AAAAAAACCAGGAGTAACAAATCAA
TIMP-1	Forward	ATGGAAAGCCTCTGTGGATATG
	Reverse	AAGCTGCAGGCACTGATGTG
TIMP-2	Forward	AAGGAGATGGCAAGATGCAC
	Reverse	GTCCATCCAGAGGCACTCAT

Custom designed primers for mouse albumin, cytochrome 7A1 (CYP7A1), cytokeratin-19 (CK-19), aquaporin and gamma glutamyl transferase (γGT) were purchased directly from Qiagen (Crawley, UK).

Custom designed primers for human Oct4 and NANOG were purchased directly from Applied Biosystems (Warrington, UK).

Custom designed primers for the eukaryotic housekeeping gene 18S was purchased directly from Applied Biosystems (Warrington, UK).

Appendix 3: Solutions for sample preparation and Western blotting

A3.1 Cell lysis buffer for protein extraction

Reagent	**Quantity**
Sodium chloride	4.38g
HEPES	5.95g
Sodium fluoride	1.05g
EDTA	372mg
Glycerol	50ml
Triton X-100	5ml
	Dissolved in 500ml distilled H_2O adjusted to pH7.6 and stored at 4°C

A3.2 Laemmli sample preparation buffer (5X) for Western blotting

Reagent	**Quantity**
Trizma base	1.5g
Sodium dodecyl sulphate (SDS)	5.0g
Bromophenol blue	250mg
Glycerol	25ml
B-mercaptoethanol	5ml
Distilled water	20ml
	Sample buffer stored at -20°C prior to use

A3.3 Polyacrylamide gel preparation for Western blotting

Reagent	**5% Stacking Gel**	**10% Resolving Gel**	**12% Resolving Gel**
Polyacrylamide Gel Stocks			
Resolving Gel Buffer (90.8g Tris base, 2g SDS in 500ml H_20, pH8.8)	N/A	40ml	40ml
Stacking Gel Buffer (30g Tris base, 2g SDS in 500ml H_20, pH6.8)	50ml	N/A	N/A
Acrylamide (30%)	32ml	53ml	64ml
Glycerol	N/A	36ml	36ml
ddH_20	118ml	31ml	20ml
Polyacrylamide Gels (2 gels)			
Resolving Gel Stock	N/A	11ml	11ml
Stacking Gel Stock	6ml	N/A	N/A
APS	40µl	60µl	60µl
TEMED	20µl	25µl	25µl

A3.4 Running and transfer buffers for Western blotting

Reagent	Running Buffer (1x)	Transfer Buffer (1x)
SDS	1g	N/A
Glycine	14.4g	14.4g
Tris base	3.03g	3.03g
ddH_2O	1000ml	800ml
Methanol	N/A	200ml

Appendix 4

Antibodies used in Western blotting

Antibody	Source	Dilution
$p21^{cip}$	Santa Cruz Biotechnology	1:1000
$p27^{kip}$	Santa Cruz Biotechnology	1:250
HNF4alpha	Santa Cruz Biotechnology	1:200
Alpha-fetoprotein	Santa Cruz Biotechnology	1:2000
Cyclin D1	Cell Signalling	1:1000
Cyclin D3	Cell Signalling	1:1000
$p\text{-}ERK^{Thr202/Tyr204}$	Cell Signalling	1:2000
ERK	Cell Signalling	1:1000
$pAkt^{Ser473}$	Cell Signalling	1:2000
Akt	Cell Signalling	1:4000
$p\text{-}FAK^{Tyr397}$	Cell Signalling	1:1000
FAK	Cell Signalling	1:1000
$p\text{-}STAT3^{Tyr705}$	Cell Signalling	1:1000
STAT3	Cell Signalling	1:1000
E-Cadherin	Cell Signalling	1:1000
Smad2/3	Cell Signalling	1:1000
$p\text{-}Smad2^{Ser465/467}$	Millipore	1:1000
$p\text{-}Smad3^{Ser423/425}$	Millipore	1:2000
Albumin	DAKO	1:2000000
N-Cadherin	DAKO	1:500
α1-Antitrypsin	QED Bioscience	1:2000
Integrin β1	Abcam	1:1000
PARP	Cell Signalling	1:1000
GAPDH	Calbiochem	1:200000
Anti-rabbit IgG-HRP	Cell Signalling	1:2000
Anti-mouse IgG-HRP	Cell Signalling	1:2000

Appendix 5

Stock solutions for production of polyacrylamide (PA) gel supports

	400Pa	1kPa	2.5kPa	6kPa	12kPa	22kPa
2% *bis*-acrylamide (µl)	3.3	8.8	22	36	70	106
30% acrylamide (µl)	125	125	125	125	125	125
250mM HEPES, pH8 (µl)	70	70	70	70	70	70
Distilled H_2O (µl)	300	295	278	270	235	200
TEMED (µl)	1.5	1.5	1.5	1.5	1.5	1.5
10% APS (µl)	5	5	5	5	5	5

*The protocol for polyacrylamide gel support fabrication was kindly provided by Prof Rebecca Wells (University of Pennsylvania)

Appendix 6

Antibodies used in immunofluorescent staining

Primary Antibody	Source	Dilution	Secondary Antibody	Source	Dilution
Anti-vinculin (Mouse anti-human)	Sigma V1931	1:100	Alexafluor 546 Goat-anti-mouse	Invitrogen	1:250
Anti-Ki67 (Rabbit anti-recombinant Ki67)	Novocastra NCL-Ki67	1:200	Alexafluor 568 Goat-anti-rabbit	Invitrogen	1:400
Anti-pFAK Tyr 397 (Rabbit anti-synthetic peptide)	AbCam AB4803	1:100	Alexafluor 568 Goat-anti-rabbit	Invitrogen	1: 200
Alexa 488-phalloidin	Invitrogen A12379	1:40	N/A	N/A	N/A

Appendix 7

A. Huh7 Cells

	1kPa		2.5kPa		12kPa		Glass	
Experiment	Ki67-positive/ Total nuclei	PI	Ki67-positive/ Total nuclei	PI	Ki67-positive/ Total nuclei	PI	Ki67-positive/ Total nuclei	PI
1	49/248	0.2	167/407	0.41	350/599	0.58	400/563	0.71
2	54/255	0.21	184/379	0.49	262/449	0.58	333/405	0.72
3	52/209	0.25	197/370	0.53	304/506	0.60	333/525	0.63
Mean		0.22		0.48		0.59		0.69
SEM		0.015		0.035		0.007		0.028

B. HepG2 Cells

	1kPa		2.5kPa		12kPa		Glass	
Experiment	Ki67-positive/ Total nuclei	PI	Ki67-positive/ Total nuclei	PI	Ki67-positive/ Total nuclei	PI	Ki67-positive/ Total nuclei	PI
1	15/312	0.048	183/320	0.57	313/479	0.653	357/542	0.714
2	13/244	0.053	344/620	0.555	404/622	0.651	386/570	0.677
3	18/302	0.060	259/475	0.545	296/447	0.662	337/493	0.684
Mean		0.054		0.557		0.656		0.692
SEM		0.0033		0.0078		0.0034		0.0114

The data presented here was used to determine the proliferative indices (PIs) presented in Figure 3.6. In each experiment cellular proliferative index (Ki67-positive nuclei/ total DAPI-positive nuclei) was calculated by direct cell counting from 15 randomly selected high power photomicrographs from Ki67- and DAPI-stained slides.

Appendix 8

A. Huh7

	1000 cells/cm^2				5000 cells/cm^2				25000 cells/cm^2			
	1kPa		12kPa		1kPa		12kPa		1kPa		12kPa	
Exp	Ki67+/ Total nuclei	PI	Ki67+ Total nuclei	PI	Ki67+ Total nuclei	PI	Ki67+/ Total nuclei	PI	Ki67+/ Total Nuclei	PI	Ki67+/ Total nuclei	PI
1	17/76	0.224	26/69	0.377	17/127	0.133	94/194	0.485	65/410	0.159	396/747	0.530
2	12/82	0.146	29/90	0.322	14/124	0.113	78/160	0.488	88/404	0.218	309/583	0.530
3	14/91	0.154	42/104	0.404	9/125	0.072	64/181	0.354	117/460	0.254	311/578	0.538
Mean		0.175		0.368		0.106		0.442		0.210		0.533
SEM		0.025		0.024		0.018		0.044		0.028		0.003

B HepG2

	1000 cells/cm^2				5000 cells/cm^2				25000 cells/cm^2			
	1kPa		12kPa		1kPa		12kPa		1kPa		12kPa	
Exp	Ki67+/ Total nuclei	PI	Ki67+ Total nuclei	PI	Ki67+ Total nuclei	PI	Ki67+/ Total nuclei	PI	Ki67+/ Total Nuclei	PI	Ki67+/ Total nuclei	PI
1	28/127	0.220	170/271	0.637	56/182	0.308	308/449	0.686	276/909	0.304	1282/2167	0.591
2	16/106	0.151	190/307	0.619	37/155	0.229	250/375	0.667	350/1016	0.344	368/565	0.651
3	17/151	0.113	153/284	0.539	30/148	0.203	190/287	0.662	156/450	0.347	471/700	0.673
Mean		0.161		0.595		0.250		0.672		0.332		0.639
SEM		0.032		0.028		0.031		0.007		0.014		0.024

The data presented here was used to determine the proliferative indices (PIs) presented in Figure 3.7. In each experiment cellular proliferative index (Ki67-positive nuclei/ total DAPI-positive nuclei) was calculated by direct cell counting from 15 randomly selected high power photomicrographs from Ki67- and DAPI-stained slides.

Appendix 9

A Huh7

	Collagen-I				Collagen-IV				Laminin				Fibronectin			
	1kPa		12kPa		1kPa		12kPa		1kPa		12kPa		1kPa		12kPa	
Experiment	Ki67-positive/ Total nuclei	PI	Ki67-positive/ Total nuclei	PI	Ki67-positive/ Total nuclei	PI	Ki67-positive/ Total nuclei	PI	Ki67-positive/ Total nuclei	PI	Ki67-positive/ Total nuclei	PI	Ki67-positive/ Total nuclei	PI	Ki67-positive/ Total nuclei	PI
1	77/218	0.353	150/211	0.711	34/204	0.167	186/301	0.618	72/208	0.346	180/245	0.735	57/201	0.283	260/318	0.818
2	53/213	0.249	149/239	0.623	60/229	0.262	217/323	0.672	49/206	0.238	202/260	0.777	53/186	0.285	202/267	0.757
3	61/212	0.288	141/219	0.644	63/194	0.325	207/333	0.622	71/195	0.364	219/270	0.811	56/199	0.281	175/246	0.711
Mean		0.297		0.659		0.251		0.637		0.316		0.774		0.283		0.762
SEM		0.031		0.026		0.046		0.017		0.039		0.022		0.001		0.031

B HepG2

	Collagen-I				Collagen-IV				Laminin				Fibronectin			
	1kPa		12kPa		1kPa		12kPa		1kPa		12kPa		1kPa		12kPa	
Experiment	Ki67-positive/ Total nuclei	PI	Ki67-positive/ Total nuclei	PI	Ki67-positive/ Total nuclei	PI	Ki67-positive/ Total nuclei	PI	Ki67-positive/ Total nuclei	PI	Ki67-positive/ Total nuclei	PI	Ki67-positive/ Total nuclei	PI	Ki67-positive/ Total nuclei	PI
1	57/454	0.126	324/496	0.653	39/401	0.095	307/494	0.621	32/315	0.102	458/698	0.616	50/324	0.154	364/724	0.641
2	59/455	0.130	229/359	0.638	41/362	0.113	360/560	0.643	42/379	0.111	293/456	0.642	47/256	0.169	288/446	0.646
3	58/449	0.129	267/423	0.631	41/392	0.105	312/482	0.647	35/295	0.119	438/698	0.628	37/256	0.145	286/430	0.665
Mean		0.128		0.641		0.103		0.637		0.111		0.642		0.156		0.651
SEM		0.001		0.006		0.005		0.4619		0.005		0.008		0.007		0.007

The data presented here was used to determine the proliferative indices (PIs) presented in Figure 3.9. In each experiment cellular proliferative index (Ki67-positive nuclei/ total DAPI-positive nuclei) was calculated by direct cell counting from 15 randomly selected high power photomicrographs from Ki67- and DAPI-stained slides.

Appendix 10

Adenocarcinoma Cell Lines

	LNCap				A549				MCF7				MDA			
	1kPa		12kPa		1kPa		12kPa		1kPa		12kPa					
Experiment	Ki67-positive/ Total nuclei	PI	Ki67-positive/ Total nuclei	PI	Ki67-positive/ Total nuclei	PI	Ki67-positive/ Total nuclei	PI	Ki67-positive/ Total nuclei	PI	Ki67-positive/ Total nuclei	PI	Ki67-positive/ Total nuclei	PI	Ki67-positive/ Total nuclei	PI
1	12/136	0.088	170/252	0.674	14/94	0.149	207/250	0.828	2/91	0.220	102/134	0.761	14/143	0.098	71/116	0.612
2	12/90	0.133	121/177	0.684	26/147	0.177	172/287	0.670	16/137	0.117	134/153	0.876	17/187	0.091	94/144	0.653
3	20/95	0.211	114/162	0.704	19/115	0.165	203/238	0.853	11/107	0.103	101/136	0.742	8/131	0.061	98/143	0.685
Mean		0.144		0.687		0.164		0.783		0.147		0.793		0.083		0.650
SEM		0.357		0.009		0.008		0.058		0.037		0.042		0.011		0.021

	HepG2				Huh7			
	1kPa		12kPa		1kPa		12kPa	
Experiment	Ki67-positive/ Total nuclei	PI	Ki67-positive/ Total nuclei	PI	Ki67-positive/ Total nuclei	PI	Ki67-positive/ Total nuclei	PI
1	57/454	0.126	324/496	0.653	77/218	0.353	150/211	0.711
2	59/455	0.130	229/359	0.638	53/213	0.249	149/239	0.623
3	58/449	0.129	267/423	0.631	61/212	0.288	141/219	0.644
Mean		0.128		0.641		0.297		0.659
SEM		0.001		0.006		0.031		0.026

The data presented here was used to determine the proliferative indices (PIs) presented in Figure 3.10. In each experiment cellular proliferative index (Ki67-positive nuclei/ total DAPI-positive nuclei) was calculated by direct cell counting from 15 randomly selected high power photomicrographs from Ki67- and DAPI-stained slides.

Appendix 11

Re-plating Experiments

	Huh7				HepG2			
	1kPa		12kPa		1kPa		12kPa	
Exp	Ki67+/ Total nuclei	PI	Ki67+ Total nuclei	PI	Ki67+ Total nuclei	PI	Ki67+/ Total nuclei	PI
1	342/548	0.624	344/606	0.568	657/994	0.661	854/1359	0.628
2	549/804	0.683	586/911	0.643	1292/2428	0.637	1165/1825	0.638
3	364/579	0.629	659/946	0.682	786/1272	0.618	476/856	0.556
Mean		0.645		0.631		0.639		0.608
SEM		0.019		0.034		0.012		0.026

The data presented here was used to determine the proliferative indices (PIs) presented in Figure 3.12. In each experiment cellular proliferative index (Ki67-positive nuclei/ total DAPI-positive nuclei) was calculated by direct cell counting from 15 randomly selected high power photomicrographs from Ki67- and DAPI-stained slides. The reference to support stiffness refers to the support stiffness on which the cells were cultured prior to transfer to tissue culture plastic.

Appendix 12

A Huh7 Cells

	Untreated		Isotype		100nM Echistatin		50µg/ml 6S6		DMSO		1µM PF573228		5µM PF573228	
Replicate	Ki67-positive/ Total nuclei	PI	Ki67-positive/ Total nuclei	PI	Ki67-positive/ Total nuclei	PI	Ki67-positive/ Total nuclei	PI	Ki67-positive/ Total nuclei	PI	Ki67-positive/ Total nuclei	PI	Ki67-positive/ Total nuclei	PI
1	53/110	0.481	65/169	0.384	48/110	0.436	19/106	0.179	42/120	0.35	46/116	0.397	18/100	0.180
2	31/81	0.382	76/160	0.475	15/100	0.15	27/86	0.314	34/65	0.523	35/125	0.278	26/111	0.234
3	51/126	0.405	36/86	0.419	34/105	0.323	34/113	0.301	47/116	0.405	53/136	0.390	30/111	0.270
4	38/101	0.376			25/96	0.260			48/146	0.329	53/138	0.384		
5	62/148	0.419							33/92	0.359	23/96	0.240		
Mean		0.413		0.426		0.293		0.265		0.393		0.338		0.228
SEM		0.019		0.026		0.060		0.043		0.035		0.033		0.026

B HepG2 Cells

	Untreated		Isotype		100nM Echistatin		50µg/ml 6S6		DMSO		1µM PF573228		5µM PF573228	
Replicate	Ki67-positive/ Total nuclei	PI	Ki67-positive/ Total nuclei	PI	Ki67-positive/ Total nuclei	PI	Ki67-positive/ Total nuclei	PI	Ki67-positive/ Total nuclei	PI	Ki67-positive/ Total nuclei	PI	Ki67-positive/ Total nuclei	PI
1	79/121	0.653	81/125	0.648	56/103	0.544	8/109	0.073	82/119	0.689	46/99	0.465	39/110	0.355
2	75/122	0.615	100/142	0.744	49/90	0.544	2/42	0.048	113/187	0.711	65/142	0.458	44/131	0.336
3	116/190	0.611	82/132	0.621	8/18	0.444	6/53	0.113	104/141	0.738	49/107	0.458	56/149	0.376
4	105/175	0.600			37/75	0.493			97/156	0.622	115/260	0.442	39/101	0.386
5	101/157	0.643			41/91	0.451			141/221	0.638	106/211	0.502	48/116	0.414
Mean		0.624		0.658		0.495		0.078		0.680		0.465		0.373
SEM		0.010		0.024		0.021		0.019		0.021		0.010		0.013

The data presented here was used to determine the proliferative indices (PIs) presented in Figure 3.18. In each experiment cellular proliferative index (Ki67-positive nuclei/ total DAPI-positive nuclei) was calculated by direct cell counting from 5 randomly selected high power photomicrographs from Ki67- and DAPI-stained slides.

Appendix 13

A Huh7 Cells

	1kPa Untreated		12kPa Untreated		Scrambled siRNA		B1-Integrin siRNA		FAK siRNA	
Replicate	Ki67-positive/ Total nuclei	PI	Ki67-positive/ Total nuclei	PI	Ki67-positive/ Total nuclei	PI	Ki67-positive/ Total nuclei	PI	Ki67-positive/ Total nuclei	PI
1	6/91	0.066	40/80	0.500	70/119	0.588	36/116	0.310	70/134	0.522
2	5/60	0.083	46/86	0.535	83/133	0.624	49/109	0.450	56/115	0.487
3	3/80	0.038	54/92	0.587	73/147	0.497	59/108	0.546	52/130	0.400
4	7/64	0.109	53/93	0.570	58/109	0.532	37/77	0.481	48/95	0.505
5	11/66	0.167	54/111	0.486	61/125	0.488	22/45	0.489	64/149	0.429
Mean		0.093		0.536		0.546		0.455		0.469
SEM		0.022		0.019		0.026		0.039		0.023

B HepG2 Cells

	1kPa Untreated		12kPa Untreated		Scrambled siRNA		B1-Integrin siRNA		FAK siRNA	
Replicate	Ki67-positive/ Total nuclei	PI	Ki67-positive/ Total nuclei	PI	Ki67-positive/ Total nuclei	PI	Ki67-positive/ Total nuclei	PI	Ki67-positive/ Total nuclei	PI
1	9/92	0.098	132/205	0.644	178/243	0.733	64/116	0.552	72/129	0.558
2	16/126	0.127	150/197	0.761	122/163	0.748	45/96	0.469	52/104	0.500
3	10/84	0.119	119/167	0.713	164/215	0.744	25/72	0.347	93/162	0.574
4	18/139	0.129	152/229	0.664	156/219	0.712	50/79	0.633	80/147	0.544
5	15/103	0.146	147/199	0.739	108/147	0.735	20/49	0.408	98/149	0.658
Mean		0.124		0.704		0.734		0.482		0.566
SEM		0.008		0.022		0.006		0.051		0.025

The data presented here was used to determine the proliferative indices (PIs) presented in Figure 3.19. In each experiment cellular proliferative index (Ki67-positive nuclei/ total DAPI-positive nuclei) was calculated by direct cell counting from 5 randomly selected high power photomicrographs from Ki67- and DAPI-stained slides.

Appendix 14

A BMol Cells

	Laminin								Collagen-IV							
	1kPa		2.5kPa		12kPa		Glass		1kPa		2.5kPa		12kPa		Glass	
Experiment	Ki67-positive/ Total nuclei	PI	Ki67-positive/ Total nuclei	PI	Ki67-positive/ Total nuclei	PI	Ki67-positive/ Total nuclei	PI	Ki67-positive/ Total nuclei	PI	Ki67-positive/ Total nuclei	PI	Ki67-positive/ Total nuclei	PI	Ki67-positive/ Total nuclei	PI
1	2/107	0.019	47/169	0.278	76/182	0.418	125/229	0.546	9/226	0.040	93/226	0.411	95/225	0.422	118/211	0.559
2	3/129	0.023	56/180	0.311	81/180	0.450	120/243	0.494	24/240	0.100	41/186	0.220	77/169	0.456	108/187	0.578
3	8/154	0.052	39/164	0.238	79/194	0.407	107/217	0.493	9/210	0.043	110/244	0.451	51/172	0.297	111/183	0.607
Mean		0.025		0.178		0.298		0.467		0.040		0.245		0.315		0.560
SEM		0.005		0.045		0.057		0.027		0.013		0.063		0.045		0.019

B Primary HPCs

	Laminin				Collagen-IV			
	1kPa		12kPa		1kPa		12kPa	
Experiment	Ki67-positive/ Total nuclei	PI	Ki67-positive/ Total nuclei	PI	Ki67-positive/ Total nuclei	PI	Ki67-positive/ Total nuclei	PI
1	10/337	0.030	41/550	0.075	8/321	0.025	40/418	0.096
2	17/310	0.055	26/394	0.066	8/250	0.032	17/263	0.065
3	15/311	0.048	34/406	0.084	15/282	0.053	29/287	0.101
Mean		0.044		0.075		0.037		0.087
SEM		0.008		0.005		0.008		0.011

The data presented here was used to determine the proliferative indices (PIs) presented in Figure 4.7. In each experiment cellular proliferative index (Ki67-positive nuclei/ total DAPI-positive nuclei) was calculated by direct cell counting from 15 randomly selected high power photomicrographs from Ki67- and DAPI-stained slides.

Appendix 15

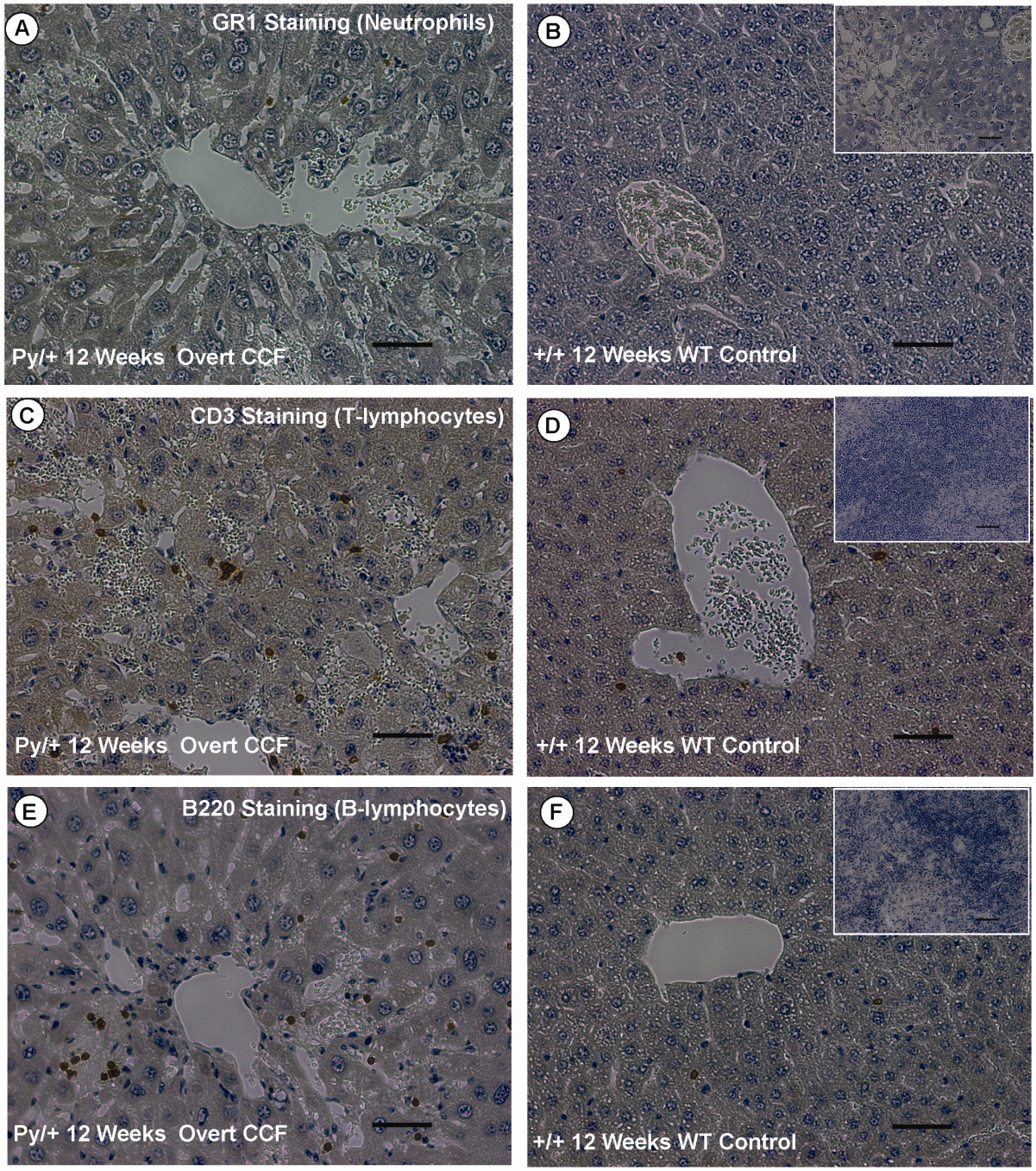

Appendix 15: High power (x200) photomicrographs of immunostained liver sections from 12-week-old Py/+ mice demonstrating features of overt CCF and age-matched wild-type controls (as indicated). Sections are stained for the presence of the neutrophil marker Ly-6C/ GR1 (A/B), T-lymphocyte marker CD3 and B-lymphocyte marker B220. Control staining with omission of the primary antibody showed no significant staining (indented images).

Reference List

1. Iredale JP. Models of liver fibrosis: exploring the dynamic nature of inflammation and repair in a solid organ. J Clin Invest 2007;117(3):539-548.

2. Fattovich G, Stroffolini T, Zagni I, Donato F. Hepatocellular carcinoma in cirrhosis: incidence and risk factors. Gastroenterology 2004;127(5 Suppl 1):S35-S50.

3. Leon DA, McCambridge J. Liver cirrhosis mortality rates in Britain from 1950 to 2002: an analysis of routine data. Lancet 2006;367(9504):52-56.

4. Deuffic S, Poynard T, Buffat L, Valleron AJ. Trends in primary liver cancer. Lancet 1998;351(9097):214-215.

5. Taylor-Robinson SD, Foster GR, Arora S, Hargreaves S, Thomas HC. Increase in primary liver cancer in the UK, 1979-94. Lancet 1997;350(9085):1142-1143.

6. El-Serag HB, Mason AC. Rising incidence of hepatocellular carcinoma in the United States. N Engl J Med 1999;340(10):745-750.

7. La VC, Lucchini F, Franceschi S, Negri E, Levi F. Trends in mortality from primary liver cancer in Europe. Eur J Cancer 2000;36(7):909-915.

8. Fattovich G, Pantalena M, Zagni I, Realdi G, Schalm SW, Christensen E. Effect of hepatitis B and C virus infections on the natural history of compensated cirrhosis: a cohort study of 297 patients. Am J Gastroenterol 2002;97(11):2886-2895.

9. Bruix J, Sherman M, Llovet JM, Beaugrand M, Lencioni R, Burroughs AK, et al. Clinical management of hepatocellular carcinoma. Conclusions of the Barcelona-2000 EASL conference. European Association for the Study of the Liver. J Hepatol 2001;35(3):421-430.

10. Nowak AK, Chow PK, Findlay M. Systemic therapy for advanced hepatocellular carcinoma: a review. Eur J Cancer 2004;40(10):1474-1484.

11. Johnson PJ. Hepatocellular carcinoma: is current therapy really altering outcome? Gut 2002;51(4):459-462.

12. Hanazaki K, Kajikawa S, Shimozawa N, Mihara M, Shimada K, Hiraguri M, et al. Survival and recurrence after hepatic resection of 386 consecutive patients with hepatocellular carcinoma. J Am Coll Surg 2000;191(4):381-388.

13. Mathurin P, Raynard B, Dharancy S, Kirzin S, Fallik D, Pruvot FR, et al. Meta-analysis: evaluation of adjuvant therapy after curative liver resection for hepatocellular carcinoma. Aliment Pharmacol Ther 2003;17(10):1247-1261.

14. Schreibman IR, Bejarano P, Martinez EJ, Regev A. Very late recurrence of hepatocellular carcinoma after liver transplantation: case report and literature review. Transplant Proc 2006;38(9):3140-3143.

15. Burkitt HG, Young B, Heath JW. In: Burkitt HG, Young B, Heath JW, eds. Wheater's Functional Histology: A Text and Colour Atlas. Third ed. Edinburgh: Chrurchill Livingstone, 1996. 271-281.

16. Reid LM, Fiorino AS, Sigal SH, Brill S, Holst PA. Extracellular matrix gradients in the space of Disse: relevance to liver biology. Hepatology 1992;15(6):1198-1203.

17. Martinez-Hernandez A, Amenta PS. The hepatic extracellular matrix. I. Components and distribution in normal liver. Virchows Arch A Pathol Anat Histopathol 1993;423(1):1-11.

18. Iredale J. Defining therapeutic targets for liver fibrosis: exploiting the biology of inflammation and repair. Pharmacol Res 2008;58(2):129-136.

19. Henderson NC, Iredale JP. Liver fibrosis: cellular mechanisms of progression and resolution. Clin Sci (Lond) 2007;112(5):265-280.

20. Benyon RC, Iredale JP. Is liver fibrosis reversible? Gut 2000;46(4):443-446.

21. Burt AD, Griffiths MR, Schuppan D, Voss B, MacSween RN. Ultrastructural localization of extracellular matrix proteins in liver biopsies using ultracryomicrotomy and immuno-gold labelling. Histopathology 1990;16(1):53-58.

22. Schuppan D. Structure of the extracellular matrix in normal and fibrotic liver: collagens and glycoproteins. Semin Liver Dis 1990;10(1):1-10.

23. Bataller R, Brenner DA. Liver fibrosis. J Clin Invest 2005;115(2):209-218.

24. Gressner AM, Haarmann R. Hyaluronic acid synthesis and secretion by rat liver fat storing cells (perisinusoidal lipocytes) in culture. Biochem Biophys Res Commun 1988;151(1):222-229.

25. Iredale JP, Benyon RC, Pickering J, McCullen M, Northrop M, Pawley S, et al. Mechanisms of spontaneous resolution of rat liver fibrosis. Hepatic stellate cell apoptosis and reduced hepatic expression of metalloproteinase inhibitors. J Clin Invest 1998;102(3):538-549.

26. Desmet VJ, Roskams T. Cirrhosis reversal: a duel between dogma and myth. J Hepatol 2004;40(5):860-867.

27. Pinzani M, Rombouts K. Liver fibrosis: from the bench to clinical targets. Dig Liver Dis 2004;36(4):231-242.

28. Lorenzini S, Bird TG, Boulter L, Bellamy C, Samuel K, Aucott R, et al. Characterisation of a stereotypical cellular and extracellular adult liver progenitor cell niche in rodents and diseased human liver. Gut 2010;59(5):645-654.

29. Roskams TA, Theise ND, Balabaud C, Bhagat G, Bhathal PS, Bioulac-Sage P, et al. Nomenclature of the finer branches of the biliary tree: canals, ductules, and ductular reactions in human livers. Hepatology 2004;39(6):1739-1745.

30. Theise ND, Saxena R, Portmann BC, Thung SN, Yee H, Chiriboga L, et al. The canals of Hering and hepatic stem cells in humans. Hepatology 1999;30(6):1425-1433.

31. Cassiman D, Libbrecht L, Desmet V, Denef C, Roskams T. Hepatic stellate cell/myofibroblast subpopulations in fibrotic human and rat livers. J Hepatol 2002;36(2):200-209.

32. Russo FP, Alison MR, Bigger BW, Amofah E, Florou A, Amin F, et al. The bone marrow functionally contributes to liver fibrosis. Gastroenterology 2006;130(6):1807-1821.

33. Forbes SJ, Russo FP, Rey V, Burra P, Rugge M, Wright NA, et al. A significant proportion of myofibroblasts are of bone marrow origin in human liver fibrosis. Gastroenterology 2004;126(4):955-963.

34. Kisseleva T, Uchinami H, Feirt N, Quintana-Bustamante O, Segovia JC, Schwabe RF, et al. Bone marrow-derived fibrocytes participate in pathogenesis of liver fibrosis. J Hepatol 2006;45(3):429-438.

35. Olaso E, Ikeda K, Eng FJ, Xu L, Wang LH, Lin HC, et al. DDR2 receptor promotes MMP-2-mediated proliferation and invasion by hepatic stellate cells. J Clin Invest 2001;108(9):1369-1378.

36. Zhou X, Murphy FR, Gehdu N, Zhang J, Iredale JP, Benyon RC. Engagement of alphavbeta3 integrin regulates proliferation and apoptosis of hepatic stellate cells. J Biol Chem 2004;279(23):23996-24006.

37. Dodig M, Ogunwale B, Dasarathy S, Li M, Wang B, McCullough AJ. Differences in regulation of type I collagen synthesis in primary and passaged hepatic stellate cell cultures: the role of alpha5beta1-integrin. Am J Physiol Gastrointest Liver Physiol 2007;293(1):G154-G164.

38. Iredale JP, Benyon RC, Pickering J, McCullen M, Northrop M, Pawley S, et al. Mechanisms of spontaneous resolution of rat liver fibrosis. Hepatic stellate cell apoptosis and reduced hepatic expression of metalloproteinase inhibitors. J Clin Invest 1998;102(3):538-549.

39. Elsharkawy AM, Oakley F, Mann DA. The role and regulation of hepatic stellate cell apoptosis in reversal of liver fibrosis. Apoptosis 2005;10(5):927-939.

40. Hammel P, Couvelard A, O'Toole D, Ratouis A, Sauvanet A, Flejou JF, et al. Regression of liver fibrosis after biliary drainage in patients with chronic pancreatitis and stenosis of the common bile duct. N Engl J Med 2001;344(6):418-423.

41. Dufour JF, DeLellis R, Kaplan MM. Reversibility of hepatic fibrosis in autoimmune hepatitis. Ann Intern Med 1997;127(11):981-985.

42. Issa R, Zhou X, Constandinou CM, Fallowfield J, Millward-Sadler H, Gaca MD, et al. Spontaneous recovery from micronodular cirrhosis: evidence for incomplete resolution associated with matrix cross-linking. Gastroenterology 2004;126(7):1795-1808.

43. Pellicoro A, Aucott RL, Ramachandran P, Robson AJ, Fallowfield JA, Snowdon VK, et al. Elastin accumulation is regulated at the level of degradation by macrophage metalloelastase (MMP-12) during experimental liver fibrosis. Hepatology 2012;55(6):1965-1975.

44. Elbjeirami WM, Yonter EO, Starcher BC, West JL. Enhancing mechanical properties of tissue-engineered constructs via lysyl oxidase crosslinking activity. J Biomed Mater Res A 2003;66(3):513-521.

45. Bruel A, Ortoft G, Oxlund H. Inhibition of cross-links in collagen is associated with reduced stiffness of the aorta in young rats. Atherosclerosis 1998;140(1):135-145.

46. Levental KR, Yu H, Kass L, Lakins JN, Egeblad M, Erler JT, et al. Matrix crosslinking forces tumor progression by enhancing integrin signaling. Cell 2009;139(5):891-906.

47. Norton GR, Tsotetsi J, Trifunovic B, Hartford C, Candy GP, Woodiwiss AJ. Myocardial stiffness is attributed to alterations in cross-linked collagen rather than total collagen or phenotypes in spontaneously hypertensive rats. Circulation 1997;96(6):1991-1998.

48. Garcia-Tsao G, Friedman S, Iredale J, Pinzani M. Now there are many (stages) where before there was one: In search of a pathophysiological classification of cirrhosis. Hepatology 2010;51(4):1445-1449.

49. Alison MR, Lovell MJ. Liver cancer: the role of stem cells. Cell Prolif 2005;38(6):407-421.

50. Sell S, Dunsford HA. Evidence for the stem cell origin of hepatocellular carcinoma and cholangiocarcinoma. Am J Pathol 1989;134(6):1347-1363.

51. Yamamoto T, Kajino K, Kudo M, Sasaki Y, Arakawa Y, Hino O. Determination of the clonal origin of multiple human hepatocellular carcinomas by cloning and polymerase chain reaction of the integrated hepatitis B virus DNA. Hepatology 1999;29(5):1446-1452.

52. Esumi M, Aritaka T, Arii M, Suzuki K, Tanikawa K, Mizuo H, et al. Clonal origin of human hepatoma determined by integration of hepatitis B virus DNA. Cancer Res 1986;46(11):5767-5771.

53. Sell S. Cellular origin of hepatocellular carcinomas. Semin Cell Dev Biol 2002;13(6):419-424.

54. Hixson DC, Brown J, McBride AC, Affigne S. Differentiation status of rat ductal cells and ethionine-induced hepatic carcinomas defined with surface-reactive monoclonal antibodies. Exp Mol Pathol 2000;68(3):152-169.

55. Dumble ML, Croager EJ, Yeoh GC, Quail EA. Generation and characterization of p53 null transformed hepatic progenitor cells: oval cells give rise to hepatocellular carcinoma. Carcinogenesis 2002;23(3):435-445.

56. Woo HG, Park ES, Thorgeirsson SS, Kim YJ. Exploring genomic profiles of hepatocellular carcinoma. Mol Carcinog 2011;50(4):235-243.

57. Yamashita T, Ji J, Budhu A, Forgues M, Yang W, Wang HY, et al. EpCAM-positive hepatocellular carcinoma cells are tumor-initiating cells with stem/progenitor cell features. Gastroenterology 2009;136(3):1012-1024.

58. Andersen JB, Loi R, Perra A, Factor VM, Ledda-Columbano GM, Columbano A, et al. Progenitor-derived hepatocellular carcinoma model in the rat. Hepatology 2010;51(4):1401-1409.

59. Trevisani F, D'Intino PE, Caraceni P, Pizzo M, Stefanini GF, Mazziotti A, et al. Etiologic factors and clinical presentation of hepatocellular carcinoma. Differences between cirrhotic and noncirrhotic Italian patients. Cancer 1995;75(9):2220-2232.

60. Stroffolini T, Andreone P, Andriulli A, Ascione A, Craxi A, Chiaramonte M, et al. Characteristics of hepatocellular carcinoma in Italy. J Hepatol 1998;29(6):944-952.

61. Van RG, Fevery J, Van SW. Hepatocellular carcinoma in Belgium: clinical and virological characteristics of 154 consecutive cirrhotic and non-cirrhotic patients. Eur J Gastroenterol Hepatol 2000;12(1):61-66.

62. Bralet MP, Regimbeau JM, Pineau P, Dubois S, Loas G, Degos F, et al. Hepatocellular carcinoma occurring in nonfibrotic liver: epidemiologic and histopathologic analysis of 80 French cases. Hepatology 2000;32(2):200-204.

63. Chiesa R, Donato F, Tagger A, Favret M, Ribero ML, Nardi G, et al. Etiology of hepatocellular carcinoma in Italian patients with and without cirrhosis. Cancer Epidemiol Biomarkers Prev 2000;9(2):213-216.

64. Le BB, Faouzi S, Boussarie L, Balabaud C, Bioulac-Sage P, Rosenbaum J. Extracellular matrix composition and integrin expression in early hepatocarcinogenesis in human cirrhotic liver. J Pathol 1997;181(3):330-337.

65. Ishizaki M, Ashida K, Higashi T, Nakatsukasa H, Kaneyoshi T, Fujiwara K, et al. The formation of capsule and septum in human hepatocellular carcinoma. Virchows Arch 2001;438(6):574-580.

66. Torimura T, Ueno T, Inuzuka S, Tanaka M, Abe H, Tanikawa K. Mechanism of fibrous capsule formation surrounding hepatocellular carcinoma. Immunohistochemical study. Arch Pathol Lab Med 1991;115(4):365-371.

67. Zhao M, Laissue JA, Zimmermann A. Tenascin and type IV collagen expression in liver cell dysplasia and in hepatocellular carcinoma. Histol Histopathol 1996;11(2):323-333.

68. Wu XZ, Chen D, Xie GR. Extracellular matrix remodeling in hepatocellular carcinoma: effects of soil on seed? Med Hypotheses 2006;66(6):1115-1120.

69. Yamamoto T, Kaneda K, Hirohashi K, Kinoshita H, Sakurai M. Sinusoidal capillarization and arterial blood supply continuously proceed with the advance of the stages of hepatocarcinogenesis in the rat. Jpn J Cancer Res 1996;87(5):442-450.

70. Yoshida K, Tadaoka Y, Manabe T. Expression of laminin in hepatocellular carcinoma: an adjunct for its histological diagnosis. Jpn J Clin Oncol 1996;26(2):70-76.

71. Antonaci S, Giannelli G. Rationale for new drugs targeting the tissue microenvironment in patients with HCC. Curr Pharm Des 2007;13(32):3288-3291.

72. Giannelli G, Fransvea E, Bergamini C, Marinosci F, Antonaci S. Laminin-5 chains are expressed differentially in metastatic and nonmetastatic hepatocellular carcinoma. Clin Cancer Res 2003;9(10 Pt 1):3684-3691.

73. Koukoulis GK, Shen J, Virtanen I, Gould VE. Immunolocalization of cellular fibronectins in the normal liver, cirrhosis, and hepatocellular carcinoma. Ultrastruct Pathol 1995;19(1):37-43.

74. Yamada S, Ichida T, Matsuda Y, Miyazaki Y, Hatano T, Hata K, et al. Tenascin expression in human chronic liver disease and in hepatocellular carcinoma. Liver 1992;12(1):10-16.

75. Albelda SM, Buck CA. Integrins and other cell adhesion molecules. FASEB J 1990;4(11):2868-2880.

76. Torimura T, Ueno T, Kin M, Harad R, Nakamura T, Sakamoto M, et al. Laminin deposition to type IV collagen enhances haptotaxis, chemokinesis, and adhesion of hepatoma cells through beta1-integrins. J Hepatol 2001;35(2):245-253.

77. Carloni V, Mazzocca A, Pantaleo P, Cordella C, Laffi G, Gentilini P. The integrin, alpha6beta1, is necessary for the matrix-dependent activation of FAK and MAP kinase and the migration of human hepatocarcinoma cells. Hepatology 2001;34(1):42-49.

78. Nejjari M, Hafdi Z, Gouysse G, Fiorentino M, Beatrix O, Dumortier J, et al. Expression, regulation, and function of alpha V integrins in hepatocellular carcinoma: an in vivo and in vitro study. Hepatology 2002;36(2):418-426.

79. Bergamini C, Sgarra C, Trerotoli P, Lupo L, Azzariti A, Antonaci S, et al. Laminin-5 stimulates hepatocellular carcinoma growth through a different function of alpha6beta4 and alpha3beta1 integrins. Hepatology 2007;46(6):1801-1809.

80. Nejjari M, Hafdi Z, Dumortier J, Bringuier AF, Feldmann G, Scoazec JY. alpha6beta1 integrin expression in hepatocarcinoma cells: regulation and role in cell adhesion and migration. Int J Cancer 1999;83(4):518-525.

81. Zhang H, Ozaki I, Mizuta T, Matsuhashi S, Yoshimura T, Hisatomi A, et al. Beta 1-integrin protects hepatoma cells from chemotherapy induced apoptosis via a mitogen-activated protein kinase dependent pathway. Cancer 2002;95(4):896-906.

82. Janmey PA, Miller RT. Mechanisms of mechanical signaling in development and disease. J Cell Sci 2011;124(Pt 1):9-18.

83. Nemir S, West JL. Synthetic materials in the study of cell response to substrate rigidity. Ann Biomed Eng 2010;38(1):2-20.

84. Folkman J, Moscona A. Role of cell shape in growth control. Nature 1978;273(5661):345-349.

85. Harris AK, Wild P, Stopak D. Silicone rubber substrata: a new wrinkle in the study of cell locomotion. Science 1980;208(4440):177-179.

86. Solon J, Levental I, Sengupta K, Georges PC, Janmey PA. Fibroblast adaptation and stiffness matching to soft elastic substrates. Biophys J 2007;93(12):4453-4461.

87. Vogel V, Sheetz M. Local force and geometry sensing regulate cell functions. Nat Rev Mol Cell Biol 2006;7(4):265-275.

88. Galbraith CG, Yamada KM, Sheetz MP. The relationship between force and focal complex development. J Cell Biol 2002;159(4):695-705.

89. Lee SE, Kamm RD, Mofrad MR. Force-induced activation of talin and its possible role in focal adhesion mechanotransduction. J Biomech 2007;40(9):2096-2106.

90. Glogauer M, Arora P, Yao G, Sokholov I, Ferrier J, McCulloch CA. Calcium ions and tyrosine phosphorylation interact coordinately with actin to regulate cytoprotective responses to stretching. J Cell Sci 1997;110 (Pt 1):11-21.

91. Ridley AJ, Hall A. The small GTP-binding protein rho regulates the assembly of focal adhesions and actin stress fibers in response to growth factors. Cell 1992;70(3):389-399.

92. Ishida T, Ishida M, Suero J, Takahashi M, Berk BC. Agonist-stimulated cytoskeletal reorganization and signal transduction at focal adhesions in vascular smooth muscle cells require c-Src. J Clin Invest 1999;103(6):789-797.

93. Zhao XH, Laschinger C, Arora P, Szaszi K, Kapus A, McCulloch CA. Force activates smooth muscle alpha-actin promoter activity through the Rho signaling pathway. J Cell Sci 2007;120(Pt 10):1801-1809.

94. Torsoni AS, Marin TM, Velloso LA, Franchini KG. RhoA/ROCK signaling is critical to FAK activation by cyclic stretch in cardiac myocytes. Am J Physiol Heart Circ Physiol 2005;289(4):H1488-H1496.

95. Pelham RJ, Jr., Wang Y. Cell locomotion and focal adhesions are regulated by substrate flexibility. Proc Natl Acad Sci U S A 1997;94(25):13661-13665.

96. Lo CM, Wang HB, Dembo M, Wang YL. Cell movement is guided by the rigidity of the substrate. Biophys J 2000;79(1):144-152.

97. Klein EA, Yin L, Kothapalli D, Castagnino P, Byfield FJ, Xu T, et al. Cell-cycle control by physiological matrix elasticity and in vivo tissue stiffening. Curr Biol 2009;19(18):1511-1518.

98. Engler AJ, Sen S, Sweeney HL, Discher DE. Matrix elasticity directs stem cell lineage specification. Cell 2006;126(4):677-689.

99. Levental I, Georges PC, Janmey PA. Soft biological materials and their influence on cell function. Soft Matter 2007;3:299-306.

100. Georges PC, Miller WJ, Meaney DF, Sawyer ES, Janmey PA. Matrices with compliance comparable to that of brain tissue select neuronal over glial growth in mixed cortical cultures. Biophys J 2006;90(8):3012-3018.

101. Rousselet MC, Michalak S, Dupre F, Croue A, Bedossa P, Saint-Andre JP, et al. Sources of variability in histological scoring of chronic viral hepatitis. Hepatology 2005;41(2):257-264.

102. Castera L, Forns X, Alberti A. Non-invasive evaluation of liver fibrosis using transient elastography. J Hepatol 2008;48(5):835-847.

103. Castera L, Vergniol J, Foucher J, Le BB, Chanteloup E, Haaser M, et al. Prospective comparison of transient elastography, Fibrotest, APRI, and liver biopsy for the assessment of fibrosis in chronic hepatitis C. Gastroenterology 2005;128(2):343-350.

104. Ziol M, Handra-Luca A, Kettaneh A, Christidis C, Mal F, Kazemi F, et al. Noninvasive assessment of liver fibrosis by measurement of stiffness in patients with chronic hepatitis C. Hepatology 2005;41(1):48-54.

105. Marcellin P, Ziol M, Bedossa P, Douvin C, Poupon R, De L, V, et al. Non-invasive assessment of liver fibrosis by stiffness measurement in patients with chronic hepatitis B. Liver Int 2009;29(2):242-247.

106. Nahon P, Kettaneh A, Tengher-Barna I, Ziol M, De L, V, Douvin C, et al. Assessment of liver fibrosis using transient elastography in patients with alcoholic liver disease. J Hepatol 2008;49(6):1062-1068.

107. Corpechot C, El NA, Poujol-Robert A, Ziol M, Wendum D, Chazouilleres O, et al. Assessment of biliary fibrosis by transient elastography in patients with PBC and PSC. Hepatology 2006;43(5):1118-1124.

108. Yoneda M, Yoneda M, Fujita K, Inamori M, Tamano M, Hiriishi H, et al. Transient elastography in patients with non-alcoholic fatty liver disease (NAFLD). Gut 2007;56(9):1330-1331.

109. Vizzutti F, Arena U, Romanelli RG, Rega L, Foschi M, Colagrande S, et al. Liver stiffness measurement predicts severe portal hypertension in patients with HCV-related cirrhosis. Hepatology 2007;45(5):1290-1297.

110. Kazemi F, Kettaneh A, N'kontchou G, Pinto E, Ganne-Carrie N, Trinchet JC, et al. Liver stiffness measurement selects patients with cirrhosis at risk of bearing large oesophageal varices. J Hepatol 2006;45(2):230-235.

111. Roulot D, Czernichow S, Le CH, Costes JL, Vergnaud AC, Beaugrand M. Liver stiffness values in apparently healthy subjects: influence of gender and metabolic syndrome. J Hepatol 2008;48(4):606-613.

112. Castera L, Forns X, Alberti A. Non-invasive evaluation of liver fibrosis using transient elastography. J Hepatol 2008;48(5):835-847.

113. Arena U, Vizzutti F, Corti G, Ambu S, Stasi C, Bresci S, et al. Acute viral hepatitis increases liver stiffness values measured by transient elastography. Hepatology 2008;47(2):380-384.

114. Bioulac-Sage P, Couffinhal T, Foucher J, Balabaud CP. Interpreting liver stiffness in the cirrhotic range. J Hepatol 2009;50(2):423-424.

115. Frulio N, Laumonier H, Balabaud C, Trillaud H, Bioulac-Sage P. Hepatic congestion plays a role in liver stiffness. Hepatology 2009;50(5):1674-1675.

116. Castera L, Forns X, Alberti A. Non-invasive evaluation of liver fibrosis using transient elastography. J Hepatol 2008;48(5):835-847.

117. Masuzaki R, Tateishi R, Yoshida H, Yoshida H, Sato S, Kato N, et al. Risk assessment of hepatocellular carcinoma in chronic hepatitis C patients by transient elastography. J Clin Gastroenterol 2008;42(7):839-843.

118. Masuzaki R, Tateishi R, Yoshida H, Goto E, Sato T, Ohki T, et al. Prospective risk assessment for hepatocellular carcinoma development in patients with chronic hepatitis C by transient elastography. Hepatology 2009;49(6):1954-1961.

119. Masuzaki R, Tateishi R, Yoshida H, Sato T, Ohki T, Goto T, et al. Assessing liver tumor stiffness by transient elastography. Hepatol Int 2007;1(3):394-397.

120. Zhao G, Cui J, Qin Q, Zhang J, Liu L, Deng S, et al. Mechanical stiffness of liver tissues in relation to integrin beta1 expression may influence the development of hepatic cirrhosis and hepatocellular carcinoma. J Surg Oncol 2010;102(5):482-489.

121. Kuriyama S, Yamazaki M, Mitoro A, Tsujimoto T, Kikukawa M, Tsujinoue H, et al. Hepatocellular carcinoma in an orthotopic mouse model metastasizes intrahepatically in cirrhotic but not in normal liver. Int J Cancer 1999;80(3):471-476.

122. Kornek M, Raskopf E, Tolba R, Becker U, Klockner M, Sauerbruch T, et al. Accelerated orthotopic hepatocellular carcinomas growth is linked to increased expression of pro-angiogenic and prometastatic factors in murine liver fibrosis. Liver Int 2008;28(4):509-518.

123. Osada S, Kanematsu M, Imai H, Goshima S, Sugiyama Y. Hepatic fibrosis influences the growth of hepatocellular carcinoma. Hepatogastroenterology 2008;55(81):184-187.

124. Klein EA, Campbell LE, Kothapalli D, Fournier AK, Assoian RK. Joint requirement for Rac and ERK activities underlies the mid-G1 phase induction of cyclin D1 and S phase entry in both epithelial and mesenchymal cells. J Biol Chem 2008;283(45):30911-30918.

125. Lin YC, Grinnell F. Decreased level of PDGF-stimulated receptor autophosphorylation by fibroblasts in mechanically relaxed collagen matrices. J Cell Biol 1993;122(3):663-672.

126. Nelson CM, Jean RP, Tan JL, Liu WF, Sniadecki NJ, Spector AA, et al. Emergent patterns of growth controlled by multicellular form and mechanics. Proc Natl Acad Sci U S A 2005;102(33):11594-11599.

127. Assoian RK, Klein EA. Growth control by intracellular tension and extracellular stiffness. Trends Cell Biol 2008;18(7):347-352.

128. Assoian RK, Schwartz MA. Coordinate signaling by integrins and receptor tyrosine kinases in the regulation of G1 phase cell-cycle progression. Curr Opin Genet Dev 2001;11(1):48-53.

129. Fringer J, Grinnell F. Fibroblast quiescence in floating or released collagen matrices: contribution of the ERK signaling pathway and actin cytoskeletal organization. J Biol Chem 2001;276(33):31047-31052.

130. Rosenfeldt H, Grinnell F. Fibroblast quiescence and the disruption of ERK signaling in mechanically unloaded collagen matrices. J Biol Chem 2000;275(5):3088-3092.

131. Kumar S, Weaver VM. Mechanics, malignancy, and metastasis: the force journey of a tumor cell. Cancer Metastasis Rev 2009;28(1-2):113-127.

132. Gilbert PM, Havenstrite KL, Magnusson KE, Sacco A, Leonardi NA, Kraft P, et al. Substrate elasticity regulates skeletal muscle stem cell self-renewal in culture. Science 2010;329(5995):1078-1081.

133. Li Z, Dranoff JA, Chan EP, Uemura M, Sevigny J, Wells RG. Transforming growth factor-beta and substrate stiffness regulate portal fibroblast activation in culture. Hepatology 2007;46(4):1246-1256.

134. Olsen AL, Bloomer SA, Chan EP, Gaca MD, Georges PC, Sackey B, et al. Hepatic stellate cells require a stiff environment for myofibroblastic differentiation. Am J Physiol Gastrointest Liver Physiol 2011;301(1):G110-G118.

135. Georges PC, Hui JJ, Gombos Z, McCormick ME, Wang AY, Uemura M, et al. Increased stiffness of the rat liver precedes matrix deposition: implications for fibrosis. Am J Physiol Gastrointest Liver Physiol 2007;293(6):G1147-G1154.

136. Millonig G, Friedrich S, Adolf S, Fonouni H, Golriz M, Mehrabi A, et al. Liver stiffness is directly influenced by central venous pressure. J Hepatol 2010;52(2):206-210.

137. Wells RG. The role of matrix stiffness in regulating cell behavior. Hepatology 2008;47(4):1394-1400.

138. Castell JV, Gomez-Lechon MJ. Liver cell culture techniques. Methods Mol Biol 2009;481:35-46.

139. Fassett J, Tobolt D, Hansen LK. Type I collagen structure regulates cell morphology and EGF signaling in primary rat hepatocytes through cAMP-dependent protein kinase A. Mol Biol Cell 2006;17(1):345-356.

140. Hansen LK, Wilhelm J, Fassett JT. Regulation of hepatocyte cell cycle progression and differentiation by type I collagen structure. Curr Top Dev Biol 2006;72:205-236.

141. Godoy P, Hengstler JG, Ilkavets I, Meyer C, Bachmann A, Muller A, et al. Extracellular matrix modulates sensitivity of hepatocytes to fibroblastoid dedifferentiation and transforming growth factor beta-induced apoptosis. Hepatology 2009;49(6):2031-2043.

142. Semler EJ, Ranucci CS, Moghe PV. Mechanochemical manipulation of hepatocyte aggregation can selectively induce or repress liver-specific function. Biotechnol Bioeng 2000;69(4):359-369.

143. Semler EJ, Lancin PA, Dasgupta A, Moghe PV. Engineering hepatocellular morphogenesis and function via ligand-presenting hydrogels with graded mechanical compliance. Biotechnol Bioeng 2005;89(3):296-307.

144. Chang TT, Hughes-Fulford M. Monolayer and Spheroid Culture of Human Liver Hepatocellular Carcinoma Cell Line Cells Demonstrate Distinct Global Gene Expression Patterns and Functional Phenotypes. Tissue Eng Part A 2008.

145. Du Y, Han R, Ng S, Ni J, Sun W, Wohland T, et al. Identification and characterization of a novel prespheroid 3-dimensional hepatocyte monolayer on galactosylated substratum. Tissue Eng 2007;13(7):1455-1468.

146. Elkayam T, mitay-Shaprut S, Dvir-Ginzberg M, Harel T, Cohen S. Enhancing the drug metabolism activities of C3A--a human hepatocyte cell line--by tissue engineering within alginate scaffolds. Tissue Eng 2006;12(5):1357-1368.

147. Hanahan D, Weinberg RA. The hallmarks of cancer. Cell 2000;100(1):57-70.

148. Takahashi K, Tanabe K, Ohnuki M, Narita M, Ichisaka T, Tomoda K, et al. Induction of pluripotent stem cells from adult human fibroblasts by defined factors. Cell 2007;131(5):861-872.

149. Yu J, Vodyanik MA, Smuga-Otto K, ntosiewicz-Bourget J, Frane JL, Tian S, et al. Induced pluripotent stem cell lines derived from human somatic cells. Science 2007;318(5858):1917-1920.

150. Wernig M, Meissner A, Foreman R, Brambrink T, Ku M, Hochedlinger K, et al. In vitro reprogramming of fibroblasts into a pluripotent ES-cell-like state. Nature 2007;448(7151):318-324.

151. Ingber DE. Can cancer be reversed by engineering the tumor microenvironment? Semin Cancer Biol 2008;18(5):356-364.

152. Lee EY, Lee WH, Kaetzel CS, Parry G, Bissell MJ. Interaction of mouse mammary epithelial cells with collagen substrata: regulation of casein gene expression and secretion. Proc Natl Acad Sci U S A 1985;82(5):1419-1423.

153. Singhvi R, Kumar A, Lopez GP, Stephanopoulos GN, Wang DI, Whitesides GM, et al. Engineering cell shape and function. Science 1994;264(5159):696-698.

154. Chen CS, Mrksich M, Huang S, Whitesides GM, Ingber DE. Geometric control of cell life and death. Science 1997;276(5317):1425-1428.

155. Paszek MJ, Zahir N, Johnson KR, Lakins JN, Rozenberg GI, Gefen A, et al. Tensional homeostasis and the malignant phenotype. Cancer Cell 2005;8(3):241-254.

156. Ingber DE, Madri JA, Jamieson JD. Role of basal lamina in neoplastic disorganization of tissue architecture. Proc Natl Acad Sci U S A 1981;78(6):3901-3905.

157. Ellison ML, Ambrose EJ, Easty GC. Differentiation in a transplantable rat tumour maintained in organ culture. Exp Cell Res 1969;55(2):198-204.

158. Ingber DE, Madri JA, Jamieson JD. Basement membrane as a spatial organizer of polarized epithelia. Exogenous basement membrane reorients pancreatic epithelial tumor cells in vitro. Am J Pathol 1986;122(1):129-139.

159. Watanabe TK, Hansen LJ, Reddy NK, Kanwar YS, Reddy JK. Differentiation of pancreatic acinar carcinoma cells cultured on rat testicular seminiferous tubular basement membranes. Cancer Res 1984;44(11):5361-5368.

160. Chung LW, Zhau HE, Ro JY. Morphologic and biochemical alterations in rat prostatic tumors induced by fetal urogenital sinus mesenchyme. Prostate 1990;17(2):165-174.

161. DeCosse JJ, Gossens CL, Kuzma JF, Unsworth BR. Breast cancer: induction of differentiation by embryonic tissue. Science 1973;181(4104):1057-1058.

162. Goldenberg DM, Pavia RA. Malignant potential of murine stromal cells after transplantation of human tumors into nude mice. Science 1981;212(4490):65-67.

163. Huang S, Ingber DE. Cell tension, matrix mechanics, and cancer development. Cancer Cell 2005;8(3):175-176.

164. Sternlicht MD, Lochter A, Sympson CJ, Huey B, Rougier JP, Gray JW, et al. The stromal proteinase MMP3/stromelysin-1 promotes mammary carcinogenesis. Cell 1999;98(2):137-146.

165. Sternlicht MD, Bissell MJ, Werb Z. The matrix metalloproteinase stromelysin-1 acts as a natural mammary tumor promoter. Oncogene 2000;19(8):1102-1113.

166. Biscoff F, BRYSON G. Carcinogenesis through solid-state surfaces. Prog Exp Tumor Res 1964;5:85-133.

167. Zhang DY, Friedman SL. Fibrosis-dependent mechanisms of hepatocarcinogenesis. Hepatology 2012;56(2):769-775.

168. Hernandez-Gea V, Toffanin S, Friedman SL, Llovet JM. Role of the microenvironment in the pathogenesis and treatment of hepatocellular carcinoma. Gastroenterology 2013;144(3):512-527.

169. Colpaert C, Vermeulen P, Van ME, Dirix L. The presence of a fibrotic focus is an independent predictor of early metastasis in lymph node-negative breast cancer patients. Am J Surg Pathol 2001;25(12):1557-1558.

170. Padera TP, Stoll BR, Tooredman JB, Capen D, di TE, Jain RK. Pathology: cancer cells compress intratumour vessels. Nature 2004;427(6976):695.

171. Beil M, Micoulet A, von WG, Paschke S, Walther P, Omary MB, et al. Sphingosylphosphorylcholine regulates keratin network architecture and visco-elastic properties of human cancer cells. Nat Cell Biol 2003;5(9):803-811.

172. Paszek MJ, Weaver VM. The tension mounts: mechanics meets morphogenesis and malignancy. J Mammary Gland Biol Neoplasia 2004;9(4):325-342.

173. Wozniak MA, Desai R, Solski PA, Der CJ, Keely PJ. ROCK-generated contractility regulates breast epithelial cell differentiation in response to the physical properties of a three-dimensional collagen matrix. J Cell Biol 2003;163(3):583-595.

174. Vega FM, Ridley AJ. Rho GTPases in cancer cell biology. FEBS Lett 2008;582(14):2093-2101.

175. Fritz G, Just I, Kaina B. Rho GTPases are over-expressed in human tumors. Int J Cancer 1999;81(5):682-687.

176. Croft DR, Sahai E, Mavria G, Li S, Tsai J, Lee WM, et al. Conditional ROCK activation in vivo induces tumor cell dissemination and angiogenesis. Cancer Res 2004;64(24):8994-9001.

177. Mitra SK, Hanson DA, Schlaepfer DD. Focal adhesion kinase: in command and control of cell motility. Nat Rev Mol Cell Biol 2005;6(1):56-68.

178. Tilghman RW, Parsons JT. Focal adhesion kinase as a regulator of cell tension in the progression of cancer. Semin Cancer Biol 2008;18(1):45-52.

179. Izaguirre G, Aguirre L, Hu YP, Lee HY, Schlaepfer DD, Aneskievich BJ, et al. The cytoskeletal/non-muscle isoform of alpha-actinin is phosphorylated on its actin-binding domain by the focal adhesion kinase. J Biol Chem 2001;276(31):28676-28685.

180. Wang HB, Dembo M, Hanks SK, Wang Y. Focal adhesion kinase is involved in mechanosensing during fibroblast migration. Proc Natl Acad Sci U S A 2001;98(20):11295-11300.

181. Mofrad MR, Golji J, bdul Rahim NA, Kamm RD. Force-induced unfolding of the focal adhesion targeting domain and the influence of paxillin binding. Mech Chem Biosyst 2004;1(4):253-265.

182. Gabarra-Niecko V, Schaller MD, Dunty JM. FAK regulates biological processes important for the pathogenesis of cancer. Cancer Metastasis Rev 2003;22(4):359-374.

183. Conti JA, Kendall TJ, Bateman A, Armstrong TA, Papa-Adams A, Xu Q, et al. The desmoplastic reaction surrounding hepatic colorectal adenocarcinoma metastases aids tumor growth and survival via alphav integrin ligation. Clin Cancer Res 2008;14(20):6405-6413.

184. Ulrich TA, de Juan Pardo EM, Kumar S. The mechanical rigidity of the extracellular matrix regulates the structure, motility, and proliferation of glioma cells. Cancer Res 2009;69(10):4167-4174.

185. Weaver VM, Petersen OW, Wang F, Larabell CA, Briand P, Damsky C, et al. Reversion of the malignant phenotype of human breast cells in three-dimensional culture and in vivo by integrin blocking antibodies. J Cell Biol 1997;137(1):231-245.

186. Georges PC, Janmey PA. Cell type-specific response to growth on soft materials. J Appl Physiol 2005;98(4):1547-1553.

187. Welch DR, Sakamaki T, Pioquinto R, Leonard TO, Goldberg SF, Hon Q, et al. Transfection of constitutively active mitogen-activated protein/extracellular signal-regulated kinase kinase confers tumorigenic and metastatic potentials to NIH3T3 cells. Cancer Res 2000;60(6):1552-1556.

188. MacKintosh FC, Kas J, Janmey PA. Elasticity of semiflexible biopolymer networks. Phys Rev Lett 1995;75(24):4425-4428.

189. Gildner CD, Lerner AL, Hocking DC. Fibronectin matrix polymerization increases tensile strength of model tissue. Am J Physiol Heart Circ Physiol 2004;287(1):H46-H53.

190. Marx G. Elasticity of fibrin and protofibrin gels is differentially modulated by calcium and zinc. Thromb Haemost 1988;59(3):500-503.

191. Halliday NL, Tomasek JJ. Mechanical properties of the extracellular matrix influence fibronectin fibril assembly in vitro. Exp Cell Res 1995;217(1):109-117.

192. Montesano R, Orci L. Transforming growth factor beta stimulates collagen-matrix contraction by fibroblasts: implications for wound healing. Proc Natl Acad Sci U S A 1988;85(13):4894-4897.

193. Wang YL, Pelham RJ, Jr. Preparation of a flexible, porous polyacrylamide substrate for mechanical studies of cultured cells. Methods Enzymol 1998;298:489-496.

194. Flanagan LA, Ju YE, Marg B, Osterfield M, Janmey PA. Neurite branching on deformable substrates. Neuroreport 2002;13(18):2411-2415.

195. Engler A, Bacakova L, Newman C, Hategan A, Griffin M, Discher D. Substrate compliance versus ligand density in cell on gel responses. Biophys J 2004;86(1 Pt 1):617-628.

196. Yeung T, Georges PC, Flanagan LA, Marg B, Ortiz M, Funaki M, et al. Effects of substrate stiffness on cell morphology, cytoskeletal structure, and adhesion. Cell Motil Cytoskeleton 2005;60(1):24-34.

197. Bondareva A, Downey CM, Ayres F, Liu W, Boyd SK, Hallgrimsson B, et al. The lysyl oxidase inhibitor, beta-aminopropionitrile, diminishes the metastatic colonization potential of circulating breast cancer cells. PLoS One 2009;4(5):e5620.

198. Noda S, Masumi S, Moriyama M, Kannan Y, Ohta M, Sugano T, et al. Population of hepatic macrophages and response of perfused liver to platelet-activating factor during production of thioacetamide-induced cirrhosis in rats. Hepatology 1996;24(2):412-418.

199. Li X, Benjamin IS, Alexander B. Reproducible production of thioacetamide-induced macronodular cirrhosis in the rat with no mortality. J Hepatol 2002;36(4):488-493.

200. Wang T, Shankar K, Ronis MJ, Mehendale HM. Potentiation of thioacetamide liver injury in diabetic rats is due to induced CYP2E1. J Pharmacol Exp Ther 2000;294(2):473-479.

201. Constandinou C, Henderson N, Iredale JP. Modeling liver fibrosis in rodents. Methods Mol Med 2005;117:237-250.

202. Tsukamoto H, Matsuoka M, French SW. Experimental models of hepatic fibrosis: a review. Semin Liver Dis 1990;10(1):56-65.

203. Ashrafian H, Docherty L, Leo V, Towlson C, Neilan M, Steeples V, et al. A mutation in the mitochondrial fission gene Dnm1l leads to cardiomyopathy. PLoS Genet 2010;6(6):e1001000.

204. Fentzke RC, Korcarz CE, Lang RM, Lin H, Leiden JM. Dilated cardiomyopathy in transgenic mice expressing a dominant-negative CREB transcription factor in the heart. J Clin Invest 1998;101(11):2415-2426.

205. Gordon H, Sweet HH. A simple method for the silver impregnation of reticulin. American Journal of Pathology 1936;12:545.

206. Bradford MM. A rapid and sensitive method for the quantitation of microgram quantities of protein utilizing the principle of protein-dye binding. Anal Biochem 1976;72:248-254.

207. Molls RR, Savransky V, Liu M, Bevans S, Mehta T, Tuder RM, et al. Keratinocyte-derived chemokine is an early biomarker of ischemic acute kidney injury. Am J Physiol Renal Physiol 2006;290(5):F1187-F1193.

208. Nakabayashi H, Taketa K, Miyano K, Yamane T, Sato J. Growth of human hepatoma cells lines with differentiated functions in chemically defined medium. Cancer Res 1982;42(9):3858-3863.

209. Aden DP, Fogel A, Plotkin S, Damjanov I, Knowles BB. Controlled synthesis of HBsAg in a differentiated human liver carcinoma-derived cell line. Nature 1979;282(5739):615-616.

210. Soule HD, Vazguez J, Long A, Albert S, Brennan M. A human cell line from a pleural effusion derived from a breast carcinoma. J Natl Cancer Inst 1973;51(5):1409-1416.

211. Cailleau R, Young R, Olive M, Reeves WJ, Jr. Breast tumor cell lines from pleural effusions. J Natl Cancer Inst 1974;53(3):661-674.

212. Sellappan S, Grijalva R, Zhou X, Yang W, Eli MB, Mills GB, et al. Lineage infidelity of MDA-MB-435 cells: expression of melanocyte proteins in a breast cancer cell line. Cancer Res 2004;64(10):3479-3485.

213. Ellison G, Klinowska T, Westwood RF, Docter E, French T, Fox JC. Further evidence to support the melanocytic origin of MDA-MB-435. Mol Pathol 2002;55(5):294-299.

214. Giard DJ, Aaronson SA, Todaro GJ, Arnstein P, Kersey JH, Dosik H, et al. In vitro cultivation of human tumors: establishment of cell lines derived from a series of solid tumors. J Natl Cancer Inst 1973;51(5):1417-1423.

215. Horoszewicz JS, Leong SS, Kawinski E, Karr JP, Rosenthal H, Chu TM, et al. LNCaP model of human prostatic carcinoma. Cancer Res 1983;43(4):1809-1818.

216. Tirnitz-Parker JE, Tonkin JN, Knight B, Olynyk JK, Yeoh GC. Isolation, culture and immortalisation of hepatic oval cells from adult mice fed a choline-deficient, ethionine-supplemented diet. Int J Biochem Cell Biol 2007;39(12):2226-2239.

217. Arthur MJ, Friedman SL, Roll FJ, Bissell DM. Lipocytes from normal rat liver release a neutral metalloproteinase that degrades basement membrane (type IV) collagen. J Clin Invest 1989;84(4):1076-1085.

218. Boulter L, Govaere O, Bird TG, Radulescu S, Ramachandran P, Pellicoro A, et al. Macrophage-derived Wnt opposes Notch signaling to specify hepatic progenitor cell fate in chronic liver disease. Nat Med 2012;18(4):572-579.

219. Yasui O, Miura N, Terada K, Kawarada Y, Koyama K, Sugiyama T. Isolation of oval cells from Long-Evans Cinnamon rats and their transformation into hepatocytes in vivo in the rat liver. Hepatology 1997;25(2):329-334.

220. Herkel J, Jagemann B, Wiegard C, Lazaro JF, Lueth S, Kanzler S, et al. MHC class II-expressing hepatocytes function as antigen-presenting cells and activate specific CD4 T lymphocyutes. Hepatology 2003;37(5):1079-1085.

221. Sethi T, Rintoul RC, Moore SM, Mackinnon AC, Salter D, Choo C, et al. Extracellular matrix proteins protect small cell lung cancer cells against apoptosis: a mechanism for small cell lung cancer growth and drug resistance in vivo. Nat Med 1999;5(6):662-668.

222. Thiery JP. Epithelial-mesenchymal transitions in tumour progression. Nat Rev Cancer 2002;2(6):442-454.

223. Zavadil J, Bottinger EP. TGF-beta and epithelial-to-mesenchymal transitions. Oncogene 2005;24(37):5764-5774.

224. Wang S, Basson MD. Protein kinase B/AKT and focal adhesion kinase: two close signaling partners in cancer. Anticancer Agents Med Chem 2011;11(10):993-1002.

225. Fujii T, Koshikawa K, Nomoto S, Okochi O, Kaneko T, Inoue S, et al. Focal adhesion kinase is overexpressed in hepatocellular carcinoma and can be served as an independent prognostic factor. J Hepatol 2004;41(1):104-111.

226. Patriarca C, Roncalli M, Gambacorta M, Cominotti M, Coggi G, Viale G. Patterns of integrin common chain beta 1 and collagen IV immunoreactivity in hepatocellular carcinoma. Correlations with tumour growth rate, grade and size. J Pathol 1993;171(1):5-11.

227. Slack-Davis JK, Martin KH, Tilghman RW, Iwanicki M, Ung EJ, Autry C, et al. Cellular characterization of a novel focal adhesion kinase inhibitor. J Biol Chem 2007;282(20):14845-14852.

228. Parsons JT, Slack-Davis J, Tilghman R, Roberts WG. Focal adhesion kinase: targeting adhesion signaling pathways for therapeutic intervention. Clin Cancer Res 2008;14(3):627-632.

229. Stokes JB, Adair SJ, Slack-Davis JK, Walters DM, Tilghman RW, Hershey ED, et al. Inhibition of focal adhesion kinase by PF-562,271 inhibits the growth and metastasis of pancreatic cancer concomitant with altering the tumor microenvironment. Mol Cancer Ther 2011;10(11):2135-2145.

230. Rountree CB, Mishra L, Willenbring H. Stem cells in liver diseases and cancer: recent advances on the path to new therapies. Hepatology 2012;55(1):298-306.

231. Yao Z, Mishra L. Cancer stem cells and hepatocellular carcinoma. Cancer Biol Ther 2009;8(18):1691-1698.

232. Marquardt JU, Factor VM, Thorgeirsson SS. Epigenetic regulation of cancer stem cells in liver cancer: current concepts and clinical implications. J Hepatol 2010;53(3):568-577.

233. Barkan D, Kleinman H, Simmons JL, Asmussen H, Kamaraju AK, Hoenorhoff MJ, et al. Inhibition of metastatic outgrowth from single dormant tumor cells by targeting the cytoskeleton. Cancer Res 2008;68(15):6241-6250.

234. Klein EA, Campbell LE, Kothapalli D, Fournier AK, Assoian RK. Joint requirement for Rac and ERK activities underlies the mid-G1 phase induction of cyclin D1 and S phase entry in both epithelial and mesenchymal cells. J Biol Chem 2008;283(45):30911-30918.

235. Yu H, Pardoll D, Jove R. STATs in cancer inflammation and immunity: a leading role for STAT3. Nat Rev Cancer 2009;9(11):798-809.

236. Owens LV, Xu L, Dent GA, Yang X, Sturge GC, Craven RJ, et al. Focal adhesion kinase as a marker of invasive potential in differentiated human thyroid cancer. Ann Surg Oncol 1996;3(1):100-105.

237. Cance WG, Harris JE, Iacocca MV, Roche E, Yang X, Chang J, et al. Immunohistochemical analyses of focal adhesion kinase expression in benign and malignant human breast and colon tissues: correlation with preinvasive and invasive phenotypes. Clin Cancer Res 2000;6(6):2417-2423.

238. Lark AL, Livasy CA, Calvo B, Caskey L, Moore DT, Yang X, et al. Overexpression of focal adhesion kinase in primary colorectal carcinomas and colorectal liver metastases: immunohistochemistry and real-time PCR analyses. Clin Cancer Res 2003;9(1):215-222.

239. van Nimwegen MJ, Verkoeijen S, van BL, Burg D, van de WB. Requirement for focal adhesion kinase in the early phase of mammary adenocarcinoma lung metastasis formation. Cancer Res 2005;65(11):4698-4706.

240. Tilghman RW, Slack-Davis JK, Sergina N, Martin KH, Iwanicki M, Hershey ED, et al. Focal adhesion kinase is required for the spatial organization of the leading edge in migrating cells. J Cell Sci 2005;118(Pt 12):2613-2623.

241. Mitra SK, Lim ST, Chi A, Schlaepfer DD. Intrinsic focal adhesion kinase activity controls orthotopic breast carcinoma metastasis via the regulation of urokinase plasminogen activator expression in a syngeneic tumor model. Oncogene 2006;25(32):4429-4440.

242. McLean GW, Brown K, Arbuckle MI, Wyke AW, Pikkarainen T, Ruoslahti E, et al. Decreased focal adhesion kinase suppresses papilloma formation during experimental mouse skin carcinogenesis. Cancer Res 2001;61(23):8385-8389.

243. McLean GW, Komiyama NH, Serrels B, Asano H, Reynolds L, Conti F, et al. Specific deletion of focal adhesion kinase suppresses tumor formation and blocks malignant progression. Genes Dev 2004;18(24):2998-3003.

244. Kalluri R, Weinberg RA. The basics of epithelial-mesenchymal transition. J Clin Invest 2009;119(6):1420-1428.

245. Zeisberg M, Neilson EG. Biomarkers for epithelial-mesenchymal transitions. J Clin Invest 2009;119(6):1429-1437.

246. Hay ED. An overview of epithelio-mesenchymal transformation. Acta Anat (Basel) 1995;154(1):8-20.

247. Greenburg G, Hay ED. Epithelia suspended in collagen gels can lose polarity and express characteristics of migrating mesenchymal cells. J Cell Biol 1982;95(1):333-339.

248. Zeisberg EM, Tarnavski O, Zeisberg M, Dorfman AL, McMullen JR, Gustafsson E, et al. Endothelial-to-mesenchymal transition contributes to cardiac fibrosis. Nat Med 2007;13(8):952-961.

249. Zeisberg M, Yang C, Martino M, Duncan MB, Rieder F, Tanjore H, et al. Fibroblasts derive from hepatocytes in liver fibrosis via epithelial to mesenchymal transition. J Biol Chem 2007;282(32):23337-23347.

250. Hollestelle A, Peeters JK, Smid M, Timmermans M, Verhoog LC, Westenend PJ, et al. Loss of E-cadherin is not a necessity for epithelial to mesenchymal transition in human breast cancer. Breast Cancer Res Treat 2013;138(1):47-57.

251. Yilmaz M, Christofori G. EMT, the cytoskeleton, and cancer cell invasion. Cancer Metastasis Rev 2009;28(1-2):15-33.

252. Guarino M, Rubino B, Ballabio G. The role of epithelial-mesenchymal transition in cancer pathology. Pathology 2007;39(3):305-318.

253. Cicchini C, Laudadio I, Citarella F, Corazzari M, Steindler C, Conigliaro A, et al. TGFbeta-induced EMT requires focal adhesion kinase (FAK) signaling. Exp Cell Res 2008;314(1):143-152.

254. Aguirre-Ghiso JA. Models, mechanisms and clinical evidence for cancer dormancy. Nat Rev Cancer 2007;7(11):834-846.

255. Naumov GN, MacDonald IC, Weinmeister PM, Kerkvliet N, Nadkarni KV, Wilson SM, et al. Persistence of solitary mammary carcinoma cells in a secondary site: a possible contributor to dormancy. Cancer Res 2002;62(7):2162-2168.

256. Naumov GN, Townson JL, MacDonald IC, Wilson SM, Bramwell VH, Groom AC, et al. Ineffectiveness of doxorubicin treatment on solitary dormant mammary

carcinoma cells or late-developing metastases. Breast Cancer Res Treat 2003;82(3):199-206.

257. Barkan D, Green JE, Chambers AF. Extracellular matrix: a gatekeeper in the transition from dormancy to metastatic growth. Eur J Cancer 2010;46(7):1181-1188.

258. Wikman H, Vessella R, Pantel K. Cancer micrometastasis and tumour dormancy. APMIS 2008;116(7-8):754-770.

259. Fisher B, Fisher ER. Experimental evidence in support of the dormant tumor cell. Science 1959;130(3380):918-919.

260. Agostino D, Cliffton EE. Organ localization and the effect of trauma on the fate of circulating cancer cells. Cancer Res 1965;25(10):1728-1732.

261. Barkan D, El Touny LH, Michalowski AM, Smith JA, Chu I, Davis AS, et al. Metastatic growth from dormant cells induced by a col-I-enriched fibrotic environment. Cancer Res 2010;70(14):5706-5716.

262. Barkan D, Kleinman H, Simmons JL, Asmussen H, Kamaraju AK, Hoenorhoff MJ, et al. Inhibition of metastatic outgrowth from single dormant tumor cells by targeting the cytoskeleton. Cancer Res 2008;68(15):6241-6250.

263. Bao G, Suresh S. Cell and molecular mechanics of biological materials. Nat Mater 2003;2(11):715-725.

264. Naumov GN, Townson JL, MacDonald IC, Wilson SM, Bramwell VH, Groom AC, et al. Ineffectiveness of doxorubicin treatment on solitary dormant mammary carcinoma cells or late-developing metastases. Breast Cancer Res Treat 2003;82(3):199-206.

265. Vessella RL, Pantel K, Mohla S. Tumor cell dormancy: an NCI workshop report. Cancer Biol Ther 2007;6(9):1496-1504.

266. Ma S, Chan KW, Hu L, Lee TK, Wo JY, Ng IO, et al. Identification and characterization of tumorigenic liver cancer stem/progenitor cells. Gastroenterology 2007;132(7):2542-2556.

267. Zhu Z, Hao X, Yan M, Yao M, Ge C, Gu J, et al. Cancer stem/progenitor cells are highly enriched in CD133+CD44+ population in hepatocellular carcinoma. Int J Cancer 2010;126(9):2067-2078.

268. Ma S, Lee TK, Zheng BJ, Chan KW, Guan XY. CD133+ HCC cancer stem cells confer chemoresistance by preferential expression of the Akt/PKB survival pathway. Oncogene 2008;27(12):1749-1758.

269. Tomuleasa C, Soritau O, Rus-Ciuca D, Pop T, Todea D, Mosteanu O, et al. Isolation and characterization of hepatic cancer cells with stem-like properties from hepatocellular carcinoma. J Gastrointestin Liver Dis 2010;19(1):61-67.

270. Levina V, Marrangoni AM, DeMarco R, Gorelik E, Lokshin AE. Drug-selected human lung cancer stem cells: cytokine network, tumorigenic and metastatic properties. PLoS One 2008;3(8):e3077.

271. Polyak K, Weinberg RA. Transitions between epithelial and mesenchymal states: acquisition of malignant and stem cell traits. Nat Rev Cancer 2009;9(4):265-273.

272. Aktas B, Tewes M, Fehm T, Hauch S, Kimmig R, Kasimir-Bauer S. Stem cell and epithelial-mesenchymal transition markers are frequently overexpressed in circulating tumor cells of metastatic breast cancer patients. Breast Cancer Res 2009;11(4):R46.

273. Zeng Z, Ren J, O'Neil M, Zhao J, Bridges B, Cox J, et al. Impact of stem cell marker expression on recurrence of TACE-treated hepatocellular carcinoma post liver transplantation. BMC Cancer 2012;12:584.

274. Sun YF, Xu Y, Yang XR, Guo W, Zhang X, Qiu SJ, et al. Circulating stem cell-like EpCAM(+) tumor cells indicate poor prognosis of hepatocellular carcinoma after curative resection. Hepatology 2012.

275. Yang ZF, Ho DW, Ng MN, Lau CK, Yu WC, Ngai P, et al. Significance of CD90+ cancer stem cells in human liver cancer. Cancer Cell 2008;13(2):153-166.

276. Becker G, Schmitt-Graeff A, Ertelt V, Blum HE, Allgaier HP. CD117 (c-kit) expression in human hepatocellular carcinoma. Clin Oncol (R Coll Radiol) 2007;19(3):204-208.

277. Bissell MJ, Labarge MA. Context, tissue plasticity, and cancer: are tumor stem cells also regulated by the microenvironment? Cancer Cell 2005;7(1):17-23.

278. Wilson JW, Leduc EH. Role of cholangioles in restoration of the liver of the mouse after dietary injury. J Pathol Bacteriol 1958;76(2):441-449.

279. Paku S, Nagy P, Kopper L, Thorgeirsson SS. 2-acetylaminofluorene dose-dependent differentiation of rat oval cells into hepatocytes: confocal and electron microscopic studies. Hepatology 2004;39(5):1353-1361.

280. Miyazaki T, Futaki S, Hasegawa K, Kawasaki M, Sanzen N, Hayashi M, et al. Recombinant human laminin isoforms can support the undifferentiated growth of human embryonic stem cells. Biochem Biophys Res Commun 2008;375(1):27-32.

281. Gaudio E, Carpino G, Cardinale V, Franchitto A, Onori P, Alvaro D. New insights into liver stem cells. Dig Liver Dis 2009;41(7):455-462.

282. Li WL, Su J, Yao YC, Tao XR, Yan YB, Yu HY, et al. Isolation and characterization of bipotent liver progenitor cells from adult mouse. Stem Cells 2006;24(2):322-332.

283. Braun KM, Thompson AW, Sandgren EP. Hepatic microenvironment affects oval cell localization in albumin-urokinase-type plasminogen activator transgenic mice. Am J Pathol 2003;162(1):195-202.

284. Yovchev MI, Grozdanov PN, Joseph B, Gupta S, Dabeva MD. Novel hepatic progenitor cell surface markers in the adult rat liver. Hepatology 2007;45(1):139-149.

285. Roskams T. Different types of liver progenitor cells and their niches. J Hepatol 2006;45(1):1-4.

286. Ueberham E, Aigner T, Ueberham U, Gebhardt R. E-cadherin as a reliable cell surface marker for the identification of liver specific stem cells. J Mol Histol 2007;38(4):359-368.

287. Shafritz DA, Oertel M, Menthena A, Nierhoff D, Dabeva MD. Liver stem cells and prospects for liver reconstitution by transplanted cells. Hepatology 2006;43(2 Suppl 1):S89-S98.

288. Zhou H, Rogler LE, Teperman L, Morgan G, Rogler CE. Identification of hepatocytic and bile ductular cell lineages and candidate stem cells in bipolar ductular reactions in cirrhotic human liver. Hepatology 2007;45(3):716-724.

289. Tsamandas AC, Antonacopoulou A, Kalogeropoulou C, Tsota I, Zabakis P, Giannopoulou E, et al. Oval cell proliferation in cirrhosis in rats. An experimental study. Hepatol Res 2007;37(9):755-764.

290. Dominguez-Gil B, Morales JM. Transplantation in the patient with hepatitis C. Transpl Int 2009;22(12):1117-1131.

291. Zylberberg H, Nalpas B, Carnot F, Skhiri H, Fontaine H, Legendre C, et al. Severe evolution of chronic hepatitis C in renal transplantation: a case control study. Nephrol Dial Transplant 2002;17(1):129-133.

292. Wells RG. The role of matrix stiffness in hepatic stellate cell activation and liver fibrosis. J Clin Gastroenterol 2005;39(4 Suppl 2):S158-S161.

293. Kallis YN, Robson AJ, Fallowfield JA, Thomas HC, Alison MR, Wright NA, et al. Remodelling of extracellular matrix is a requirement for the hepatic progenitor cell response. Gut 2011;60(4):525-533.

294. Fellous TG, Islam S, Tadrous PJ, Elia G, Kocher HM, Bhattacharya S, et al. Locating the stem cell niche and tracing hepatocyte lineages in human liver. Hepatology 2009;49(5):1655-1663.

295. Akhurst B, Croager EJ, Farley-Roche CA, Ong JK, Dumble ML, Knight B, et al. A modified choline-deficient, ethionine-supplemented diet protocol effectively induces oval cells in mouse liver. Hepatology 2001;34(3):519-522.

296. Ueberham E, Lindner R, Kamprad M, Hiemann R, Hilger N, Woithe B, et al. Oval cell proliferation in p16INK4a expressing mouse liver is triggered by chronic growth stimuli. J Cell Mol Med 2008;12(2):622-638.

297. Gilmore AP, Romer LH. Inhibition of focal adhesion kinase (FAK) signaling in focal adhesions decreases cell motility and proliferation. Mol Biol Cell 1996;7(8):1209-1224.

298. Bryant P, Zheng Q, Pumiglia K. Focal adhesion kinase controls cellular levels of p27/Kip1 and p21/Cip1 through Skp2-dependent and -independent mechanisms. Mol Cell Biol 2006;26(11):4201-4213.

299. Xu B, Song G, Ju Y, Li X, Song Y, Watanabe S. RhoA/ROCK, cytoskeletal dynamics, and focal adhesion kinase are required for mechanical stretch-induced tenogenic differentiation of human mesenchymal stem cells. J Cell Physiol 2012;227(6):2722-2729.

300. Lozoya OA, Wauthier E, Turner RA, Barbier C, Prestwich GD, Guilak F, et al. Regulation of hepatic stem/progenitor phenotype by microenvironment stiffness in hydrogel models of the human liver stem cell niche. Biomaterials 2011;32(30):7389-7402.

301. Arcidi JM, Jr., Moore GW, Hutchins GM. Hepatic morphology in cardiac dysfunction: a clinicopathologic study of 1000 subjects at autopsy. Am J Pathol 1981;104(2):159-166.

302. Dunn GD, Hayes P, Breen KJ, Schenker S. The liver in congestive heart failure: a review. Am J Med Sci 1973;265(3):174-189.

303. Seeto RK, Fenn B, Rockey DC. Ischemic hepatitis: clinical presentation and pathogenesis. Am J Med 2000;109(2):109-113.

304. Sherlock S. The liver in heart failure; relation of anatomical, functional, and circulatory changes. Br Heart J 1951;13(3):273-293.

305. McMurray JJ, Stewart S. Epidemiology, aetiology, and prognosis of heart failure. Heart 2000;83(5):596-602.

306. Ghaferi AA, Hutchins GM. Progression of liver pathology in patients undergoing the Fontan procedure: Chronic passive congestion, cardiac cirrhosis, hepatic adenoma, and hepatocellular carcinoma. J Thorac Cardiovasc Surg 2005;129(6):1348-1352.

307. Kendall TJ, Stedman B, Hacking N, Haw M, Vettukattill JJ, Salmon AP, et al. Hepatic fibrosis and cirrhosis in the Fontan circulation: a detailed morphological study. J Clin Pathol 2008;61(4):504-508.

308. Kiesewetter CH, Sheron N, Vettukattill JJ, Hacking N, Stedman B, Millward-Sadler H, et al. Hepatic changes in the failing Fontan circulation. Heart 2007;93(5):579-584.

309. Narkewicz MR, Sondheimer HM, Ziegler JW, Otanni Y, Lorts A, Shaffer EM, et al. Hepatic dysfunction following the Fontan procedure. J Pediatr Gastroenterol Nutr 2003;36(3):352-357.

310. Fontan F, Baudet E. Surgical repair of tricuspid atresia. Thorax 1971;26(3):240-248.

311. Tanaka A, Kobayashi S, Fujiki Y. Peroxisome division is impaired in a CHO cell mutant with an inactivating point-mutation in dynamin-like protein 1 gene. Exp Cell Res 2006;312(9):1671-1684.

312. Koch A, Thiemann M, Grabenbauer M, Yoon Y, McNiven MA, Schrader M. Dynamin-like protein 1 is involved in peroxisomal fission. J Biol Chem 2003;278(10):8597-8605.

313. Koch A, Schneider G, Luers GH, Schrader M. Peroxisome elongation and constriction but not fission can occur independently of dynamin-like protein 1. J Cell Sci 2004;117(Pt 17):3995-4006.

314. Waterham HR, Koster J, van Roermund CW, Mooyer PA, Wanders RJ, Leonard JV. A lethal defect of mitochondrial and peroxisomal fission. N Engl J Med 2007;356(17):1736-1741.

315. Duymelinck C, Dauwe SE, De Greef KE, Ysebaert DK, Verpooten GA, De Broe ME. TIMP-1 gene expression and PAI-1 antigen after unilateral ureteral obstruction in the adult male rat. Kidney Int 2000;58(3):1186-1201.

316. Simpson KJ, Henderson NC, Bone-Larson CL, Lukacs NW, Hogaboam CM, Kunkel SL. Chemokines in the pathogenesis of liver disease: so many players with poorly defined roles. Clin Sci (Lond) 2003;104(1):47-63.

317. Yamaguchi Y, Matsumura F, Liang J, Okabe K, Ohshiro H, Ishihara K, et al. Neutrophil elastase and oxygen radicals enhance monocyte chemoattractant protein-expression after ischemia/reperfusion in rat liver. Transplantation 1999;68(10):1459-1468.

318. Nanji AA, Jokelainen K, Rahemtulla A, Miao L, Fogt F, Matsumoto H, et al. Activation of nuclear factor kappa B and cytokine imbalance in experimental alcoholic liver disease in the rat. Hepatology 1999;30(4):934-943.

319. Lentsch AB, Yoshidome H, Cheadle WG, Miller FN, Edwards MJ. Chemokine involvement in hepatic ischemia/reperfusion injury in mice: roles for macrophage inflammatory protein-2 and KC. Hepatology 1998;27(4):1172-1177.

320. Fentzke RC, Korcarz CE, Shroff SG, Lin H, Leiden JM, Lang RM. The left ventricular stress-velocity relation in transgenic mice expressing a dominant negative CREB transgene in the heart. J Am Soc Echocardiogr 2001;14(3):209-218.

321. Isoda T, Paolocci N, Haghighi K, Wang C, Wang Y, Georgakopoulos D, et al. Novel regulation of cardiac force-frequency relation by CREM (cAMP response element modulator). FASEB J 2003;17(2):144-151.

322. Ofir R, Dwarki VJ, Rashid D, Verma IM. CREB represses transcription of fos promoter: role of phosphorylation. Gene Expr 1991;1(1):55-60.

323. Lamph WW, Dwarki VJ, Ofir R, Montminy M, Verma IM. Negative and positive regulation by transcription factor cAMP response element-binding protein is modulated by phosphorylation. Proc Natl Acad Sci U S A 1990;87(11):4320-4324.

324. Huggins GS, Lepore JJ, Greytak S, Patten R, McNamee R, Aronovitz M, et al. The CREB leucine zipper regulates CREB phosphorylation, cardiomyopathy, and lethality in a transgenic model of heart failure. Am J Physiol Heart Circ Physiol 2007;293(3):H1877-H1882.

325. Myers RP, Cerini R, Sayegh R, Moreau R, Degott C, Lebrec D, et al. Cardiac hepatopathy: clinical, hemodynamic, and histologic characteristics and correlations. Hepatology 2003;37(2):393-400.

326. Rockey DC, Boyles JK, Gabbiani G, Friedman SL. Rat hepatic lipocytes express smooth muscle actin upon activation in vivo and in culture. J Submicrosc Cytol Pathol 1992;24(2):193-203.

327. Corpechot C, Barbu V, Wendum D, Kinnman N, Rey C, Poupon R, et al. Hypoxia-induced VEGF and collagen I expressions are associated with angiogenesis and fibrogenesis in experimental cirrhosis. Hepatology 2002;35(5):1010-1021.

328. Nath B, Szabo G. Hypoxia and hypoxia inducible factors: diverse roles in liver diseases. Hepatology 2012;55(2):622-633.

329. Sakata R, Ueno T, Nakamura T, Ueno H, Sata M. Mechanical stretch induces TGF-beta synthesis in hepatic stellate cells. Eur J Clin Invest 2004;34(2):129-136.

330. Balkwill F, Mantovani A. Inflammation and cancer: back to Virchow? Lancet 2001;357(9255):539-545.

331. Coussens LM, Werb Z. Inflammation and cancer. Nature 2002;420(6917):860-867.

332. Lai KK, Shang S, Lohia N, Booth GC, Masse DJ, Fausto N, et al. Extracellular matrix dynamics in hepatocarcinogenesis: a comparative proteomics study of PDGFC transgenic and Pten null mouse models. PLoS Genet 2011;7(6):e1002147.

333. Kalluri R, Zeisberg M. Fibroblasts in cancer. Nat Rev Cancer 2006;6(5):392-401.

334. Hoshida Y, Villanueva A, Kobayashi M, Peix J, Chiang DY, Camargo A, et al. Gene expression in fixed tissues and outcome in hepatocellular carcinoma. N Engl J Med 2008;359(19):1995-2004.

335. Okamoto M, Utsunomiya T, Wakiyama S, Hashimoto M, Fukuzawa K, Ezaki T, et al. Specific gene-expression profiles of noncancerous liver tissue predict the risk for multicentric occurrence of hepatocellular carcinoma in hepatitis C virus-positive patients. Ann Surg Oncol 2006;13(7):947-954.

336. Todorovic V, Rifkin DB. LTBPs, more than just an escort service. J Cell Biochem 2012;113(2):410-418.

337. Kawarabayashi N, Seki S, Hatsuse K, Ohkawa T, Koike Y, Aihara T, et al. Decrease of CD56(+)T cells and natural killer cells in cirrhotic livers with hepatitis C may be involved in their susceptibility to hepatocellular carcinoma. Hepatology 2000;32(5):962-969.

338. Tilghman RW, Cowan CR, Mih JD, Koryakina Y, Gioeli D, Slack-Davis JK, et al. Matrix rigidity regulates cancer cell growth and cellular phenotype. PLoS One 2010;5(9):e12905.

339. Tilghman RW, Blais EM, Cowan CR, Sherman NE, Grigera PR, Jeffery ED, et al. Matrix rigidity regulates cancer cell growth by modulating cellular metabolism and protein synthesis. PLoS One 2012;7(5):e37231.

340. Castera L, Forns X, Alberti A. Non-invasive evaluation of liver fibrosis using transient elastography. J Hepatol 2008;48(5):835-847.

341. Schardt JA, Meyer M, Hartmann CH, Schubert F, Schmidt-Kittler O, Fuhrmann C, et al. Genomic analysis of single cytokeratin-positive cells from bone marrow reveals early mutational events in breast cancer. Cancer Cell 2005;8(3):227-239.

342. Katoh H, Ojima H, Kokubu A, Saito S, Kondo T, Kosuge T, et al. Genetically distinct and clinically relevant classification of hepatocellular carcinoma: putative therapeutic targets. Gastroenterology 2007;133(5):1475-1486.

343. Boyault S, Rickman DS, de RA, Balabaud C, Rebouissou S, Jeannot E, et al. Transcriptome classification of HCC is related to gene alterations and to new therapeutic targets. Hepatology 2007;45(1):42-52.

344. Lee JS, Heo J, Libbrecht L, Chu IS, Kaposi-Novak P, Calvisi DF, et al. A novel prognostic subtype of human hepatocellular carcinoma derived from hepatic progenitor cells. Nat Med 2006;12(4):410-416.

345. Williams MJ, Boulter LG, Lu WY, Bird TB, Fujiwara H, Watt FM, et al. The extracellular matrix protein laminin alpha 5 regulates the behaviour of hepatic progenitor cells in regenerating mouse liver. Journal of Hepatology 2013;58(1):2-3.

346. Levental I, Levental KR, Klein EA, Assoian R, Miller RT, Wells RG, et al. A simple indentation device for measuring micrometer-scale tissue stiffness. J Phys Condens Matter 2010;22(19):194120.

Transcript of publications arising from this thesis

Matrix Stiffness Modulates Proliferation, Chemotherapeutic Response, and Dormancy in Hepatocellular Carcinoma Cells

Jörg Schrader,[1,2]* Timothy T. Gordon-Walker,[1]* Rebecca L. Aucott,[1] Mariëlle van Deemter,[1] Alexander Quaas,[3] Shaun Walsh,[4] Daniel Benten,[2] Stuart J. Forbes,[1] Rebecca G. Wells,[5] and John P. Iredale[1]

There is increasing evidence that the physical environment is a critical mediator of tumor behavior. Hepatocellular carcinoma (HCC) develops within an altered biomechanical environment, and increasing matrix stiffness is a strong predictor of HCC development. The aim of this study was to establish whether changes in matrix stiffness, which are characteristic of inflammation and fibrosis, regulate HCC cell proliferation and chemotherapeutic response. Using an *in vitro* system of "mechanically tunable" matrix-coated polyacrylamide gels, matrix stiffness was modeled across a pathophysiologically relevant range, corresponding to values encountered in normal and fibrotic livers. Increasing matrix stiffness was found to promote HCC cell proliferation. The proliferative index (assessed by Ki67 staining) of Huh7 and HepG2 cells was 2.7-fold and 12.2-fold higher, respectively, when the cells were cultured on stiff (12 kPa) versus soft (1 kPa) supports. This was associated with stiffness-dependent regulation of basal and hepatocyte growth factor–stimulated mitogenic signaling through extracellular signal-regulated kinase, protein kinase B (PKB/Akt), and signal transducer and activator of transcription 3. β1-Integrin and focal adhesion kinase were found to modulate stiffness-dependent HCC cell proliferation. Following treatment with cisplatin, we observed reduced apoptosis in HCC cells cultured on stiff versus soft (physiological) supports. Interestingly, however, surviving cells from soft supports had significantly higher clonogenic capacity than surviving cells from a stiff microenvironment. This was associated with enhanced expression of cancer stem cell markers, including clusters of differentiation 44 (CD44), CD133, c-kit, cysteine-X-cysteine receptor 4, octamer-4 (CXCR4), and NANOG. *Conclusion:* Increasing matrix stiffness promotes proliferation and chemotherapeutic resistance, whereas a soft environment induces reversible cellular dormancy and stem cell characteristics in HCC. This has implications for both the treatment of primary HCC and the prevention of tumor outgrowth from disseminated tumor cells. (HEPATOLOGY 2011;53:1192-1205)

Hepatocellular carcinoma (HCC) is the third most common cause of cancer-related mortality worldwide.[1] The majority (80%) of HCCs develop in the context of advanced liver fibrosis or cirrhosis and liver cirrhosis is the single most important risk factor for HCC development.[2] Liver

Abbreviations: 5-FU, 5-fluorouracil; AFP, alpha fetoprotein; DAPI, 4′,6′-diamidino-2-phenyl-indole dihydrochloride; DMSO, dimethylsulfoxide; ECM, extracellular matrix; ERK, extracellular signal-regulated kinase; FAK, focal adhesion kinase; GAPDH, glyceraldehyde 3-phosphate dehydrogenase; HCC, hepatocellular carcinoma; HGF, hepatocyte growth factor; HNF4α, hepatocyte nuclear factor 4 alpha; MTT, 3-(4,5-dimethylthiazol-2-yl)-2,5-diphenyltetrazolium bromide; OCT4, octamer-4; PA, polyacrylamide; PARP, poly-ADP-ribose polymerase; PE, phycoerythrin; CXCR4, cysteine-X-cysteine receptor 4; PKB/Akt, protein kinase B; STAT3, signal transducer and activator of transcription 3; TGFβ, transforming growth factor beta.

From the [1]Medical Research Council (MRC) Centre for Inflammation Research, University of Edinburgh, Edinburgh, United Kingdom; [2]Department of Medicine I, University Medical Center Hamburg-Eppendorf, Hamburg, Germany; [3]Department of Pathology, University Medical Center Hamburg-Eppendorf, Hamburg, Germany; [4]Department of Pathology, Ninewells Hospital, Dundee, United Kingdom; and [5]Department of Medicine (Gastroenterology), University of Pennsylvania School of Medicine, Philadelphia, PA.

Received July 26, 2010; accepted November 27, 2010.

This study was supported by a fellowship from the Deutsche Forschungsgemeinschaft to J.S. (SCHR1213/1), by grants from the Medical Research Council to T.T.G.W. (G07000582) and J.P.I. (G0600033), by a grant from the National Institutes of Health (DK 058123) to R.G.W and grants from the European Association for the Study of the Liver, UK Stem Cell Foundation and Stem Cell Translational Fund to M.D..

**These authors contributed equally to this work.*

Address reprint requests to: John P. Iredale, D.M., F.R.C.P., F.Med.Sci., MRC Centre for Inflammation Research, University of Edinburgh, 47 Little France Crescent, Edinburgh, EH16 4TJ, United Kingdom. E-mail: John.Iredale@ed.ac.uk; Fax: +44 131 2426682.

fibrosis is defined by stereotypical changes in both the biochemical and physical properties of the cellular microenvironment. However, the role of mechanical factors in modulating the growth and progression of HCC remain poorly defined. Recent studies involving ultrasound elastography (FibroScan) demonstrate that liver stiffness measurements are a strong predictor of HCC development.[3] Furthermore, once established, tumor development is associated with further increases in matrix stiffness to values greater than those of the surrounding hepatic parenchyma.[4] It is therefore evident that HCC develops in a niche with mechanical properties distinct from those encountered in the normal liver.

Cancer development and progression is dependent on both intrinsic genetic abnormalities and external structural determinants.[5] Matrix stiffness has recently been directly implicated in aiding tumor development. Increases in matrix stiffness that enhance cell contractility have been found to be sufficient to enhance the transformation of mammary epithelial cells.[6] Conversely, a reduction in tissue stiffness by inhibition of collagen cross-linking impedes malignant growth and tumor development in a murine model of breast cancer.[7] Cellular stiffness sensing relies upon intracellular tension, which is determined by a dynamic equilibrium between forces generated by a contractile cytoskeleton and the elastic resistance (stiffness) provided by the extracellular matrix (ECM). In this context, cancer progression (tumor growth, invasion, and dissemination) is accompanied by changes in both the mechanical properties of the cancer cell niche and changes in cellular contractility (modified by genetic and epigenetic factors) that regulate tumor cell behavior.

HCC continues to have a poor prognosis (median survival less than 12 months), reflecting its late presentation and lack of effective therapies.[8,9] The effectiveness of both hepatic resection and liver transplantation for HCC is limited by tumor recurrence, which can occur months or years following resection of a primary tumor.[10] Furthermore, systemic chemotherapy has proved ineffective both for the treatment of advanced HCC and in an adjuvant/neoadjuvant setting for the eradication of disseminated (dormant) tumor cells, the progenitors of clinical metastases. The mechanisms underlying chemotherapy resistance in HCC have not been fully elucidated. Although it has previously been demonstrated that the composition of the matrix can enhance chemotherapy resistance in a range of epithelial cancers,[11,12] the role of matrix stiffness has not been specifically addressed for HCC or other epithelial cancers.

Here, we demonstrate that mechanical factors regulate both the proliferation and chemotherapeutic response of HCC cells. In addition, we show that both tumor cell differentiation and cancer stem cell characteristics are influenced by the mechanical properties (that is, stiffness) of the cancer cell niche.

Materials and Methods

Cell Culture and Microscopy. Human HCC cell lines Huh7 and HepG2 (kindly provided by S. Wigmore, Edinburgh, UK) were cultured in Dulbecco's modified Eagle medium (Gibco, Paisley, UK) supplemented with 10% fetal bovine serum, penicillin/streptomycin and L-glutamine. For all experiments, cells were plated at semiconfluent density in 1% fetal bovine serum. Chemical reagents were purchased from Sigma (Poole, UK) unless otherwise stated. Transforming growth factor-beta (TGFβ) and hepatocyte growth factor (HGF) (Peprotech, London, UK) were used at concentrations of 5 ng/mL and 10 ng/mL, respectively. Anti–β1-integrin, clone 6S6 (Millipore, Watford, UK) and control immunoglobulin G1 (IgG1; AbD Serotec, Oxford, UK) were used for cell culture experiments at 50 μg/mL. Echistatin (Tocris, Bristol, UK) was used in cell culture experiments at 100 nM concentration. The chemical focal adhesion kinase (FAK) inhibitor, PF573228 (Tocris, Bristol, UK) was solubilized in dimethylsulfoxide (DMSO) and used for cell culture experiments at a concentration of 1-5 μM. A detailed description of microscopy and morphological analysis can be found in the Supporting Methods online.

Preparation of Polyacrylamide Gel Supports. Polyacrylamide (PA) gels of variable stiffness were prepared on glass coverslips using modifications[13] to the method initially described by Pelham and Wang.[14] A detailed description can be found in the Supporting Methods online.

View this article online at wileyonlinelibrary.com.
DOI 10.1002/hep.24108
Potential conflict of interest: Nothing to report.
Additional Supporting Information may be found in the online version of this article.

Immunofluorescence Staining. Cells were fixed in 4% paraformaldehyde in phosphate-buffered saline and permeabilized with 0.2% Triton-X-100 in phosphate-buffered saline. Slides were stained with anti-Ki67 (Novocastra, Newcastle, UK) and anti-vinculin (Sigma, Poole, UK); corresponding Alexa Fluor-555 secondary antibodies were used for detection (Invitrogen, Paisley, UK). Actin stress fibers were stained with Alexa-488 phalloidin (Invitrogen). Nuclear DNA was counterstained with 4′,6′-diamidino-2-phenyl-indole dihydrochloride (DAPI; Dako, Ely, UK). Cellular proliferative index (Ki67-positive cells/total cells) was calculated by direct cell counting from 15 randomly selected high magnification photomicrographs from Ki67-stained slides (n = 3).

Western Blot. A detailed description of western blotting and a complete list of antibodies are provided in the Supporting Methods.

Immunohistochemistry. Human HCC specimens were obtained from archived tissue held by Tayside Tissue Bank and the Department of Pathology, University Medical Center Hamburg-Eppendorf with appropriate ethical approval (UK-LREC: TR000216). Immunohistochemistry was performed as previously described.[15] The primary antibodies and antigen retrieval regimes used were anti-pFAK (pY397) (Invitrogen, Paisley, UK/Microwave pH9) and anti-β1-integrin (Abcam, Cambridge, UK/Microwave pH9). Negative controls with isotype immunoglobulins (Santa Cruz, Heidelberg, Germany) and species-specific serum alone showed no specific staining.

Clonogenic Assay. Cells were plated at semi-confluent density onto PA gels. After 48 hours, cells either received cisplatin (HepG2, 10 μM/Huh7, 20 μM) or 5-fluorouracil (5FU; 25 μM) or were left untreated in plating medium. After 24 hours, the medium was changed to normal culture medium and the cells were incubated further for 48 hours, for a total of 5 days of culture. Cells were then retrieved by trypsinization, counted and plated at clonal density (10,000 cells/well) into 12-well plates in normal culture medium. Cells were fixed at between 5-10 days in 4% paraformaldehyde and stained with 0.5% crystal violet solution. Colonies were visualized with a VersaDoc system and analyzed with Quantify-One (Bio-Rad Laboratories, Hercules, CA).

Flow-Cytometric Analysis. Cells were harvested by trypsinization and single cell suspension generated by passing cells through a 40 μm cell strainer. Cells were stained with the following antibodies: CD44-phycoerythrin (PE), CD117-PE (c-kit), CD133-PE, CD184-PE (cysteine-X-cysteine receptor 4 [CXCR-4]), and corresponding PE-labeled isotype controls (E-Bioscience, Hatfield, UK). After staining, cells were washed, post-fixed in 1% paraformaldehyde and analyzed on a FACScan (BD Biosciences, Franklin Lakes, NJ). Data analysis was performed using FlowJo software (TreeStar, Inc., Ashland, OR).

cDNA Synthesis and Real-Time PCR. Relative mRNA expression for genes of interest was determined by real-time PCR using an Applied Biosystems 7700 Sequence Detection System. Primer sequences for the genes of interest and the 18*S* housekeeping gene were purchased from Applied Biosystems (Warrington, UK).

Statistics. Data are expressed as mean ± standard error of the mean (SEM) of at least three independent experiments unless stated otherwise. Comparisons between groups were performed using a two-tailed Student *t* test.

Results

Increasing Matrix Stiffness Is Associated With a Mesenchymal Shift in HCC Cells. The response of HCC cells to alterations in matrix stiffness was investigated using a system of mechanically-tunable ligand-coated PA gels.[13,14] In this system, matrix stiffness is altered by modulating the *bis*-acrylamide crosslink density of thin PA gels without altering the surface composition or density of ligands to which the cells are exposed.[13] Matrix stiffness (expressed as shear modulus, G′) was modeled across a range of pathophysiologically-relevant stiffness values (1-12 kPa) corresponding to values encountered in normal and fibrotic livers.[16] The PA gels used in this study were coated with collagen-I, representing the predominant ECM protein encountered in the fibrotic liver.

For both Huh7 and HepG2 cells we observed a consistent morphological response to changes in support stiffness. HCC cells on soft (1 kPa) supports were small and rounded in contrast to the well-spread and flattened cells seen on stiff (12 kPa) supports (Fig. 1). Differences in cellular spreading as a function of support stiffness develop rapidly (within 1 hour) and are maximal at 24 hours (Supporting Fig. 1). Confocal microscopy showed that increasing matrix stiffness was associated with the development of prominent actin stress fibers and mature (vinculin-positive) focal adhesions (Fig. 2). These features were absent in cells cultured on soft supports. The presence of stress fibers is linked to acquisition of mesenchymal properties (mesenchymal-shift) and de-differentiation in epithelial cells. In accordance with this we demonstrated up-

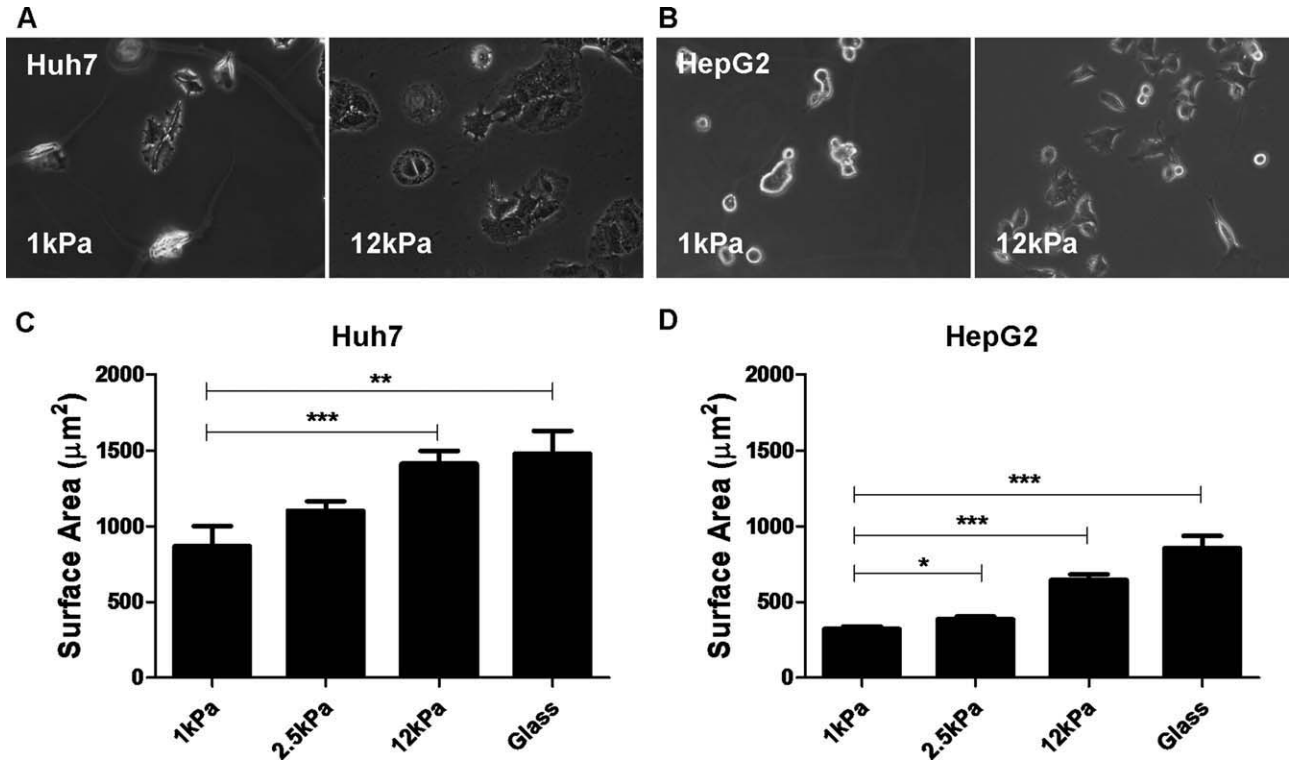

Fig. 1. Changes in matrix stiffness regulate HCC cell morphology and spreading. Huh7 and HepG2 cells were cultured on collagen-I–coated polyacrylamide (PA) gels with "tunable stiffness" (expressed as shear modulus, G′) in the range of 1-12 kPa and collagen-I–coated glass. The stiffness values of the PA gel supports used were selected in order to reflect range of stiffness values encountered in normal and fibrotic livers. Phase-contrast photomicrographs demonstrate the regulation of cellular morphology by support stiffness in both (A) Huh7 and (B) HepG2 cells. The surface area (square micrometers) of (C) Huh7 and (D) HepG2 cells was calculated by digital image analysis of phase-contrast images of cells on PA gel supports. In each case, values reflect the mean (±SEM) of measurements from 50 cells in three independent experiments (*$P < 0.05$, **$P < 0.01$, and ***$P < 0.001$).

regulation of the mesenchymal markers N-cadherin (Huh7/HepG2) and vimentin (shown for Huh7; vimentin is not expressed in HepG2 cells under either condition) in HCC cells cultured on stiff supports (Fig. 3A). There was no change in the expression of the epithelial marker E-cadherin. HepG2 and Huh7 cells cultured on soft supports expressed higher levels of albumin, hepatocyte nuclear factor-4α (HNF4α), alpha-1-antitrypsin and alpha-fetoprotein (AFP) than cells cultured on stiff supports (Fig. 3B). This suggests that a soft environment promotes a differentiated hepatocyte phenotype, whereas increasing support stiffness is associated with cellular de-differentiation toward a mesenchymal phenotype.

TGFβ is a potent inducer of mesenchymal changes in both primary and transformed epithelial cells. We therefore investigated whether support stiffness regulated TGFβ-induced Smad signaling activity in HCC cells. The Huh7 cell line demonstrated increased basal activity of the TGFβ signaling pathway (as indicated by increased Smad3 phosphorylation) in cells cultured on stiff supports (Fig. 3C,D). In addition, upon stimulation with TGFβ there was enhanced Smad2 and Smad3 phosphorylation in cells from stiff supports.

Increasing Matrix Stiffness Promotes HCC Proliferation. In both HCC cell lines, matrix stiffness regulated HCC cell proliferation (Fig. 4A). The proliferative indices of Huh7 and HepG2 cells (assessed by nuclear localization of Ki67) were 2.7-fold ($P < 0.001$) and 12.2-fold ($P < 0.001$) higher, respectively, when the cells were cultured on stiff (12 kPa) versus soft (1 kPa) supports. Maximal proliferative index was seen when cells were cultured on collagen-I–coated glass, which has a shear modulus several orders of magnitude higher than any physiological matrix. Both MTT assay (Supporting Fig. 2) and direct cell counting (data not shown) confirmed an increase in total cell number with increasing support stiffness. A similar trend for cellular proliferation was observed in primary mouse hepatocytes (Supporting Fig. 3). Matrix stiffness had a corresponding effect on the expression of cell cycle regulators of G1 progression (Fig. 4B,C). We observed a strong reduction in the expression of cyclin-D1 and cyclin-D3 in cells cultured on soft

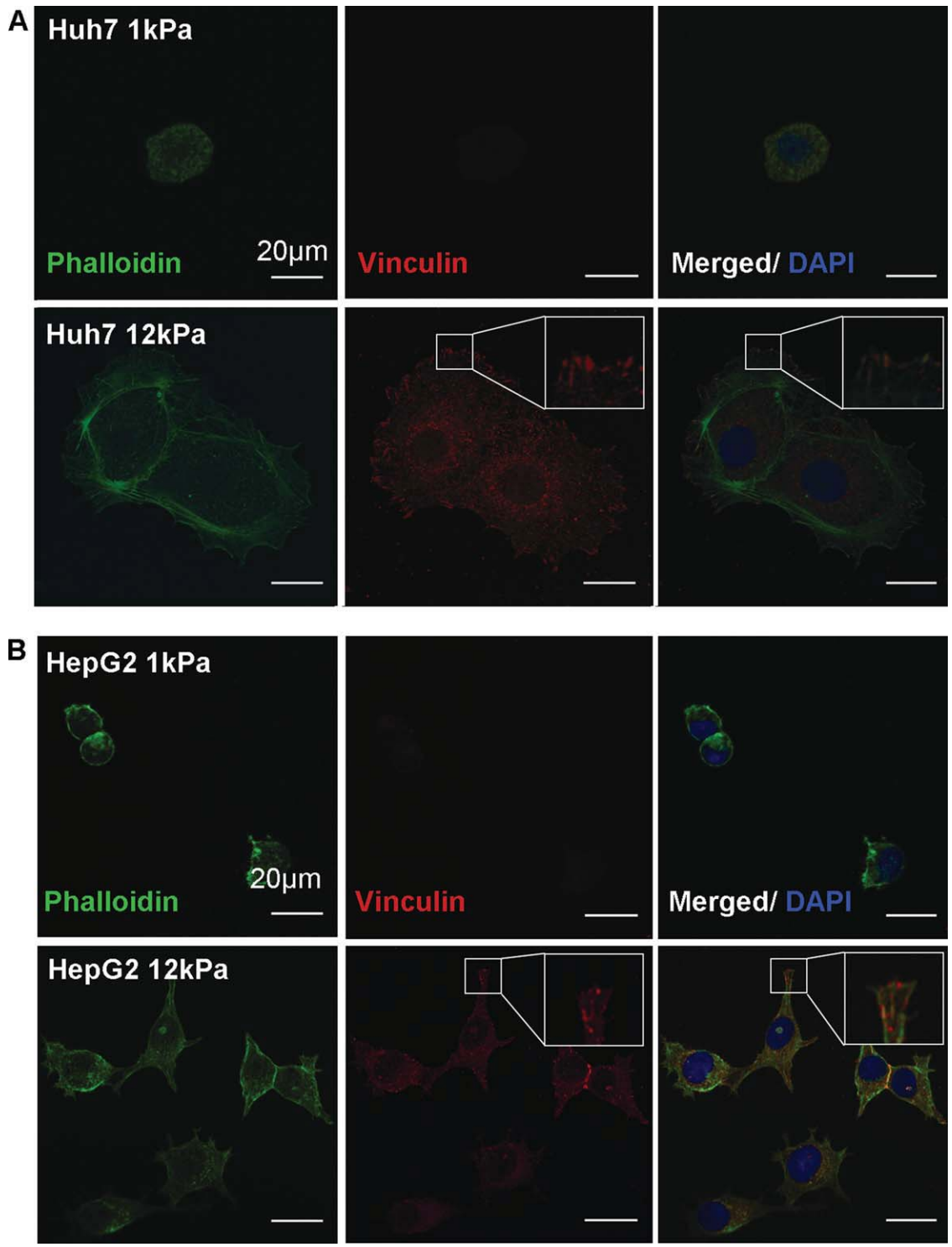

Fig. 2. Changes in matrix stiffness regulate the formation of actin stress fibers and focal adhesion maturation in HCC cells. Confocal microscopy (×320 magnification) of (A) Huh7 and (B) HepG2 cultured on soft (1 kPa) and stiff (12 kPa) collagen-I–coated PA supports as indicated. The photomicrographs displayed are of cells stained for the presence of actin stress fibers (phalloidin: green), mature focal adhesions (anti-vinculin: red), and nuclear DNA (DAPI: blue). The merged image (right panel) demonstrates the spatial relationship between actin stress fibers and mature focal adhesions. Insets display high-magnification images for Huh7 and HepG2 cells cultured on stiff (12 kPa) supports demonstrating the insertion of actin stress fibers into mature focal adhesions. In each image, the scale bars represent 20 μm.

supports. There was no evidence of up-regulation of the cyclin-dependent kinase inhibitors $p21^{cip}$ or $p27^{kip}$ on soft gels and indeed a moderate down-regulation of $p27^{kip}$ was observed on soft gels. Induction of terminal senescence on soft supports was excluded by showing that upon transfer to a stiff matrix, cells resumed

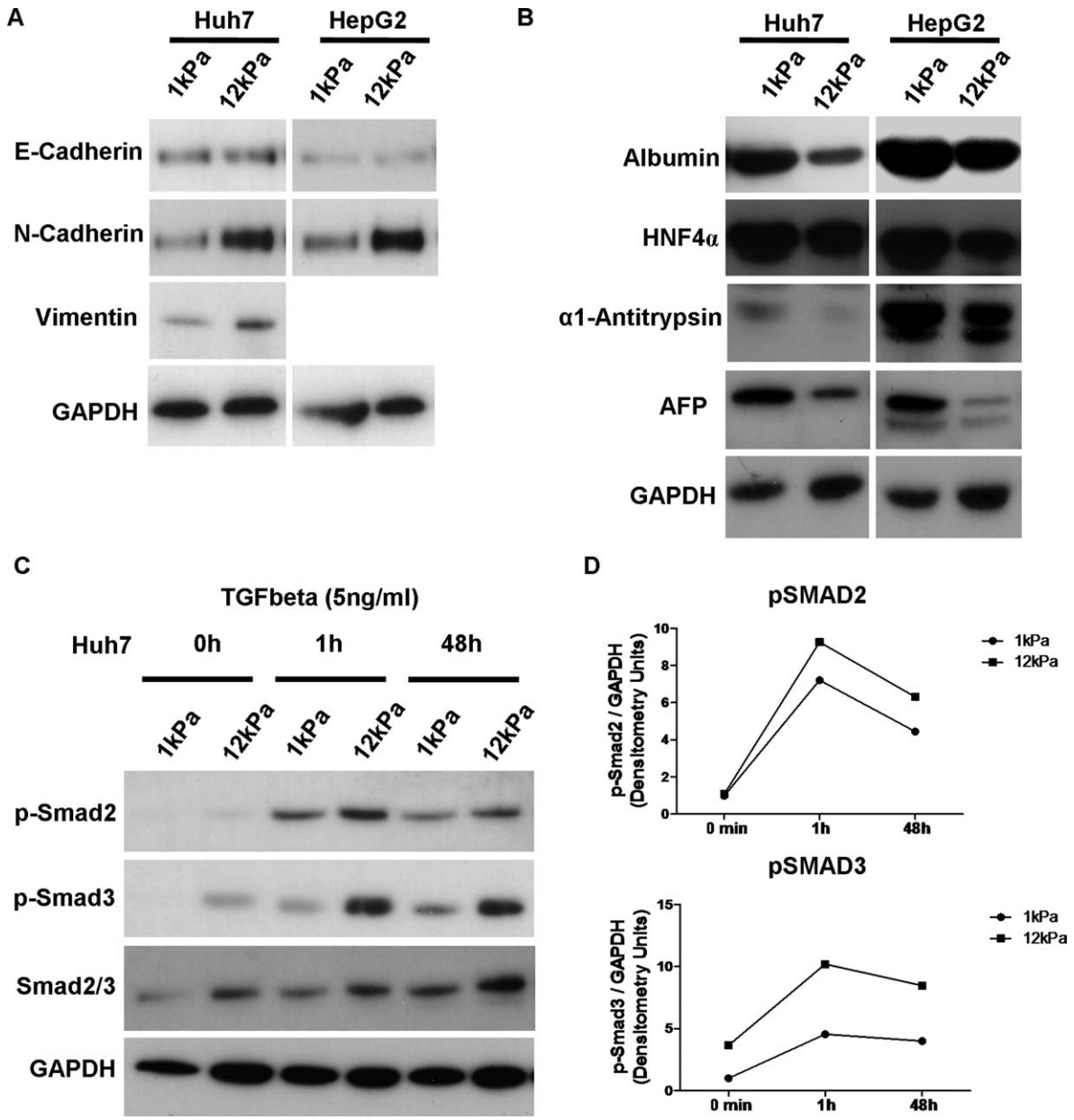

Fig. 3. Increased matrix stiffness is associated with mesenchymal shift in HCC cells. (A) Western blot from whole-cell lysates showing expression of E-cadherin, N-cadherin, and vimentin in Huh7 and HepG2 cells cultured on soft (1 kPa) and stiff (12 kPa) collagen-I–coated PA gel supports (as indicated). (B) Western blots from whole-cell lysates showing expression of albumin, hepatocyte nuclear factor 4 alpha (HNF4α), alpha-1-antitrypsin, and alpha-fetoprotein (AFP) in Huh7 and HepG2 cells. (C) Western blots from whole-cell lysates from Huh7 cells showing the expression of phospho-Smad2, phospho-Smad3, and total Smad2/3 following stimulation with transforming growth factor beta (TGFβ; 5 ng/mL). In each western blot, equal quantities of protein were loaded and equal loading was confirmed in relation to glyceraldehyde 3-phosphate dehydrogenase (GAPDH) expression. In each case, the western blots shown are representative examples from three independent experiments. (D) The line graphs show a schematic representation of densitometry analysis of phosphorylated Smad2 and Smad3, expressed relative to GAPDH. Each time point represents the mean of three independent experiments.

proliferation to levels comparable to cells coming from a stiff matrix (Supporting Fig. 4A). Furthermore, cells on both soft and stiff supports showed no evidence of beta-galactosidase accumulation (data not shown). In each cell line, differences in cellular proliferation as a function of stiffness were evident across a wide range of plating densities (Supporting Fig. 5).

In order to exclude a specific effect related to collagen-I, we investigated the effect of different ECM coatings on HCC cell proliferation on PA gels (Fig. 4D). Although minor differences were observed with respect to cellular morphology and spreading (Supporting Fig. 6) when cells were plated on collagen-I, collagen-IV, laminin and fibronectin-coated

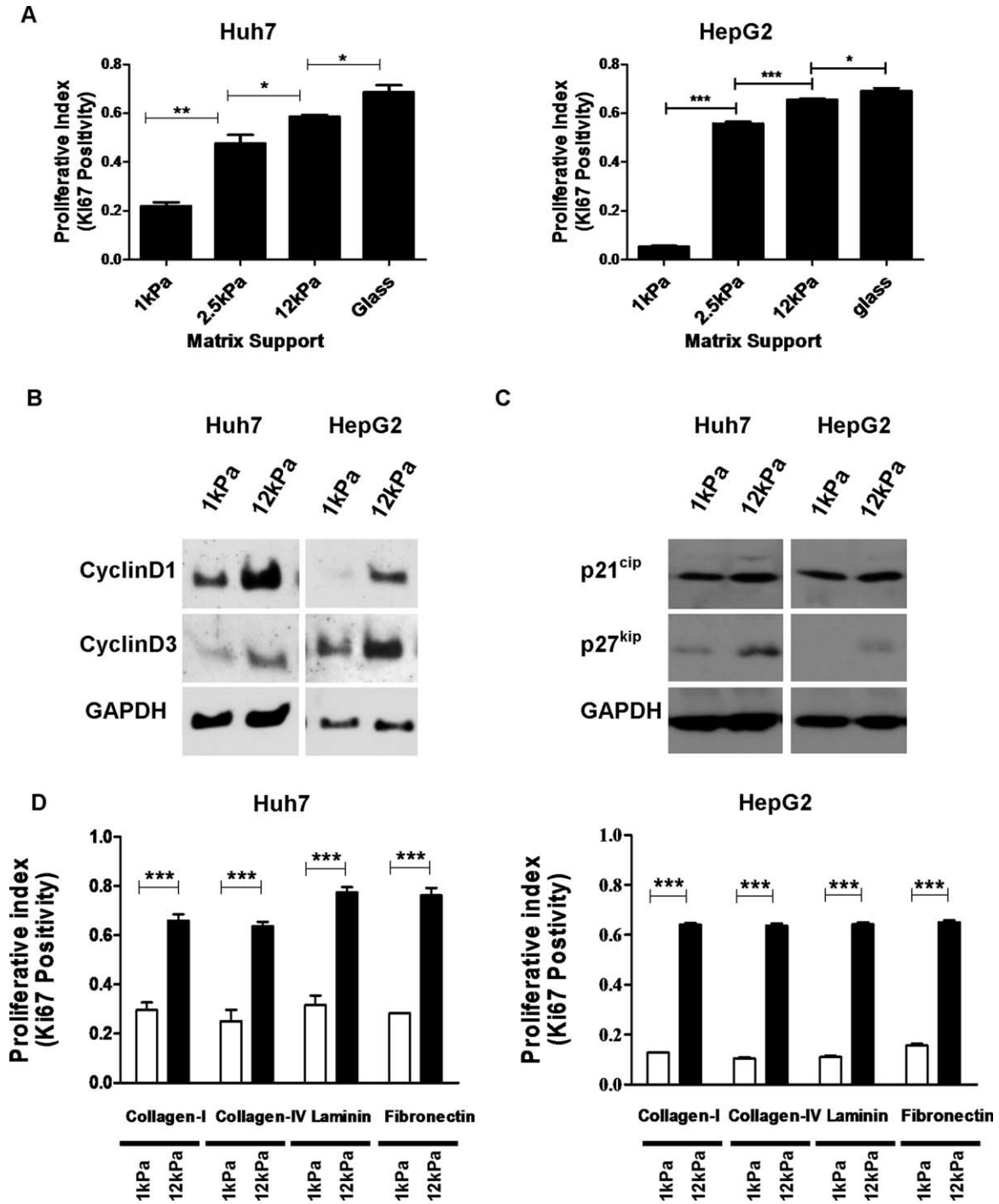

Fig. 4. Increased matrix stiffness promotes HCC cell proliferation. (A) Graphs showing the mean proliferative index (Ki67 positivity) of Huh7 and HepG2 cells cultured on collagen-I–coated polyacrylamide gel supports across a range of stiffness values (1-12 kPa), as indicated, and collagen-I–coated glass (n = 3). (B) Western blots from whole-cell lysates showing expression of cyclin-D1 and cyclin-D3 in Huh7 and HepG2 cells cultured on soft (1 kPa) and stiff (12 kPa) supports, as indicated. (C) Western blots from whole-cell lysates showing expression of cyclin-dependent kinase inhibitors, $p21^{cip}$, and $p27^{kip}$ in Huh7 and HepG2, cultured on soft (1 kPa) and stiff (12 kPa) supports, as indicated. In each western blot, equal quantities of protein were loaded and equal loading confirmed in relation to GAPDH expression. The western blots shown are representative examples from three to six independent experiments. (D). Graphs showing the mean proliferative index (Ki67 positivity) of Huh7 (left panel) and HepG2 (right panel) cells cultured on both soft (1 kPa) and stiff (12 kPa) polyacrylamide supports coated with collagen-I, collagen-IV, laminin, or fibronectin (n = 3). In each case, error bars represent SEM, $*P < 0.05$, $**P < 0.01$, and $***P < 0.001$.

gels, the biochemical composition of the surface coating did not significantly alter the stiffness-dependent regulation of cell proliferation. In other words, the physical rather than the biochemical properties of the PA gels exerted the predominant effect on HCC cell proliferation.

Matrix Stiffness Modulates Basal and HGF-Induced Signaling Responses. Using immunoblotting with phosphorylation-specific antibodies we analyzed stiffness-dependent differences in the activity of critical mitogenic signaling pathways. Growth on stiff (12 kPa) versus soft (1 kPa) supports was associated with enhanced FAK, extracellular signal-regulated kinase (ERK), protein kinase B (PKB/Akt) (Huh7 cells only), and signal transducer and activator of transcription 3 (STAT3) phosphorylation (Fig. 5A). Substrate stiffness significantly modulated growth factor-induced mitogenic signaling in response to HGF. Upon stimulating cells plated on both soft and stiff PA gels with HGF, we observed an increase in the magnitude of ERK, PKB/Akt, and STAT3 activation in cells cultured on stiff gels (Fig. 5C, Supporting Fig. 7). Substrate stiffness also modulated cyclin-D1 expression in response to HGF stimulation. Following HGF stimulation in HepG2 and Huh7 cells, there was up-regulation of cyclin-D1 expression in cells cultured on both soft and stiff supports (Fig. 5B). Importantly, the magnitude of cyclin-D1 induction following HGF stimulation was substantially higher in cells cultured on stiff supports.

***β1-Integrin and Phospho-FAK Are Expressed in Human HCC Tumors and Regulate the Stiffness-Dependent Proliferation of Human HCC Cells* In Vitro.** Integrins and integrin-associated focal adhesions are known to be important mediators of mechanotransduction. We therefore used immunohistochemistry to investigate the prevalence of β1-integrin and phospho-FAK^{Tyr397} expression in HCC tissue from an unselected cohort of 15 HCC specimens obtained at the time of tumor resection or biopsy (Fig. 6A). β1-Integrin was expressed in tumor tissue in all 15 of 15 HCC specimens tested. In addition, we found up-regulation of FAK expression in tumor tissue relative to the surrounding parenchyma in 8/15 (53%) HCC specimens tested. These results are consistent with published histological studies.[17,18] We subsequently investigated the effect of the β1-integrin inhibition on HCC cell proliferation *in vitro* using a function blocking anti–β1-integrin antibody (6S6) and the disintegrin echistatin (Fig. 6C). Anti–β1-integrin antibody and echistatin promoted cellular rounding in both the Huh7 and HepG2 cells cultured on collagen-I–coated 12 kPa (stiff) supports. Huh7 cell proliferation was reduced by treatment with both 6S6 antibody (38% reduction, $P < 0.05$) and echistatin (29% reduction, $P = 0.07$) relative to relevant controls. Similarly, in HepG2 cells, cell proliferation was reduced by treatment with both 6S6 antibody (92% reduction, $P < 0.001$) and echistatin (21% reduction, $P < 0.01$). The effect of FAK activation on HCC cell proliferation was investigated in experiments with the small molecular FAK inhibitor PF573228 (Fig. 6B,C). Treatment with PF573228 (5 μM) was associated with a reduction in the proliferation of both Huh7 (42% reduction, $P < 0.01$) and HepG2 cells (45% reduction, $P < 0.001$) cultured on collagen-I–coated 12 kPa polyacrylamide gels. Furthermore, inhibition of β1-integrin or FAK expression in HepG2 cells with siRNA resulted in a significant reduction in cellular proliferation relative to control siRNA transfection (Supporting Fig. 8). A similar trend in respect to cellular proliferation was observed following siRNA-dependent inhibition of β1-integrin or FAK expression in Huh7 cells, although in this case the reduction was not statistically significant.

Matrix Stiffness Modulates HCC Apoptosis and Clone-Forming Capability Following Chemotherapy. HCC is resistant to treatment with conventional chemotherapeutic agents. We therefore investigated whether the stiffness of the cancer cell niche regulates the susceptibility of HCC cells to chemotherapy-induced apoptosis. In both cell lines, there was decreased apoptosis in cells cultured on stiff supports, as indicated by reduced poly-ADP-ribose polymerase (PARP) cleavage (Fig. 7A). There was a nonsignificant trend toward increased numbers of surviving cells on stiff supports (data not shown). We also performed a series of clonogenic assays to investigate whether changes in matrix stiffness modulate the survival and behavior of tumor-initiating cells after chemotherapy. Following cisplatin treatment, the surviving cell population included an increased frequency of clone-initiating cells for both HepG2 (2.4-fold, $P < 0.001$) and Huh7 cells (2.2-fold, $P < 0.05$) cultured on soft (1 kPa) versus stiff (12 kPa) supports (Fig. 7B). In addition, there was a nonsignificant trend toward an absolute increase in the total number of clone-forming cells from soft supports (data not shown). To assess the validity of this finding, experiments were repeated using a second, unrelated chemotherapeutic agent, 5-fluorouracil (5-FU). Consistent with our findings with cisplatin, following 5-FU chemotherapy there was an increased frequency of clone-initiating cells from HepG2 (3.6-fold, $P < 0.001$) and Huh7 cells (1.9-fold, $P < 0.05$) cultured on soft versus stiff supports. There was no difference in the frequency of clone-initiating cells in untreated HepG2 or Huh7 cells after culture on soft or stiff supports in the absence of chemotherapy.

The paradoxical increase in the clone-initiating capability of chemotherapy-treated cells from a low stiffness environment could be explained by selective

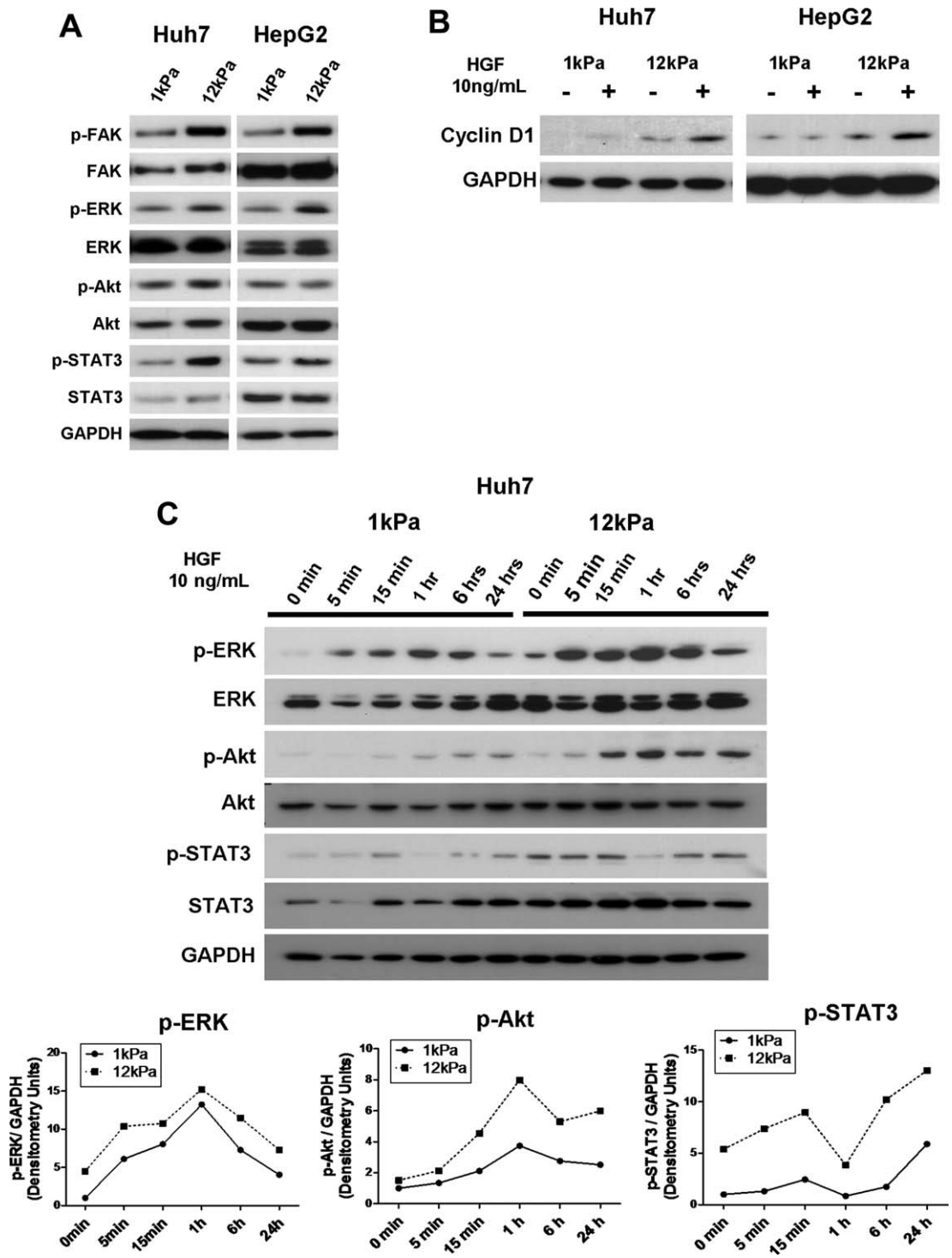

Fig. 5. Matrix stiffness regulates mitogenic signaling in HCC. (A) Western blots showing basal expression of phosphorylated and total FAK, ERK, protein kinase B (PKB/Akt), and STAT3 in Huh7 and HepG2 cells cultured on soft (1 kPa) and stiff (12 kPa) supports, as indicated. (B) Western blots showing cyclin-D1 expression in Huh7 and HepG2 cells cultured for 24 hours on soft (1 kPa) and stiff (12 kPa) supports in the presence (+) or absence (−) of HGF (10 ng/mL). (C) Western blots showing a time-course analysis for expression of phosphorylated and total ERK, PKB/Akt, and STAT3 in Huh7 cells cultured on soft (1 kPa) and stiff (12 kPa) supports. Whole-cell lysates were harvested at baseline and specific time points (as indicated) following the addition of HGF (10 ng/mL) to culture media. In each western blot, equal quantities of protein were loaded and equal loading was confirmed in relation to GAPDH expression. The line graphs (right panel) show a schematic representation of densitometry analysis of phosphorylated ERK, PKB/Akt, and STAT3 expressed relative to GAPDH. Each time point represents the mean of three independent experiments.

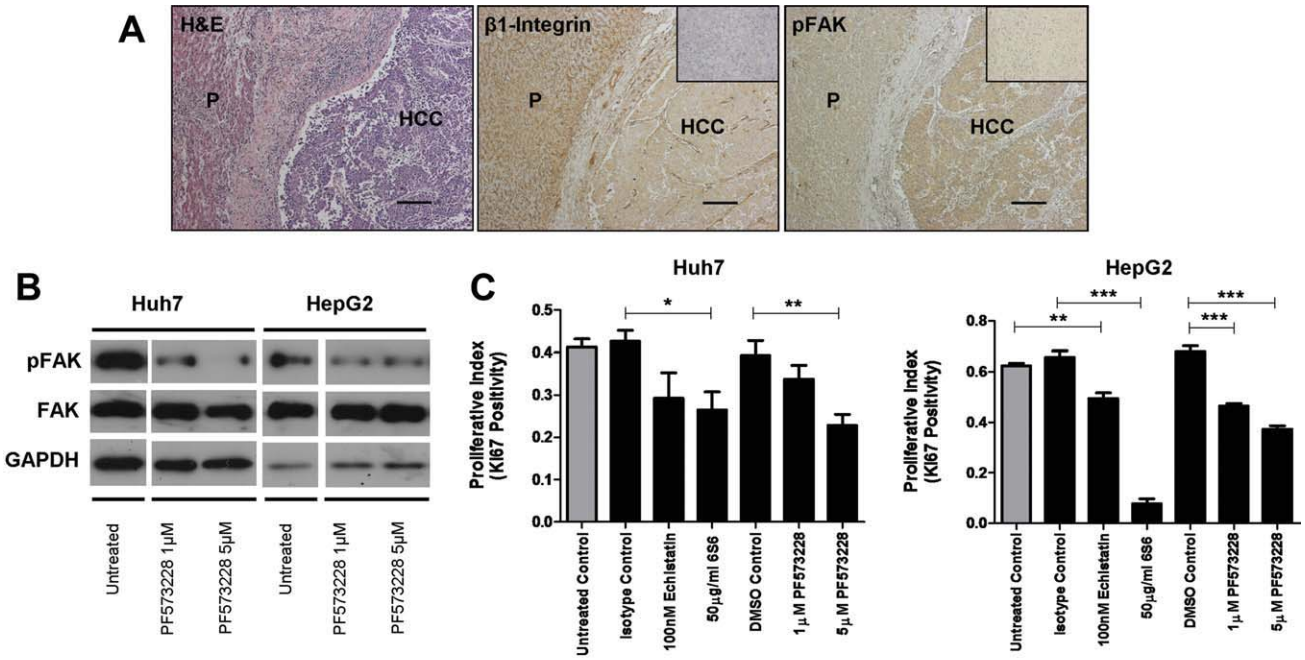

Fig. 6. β1-Integrin and phospho-FAK are expressed in human HCC tumors and regulate the stiffness-dependent proliferation of human HCC cells *in vitro*. (A) Low magnification ($\times$50) photomicrographs from a human HCC resection specimen stained with hematoxylin and eosin (left panel), anti-β1-integrin (middle panel) and anti-phospho-FAK (right panel). Negative control staining is represented by the indented images in the top righthand corner of each image. β1-integrin is expressed in both the HCC tumor (HCC) and surrounding hepatic parenchyma (P), as indicated. Phospho-FAK^{Tyr397} is strongly expressed in the HCC tissue relative to the hepatic parenchyma. Scale bars represent 200 micrometers. (B) Western blots showing the expression of phospho-FAK^{Tyr397} in Huh7 and HepG2 cells either left untreated or treated for 24 hours with the focal adhesion kinase (FAK) inhibitor PF573228 at concentrations of 1 μM and 5 μM, as indicated. In each western blot, equal quantities of protein were loaded and equal loading confirmed in relation to GAPDH expression. (C) Graphs showing the mean proliferative index (Ki67 positivity) of Huh7 and HepG2 cells cultured on 12 kPa (stiff) collagen-I-coated polyacrylamide supports. Cells were treated with the anti-β1-integrin antibody 6S6 (50 μg/mL), isotype control IgG1 antibody (50 μg/mL), echistatin (100 nm), PF573228 (1 μM), PF573228 (5μM), DMSO (vehicle control), or left in media alone (untreated control) for 24 hours, as indicated (n = 3-5). In each case, error bars represent SEM, *$P < 0.05$, **$P < 0.01$, and ***$P < 0.001$.

enrichment for clone-initiating cells with stem cell characteristics. We therefore performed flow-cytometric analyses for putative cancer stem cell markers in HCC cells cultured on soft (1 kPa) and stiff (12 kPa) supports, both without and following cisplatin treatment (Fig. 8A). Culture on soft versus stiff supports was associated with an enrichment for the cell surface markers CD133 (1.5-fold, $P < 0.001$), c-kit (1.3-fold, $P = 0.78$), CD44 (6.4-fold, $P < 0.001$), and CXCR-4 (2.9-fold, $P < 0.01$). Following cisplatin treatment, there was statistically significant up-regulation of CD44 (1.7-fold, $P < 0.01$), CD133 (1.6-fold, $P < 0.01$) and c-kit (15.8-fold, $P < 0.01$) for cells maintained on soft but not stiff supports. Additionally, real-time PCR demonstrated up-regulation of stem cell-associated transcription factors OCT4 and NANOG in HepG2 cells cultured on soft versus stiff supports, both in untreated controls (OCT4 2.0-fold increase, $P < 0.05$; NANOG 2.7-fold increase, $P < 0.05$) and following cisplatin treatment (OCT4 2.0-fold increase, $P < 0.05$; NANOG 3.4-fold increase, $P < 0.05$) (Fig. 8B).

Discussion

In this study, we demonstrated that the stiffness of the subcellular matrix profoundly alters the phenotype and behavior of HCC cells *in vitro*. Pathophysiological increases in matrix stiffness, as encountered in fibrotic and cirrhotic livers,[19] promote the proliferation of HCC cells. Our work defines novel mechanisms linking the physical properties of the fibrotic liver and the malignant behavior of HCC. Our data is consistent with *in vivo* evidence, not only of *de novo* HCC development and progression against a background of cirrhosis, but also animal studies showing that the induction of liver fibrosis is associated with accelerated tumor growth following orthotopic HCC implantation.[20,21] Furthermore, histological examination of human HCC specimens demonstrates a significant association between the presence of hepatic fibrosis and enhanced tumor cell proliferation.[22] Critically, our findings suggest that a reduction in the stiffness of the cancer cell niche, as would be encountered by a

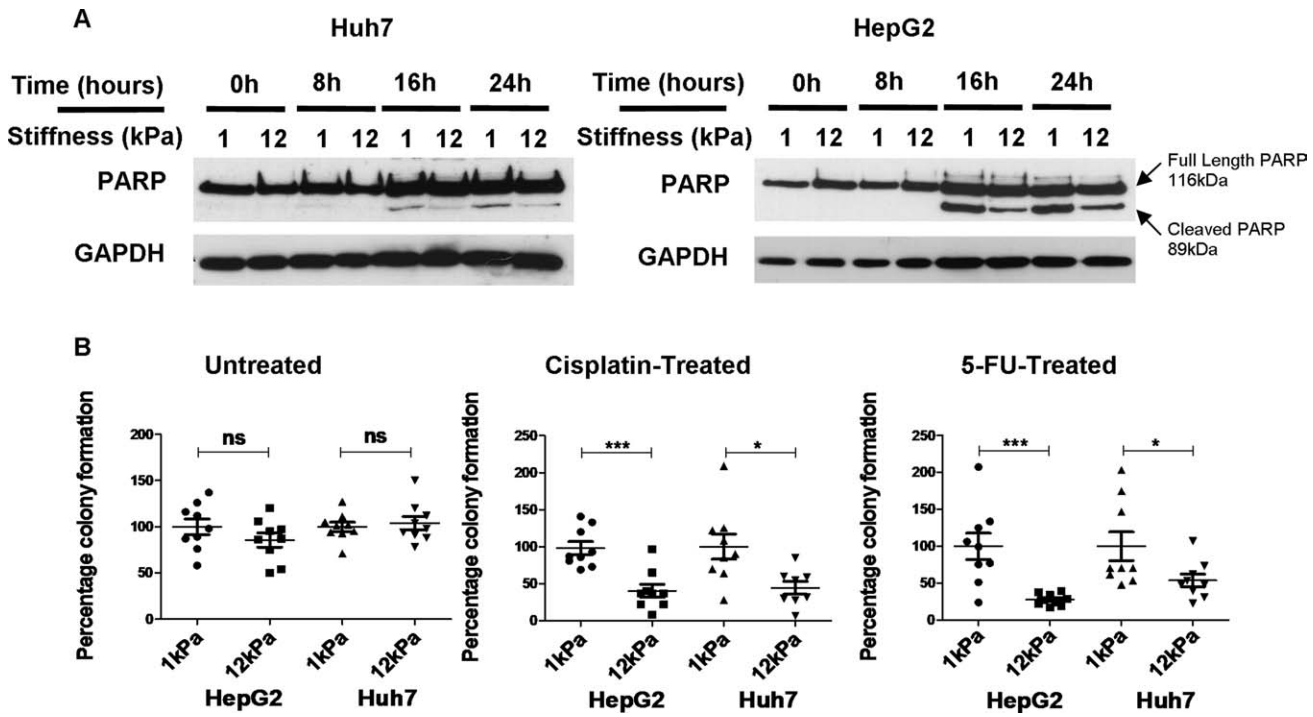

Fig. 7. Matrix stiffness regulates apoptosis and clonogenic capacity following chemotherapy. (A) Western blot showing full-length (116 kDa) and cleaved poly-ADP-ribose polymerase (PARP) (89 kDa) expression in Huh7 and HepG2 cells following treatment with cisplatin on soft (1 kPa) and stiff (12 kPa) supports, as indicated. In each western blot, equal quantities of protein were loaded and equal loading was confirmed in relation to GAPDH expression. The western blots shown are representative examples from three independent experiments. (B) Colony formation potential of Huh7 and HepG2 cells following chemotherapy. Huh7 and HepG2 cells were cultured for 48 hours on either soft (1 kPa) or stiff (12 kPa) polyacrylamide supports. Cells were then left untreated (left panel) or treated with cisplatin (middle panel) or 5-fluorouracil (5-FU) (right panel) for 24 hours prior to media change. After a further 48 hours in culture, the cells were trypsinized and equal numbers re-plated at clonal density in 12-well plates. Clonogenic capacity was calculated by direct counting of the resulting colonies. The results are expressed as the percentage colony formation relative to the number of colonies obtained from 1 kPa supports from three independent experiments. In each case, error bars represent SEM, *$p<0.05$, ***$p<0.001$ and ns=not significant.

disseminated tumor cell entering an unaffected secondary site, would be sufficient to promote reversible cellular quiescence and cancer cell dormancy.

It has previously been demonstrated that matrix stiffness can regulate proliferation in nontransformed cells. More recently increased matrix stiffness has been shown to promote cellular proliferation in glioma cells.[23] We have extended these findings to a range of epithelial malignancies, including HCC (Supporting Fig. 9). Furthermore, we have shown that β1-integrin and FAK (the canonical mediator of integrin-related signaling) regulate stiffness-dependent proliferation in HCC cells. In both fibroblasts and nontransformed mammary epithelial cells, a critical role for ERK-induced cyclin-D induction has been established in the stiffness-dependent regulation of cell proliferation.[24] In accordance with these findings we demonstrate both an up-regulation of cyclin-D levels and increased mitogenic signaling through ERK in HCC cells on stiff substrates. Interestingly, reduced ERK activation has previously been linked to cellular quiescence in a cell line-specific model of cancer dormancy.[25] Additionally, for the first time, we demonstrate a role for matrix stiffness in modulating the activation of the STAT3 pathway. STAT3 has recently been identified as a central component in tumor progression and a potential target of cancer therapy in HCC and other epithelial malignancies.[26] The STAT3 pathway is activated in response to multiple cytokines and growth factors during cancer-associated inflammation (e.g., interleukin-6, interleukin-10, epidermal growth factor, and HGF). Our findings demonstrate that matrix stiffness has a substantial impact upon the intrinsic and extrinsic (growth factor-induced) activation of the STAT3 pathway. This indicates an additional role for biophysical factors in regulating this critical signaling pathway. Interactions between pathways conveying information from both soluble mediators and the ECM are integrated at the level of the cytoskeleton. In this context, the role of cytoskeletal tension has been likened to a cellular rheostat, acting to dampen or augment the responses of multiple signaling pathways to growth factor stimulation, thereby blocking or facilitating mitogenic responses.

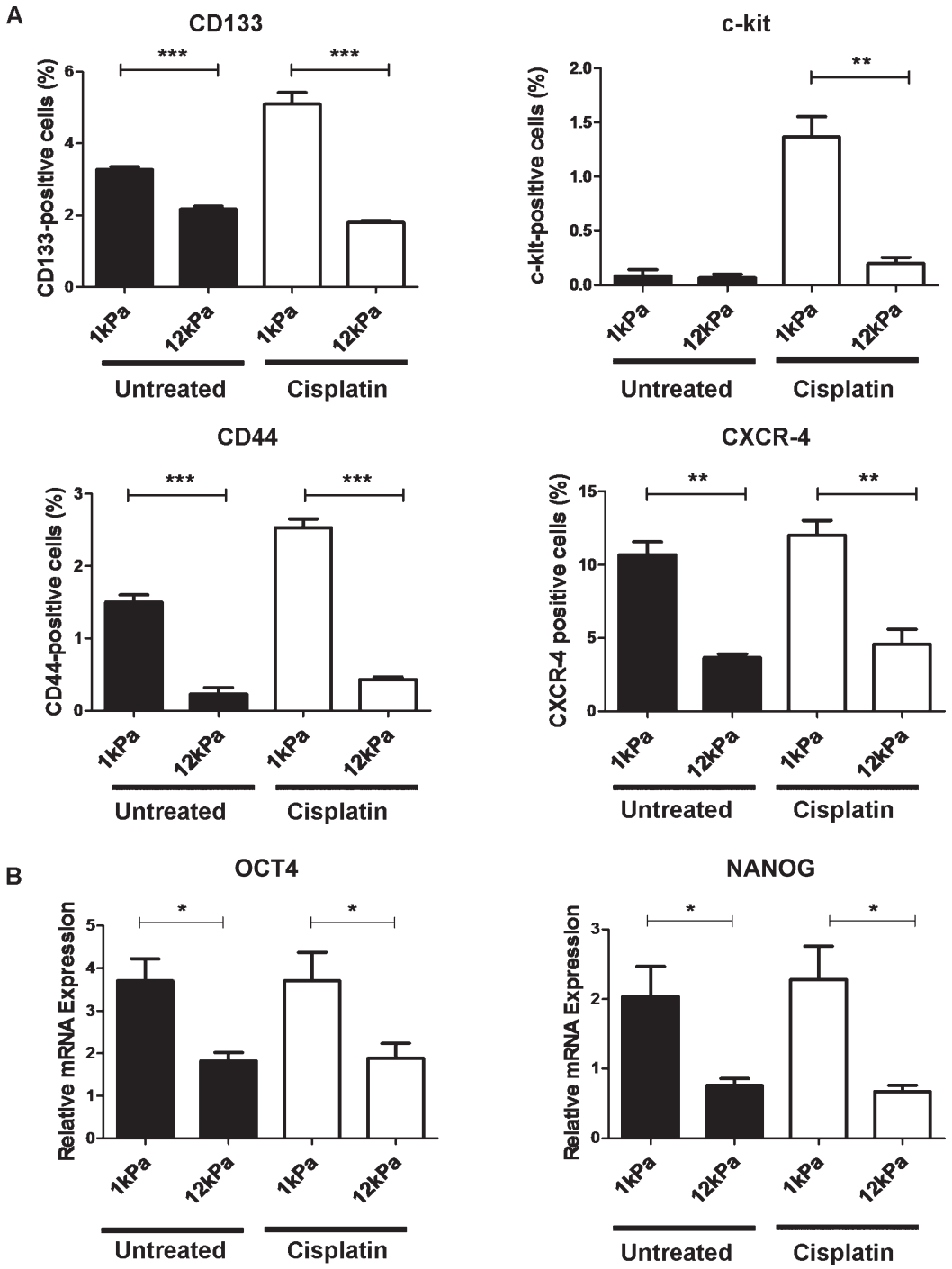

Fig. 8. Matrix stiffness and chemotherapy regulate stem cell marker expression in HepG2 cells. (A) Quantification by flow cytometric analysis of putative cancer stem cell markers CD133, c-kit, CD44 and CXCR-4 in HepG2 cells cultured for 5 days on soft (1 kPa) or stiff (12 kPa) supports. Cells were either left untreated (black) or treated for 24 hours with cisplatin (white). Results are representative of three independent experiments. (B) Real-time quantitative PCR analysis of octamer-4 (OCT4) (left panel) and NANOG (right panel) expression in HepG2 cells cultured for 5-days on soft (1 kPa) or stiff (12 kPa) supports. Cells were either left untreated (black) or treated for 24 hours with cisplatin (white). Expression is relative to the 18S housekeeping gene. In each case, error bars represent SEM, $*P < 0.05$, $**P < 0.01$, and $***P < 0.001$.

It has been proposed that the ECM is a critical regulator of cellular dormancy[27]; however the role of matrix stiffness in regulating this process has not been specifically addressed. The growth, invasion and dissemination of tumor cells are accompanied by dramatic changes in the mechanical properties (stiffness) of the cancer cell niche. The bone marrow, a common reservoir site for disseminated tumor cells, provides a microenvironment with stiffness significantly lower than that encountered in most epithelial tumors.[28]

Our findings suggest that a reduction in the stiffness of the cancer cell niche would be sufficient to promote reversible cellular quiescence (dormancy). Furthermore, increases in environmental stiffness (as may occur with inflammation, surgery or stromal reaction to tumor) or alteration in the stiffness-sensing machinery of the cell (as a result of genomic instability) might facilitate reactivation. Indeed, early work on cancer cell dormancy in animal models established inflammation and surgical trauma as a mechanism of reactivation of dormant cells.[29,30] More recently, fibrosis-associated collagen-I has been linked to reactivation of tumor cells in an *in vivo* model of cancer cell dormancy.[31] With respect to the liver, tumor growth and intrahepatic metastasis have been shown to be enhanced in a fibrotic environment.[20-22]

The precise phenotype of disseminated tumor cells derived from epithelial malignancies remains poorly defined.[32] During tumor dissemination, tumor cells are believed to acquire mesenchymal properties, enabling them to migrate through and invade surrounding tissues and enter the bloodstream.[33] However, at secondary sites, tumor cells are primarily detected by their epithelial characteristics and outgrowing metastases recapitulate the epithelial phenotype of the primary tumor.[34] Despite our increasing understanding of the regulation of epithelial-to-mesenchymal transition, the reverse process—mesenchymal-to-epithelial transition—is largely uncharacterized. We have demonstrated that HCC cells lose mesenchymal features, including stress fibers, N-cadherin, and vimentin expression, and the cells up-regulate markers of hepatocyte differentiation when maintained in a soft environment. This is consistent with previous findings showing that nontransformed mammary epithelial cells revert to an organized epithelial phenotype in a soft environment[6] and that hepatocytes retain an epithelial phenotype on soft collagen gels.[35] FAK activation has been implicated in the process of epithelial-to-mesenchymal transition and responsiveness to TGFβ.[36] It remains unclear whether reduced FAK activation and TGFβ signaling in cells in a low stiffness environment is a mechanistic link to mesenchymal-to-epithelial transition.

The high rate of chemotherapy resistance in HCC is a major obstacle in treating patients with advanced disease. Identifying the mechanism of this resistance has the potential to reveal new treatment options for this group of patients. We have provided evidence that increasing ECM stiffness, as encountered by cells within an established tumor,[4] reduces chemotherapy-induced apoptosis. However, the clinical utility of systemic chemotherapy is also limited by the failure of adjuvant/neoadjuvant chemotherapy to target disseminated tumor cells that give rise to late tumor recurrence and metastases.[32,37] Intriguingly, we have been able to demonstrate an increase in clone-initiating capability following chemotherapy in cells from a low stiffness environment. This was accompanied by an increase of cells positive for cancer stem cell markers (CD44, CD133, c-kit, CXCR-4, OCT4, and NANOG).[38] This provides a potential mechanism for long-term survival and clone-initiating capability of disseminated tumor cells in a soft environment (e.g., bone marrow) following chemotherapy. Whether the higher frequency of cells with a cancer stem cell phenotype is due to positive selection or active induction of cancer stem cell characteristics needs to be determined.

In summary, we have provided evidence that the biomechanical composition of the ECM is a critical regulator of HCC behavior. We suggest that the high stiffness environment encountered in chronic fibrotic liver disease fosters HCC progression by promoting cellular proliferation, a mesenchymal phenotype and resistance to chemotherapy. Conversely, a soft physiological environment (as might be encountered by a disseminated tumor cell) induces cellular dormancy, a stem cell phenotype and enhanced clonogenic capacity following chemotherapy. Indeed, we propose that alterations in the stiffness of the cancer cell niche are responsible for regulating cancer cell proliferation and phenotype throughout the natural history of HCC. Manipulation of environmental stiffness or interference with the stiffness-sensing apparatus of HCC cells has the potential to impede both tumor growth and reactivation of dormant tumor cells, thereby limiting recurrence. In concert with future *in vivo* models of HCC, these findings will provide a platform for the future design of therapies targeting the biomechanical properties of the cancer cell niche.

Acknowledgment: The authors would like to acknowledge the assistance of Dr. David Hay (University of Edinburgh), who was supported by a fellowship from the Research Council UK, for his intellectual input with respect to experimental design. They would also like to thank Prof. Margaret Frame (University of Edinburgh) and Dr. Jim Norman (University of Glasgow) for advice in respect to experimental reagents.

References

1. Parkin DM, Bray F, Ferlay J, Pisani P. Estimating the world cancer burden: Globocan 2000. Int J Cancer 2001;94:153-156.

2. Fattovich G, Stroffolini T, Zagni I, Donato F. Hepatocellular carcinoma in cirrhosis: incidence and risk factors. Gastroenterology 2004;127(5 Suppl 1):S35-S50.
3. Masuzaki R, Tateishi R, Yoshida H, Goto E, Sato T, Ohki T, et al. Prospective risk assessment for hepatocellular carcinoma development in patients with chronic hepatitis C by transient elastography. HEPATOLOGY 2009;49:1954-1961.
4. Masuzaki R, Tateishi R, Yoshida H, Sato T, Ohki T, Goto T, et al. Assessing liver tumor stiffness by transient elastography. Hepatol Int 2007;1:394-397.
5. Ingber DE. Can cancer be reversed by engineering the tumor microenvironment? Semin Cancer Biol 2008;18:356-364.
6. Paszek MJ, Zahir N, Johnson KR, Lakins JN, Rozenberg GI, Gefen A, et al. Tensional homeostasis and the malignant phenotype. Cancer Cell 2005;8:241-254.
7. Levental KR, Yu H, Kass L, Lakins JN, Egeblad M, Erler JT, et al. Matrix crosslinking forces tumor progression by enhancing integrin signaling. Cell 2009;139:891-906.
8. Nowak AK, Chow PK, Findlay M. Systemic therapy for advanced hepatocellular carcinoma: a review. Eur J Cancer 2004;40:1474-1484.
9. Bruix J, Sherman M, Llovet JM, Beaugrand M, Lencioni R, Burroughs AK, et al. Clinical management of hepatocellular carcinoma. Conclusions of the Barcelona-2000 EASL conference. European Association for the Study of the Liver. J Hepatol 2001;35:421-430.
10. Mathurin P, Raynard B, Dharancy S, Kirzin S, Fallik D, Pruvot FR, et al. Meta-analysis: evaluation of adjuvant therapy after curative liver resection for hepatocellular carcinoma. Aliment Pharmacol Ther 2003; 17:1247-1261.
11. Sethi T, Rintoul RC, Moore SM, MacKinnon AC, Salter D, Choo C, et al. Extracellular matrix proteins protect small cell lung cancer cells against apoptosis: a mechanism for small cell lung cancer growth and drug resistance in vivo. Nat Med 1999;5:662-668.
12. Conti JA, Kendall TJ, Bateman A, Armstrong TA, Papa-Adams A, Xu Q, et al. The desmoplastic reaction surrounding hepatic colorectal adenocarcinoma metastases aids tumor growth and survival via alpha(v) integrin ligation. Clin Cancer Res 2008;14:6405-6413.
13. Engler A, Bacakova L, Newman C, Hategan A, Griffin M, Discher D. Substrate compliance versus ligand density in cell on gel responses. Biophys J 2004;86(1 Pt 1):617-628.
14. Pelham RJ Jr, Wang Y. Cell locomotion and focal adhesions are regulated by substrate flexibility. Proc Natl Acad Sci U S A 1997;94: 13661-13665.
15. Kendall TJ, Hennedige S, Aucott RL, Hartland SN, Vernon MA, Benyon RC, et al. p75 Neurotrophin receptor signaling regulates hepatic myofibroblast proliferation and apoptosis in recovery from rodent liver fibrosis. HEPATOLOGY 2009;49:901-910.
16. Georges PC, Hui JJ, Gombos Z, McCormick ME, Wang AY, Uemura M, et al. Increased stiffness of the rat liver precedes matrix deposition: implications for fibrosis. Am J Physiol Gastrointest Liver Physiol 2007; 293:G1147-G1154.
17. Patriarca C, Roncalli M, Gambacorta M, Cominotti M, Coggi G, Viale G. Patterns of integrin common chain beta 1 and collagen IV immunoreactivity in hepatocellular carcinoma. Correlations with tumour growth rate, grade and size. J Pathol 1993;171:5-11.
18. Fujii T, Koshikawa K, Nomoto S, Okochi O, Kaneko T, Inoue S, et al. Focal adhesion kinase is overexpressed in hepatocellular carcinoma and can be served as an independent prognostic factor. J Hepatol 2004;41:104-111.
19. Castera L, Vergniol J, Foucher J, Le Bail B, Chanteloup E, Haaser M, et al. Prospective comparison of transient elastography, Fibrotest, APRI, and liver biopsy for the assessment of fibrosis in chronic hepatitis C. Gastroenterology 2005;128:343-350.
20. Kornek M, Raskopf E, Tolba R, Becker U, Klockner M, Sauerbruch T, et al. Accelerated orthotopic hepatocellular carcinomas growth is linked to increased expression of pro-angiogenic and prometastatic factors in murine liver fibrosis. Liver Int 2008;28:509-518.
21. Kuriyama S, Yamazaki M, Mitoro A, Tsujimoto T, Kikukawa M, Tsujinoue H, et al. Hepatocellular carcinoma in an orthotopic mouse model metastasizes intrahepatically in cirrhotic but not in normal liver. Int J Cancer 1999;80:471-476.
22. Osada S, Kanematsu M, Imai H, Goshima S, Sugiyama Y. Hepatic fibrosis influences the growth of hepatocellular carcinoma. Hepatogastroenterology 2008;55:184-187.
23. Ulrich TA, de Juan Pardo EM, Kumar S. The mechanical rigidity of the extracellular matrix regulates the structure, motility, and proliferation of glioma cells. Cancer Res 2009;69:4167-4174.
24. Klein EA, Campbell LE, Kothapalli D, Fournier AK, Assoian RK. Joint requirement for Rac and ERK activities underlies the mid-G1 phase induction of cyclin D1 and S phase entry in both epithelial and mesenchymal cells. J Biol Chem 2008;283:30911-30918.
25. Aguirre Ghiso JA, Kovalski K, Ossowski L. Tumor dormancy induced by downregulation of urokinase receptor in human carcinoma involves integrin and MAPK signaling. J Cell Biol 1999;147:89-104.
26. Hedvat M, Huszar D, Herrmann A, Gozgit JM, Schroeder A, Sheehy A, et al. The JAK2 inhibitor AZD1480 potently blocks Stat3 signaling and oncogenesis in solid tumors. Cancer Cell 2009;16:487-497.
27. Barkan D, Green JE, Chambers AF. Extracellular matrix: a gatekeeper in the transition from dormancy to metastatic growth. Eur J Cancer 2010;46:1181-1188.
28. Levental I, Georges PC, Janmey PA. Soft biological materials and their influence on cell function. Soft Matter 2007;3:299-306.
29. Fisher B, Fisher ER. Experimental evidence in support of the dormant tumor cell. Science 1959;130:918-919.
30. Agostino D, Cliffton EE. Organ localization and the effect of trauma on the fate of circulating cancer cells. Cancer Res 1965;25: 1728-1732.
31. Barkan D, El Touny LH, Michalowski AM, Smith JA, Chu I, Davis AS, et al. Metastatic growth from dormant cells induced by a col-I-enriched fibrotic environment. Cancer Res 2010;70:5706-5716.
32. Vessella RL, Pantel K, Mohla S. Tumor cell dormancy: an NCI workshop report. Cancer Biol Ther 2007;6:1496-1504.
33. Yilmaz M, Christofori G. EMT, the cytoskeleton, and cancer cell invasion. Cancer Metastasis Rev 2009;28:15-33.
34. Guarino M, Rubino B, Ballabio G. The role of epithelial-mesenchymal transition in cancer pathology. Pathology 2007;39:305-318.
35. Godoy P, Hengstler JG, Ilkavets I, Meyer C, Bachmann A, Muller A, et al. Extracellular matrix modulates sensitivity of hepatocytes to fibroblastoid dedifferentiation and transforming growth factor beta-induced apoptosis. HEPATOLOGY 2009;49:2031-2043.
36. Cicchini C, Laudadio I, Citarella F, Corazzari M, Steindler C, Conigliaro A, et al. TGFbeta-induced EMT requires focal adhesion kinase (FAK) signaling. Exp Cell Res 2008;314:143-152.
37. Naumov GN, Townson JL, MacDonald IC, Wilson SM, Bramwell VH, Groom AC, et al. Ineffectiveness of doxorubicin treatment on solitary dormant mammary carcinoma cells or late-developing metastases. Breast Cancer Res Treat 2003;82:199-206.
38. Lee TK, Castilho A, Ma S, Ng IO. Liver cancer stem cells: implications for a new therapeutic target. Liver Int 2009;29:955-965.